Study of the mechanical behavior of steel/concrete interfaces : contribution of the analysis at the mesoscopic scale

Mohammad Abbas

To cite this version:

Mohammad Abbas. Study of the mechanical behavior of steel/concrete interfaces : contribution of the analysis at the mesoscopic scale. Structures. Université Paris-Saclay, 2022. English. NNT : 2022UPAST140 . tel-04319572

HAL Id: tel-04319572
https://theses.hal.science/tel-04319572

Submitted on 3 Dec 2023

Study of the mechanical behavior of steel/concrete interfaces: contribution of the analysis at the mesoscopic scale

Etude du comportement mécanique des interfaces acier/béton: apport de l'analyse à l'échelle mésoscopique

Thèse de doctorat de l'université Paris-Saclay

École doctorale n° 579, sciences mécaniques et énergétiques, matériaux et géosciences (SMEMaG)
Spécialité de doctorat : Génie civil
Graduate School : Sciences de l'ingénierie et des systèmes
Référent : Faculté des sciences d'Orsay

Thèse préparée dans l'unité de recherche **Service d'Étude du Comportement des Radionucléides** (Université Paris-Saclay, CEA),
sous la direction de **Benoît BARY**, Ingénieur chercheur (CEA Saclay),
et la co-direction de **Ludovic JASON**, Ingénieur chercheur (CEA Saclay)

Thèse soutenue à Paris-Saclay, le 2 décembre 2022, par

Mohammad ABBAS

Composition du Jury

Membres du jury avec voix délibérative

Christian LA BORDERIE Professeur des Universités, Université de Pau et des Pays-de-l'Adour	Président
Luc DAVENNE Professeur des Universités, Université Paris Nanterre	Rapporteur & Examinateur
Matthieu BRIFFAUT Professeur, École Centrale de Lille	Rapporteur & Examinateur
Benjamin RICHARD Ingénieur chercheur, IRSN	Examinateur

THESE DE DOCTORAT

NNT : 2022UPAST140

Titre : Etude du comportement mécanique des interfaces acier/béton : apport de l'analyse à l'échelle mésoscopique

Mots clés : Béton armé, Interfaces acier-béton, Échelle mésoscopique, Modèle de zone cohésive avec frottement, nervures en acier

Résumé : Afin de prédire l'importance et la répartition des dommages dans les structures en béton armé soumises à des chargements sévères, la modélisation du comportement de l'interface entre les armatures en acier et le béton est essentielle, car elle influence directement la distribution des fissures. Les modèles d'interface macroscopiques couramment utilisés dans les simulations de structures incluent différents paramètres dont la signification physique est parfois limitée et pour lesquels l'identification reste difficile. Pour améliorer la compréhension du comportement de l'interface, l'échelle mésoscopique est retenue pour développer des outils de modélisation à l'échelle de la nervure. Pour ce faire, des volumes tridimensionnels de béton armé représentant des spécimens d'essais de « pullout » et contenant explicitement l'armature sont modélisés, en y intégrant des barres d'acier nervurées ou lisses. Des simulations linéaires sont tout d'abord effectuées à l'aide d'un modèle d'interface de type "ressort" pour vérifier l'effet des paramètres de rigidité. Ensuite, afin de décrire la fissuration dans le béton dans le cadre de simulations non linéaires, le modèle d'endommagement isotrope de Mazars est introduit avec régularisation en traction et en compression. Des simulations sont ensuite effectuées sur un échantillon de "pullout test" avec une barre lisse en associant à l'interface soit un modèle de zone cohésive modifié (CZM) basé sur l'approche de Tvergaard, soit un modèle de frottement, pour montrer les limites de ces modèles. Pour pallier ces limites, un modèle d'interface de zone cohésive avec frottement en 3D (FCZM) est proposé et implémenté. Dans ce modèle, l'interface est divisée en une partie non endommagée où le modèle CZM s'applique et une partie endommagée où le modèle de frottement domine. La réponse globale des essais de pullout est étudiée en termes d'endommagement et de distribution des contraintes principales à proximité de la barre d'acier. Les courbes force appliquée - déplacement à l'extrémité libre de la barre sont comparées aux données expérimentales disponibles. Un bon accord entre les simulations et les résultats expérimentaux est obtenu en utilisant le modèle mis en œuvre, à la fois pour les barres lisses et nervurées

A l'aide du modèle FCZM, l'impact de l'introduction explicite des granulats est étudié en remplaçant la partie homogène par un béton hétérogène à deux phases constituées des granulats ayant des formes polyhédriques et de la matrice de mortier. Les résultats montrent également un bon accord avec les résultats expérimentaux moyennant une calibration adéquate des paramètres du mortier, mais avec un coût de calcul plus élevé, ce qui milite en faveur de l'utilisation d'un béton homogène. Un autre aspect important est l'analyse des effets de la forme et des dimensions des nervures. Ainsi une étude est réalisée en utilisant une barre d'acier avec une seule nervure, et en faisant varier ses dimensions. Des simulations sont également effectuées sur des barres à chevrons et des barres nervurées rectangulaires. Les résultats confirment les quelques conclusions de la littérature qui relient l'augmentation de la force d'adhérence à l'augmentation de la surface de la nervure. Néanmoins, le paramètre le plus influent pour l'effort de liaison est la surface projetée normale de la nervure, et non la surface totale habituellement calculée. La surface normale projetée est donc proposée comme un paramètre pouvant être utilisé par des modèles macroscopiques de liaison. Enfin, l'effet du confinement externe est étudié et les résultats montrent que l'approche développée permet de décrire correctement cet aspect.

université PARIS-SACLAY

ÉCOLE DOCTORALE
Sciences mécaniques et
énergétiques, matériaux
et géosciences (SMEMAG)

Title : Study of the mechanical behavior of steel/concrete interfaces: contribution of the analysis at the mesoscopic scale

Keywords : Reinforced Concrete, Steel-concrete interfaces, Mesoscopic Scale, Frictional coheisve zone model, steel ribs

Abstract : In order to predict the importance and distribution of damage in reinforced concrete structures subjected to severe loadings, the modeling of the behavior of the interfaces between reinforcement steel and concrete is essential, because it directly influences the crack patterns. The macroscopic interface models commonly used in structure simulations are functions of various parameters whose physical significance is sometimes not very clear and identification is difficult. Hence, the mesoscopic scale is investigated here to improve the understanding of the behavior of the interface by developing modeling tools at the scale of the rib. To do so, numerical three dimensional reinforced concrete volumes designed for classical pullout tests containing explicitly the reinforcement are generated, using either ribbed or smooth steel bars. Linear pull-out test simulations are first performed using spring interface model to check the effect of stiffness parameters. Following, in order to describe cracking in concrete in non-linear simulations, Mazars isotropic damage approach is introduced with regularization in tension and in compression. Simulations are then performed on a sample with a smooth bar by assigning a modified cohesive zone model (CZM) based on Tvergaard’s approach, and a frictional model to the steel-concrete interface, to show the limitations in such models. To overcome these limitations, a 3D frictional cohesive zone interface model (FCZM) is proposed and implemented. In this model, the interface is divided into an undamaged part where the CZM model applies and a damaged part where the frictional model dominates. The overall response of the pullout test simulations is studied in terms of damage and distribution of the principle stresses near the steel bar, and the applied force versus free end displacements curves which are compared to available experimental data. A good agreement between simulations and experimental results for both smooth and ribbed bars cases is obtained using the implemented model.

Using FCZM, the impact of introducing explicitly the aggregates is studied by replacing the homogenous part by a two phase heterogeneous concrete made up of coarse aggregates having polyhedrons shapes and the surrounding mortar. The results showed good agreement with experimental data after providing an appropriate calibration of the mortar parameters, still with a higher computation cost encouraging the usage of homogenous concrete. Another important aspect is varying shapes and dimensions of the ribs. In this regard, a study is done by using a steel bar with only one rib and varying the dimensions of this rib to characterize the corresponding effects. In addition, simulations are performed on herringbone bar and rectangular ribbed bars. Eventually, the results coincide with some conclusions in literature which relate the increase in the bond strength to the increase of the rib surface area. Still, it has been found that the most important part is the normal projected surface of the rib, and not the total surface area usually calculated. In addition, the overall formation of the ribs have an effect and may affect importantly the bond strength. The projected normal surface area is then proposed as a parameter that can be sued by macroscopic models to predict the increase in the bond strength. Finally, the effect of external confinement is investigated, and the results show that the model can correctly describe this aspect.

TABLE OF CONTENTS

LIST OF FIGURES

LIST OF TABLES

1 GENERAL INTRODUCTION

1.1 INTRODUCTION

Civil Engineering structures do not only aim to sustain external loadings. Their success or failure is neither only evaluated by their simple mechanical resistance nor only dependent on it. For instance, cracking has a direct impact on the transfer properties that govern the potential leakage rate in containment buildings for nuclear power plants. In some cases, information about the cracking behavior related to the quasi-brittle evolution of concrete can become essential. This complex quasi-brittle failure characteristics can be associated with the local or meso scale heterogeneities of concrete and to the localization behavior with micro-scale cracking, due the heterogeneous nature of concrete.

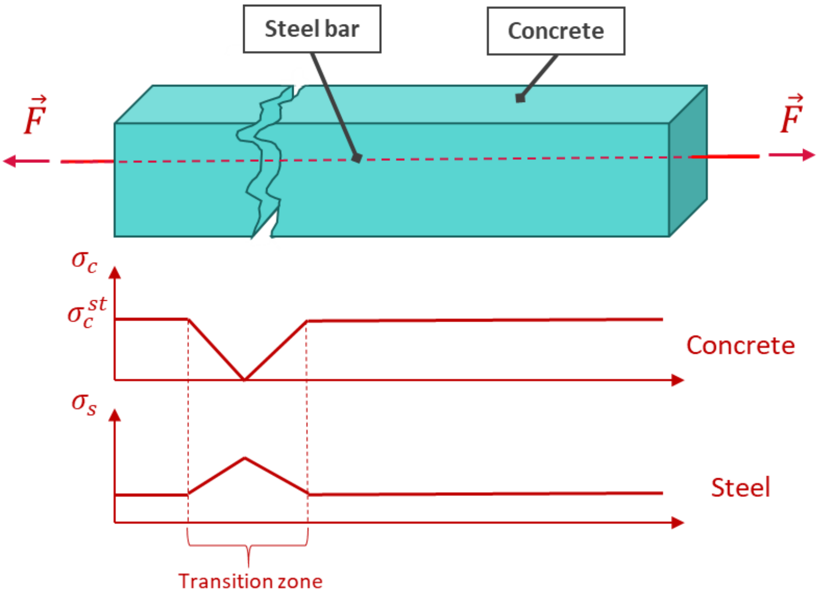

Figure 1.1 Distribution of stresses in steel and concrete in a reinforced concrete tie after the first crack; $\boldsymbol{\sigma_c}$ and $\boldsymbol{\sigma_s}$ are the stresses in concrete and steel respectively, and $\boldsymbol{\sigma_c^{st}}$ is the concrete strength, based on (Casanova et al., 2012)

For reinforced concrete structures, the bond between steel and concrete plays an essential role in determining the structural performance. In the case of a reinforced concrete tie for example, once the first crack appears in the weakest point of the structure, the concrete stress in the cracked zone drops to zero while the load is totally supported by the steel reinforcement. A part of stresses in the steel is then progressively transferred from steel to concrete (Figure 1.1). This transition zone has an impact on the crack properties and is directly influenced by the bond between steel and concrete (Casanova et al., 2012). The mechanical behavior of the steel-concrete interface is very complicated due to the presence of various phenomena at this region as can be seen in Figure 1.2. For instance, they include corrosion of steel, air voids, moisture, bleed water zones, slip/separation phenomenon and the overall inhomogeneity of concrete. Thus, numerical approaches are necessary to evaluate the bond properties and their impact on the structural performance.

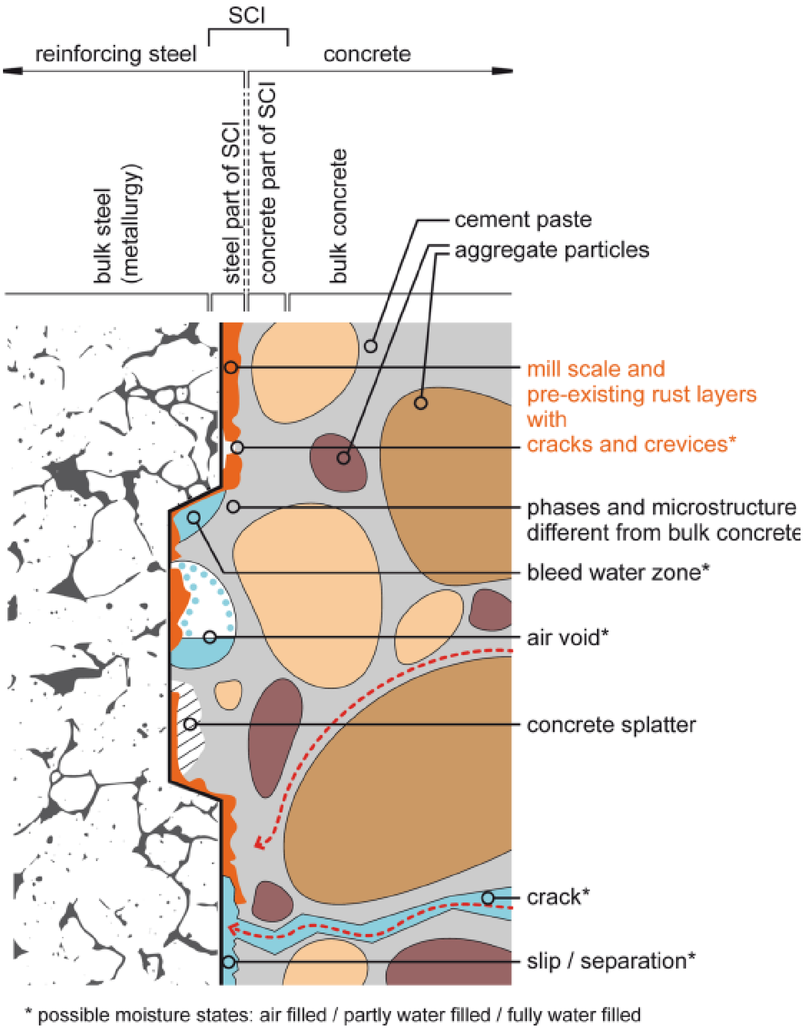

Figure 1.2 Schematic illustration of selected characteristics at the steel–concrete interface (SCI) (Angst et al., 2017)

This steel-concrete interface is usually characterized by pull-out tests (RILEM, 1970). Numerically, macroscopic approaches were widely used to model the bond for huge concrete structures. Such models depend on plenty of parameters, which are measured in tests, and they are generally developed for specific loading histories and bond conditions. In addition, it is also hard to show the mechanical behavior at the mesoscopic scale for the steel-concrete bond. Hence, mesoscopic approaches, which are at the scale of the steel rib, can be used to help the calibration process. The steel bars used can be either smooth bar having no ribs, or ribbed bars having different shapes of the ribs, and the latter being the most commonly used in practice. For instance, as smooth bar behavior may be seen as an initial step to capture the more complex ribbed bar behavior, it is believed that a comprehensive mesoscopic model should be able to reproduce the response of both bar types.

1.2 OBJECTIVES

In order to predict the importance and distribution of damage in reinforced concrete structures subjected to severe loadings, the modelling of the behavior of the interfaces between reinforcement steel and concrete is essential, because it directly influences the crack patterns.

The global objective here is to develop modeling tools at the mesoscopic scale to better understand the underlying phenomena of the steel concrete bond, and that can be helpful to calibrate the macroscopic interface laws. The aim is to propose a mesoscopic methodology with the necessary components to reproduce the pull-out test behavior by performing simulations on generated samples. After validation of the model on reference cases, it is applied by launching different numerical applications. This model, which is developed in 3D, is expected to improve the understanding and the prediction of the mesoscopic steel-concrete interface behavior in various configurations and loading conditions. Ultimately, it can be used as a future perspective to help calibrating a macroscopic simplified interface model developed for structure simulations, whose parameters identification would necessitate a complex experimental procedure. In this regard, the developed model is not intended to be applied at the structure level, which enables the use of fine meshes at the local scale.

The numerical representation of the interface between steel and concrete is a key component of the simulation. In this document, a new interface model is especially developed and compared to more classical interface models. This newly proposed and implemented frictional cohesive zone model combines a modified Tvergaard's approach initially presented in (Tvergaard, 2003, 1990), and Coulomb's simple friction. It should be able to capture the behavior of the pull-out test when using either ribbed or smooth bars. The impact on the interface behavior of various factors such as the presence of aggregates, the external loading and confinement effect, the different shapes of the ribs of steel bar, will be investigated. The numerical responses in terms of mean bond stress versus free end displacement are compared to available experimental data. The propagation of damage and the principle stresses and strains that develop in the concrete and the interfaces are analyzed locally to highlight their role in the bond behavior.

This approach will help in the understanding of the cracking phenomena near the steel-concrete interface, especially in the presence of particles (i.e. aggregates, sand grains) having complex shapes near the rebar.

1.3 METHODOLOGY

In order to reach the objective, a certain methodology is followed:

A bibliographic study on the whole topic from literature is first done in **Chapter 2**, including the different modelling scales and methods used to study the steel-concrete interface. In addition, its description and representation are discussed, along with the description of the pullout test, which is used to identify the model parameters.

In **Chapter 3**, the detailed generation procedure of the 3D pullout reinforced concrete samples is presented, using either homogenous or heterogeneous concrete. Following that, linear simulations are carried out on the meshed samples to study the effect of the stiffness parameters in the linear spring model applied for the interface and described in Chapter 2. Mazars classical damage model (Mazars, 1986, 1984) is presented, followed by its regularization method in tension and in compression. The formulations of Tvergaard's cohesive zone model (Tvergaard, 2003, 1990; Wu and Wriggers, 2015) and Coulomb's interface models are shown, then pullout test simulations are performed on a sample with a smooth bar, and compared to experimental results to highlight the drawbacks of these two models to reproduce the behavior separately.

A new frictional cohesive zone model (FCZM) is proposed in **Chapter 4**, and its detailed formulation and implementation are presented throughout the chapter. The calibration process of the FCZM is discussed by using the smooth bar case, and a more complicated spiral-ribbed bar sample, in order to complete the calibration process. Finally, another spiral-ribbed bar case is chosen to verify the applied procedure.

In **Chapter 5**, several numerical applications of the frictional cohesive zone model are presented, including simulations on samples having coarse aggregates and mortar, i.e. heterogeneous concrete. In addition, a study is performed using different shapes of the ribs of the steel bar to understand the effect of the mechanical interlock on the bond behavior, and on the overall behavior, whose purpose is to check the ability of the proposed procedure to improve the calibration of the macroscopic approaches. Eventually, simulations are performed by applying external confining pressure on the sample, and compared to experimental cases.

Finally, the conclusions and perspectives are discussed in **Chapter 6**.

2 BIBLIOGRAPHIC STUDY - STATE OF THE ART

2.1 INTRODUCTION

This chapter presents the main characteristics related to the steel-concrete interface, previously dealt with in literature. The following aspects are detailed:

- Physical description of the steel-concrete interface and the influential parameters

- Principle of the pull-out test and the representation of the behavior of the steel-concrete interface.

- Scales of the simulations and modeling procedures at the mesoscopic scale

- Models assigned for concrete at the mesoscopic scale

- Interface models, including frictional, cohesive zone models and frictional cohesive zone models are shortly introduced, mainly the one that was initially proposed by (Alfano and Sacco, 2006).

2.2 STEEL-CONCRETE BOND BEHAVIOR

2.2.1 Main parameters affecting the steel-concrete interface behavior

The behavior of steel concrete interface is very complicated due to the existence of different phenomena that affect this zone (Figure 1.2). One important aspect is the presence of corrosion and rust layers, which was studied previously in plenty of studies such as (Andrade et al., 1993; Bensabra and Azzouz, 2013; Bhargava et al., 2006; Liu et al., 2022a, 2022b; Mammoliti et al., 1996; Mohammed and Hamada, 2006; Nguyen et al., 2011, 2015; Pantazopoulou and Papoulia, 2001; Suda et al., 1993). Corrosion of steel is one of the main phenomenon that leads to a mechanical damage in both the medium and long range due to the formation of expansive corrosion products. These expansions are at the origin of tensile stresses initiating internal cracks that propagate from this interface into the concrete bulk.

Another phenomenon at the steel interface is the existence and formation of mill scale on the steel surface (Raman, 2006), which consists of iron oxides, and may also contain magnetite, hematite and maghemite. It is different from corrosion and rust products in origin, formation, morphology and composition (Angst et al., 2017). This product is more brittle and may crack during bending of reinforcing steel bars, which may lead to the formation of corrosion products at the exposed surface after breakage (Doi et al., 2020; Zhao et al., 2013). Thus, mill scale presence on the steel surface can reduce the resistance of the bars to corrosion, except if there are no initial defects, which cannot be avoided (Doi et al., 2020).

Passive protective iron oxide films can also be found at the steel surface in the steel-concrete region (Angst et al., 2017). The existence of these passive films thin layers reduce the corrosion rate (Li and Sagüés, 2001; Sanchez et al., 2007; Volpi et al., 2015), which are less damageable under tensile stresses than under compressive stresses (Feng et al., 2011).

In addition, the interfaces may be affected by different aspects and characteristics, like macroscopic voids of different natures. When rising air bubbles become trapped beneath horizontal surfaces of the steel bars during concrete compaction, it produces air voids at the steel concrete interface. Since air does not mix with the surrounding concrete, it exists in the form of bubbles in concrete, which differ both in shapes and sizes (Mielenz et al., 1958). In addition, bleed water may accumulate at the steel concrete interface in the form of voids having limited lateral dimensions, which can appear similar to entrapped air voids, according to (Angst et al., 2017). Compared to the air voids, the bleed water voids are able to achieve bigger contact area with the steel bar surface, because of their more elongated nature.

Moreover, the capillary porosity in the bulk concrete that is further far from the steel-concrete bond is lower than those at the steel-concrete interface (Angst et al., 2017). This affects the degree of saturation at a given relative humidity and the rate of diffusion of air. For instance, there may exist a non-equilibrium moisture conditions, which might lead to condensation at the steel surface because of cooling of the steel, due to the possible temperature differences between steel and concrete. This may lead to an increase in the corrosion rate as relative humidity increases (Stefanoni et al., 2018), which further weakens the bond. Furthermore, another phenomena is the precipitation of ettringite that is a hydrous calcium aluminum sulfate mineral, which is thermodynamically possible in voids, and it is not limited to partially saturated conditions (Samson et al., 2002), which may lead to internal cracks that is because of volume expansion due to its late formation and precipitation.

Furthermore, when primary cracks are formed, internal micro cracks are produced around the steel bar ribs near the primary crack as a result of the transfer of tensile load through the ribs of the steel bar into the concrete and it extends with increasing load, leading to additional damage at the steel-concrete interface (Angst et al., 2017).

The flow direction of concrete during its placement may lead to the concrete inhomogeneity, which may decrease the content of coarse aggregates behind the steel bar and may also lead to the additional formation of voids. Likewise, the compaction and flow of concrete at the steel concrete interface can be geometrically restricted by tie wires when steel bar intersects. Moreover, spacers, which are usually used when reinforcing to maintain the cover (Lancaster, 1989), also affects the concrete micro structure locally leading to additional crevices at the steel-concrete interface (Alzyoud et al., 2016; Angst et al., 2017). Additionally, substance like oil and dust may be deposited on the steel surface before casting (Taber et al., 2002).

Such aspects reflect the complicated nature of the steel concrete interface, making it extremely hard to deal with numerically, especially in terms of exact representation. Hence, different simplified approaches have been used to represent this zone.

2.2.2 Experimental characterization throughout pull-out tests

According to RILEM recommendations (RILEM TC, 1994) the steel-concrete bond can be characterized by pull out tests. These tests consist in the direct wrenching of a steel bar from a concrete specimen. The pull-out test, described below, is intended to determine the adhesion of non-prestressed steel reinforcements, which is to serve as a basis for the comparison of shaped reinforcements of different kinds.

2.2.2.1 Description of the pull-out test

In the pull-out test, a bar incorporated in a concrete cube along a defined length is strained at one end by a tensile force, the other end remaining without stress. The relation between the tensile force and the relative displacement between steel and concrete is measured. The load is increased up to failure of the adhesion (RILEM, 1970).

According to (RILEM, 1970), the effective encasement height of the bar corresponds only to the half-height of the specimen: in the other half the bar does not adhere, this is in order to reduce the influence of the disturbed area that forms close to the bearing plate. The bar to be tested extends beyond the two sides of the specimen; the tension is applied to the longer end, and the device for measuring the displacement between steel and concrete is set on the shorter end. The height of the concrete specimen is $10d$ with d as the diameter of the bar: encasement height or the adhesive length of the bar l_{adh} is $5d$ and pre-length is $5d$ (without adhesion), and the length of the sides of the concrete specimen is 10d (Figure 2.1).

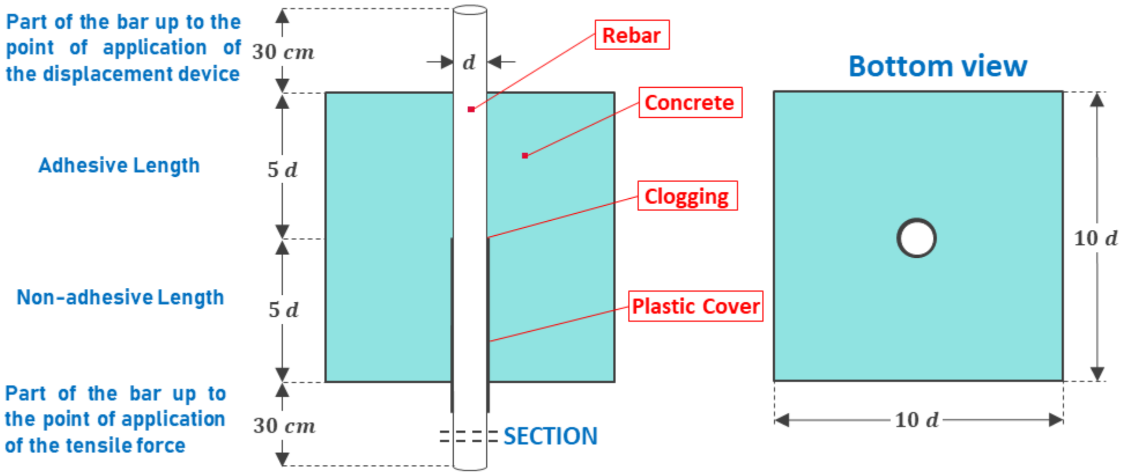

Figure 2.1 Description and dimensions of the test piece, based on (RILEM, 1970)

The results of this test are generally expressed by a sliding curve representing the variation of the pull out force as a function of the bar sliding measured at the free end of the bar, as shown in Figure 2.2.

The applied pull force F can be replaced by the mean bond stress σ_{mb}, which is calculated as follows:

$$\sigma_{mb} = \frac{F}{\pi \cdot d \cdot l_{adh}} \tag{2.1}$$

Several pull-out tests were performed in literature using the RILEM recommendations, with some minor differences. In (Torre-Casanova et al., 2013), instead of dividing the bar section which is within the concrete section into two parts, it was divided into three parts. The effective encasement length of the bar or the anchorage is the center part of the bar, as seen in

Figure 2.3.

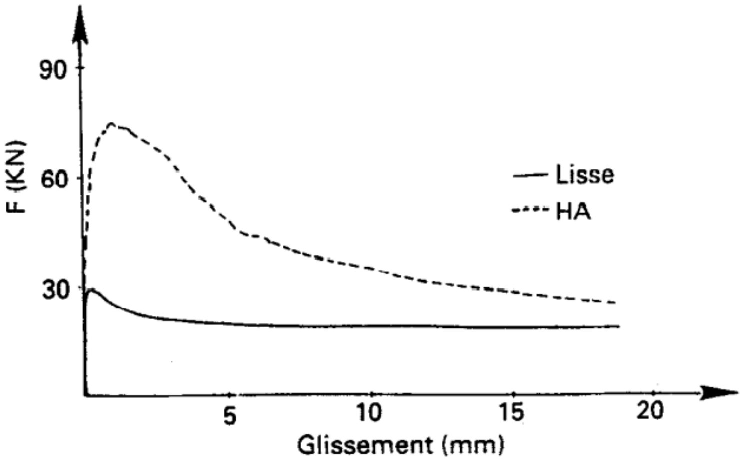

Figure 2.2 Experimental result for a pull-out test showing the applied Force versus slip (glissement) for samples having a smooth (lisse) and a ribbed bar (Hamouine and Lorrain, 1995)

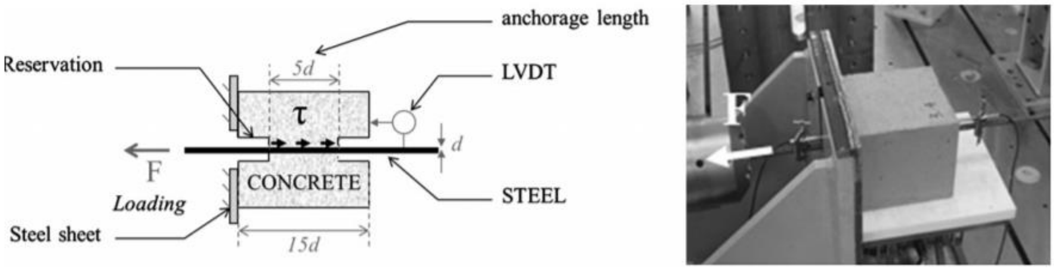

Figure 2.3 Pull-out set up (Torre-Casanova et al., 2013)

2.2.2.2 Description of the steel-interface bond behavior

The bond between steel and concrete maintains the transfer of forces between the two materials. This phenomenon is directly related to the shape of the steel bar and to the degradation of the concrete on its outer surface. Tangential stresses parallel to the surface of the steel bar, and radial stresses perpendicular to the surface develop. This causes content to fail forming inclined surfaces at an angle 45° with respect to the axis of the steel bar (Tepfers, 1979; Tilanter et al., 1977), which can be seen as a group of inclined cracks, as observed by (Goto, 1971), and showing regions of total de-cohesion between the concrete and the embedded steel bar.

According to (Eligehausen et al., 1983; Lin et al., 2019; Lutz and Gergely, 1967; Park and Paulino, 2013; Tepfers, 1979; Xu et al., 2017), the steel-concrete bond process can be divided into three different phenomena:

- Chemical adhesion between the steel and concrete, which is related to the composition and the initial procedure of placement of each material
- Micro interlocking resembles the different mechanical interactions that exists, mainly due to the presence of ribs along the steel bars.
- Friction phenomenon, which is due to the contact between the two surfaces

Usually, an adhesion law is used to associate the adhesive stress at the interface with the tangential slip, which is the relative displacement between steel and concrete in the direction parallel to the steel bar. The phases of this law can be directly related to the three phenomena observed. The three successive phases of this constitutive law, shown in Figure 2.4, is described as follows:

1) **Initial phase (A → B):**

   At the initial stage, the cohesion between concrete and steel is perfectly maintained, which is due to chemical adhesion and static friction that prevents the relative movement between the steel bar and the surrounding concrete. Adhesive stresses start developing with a very little increase in the slip. According to some studies such as (Lin et al., 2019; Xu et al., 2017), the cementing adhesive force between the steel bar and concrete has a little effect.

2) **Cracking phase (B → C → D):**

   After the breakage of the chemical adhesion, the steel bar starts relative movement with respect to the surrounding concrete. Based on the mechanical characteristic of the interface, including the existence of ribs and their corresponding geometry, and roughness of this steel-concrete surface of contact, concrete resists the movement of the steel bar causing an increase in the bond stress. Micro cracks start appearing in the concrete at an angle of about 45° with respect to the axis of the steel bar. These cracks are gradually localized, causing the de-cohesion of the steel bar, and eventually a softening of the adhesive behavior is observed in the post peak, as seen from C to D. Notice that this micro interlocking phenomenon has important effect only if ribbed bars are considered (Park and Paulay, 1991; Tepfers, 1979), more precisely in the presence of ribs, since using a smooth bar the behavior will be similar to a purely frictional behavior.

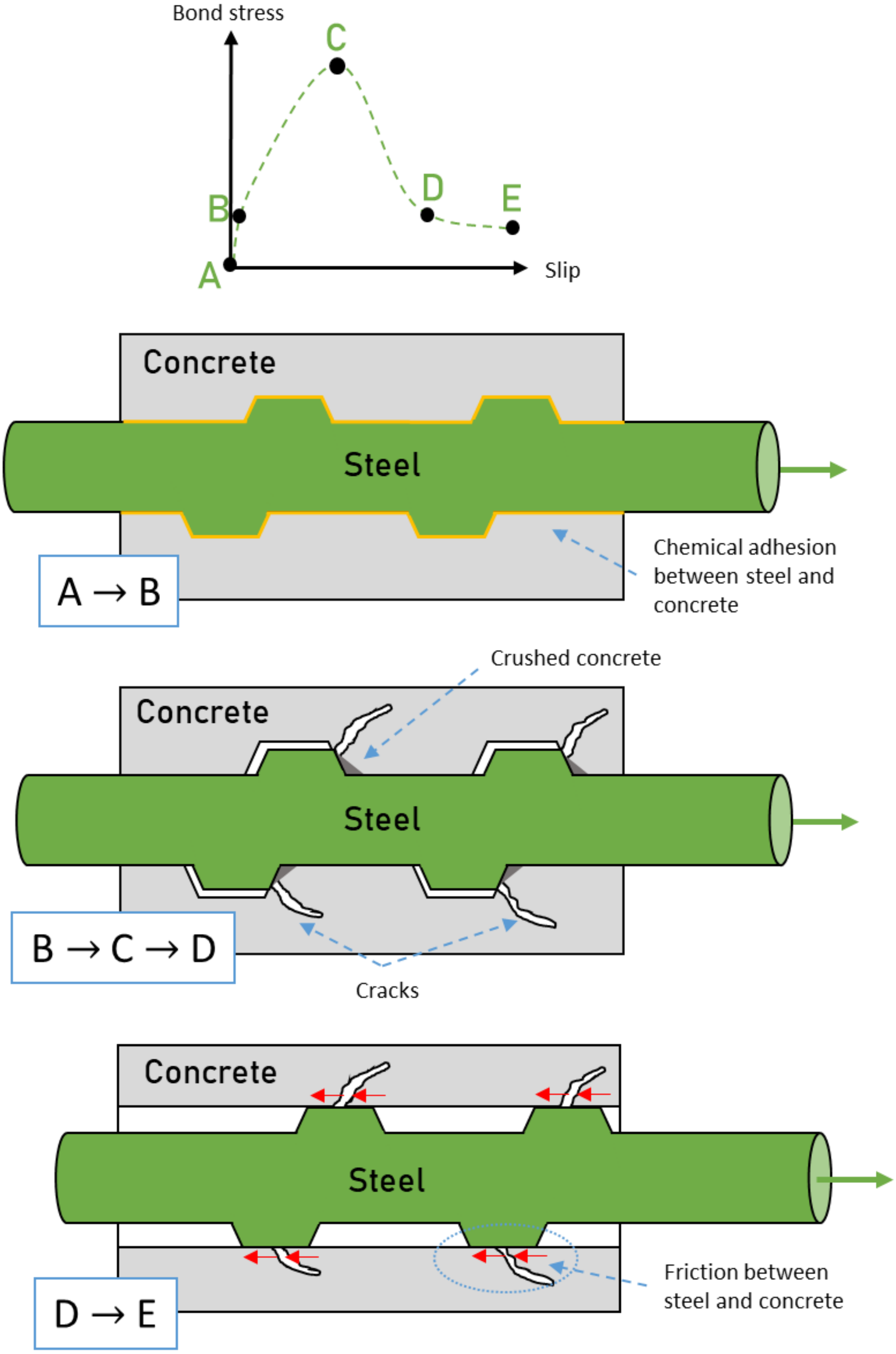

Figure 2.4 Illustration of adhesion law and shear transfer mechanism in steel-concrete interface, based on (Torre-Casanova, 2012)

3) Rupture phase (D → E):

As the applied loading keeps increasing, the propagation of the cracks leads to the final rupture of the interface region. The behavior is fully controlled by the friction between steel and concrete and the zone between the two materials can no more resist. Hence, the slip finally generates a constant residual stress.

2.2.2.3 Properties affecting the bond stress - bond slip law

In pull-out tests, steel and concrete properties are considered very important parameters that affect the response of the bond behavior. Several parameters that influence this behavior have been previously tested during experimental pullout tests. The main parameters are as follows:

A. Characteristics of the steel bar

The two main geometric characteristics of the steel bar are its diameter and its roughness. The mechanical properties of the steel are less effective considering that steel bars usually used have very similar properties, and the bar in pull-out test hardly reaches its yield stress.

A.1.1. Effect of the roughness of the steel bar:

The roughness of the steel bar is usually observed by using the relative rib area parameter, which is defined as the ratio between the rib area above the core, projected on a plane perpendicular to the steel bar axis, and the nominal bar surface area between two consecutive ribs. For instance, (Cairns and Jones, 1995) showed that, the bond strength increased by 30% after increasing the relative rib area from 0.05 to 0.10, because of the lower bursting force generated by more highly ribbed bars, in an experimental study on the strength of lapped joints. Similarly, (Darwin and Graham, 1993; Metelli and Plizzari, 2014; Tastani and Pantazopoulou, 2010; Zuo and Darwin, 2000) observed an increase in the bond stress with the increase of the relative rib area of the steel bar. Hence, one can conclude that the increase of the relative rib area of steel bar increases the mechanical effect of the ribs on the bond stress.

A.1.2. Effect of the diameter of the steel bar:

More water is hold under the steel bar forming a thicker transition zone, when the diameter and the ribs of the bar are larger, making it more porous, thus aiding the crushing phenomenon under compression by steel bar ribs. However, different experimental observations are reached making it difficult to give a clear conclusion. For instance, (Bouazaoui and Li, 2008) have seen a better resistance of the bond for ribbed bars of small diameters than for those with a larger diameter, which was previously observed for smooth bars by (Abrams, 1913). Still, (Daoud et al., 2002) showed the opposite and (Walker et al., 1997) two different behaviors depending on the compressive strength of the concrete.

B. Characteristics of concrete

The characteristics that are usually studied are the tensile and compressive strength of concrete, along with the dimensions and distribution of aggregates in the interface zone.

B.1.1. Tensile and compressive strength of concrete

(Tepfers, 1979) has assumed that there is a proportional relationship between the bond stress and the tensile stress of concrete, and it confirmed this hypothesis using a group of pull-out tests on samples with a very low concrete cover. For compression, (Eligehausen et al., 1983) noticed that the peak bond stress was proportional to the square root of the compressive stress of concrete, while (Barbosa et al., 2008) focused on the initial bond behavior before the peak, and have shown the bond strength increases with the compressive strength of the concrete using identical steel bars. Similarly, (Torre-Casanova et al., 2013) showed that the maximum bond stress and the corresponding slip were a function of tensile and compressive strength of concrete. For instance, the presence of fly ash increases the strength and the bond of the concrete (Barbosa, 2002; Daoud et al., 2002), which is due to the more compacted concrete and the reduced thickness of the transition zone. Thus, one can conclude that the increase in the tensile and compressive strength of concrete increases the bond strength.

B.1.2. Placement of concrete

(Daoud and Lorrain, 2003) have previously studied the effect of placement process of concrete, while (Söylev and François, 2006) studied the quality of the interface after drying of concrete, which concluded that bond strength decreases as a function of the concrete depth underneath horizontal bars and that the bleeding of fresh concrete leads to the formation of a void under these bars and reduce the bond strength. One can conclude that the production and placement of concrete influences the bond in the same way as the strength of concrete (Barbosa, 2002).

B.1.3. Age effect:

Not only the age affects the mechanical strength of the concrete, but it also influences the steel-concrete bond in the same way. For instance, (Chapman and Shah, 1987) performed pullout tests on samples having different ages varying from 1 day up to 28 days. They observed that smooth bars did not show any age effect, while the corresponding bond characteristics of ribbed bars has shown an important age effect.

C. Confinement of concrete

Concrete confinement can either be active, by applying external loading, or passive, either by using secondary reinforcements that prevent the concrete from cracking in certain directions or by increasing the concrete cover. In another words, confinement is eventually applying load perpendicular to the steel-concrete interface.

C.1.1. Active confinement:

In such cases, the external compressing load is applied on the sample on the external surfaces of concrete. Thus, the resistance of concrete increases by reducing its potentiality to crack. For instance, (Malvar, 1992) have seen an increase in the peak bond stress and the residual stress with the increase in the external confinement, applied on samples with a thin concrete cover. In (La Borderie and Pijaudier-Cabot, 1992), a similar increase in peak bond stress is observed using less thinner samples. Still, the percentage of increase is much less than that observed in (Malvar, 1992) for thin covered samples. Obviously, active confinement has an influence on the bond stress, but still less effective when concrete cover around the steel bar increases.

C.1.2. Passive confinement:

In such cases, secondary reinforcements can be added to prevent the concrete from cracking in certain directions, or as a replacement, the concrete cover can be increased. This type of confinement has a similar role like the active confinement through reducing the cracking of the concrete, by increasing the resistance of the sample in the direction of the tensile stresses and by preventing the micro cracking expansion in the concrete. (Eligehausen et al., 1983) used additional stirrups in the samples, which have shown an obvious increase in the peak bond stress, and similar effects were seen in (Desnerck et al., 2010). Concrete cover has an important effect on the bond stress, as it can lead to differentiate between a pullout failure and a splitting failure like in (Jin et al., 2020a; Torre-Casanova et al., 2013). Hence, passive confinement has an influence on the bond stress, just like active confinement.

2.3 NUMERICAL REPRESENTATION OF THE BOND

2.3.1 Introduction to the different modelling scales

Concrete can be modelled on four hierarchical levels as proposed by (Zaitsev and Wittmann, 1981): macroscopic, mesoscopic, microscopic and nanoscopic levels, as shown in Figure 2.5. The microscopic and nanoscopic levels are mainly related to the physical properties of mortar, coarse aggregates and the interface between them. However, the macroscopic and mesoscopic levels are usually used to characterize the mechanical behavior of overall concrete structures. For instance, the macroscopic level is used for the structural analysis of an overall concrete structure, while the mesoscopic level is usually employed to calibrate the macroscopic level analysis by obtaining a constitutive relation.

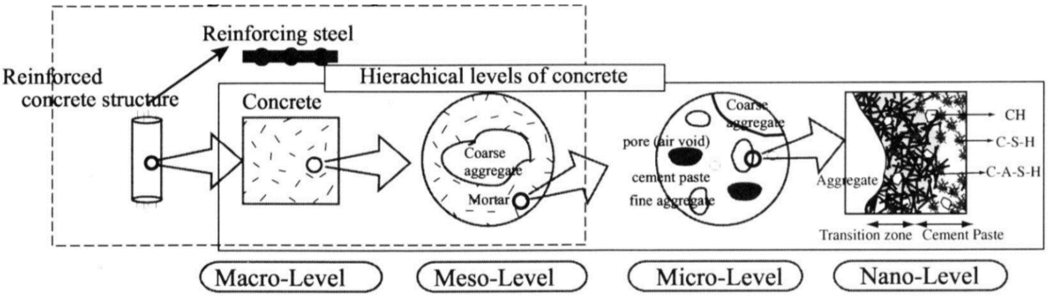

Figure 2.5 Structural scales and simulation models for concretes and reinforced concrete structures (Asai et al., 2003)

In principle, macroscopic models capture the global behavior; nevertheless, they have generally a poor description of the local one. They include enriched models or interface elements, some of which are composed of bond geometries, in which their calibration depends on many parameters too. Mesoscopic models are considered a better way for describing the local behavior. Still, it is difficult to have the structural scale at this scale due to the huge number of elements and details necessary to represent the structures. Therefore, these meso-models could be used to help in the calibration process of macro-models.

In other words, the bond response, which controls the cracking phenomena in concrete that, in general, follows the weakest links in such heterogeneous materials, may be modelled at three different scales: the dimensions of the structural elements, the reinforcing steel bar and the ribs on the steel bar. In order to model the bond behavior at the structural scale, a model that characterizes the effect of bond-zone response on beam, column or connection response is usually developed. The bond zone is represented as a homogenous continuum at the bar scale that is characterized by concrete and steel material properties (Rehm, 1961), which are defined by standardized tests such as pull-out tests and beam tests. At the scale of the ribs of the steel bar, the response depends on several aspects, such as the material properties of the mortar and coarse aggregates and the steel bar deformation pattern (Rehm, 1961). In addition, the load transfer between both mortar and coarse aggregates can also play a certain role in the whole response.

2.3.2 Bond models at the macroscopic scale

In macroscopic models, concrete is modelled as a homogeneous material and the governing equations are formulated within the framework of continuum mechanics. Different models were built to represent the steel-concrete interface behavior such as (Ngo and Scordelis, 1967) that proposed a spring element, associated with a linear law, to relate concrete and steel nodes. The bond behavior was improved by developing interface elements. Such zero thickness elements, which are introduced at the interface between concrete and steel, allow the use of a nonlinear law like in (Brancherie and Ibrahimbegovic, 2009; Dominguez et al., 2005; Lowes et al., 2004; Richard et al., 2010). (Dominguez, 2005; Ibrahimbegovic et al., 2010) and others, developed embedded elements that aim to describe the steel-concrete bond behavior through an enrichment of the degrees of freedom. By treating steel bar as ribbed rod elements, they took into account adhesion between the steel bar and concrete by adding cohesive elements like (Dehestani and Mousavi, 2015; Rezazadeh et al., 2017; Richard et al., 2010), or spring elements like in (Jin et al., 2019a). The rust behavior of steel bars was simulated in 2D by using a damage method in (Berto et al., 2008), in which elastic quadrilateral elements are inserted between concrete and steel bars. In addition, an axisymmetric model was used in (Lundgren, 2005) to insert a contact element between concrete and steel bar to study the anchorage bond of the rusted concrete.

In (Monti et al., 1997), finite elements were proposed to enclose the material behavior and the bond effects in the same concrete or steel element. These models require representing explicitly the interface between steel and concrete, which increases the computational cost. As a result, some models like (Ilgadi, 2013) used a perfect relation between steel and concrete and modelled the reinforcement using truss elements to overcome the previous problem, thus imposing the same strain in both materials using this approach.

(Mang et al., 2015) combined the advantages of these two approaches, in which the model proposed neither needs the explicit representation of the steel-concrete interface nor uses a perfect relation, representing a good alternative for such computations in the macroscopic scale. This approach, used in (Mang et al., 2016), is based on what was first proposed by (Casanova et al., 2012), in order to represent bond effects between the 3D concrete and the embedded steel, modeled with truss elements, through a 1D-3D interface element. This approach was improved in (Turgut et al., 2020) in order to take into account the influence of the stress state of the bond behavior.

Such macroscopic models depend on bond slip-stress constitutive relationships that are measured in tests. It is also hard to show the mechanical behavior at the mesoscopic scale for the steel-concrete bond. Hence, the mesoscopic scale is an important alternative in order to overcome such difficulties.

2.4 MESOSCOPIC REPRESENTATION OF THE STEEL-CONCRETE INTERACTIONS

At another level, the mesoscale analysis can reveal the local responses of concrete and reinforcement and their interactions with cracking. It aims to capture the behavior at the scale of the ribs of the steel bar.

2.4.1 Mesoscopic representation of the concrete behavior

The modeling and representation of concrete can be essential at the mesoscopic scale, since the steel-concrete interface is considered as a continuation of the concrete volume, with different properties. Based on the concrete model, the interface model and representation can change, which is not limited to the steel-concrete bond behavior.

Different methods are available to represent the concrete numerically at the mesoscopic scale. In most of the mesoscopic models, the concrete is subdivided into matrix and coarse aggregates. In 2D representations, circular shapes resembling the coarse aggregates in the concrete sample were used in studies such as (Daoud et al., 2013; Jin et al., 2019b; Wang et al., 2019; Xu et al., 2012a, 2012b), while more complex geometries were considered in (Zheng et al., 2022), and discussed in details in (Thilakarathna et al., 2020; Zhou et al., 2019), in which a laser scanning technique was used to scan aggregate particles in order to obtain their real shape, then generated a 2D aggregate shape library by a spatial random cutting technique. In (Asai et al., 2003), tomographic images of a concrete section were used in order to reproduce the shapes of these particles in 2D.

In the 3D representation, spherical particles were used in studies (Jin et al., 2019a, 2020b, 2021b; Nguyen et al., 2010, 2012; Wu and Wriggers, 2015) and ellipsoidal particles in other studies (Häfner et al., 2006; Leite et al., 2004). In addition, more complex shapes were used in other 3D studies, such as (Zhang et al., 2018), in which concave polyhedrons were generated by shrinking algorithms based on 3D Voronoi technique. Also, in (Caballero et al., 2006) similar polyhedron particles have been used, where the polyhedral geometry was numerically generated by standard Voronoi technique from a regular array of points that is slightly perturbed. These polyhedra were then shrunk to become the aggregate particles while the space between them represents the mortar. Moreover, convex polyhedrons were used too, such as in (Bary et al., 2017; Bernachy-Barbe and Bary, 2019; Larrard et al., 2013; Nguyen et al., 2015), but they used a different generation technique of the sample. (Bernachy-Barbe and Bary, 2019) also used real shapes obtained by tomography imaged. Aggregates in concrete were generated in (Mazzucco et al., 2018) using a laser scanner to generate their accurate geometry, then these laser scanned particles were simplified using a CAD software in order to reduce the computational costs.

Some 3D mesoscopic models that were applied to study the steel-concrete bond did not consider concrete as heterogeneous material, but as a homogeneous material like recently in (Jin et al., 2021a, 2020a; Liu et al., 2022a). Still, the detailed geometry of the ribs was modelled as a replacement in order to consider the complexity of the bond at this scale. In addition, homogenous concrete was used in several other studies, such as (Eddy and Nagai, 2016; Hayashi et al., 2017; Yamamoto et al., 2014).

2.4.1.1 Numerical modelling methods for the steel-concrete bond

Lattice models are used to simulate structural elements using either truss elements or beam elements. Such approaches were used in plenty of studies (Bazant et al., 1990; Fraternali et al., 2002; Hansen, A. et al., 1989; Herrmann et al., 1989; Hrennikoff, 1941; Kiousis et al., 2010; Li and Tran, 2008; Lilliu and Mier, 2003; Niwa et al., 1995; Salem and Maekawa, 2004; Schlangen and Garboczi, 1997, 1996; Schlangen and van Mier, 1992; Van Mier and Van Vliet, 2003). The main difference between the two approaches is that beam elements have 6 translational and 6 rotational degrees of freedom, which are divided equally at each end of the beam, while the deformation of truss elements is expressed by a total of 6 translational degrees of freedom, 3 at each end of the truss element.

The truss model is one of the discrete element methods previously used in (Bazant et al., 1990), in which the coarse aggregates are connected to each other by truss members linking both mass centers. Each truss member is subdivided into three segments, two representing the radius of the two particles, which are considered circular, and the third part representing the mortar in between. The center of each particle, resembling a joint between truss elements, is connected to all the adjacent particles. A truss element breakage resembles a crack in the mortar at this position.

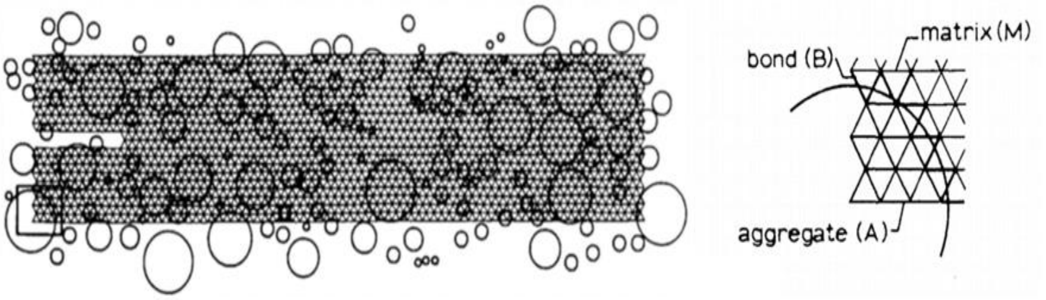

Figure 2.6 Lattice method used in (Schlangen and van Mier, 1992) showing the triangular lattice projected on the grain skeleton and the definition of aggregate, bond and matrix bars

In (Schlangen and van Mier, 1992), a regular triangular mesh was imposed on the numerical sample, and the bars connecting the nodes of the mesh were considered as the elements resembling materials in the simulations. A bar inside an aggregate has the properties of an aggregate material, a bar fully inside the matrix has the properties of the mortar and a bar intersecting the interface of the particle has the properties of the interface (Figure 2.6). Similarly, (Asai et al., 2003) used the same model, but the nodes in the previous case were replaced by the centers of the pixels, where the concrete sample built was based on tomography images. These centers are connected to all the adjacent nodes by bars, of which each bar takes the same properties of the materials it is fully embedded inside, or the properties of the interface if it is connecting two pixels of different materials, as previously mentioned.

Rigid Body Spring Model (RBSM) was also used for numerical concrete in several studies such as (Bolander et al., 2008; Eddy and Nagai, 2016; Gedik et al., 2011; Hayashi et al., 2017; Yamamoto et al., 2014) and others. In such discrete element model, concrete is considered as a homogenous material. This homogeneous material is meshed using a Voronoi diagram, or any similar method while it was constructed manually near the steel bar, like in (Eddy and Nagai, 2016). Each element has six degrees of freedom, consisting of three translational degrees of freedom and three rotational degrees of freedom. Moreover, each element is connected to other elements by three springs. Two are shear springs and one is a normal spring as shown in Figure 2.7 .

In (Daoud et al., 2013), which used finite element method (FEM) the mesoscopic mesh is obtained by using the diffuse meshing method as in (Nguyen et al., 2010), where the heterogeneous material properties are projected on the shape functions of the finite element mesh, in which the corresponding material properties is taken by each gauss point. Recently, (Wang et al., 2019) used FEM to study the steel-concrete behavior in 2D while (Jin et al., 2021a, 2020a) studied the bond behavior in 3D. For instance, FEM can be more adapted at the mesoscopic scale in order to take advantage of methods and tools developed for other finite element applications, like Cast3M (*The Finite element code Cast3M*, www-cast3m.cea.fr) and Salome (*Salome*, www.salome-platform.org), which were used in different studies like (Bary et al., 2017; Bernachy-Barbe and Bary, 2019; Daoud et al., 2013; Mang et al., 2015; Nguyen et al., 2015; Richard et al., 2010; Torre-Casanova, 2012; Turgut et al., 2020). Finite element modelling is also a good choice for complex geometries, like that of the concrete, aggregates and the steel-concrete interface, in this study.

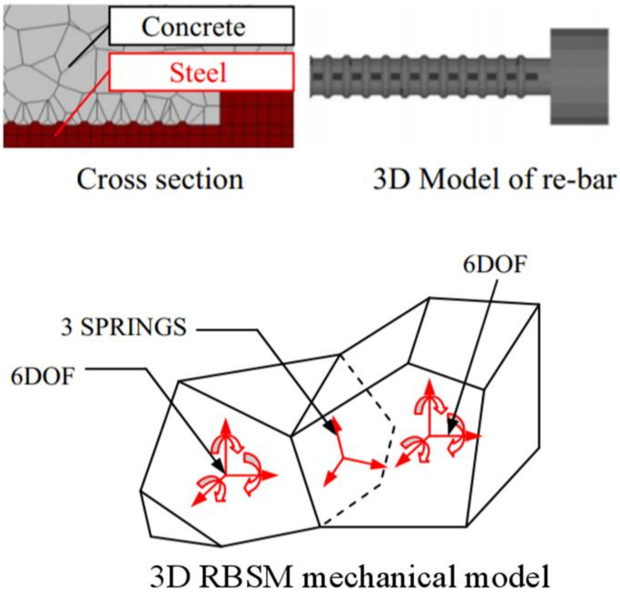

Cross section

3D Model of re-bar

3D RBSM mechanical model

Figure 2.7 3D RBSM mechanical model and steel concrete sample in (Eddy and Nagai, 2016)

2.4.1.2 Constitutive models for concrete

The type of microstructural evolution in concrete mainly depends on the stress state. The cracking can be dealt with by Continuum Damage Mechanics (CDM), which is based on the progressive reduction of the material stiffness in the framework of continuum mechanics at the mesoscopic scale.

In some mesoscopic studies, like (Jin et al., 2020a), concrete was assigned the plastic-damage model proposed in (Chi et al., 2017; Lubliner et al., 1989) and improved by (Lee and Fenves, 1998). It is a continuum, plasticity based model for concrete, which assumes that the main failure mechanisms of the concrete are cracking in tension and crushing in compression. (Daoud et al., 2013) has used Fichant's damage model (Fichant et al., 1999) which is based on Mazars model (Mazars, 1986, 1984), which simplifies the number of input parameters defining the tension and compression asymmetry. Modified Drucker–Prager plasticity model, as defined initially by (Drucker and Prager, 1952), was used in (Serpieri and Alfano, 2011), as it has been applied to describe pressure-sensitive materials like concrete. In the studies that used

RBSM, (Eddy and Nagai, 2016; Hayashi et al., 2017; Yamamoto et al., 2014), compressive failure of concrete is not allowed at the mesoscale according to the same concept as adopted in the original simulation system developed by (Nagai et al., 2005). Local damage is uniquely represented by local cracking when the tensile stress of a spring exceeds the tensile strength and the shear failure. In such models, the cracking width is calculated as the relative displacement between two rigid bodies.

The phase field approach has been used to simulate fracture as in (Ambati et al., 2015), which tracks the evolution of the cracks approximated as continuous entities in the domain. As developed by (Bourdin et al., 2000), a surface density function is used to represent the crack that depends on a process zone parameter l_0 (Figure 2.8). Although the failure due to crack initiation and propagation was first treated by (Griffith, 1921; Irwin, 1958), in which crack propagates in the body when a critical value for the energy released rate is reached, the criterion was unable to determine the curvilinear cracks paths and cracking angles. This was solved by (Francfort and Marigo, 1998), in which the variational formulation of Griffith's theory based on energy minimization for brittle fracture was introduced. After that, (Bourdin et al., 2008) developed the regularized version for this approach, detailed in (Bourdin et al., 2008), after which (Miehe et al., 2010) established the thermodynamic framework, which was then extended to dynamic fracture in (Borden et al., 2014; Hofacker and Miehe, 2013). To the best of our knowledge, this approach has not been previously used for concrete in pull-out test simulations, but widely used for concrete representation in other applications like (Cheng et al., 2022; Feng and Wu, 2018; Wu, 2017; Yang et al., 2019).

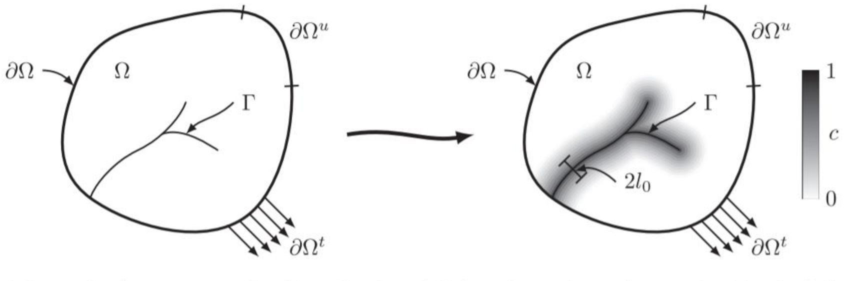

Figure 2.8 Schematic depiction of the phase field method, in which the crack is modelled by the field c where a black color corresponds to a fully damaged material ($\boldsymbol{C} = \mathbf{1}$*) and a white color corresponds to a fully intact material (*$\boldsymbol{C} = \mathbf{0}$*); the *$\boldsymbol{l_0}$* parameter controls the width of the process zone (Arriaga and Waisman, 2018)*

2.4.2 Interface models

2.4.2.1 General context

In most of the mesoscopic numerical studies dealing with steel-concrete bond, an interfacial transition zone (ITZ) between the aggregates and mortar (Jin et al., 2019a), or between mortar and steel, depending on the case, which affects the initiation and propagation of cracks, is considered. Since the mechanical behavior of the concrete portion belonging to this zone is different from that of the surrounding concrete, and due to its tiny dimensions, it is very difficult to obtain the mechanical parameters of this zone.

In (Asai et al., 2003; Grassl, 2009), the bars in the lattice model connecting two centers of pixels that represent different materials were considered to be interface bars. The tensile strength of these bars representing the aggregate-mortar interface was considered to be three-fifths that of mortar, and the same applied for the bars representing the steel-mortar interface but with different values. In (Eddy and Nagai, 2016), which used a rigid body spring model RBSM, the springs connecting a steel element with a concrete element was assigned a tensile strength that is half the tensile strength of the springs connecting concrete elements to each other. Similarly, the thickness of the ITZ was taken to be equal to the length of one element surrounding the aggregate particle in (Bernard et al., 2008) which used a finite element approach. Some models tried to add joint element in between the two different materials and assign certain opening and closing behavior such as (Salem and Maekawa, 2004). Still, it is difficult to choose the behavior of this interface, which certainly controls at least partially the crack initiation and propagation, thus impacting significantly the simulations. This is one of the concerns in this study. In addition, zero-thickness elements were used in e.g. (Raous and Karray, 2009; Serpieri and Alfano, 2011), in which the surface of contact between concrete and steel represented the interface, while a contact friction was recently deployed in (Jin et al., 2020a) to simulate the steel-concrete bond without using any interface elements. In such zero-thickness approaches, friction can be applied directly to the surface of contact, along with other phenomena that are a direct reflection of properties of concrete, thus combining both concrete properties and contact friction between the two surfaces. For instance, a frictional model called the RCCM was previously used to simulate the behavior of smooth bars in (Raous and Karray, 2009), using a variable friction coefficient that depends on the sliding displacements.

One basic interface model is the linear elastic spring model (LSM). The two stiffness parameters included in this model are commonly used in other interface models. These two parameters are the normal stiffness K_n and the shear stiffness K_s (Figure 2.9). Usually, it is hard to determine these two parameters without using any experimental results, as they are purely numerical parameters resembling both the normal and shear resistance at the interface. As the behavior at the interface is controlled by different parameters such as friction, applying the elastic spring model with only the two aforementioned stiffnesses is necessarily a strong simplification, and the results may be seen as merely approximate.

According to (Duan et al., 2007; Hashin, 1991; Qu, 1993; Wang et al., 2005), the interface conditions for the linear spring model can be written as:

$$[\sigma]\cdot n = 0 \quad ; \quad K\cdot[u] = \sigma\cdot n \tag{2.2}$$

where n is the unit normal vector to the interface Γ between the steel and mortar, and $[.]$= (out) - (in) is the jump operator.

K is a second-order tensor, $K = K_n n \otimes n + K_s s \otimes s + K_t t \otimes t$, where K_n, K_s and K_t represent the interface elastic parameters in the normal and tangential directions, respectively, and s and t represent the two orthogonal unit vectors in the tangent plane of the interface.

The linear-spring model can be used to simulate a thin interphase. In such case, K_n, K_s and K_t can be expressed by the interphase modulus and interphase thickness as follows:

$$K_n = \frac{2G_{int}(1-\nu_{int})}{t(1-2\nu_{int})} = \frac{E_{int}(1-\nu_{int})}{t(1+\nu_{int})(1-2\nu_{int})} \tag{2.3}$$

$$K_s = K_t = \frac{G_{int}}{t} = \frac{E_{int}}{2(1+\nu_{int})t} \tag{2.4}$$

where t is the thickness of the interphase, and ν_{int}, E_{int} and G_{int} are the Poisson's ratio, Young's modulus and shear modulus of the interfacial element, respectively. Since K_s and K_t are identical, K_s will be used to represent both shear directions in this document, for the sake of simplicity.

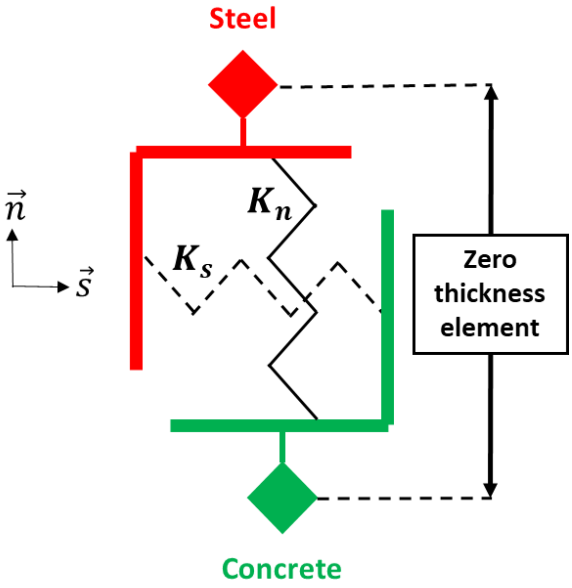

Figure 2.9 Normal and shear spring stiffnesses between a steel element and a concrete element

2.4.2.2 Frictional behavior

Due to the complexity of the steel-concrete zone, the choice of the interface model representing the complex behavior of this bond is not trivial. In pullout tests, friction is an important parameter in such partial sliding situations (Lin et al., 2019; Xu et al., 2017).

Contact friction was recently used in (Jin et al., 2021a, 2020a; Yi et al., 2020) to simulate the steel-concrete bond. In addition, a frictional model called the RCCM was previously used to simulate the behavior of smooth bars in (Raous and Karray, 2009), but using a variable friction coefficient that depends on the sliding displacements. To investigate such approaches, Coulomb's 3D interface frictional model is going to be used that is based on Mohr-Coulomb's failure criterion, in order to describe the debonding between concrete and steel bar. In such model, interface failure occurs due to either shear or tension according to the aforementioned failure criterion, while compression is entirely elastic. It will be described more in subsection 3.4.5.1. It was previously used in several applications to represent a sliding friction between two materials, such as recently in (Bui et al., 2021) where it was applied to represent the mortar joint element between each two blocks in masonry walls.

2.4.2.3 Cohesive zone models

The concept of cohesive zone model (Figure 2.10) was first introduced by (Dugdale, 1960) and (Barenblatt, 1962). The former suggested that in the zone ahead of slits in steel plates, which are subjected to a static tension load, the stress in this zone is constant and equal to the yield strength of the material. On the contrary, the latter pointed out the stresses in the softening region were variable. Since then, the cohesive zone model has been applied to predict failure in various materials, such as composites (Li et al., 2005) and concrete (Elices et al., 2009), and many others. Such approaches were discussed or used in several studies (Alfano and Crisfield, 2001; Camacho and Ortiz, 1996; Chandra et al., 2002; Foulk et al., 2000; Geubelle and Baylor, 1998; Hutchinson and Evans, 2000; Mohammed and Liechti, 2000; Needleman, 1997; Park and Paulino, 2013; Rahulkumar et al., 2000; Rice and Wang, 1989; Tvergaard, 2003, 1990; Tvergaard and Hutchinson, 1992; Wells et al., 2002; Xu and Needleman, 1994).

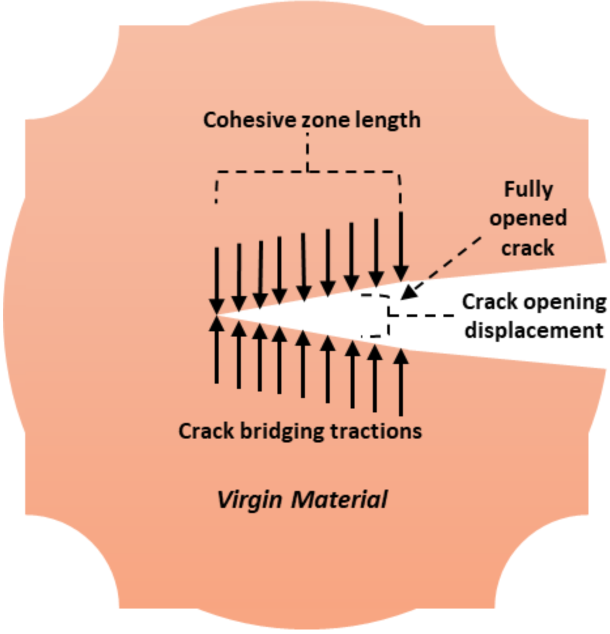

Figure 2.10 Schematics of the cohesive zone model, based on (Hallett and Harper, 2015)

This approach describes the failure of the material by introducing a strength-based fracture criterion along with an energy based fracture criterion for the part ahead of the crack tip that somehow preserves Griffith energy balance. The Cohesive zone elements are embedded along the fracture plane, which deforms according to a traction–separation law that takes into account the appropriate strength and toughness (Needleman, 1987).

Such models gave good solutions when they were previously assigned to aggregates-mortar interface (Wu and Wriggers, 2015), fiber reinforced polymer FRP-steel joints (Heshmati et al., 2018), FRP-concrete interface (zhang and Huang, 2022). Recently, it has been assigned to retarded-bonded tendons and concrete interface in (Xiong and Xiao, 2021), encouraging its introduction to steel-concrete interfaces at the mesoscopic scale. In such model, damage initiates in the interface element when a certain threshold is exceeded, either in shear or tension, while the compressive behavior is fully elastic. Tvergaard's model (Tvergaard, 2003, 1990; Wu and Wriggers, 2015) is going to be detailed in subsection 3.4.5.2.

2.4.2.4 Frictional cohesive zone models

The steel-concrete interfacial region, where friction plays an essential role, is still a continuation of the surrounding concrete. Since intense stresses develop in this region in loaded structures, cracks will generally propagate in concrete starting from the surface that is in direct contact with the steel bar. Similar to the cracking in concrete volume, the cracks at the interface can be represented by a damage parameter, which was previously combined with friction in a 2D steel-concrete interface model in (Serpieri and Alfano, 2011).

The frictional cohesive zone model approach is based on what was initially proposed by (Alfano et al., 2006; Alfano and Sacco, 2006) as a 2D model, in which the cohesive crack propagation phenomena, which are governed by nonlinear fracture mechanics, can be modelled at a meso-mechanical level by assuming that a representative elementary area A of the interface can be decomposed into an undamaged part and a completely damaged part. This 2D model, which was extended in (Roberto Serpieri et al., 2015; R Serpieri et al., 2015; Serpieri and Alfano, 2011) to a 3D approach, is able to capture crack initiation, damage propagation and their coupling with friction, interlocking and associated dilation. It was generalized to 3D in (Albarella et al., 2015; Roberto Serpieri et al., 2017; R. Serpieri et al., 2017). In these formulations, damage evolves based on Crisfield's bilinear damage model presented in (Alfano and Crisfield, 2001), while the frictional behavior is governed by a Coulomb's law. This approach was used once to study steel-concrete interface in (Serpieri and Alfano, 2011) in 2D. Recently, (Jaaranen and Fink, 2021) used this 2D model to represent the contact between timber and concrete by varying the friction coefficient. In addition, (Venzal et al., 2020) proposed a similar frictional cohesive zone model for masonry simulations applied in 2D using discrete element modelling.

2.5 CONCLUSIONS

In this chapter, a bibliographic study related to the steel-concrete interface was presented. This includes the physical description of the steel-concrete interface showing the complexity in this region, followed by description of the pull-out test and different properties that affect the resulting bond stress-bond slip law. The scales of the modeling of the bond were presented, mainly the macroscopic scale and the mesoscopic scale, and the procedures of modeling previously adopted for numerical concrete and for the steel-concrete bond. Furthermore, the formulations of the linear spring model and Coulomb model were introduced. Finally, the concept of the frictional cohesive zone approach was stated.

A large part of the mesoscopic studies used 2D simulations when studying the steel-concrete interface. The aggregates were also mainly considered circular or spherical, unlike the RBSM that used 3D simulations to study this interface, but used concrete as a homogenous material. Other studies used smooth steel bar in the simulation or ribbed bars having a square ribbed section like (Wang et al., 2019).

Therefore, it is important to conduct a 3D study that considers the detailed geometry of the steel ribs. This is essential in order to take into account the geometrical interlock of the steel-concrete interface, which is a crucial parameter itself at this scale. The importance of the interlock at the mesoscopic scale will be demonstrated, which is not deeply studied previously. This can pave the way for including the effect of different interlocks on the macroscopic behavior in macroscopic models. Finite element methods will be used in order to take advantage of the tools developed, mainly Cast3M and Salome, which can be effectively used for different finite element applications. This makes it possible to model the complex geometry of the sample, including that of the concrete, coarse aggregates and the steel-concrete interface. For instance, due to the computational costs and difficulty of convergences at this scale, homogenous concrete will be considered, mainly to limit the number of elements in the mesh, like in (Jin et al., 2021a, 2020a). Nonetheless, heterogeneous concrete will be adopted at a certain stage to investigate the effects of the presence of aggregates. On this matter, polyhedrons will be used, which are more realistic, compared to spherical or even ellipsoidal shapes, to represent aggregates in concrete as shown in (Thilakarathna et al., 2020). Still, aggregates add an important computational cost, which encourages the investigation of the importance of adding it compared to this corresponding cost. The capability of classical interface models, like frictional model and cohesive zone model, to reproduce the bond behavior in 3D will be studied at the first stage. The results will be a motivator for the development of a frictional cohesive zone interface model, based on the two aforementioned approaches, and to relate its parameters to the surrounding steel and concrete, which is rarely done in other models. The model should be able to reproduce the behavior for both smooth and ribbed bars.

The next chapter deals with the generation process of the pullout test samples. It includes the linear simulations using LSM, and pullout test simulations using a smooth bar and two classical interface models, whose results are compared to experimental ones. Additionally, Mazars classical damage model and a regularization procedure in tension and the corresponding modification of the model in compression is presented.

3 SIMULATIONS WITH CLASSICAL INTERFACE MODELS

3.1 INTRODUCTION

The aim of this chapter is to investigate the ability and limitations of classical interface models to reproduce the experimental behavior of pull-out tests, regardless of the assigned parameters. To fulfill this objective, a certain methodology is followed.

First, in order to perform pullout test simulations on reinforced concrete, different samples are to be generated. As explained in section 2.4, various representations were previously used for both numerical concrete and steel-concrete bond. In the current study, the detailed representation of the reinforced concrete samples is taken into account in order to preserve their geometrical complexity, in particular regarding the steel bar ribs. Thus, in the whole study, three-dimensional samples are only used in order to guarantee a behavior as realistic as possible. The generation process is detailed in this chapter, starting by smooth and ribbed steel bars, and then the detailed generation procedure of the aggregates is explained, followed by the final step of filling concrete or mortar. Those generated samples are eventually meshed to finalize the process.

Following, linear simulations are performed using linear spring interface model in order to elucidate the effect of the two stiffness parameters for the different shapes of steel bar, which are a part of different interface models, defined initially in subsection 2.4.1.2.

Nonlinear calculations are then perform to achieve the objective. First, concrete is assigned Mazars damage model. The regularization in tension and the proposed modification of the response in compression is detailed, which is important to avert mesh dependency of the results. Then, a simple nonlinear yield model for steel is assigned. Coulomb's interface model, which reflects mainly the effect of friction, is presented in the next section, based on the importance of friction in the bond behavior as discussed in subsections 2.2.2.2 and 2.4.2.2. In addition, the detailed formulation of the damageable Tvergaard's cohesive zone model as discussed in subsection 2.4.2.3, with certain modifications in its elastic part, is shown (Tvergaard, 2003, 1990; Wu and Wriggers, 2015).

In the final part of the chapter, these two interface models coupled with concrete damage model are used separately on the generated sample having smooth bar to prove their ineffectiveness to reproduce the behavior of pull-out tests as observed experimentally in terms of mean bond vs free end displacement.

3.2 METHOD OF SAMPLES GENERATION

3.2.1 General description

The aim is to generate different pull-out test samples with different characteristics. In these pull-out samples, a steel bar is placed in the central axis of a concrete sample, as mentioned in subsection 2.2.2.1. The contact area between concrete and steel is divided into an adhesive surface area that is the position where the steel-concrete interface is effective, which is termed either ribbed or smooth depending on the shape of the bar, and a non-adhesive surface area with no contact between concrete and steel, which is always kept smooth to simplify. This adhesive length can either be half the full embedded length of the bar in the concrete section as shown in Figure 2.1, or any other value depending on the test case considered, like in Figure 2.3.

The geometry of the samples is generated via a script, *Combs* (Bourcier et al., 2014), developed in python language, which makes use of the geometry module of the integration platform for numerical simulations Salome (*Salome*, www.salome-platform.org). This procedure was developed and applied in several studies previously such as (Bary et al., 2017; Bernachy-Barbe and Bary, 2019; Larrard et al., 2013; Nguyen et al., 2015). In here, each cubic sample is composed of different phases:

- Steel bar embedded in the central axis of the sample.
- Concrete surrounding the steel bar, which can be either:
    - Homogenous, as one phase material.
    - Heterogeneous, as a two phase material. It is made up of coarse aggregates spread inside the sample around the steel bar, and of mortar, which fills the space between the coarse aggregates and the steel bar (resembling the mixture of cementitious material and fine aggregates).
- Steel-concrete or steel-mortar interface, which is a small zone surrounding the steel bar.

3.2.2 Steel bar generation

Steel bar is widely considered as one of the most important component in any construction work with reinforced concrete. Steel bars have different shapes and sizes; there are angle bars, square bars, round bars and flat bars, the bars with circular sections being much more commonly used. In pull-out tests, round bars are used, either smooth or ribbed depending on the purpose of each test. The objective is to model a ribbed steel bar taking into account the detailed geometry of ribs. The spiral shape is modelled in here, which is one of the most common steel bars used in construction work. In addition, a smooth bar is also modelled, as well as a herringbone shape bar, which has different ribs than the spiral bar. The three modelled bars can be seen in Figure 3.1, in which the adhesive part is half the full embedded length of the bar in the concrete cube. This process of generation of steel bars is developed specifically and introduced in the program.

The spiral steel bar modelled can be described as follows:

- Core: They all have a cylindrical round shape, whose radius is the radius of the steel bar. Its length is the total embedded length of the steel bar in the concrete sample in a pull-out test (adhesive and non-adhesive length).
- Longitudinal ribs: They all have two longitudinal ribs along the length of the cylinder that are exactly opposite to each other, having an isosceles trapezoidal section.
- Transversal ribs: Each rib spans from one of the longitudinal ribs to the other longitudinal rib, thus covering half a circle (an angle of 180°) and it is inclined a certain angle with respect to the plane whose normal vector is the axis of the bar. In addition, the ribs on one side are symmetric to the ribs of the other side with respect to the axis of the steel bar. They have an isosceles trapezoidal section.

The smooth bar is made up of the cylindrical part only, as shown in Figure 3.1 . The herringbone bar differs from the spiral bar in the shapes and the orientation of the transversal ribs. Its transversal ribs, which also spans from one of the longitudinal ribs to the other longitudinal rib, are not inclined but normal to the axis of the bar. In addition, the distance between two consecutive ribs on the same side is two times the distance between two consecutive ribs each on an opposite side.

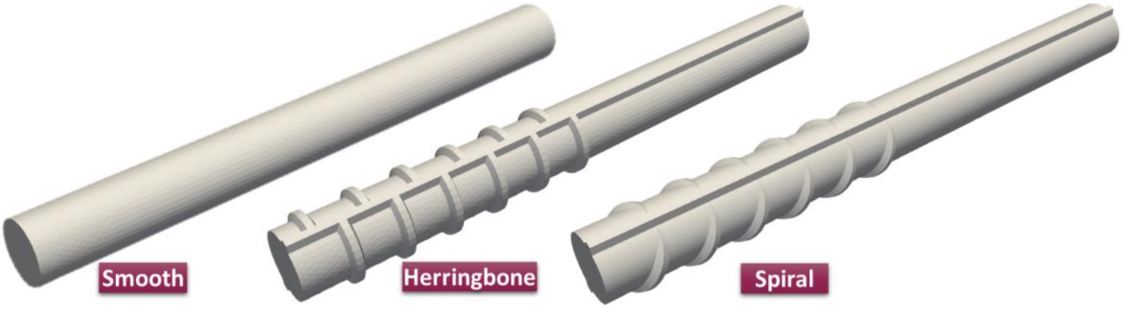

Figure 3.1 The three modelled steel bars; smooth bar, herringbone-ribbed bar and spiral-ribbed bar

3.2.3 Coarse aggregates

Following the generation of the steel bar, coarse aggregates were generated and positioned. Unlike previous studies in literature that used either circles for two-dimensional cases or spherical shapes for three-dimensional cases, the aggregates in here were modelled as convex polyhedrons that are Voronoi particles (Figure 3.2), whose shape is believed to be more realistic. However, different shapes can be considered, including real ones coming from tomography images.

In here, 15 different shapes of polyhedrons are considered, and for each shape different scaling ratios of dimensions which makes the particle unique to a certain point.

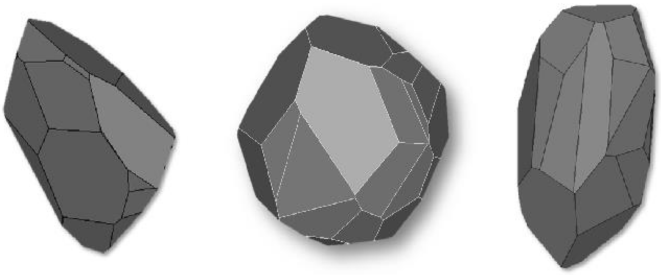

Figure 3.2 Polyhedrons resembling coarse aggregates

During the generation process, aggregates can be neither in contact with the steel bar nor in contact with each other. In addition, they cannot be in contact with the outer face of concrete, which means that they cannot be visible for an outside viewer. However, it is possible to generate a sample whose particles are allowed to be in contact with the outer surface, but this is ignored in the current generation of particles, since each aggregate will be covered by a layer of mortar in any sample, even a very thin layer of mortar.

The dimensions of the whole sample and the dimensions of the desired steel bar are initially defined and the steel bar is then generated. Following the generation of the steel bar, aggregates are generated (for the heterogeneous concrete cases). The procedure for the generation, scaling and spreading of the particles, which was used in (Bary et al., 2017; Bernachy-Barbe and Bary, 2019; Larrard et al., 2013; Nguyen et al., 2015) and others, is used as is it with no proposed modification. It is explained in details as follows:

1) For the heterogeneous concrete samples the polyhedrons shapes intended to be used for resembling the particles are defined. The range of dimensions of the aggregates, the maximum dimensions of the aggregates (called *maxdim*) and the volume fractions for each dimension are assigned based on experimental granulometry of aggregates in concrete. In addition, the intervals for the scaling of the dimensions of the polyhedron shapes are defined.
2) The total volume of the sample is calculated using the predefined dimensions.
3) For each dimension range of aggregates, and starting by the larger one, a particle shape is chosen from the predefined polyhedron shapes. One of the three dimensions (local x, y and z directions of the particle) of this particle is fixed, while the other two dimensions are resized by randomly choosing a ratio for each of these two dimensions from the interval used for scaling. For example, for a scaling interval [a,b], two ratios c and d that are in between a and b are randomly chosen by the program. These two ratios are used to resize the dimensions of the initial chosen particle; first dimension (x direction) is kept fixed, second dimension (y direction) is multiplied by c and the third one (z direction) is multiplied by d. An example of the resizing of one dimension is shown in Figure 3.3 .
4) Following the resizing of the particle, the box bounding the particle is formed and then the corresponding three dimensions of this box are extracted. These dimensions are then sorted and the middle value is considered (called *mid*), which is expected to be the greatest one that passes through the sieve, as it is enough for two dimensions of the particle to

be less than or equal to the sieve size, for the particle to pass through this sieve, regardless of the third dimension of the particle (which is called *larg*).

5) From the dimension range, a random value belonging to the interval is chosen as a dimension for this particle (called *dim*), then the following ratio is calculated:

$$\frac{dim}{mid} \times larg \tag{3.1}$$

If this ratio is greater than the predefined maximum dimension of aggregates *maxdim*, then the middle dimension is corrected as follow:

$$mid = larg \times \frac{dim}{maxdim} \tag{3.2}$$

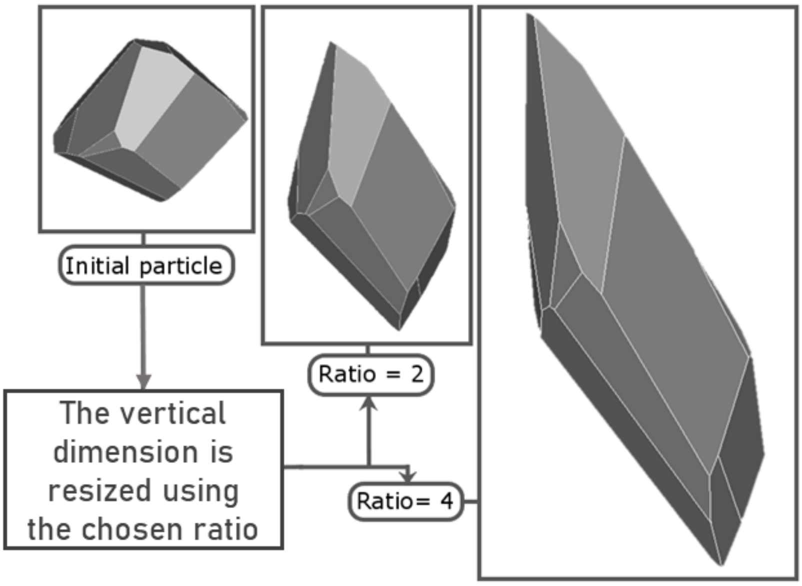

Figure 3.3 Resizing one dimension of a polyhedron particle

6) The whole particle is then scaled, from its center of gravity, using the following ratio:

$$scale = \frac{dim}{mid} \tag{3.3}$$

At this point, the particle is well scaled and can pass through the corresponding sieve; two of its dimensions are less than or equal to the chosen dimension which is within the dimension range of this particle, and the third dimension of this particle is now less than the maximum dimension of aggregates defined for the whole sample.

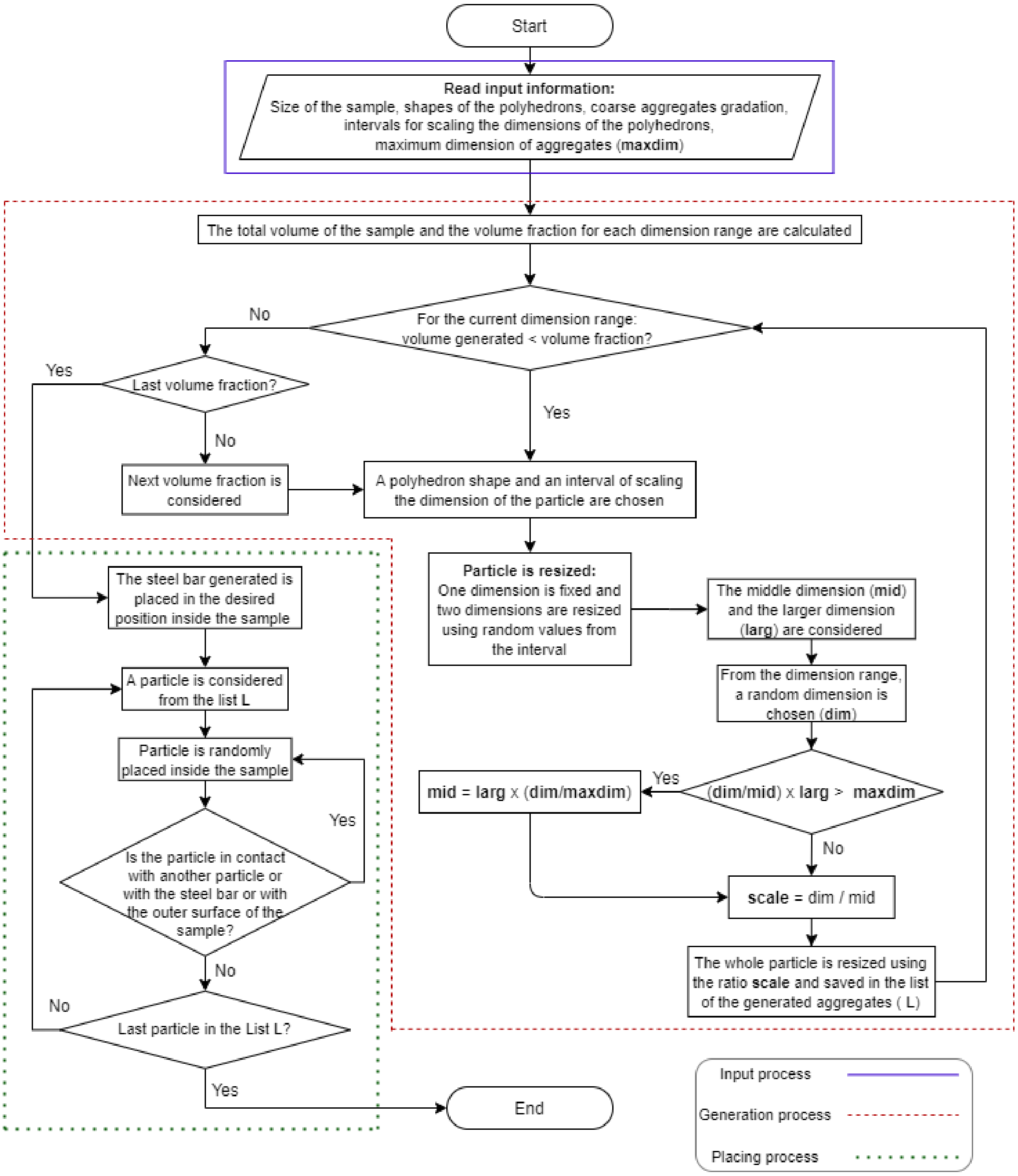

Figure 3.4 Flowchart to generate and place the aggregates

7) This particle with its new dimensions is saved in a list that includes all the particles generated. The volume of this particle is calculated and added to the total volume of particles generated. The same procedure for generating particles is repeated for the same dimension range until the corresponding volume fraction is reached.
8) The procedure is then repeated for all dimension ranges, and the generated particles are saved in the previously mentioned list. Note that the particles are sorted from the greater to the lower dimension in the sense of their bounding box.
9) After placing the steel bar in its right position inside the sample, the placement of the aggregates starts. The particles from the list are added from the greater to the lower one by randomly choosing a position inside the sample; then the program checks if its boundaries are overlapping the boundaries of the steel bar, of the sample or of the already placed particles. If so, a new position is randomly chosen and the same conditions are checked again until they are fulfilled. This procedure is repeated for every particle in the list.

At this point, the steel bar is in its right position and all the aggregates are in their right positions surrounding the steel bar; each particle is standing independently without overlapping any of the surrounding particles, the steel bar and the boundaries of the sample.

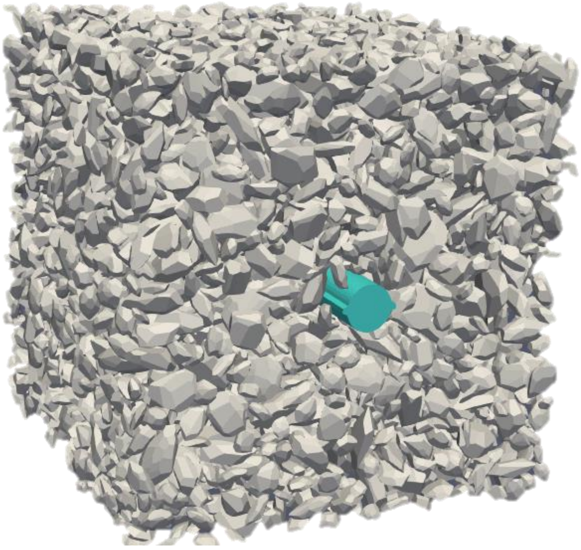

Figure 3.5 The generated aggregates surrounding the steel bar (colored cyan) in a modelled sample

This whole procedure, which is divided into three phases, input, generation and placing, is shown in details in Figure 3.4. An example of mesostructure obtained is shown in Figure 3.5.

3.2.4 Adding concrete or mortar

Following the generation and the placement of both steel bar and coarse aggregates, the mortar is automatically generated via the *Combs* scipt: the program subtracts the volume of the steel bar and the volume of the aggregates from the total volume of the sample previously calculated, using a Boolean operator. The geometry of the mortar is then not defined but controlled by the geometries of the steel bar and aggregates phases, and its boundaries are defined as follows:

- The six exterior surfaces of the sample forming the boundaries of the cube.
- The exterior surfaces of the steel bar previously generated and placed inside the sample.
- The exterior surfaces of the coarse aggregates previously generated and placed inside the sample.

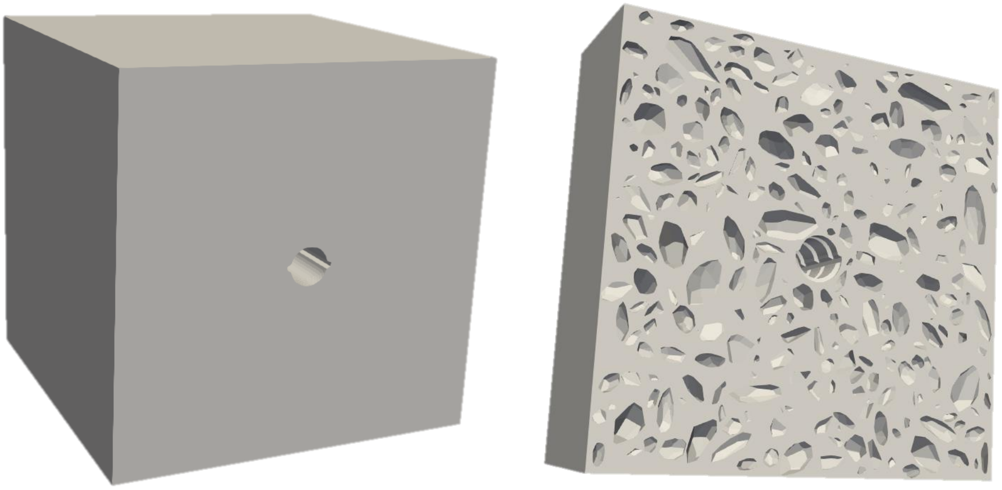
(a) *(b)*

Figure 3.6 (a) Mortar generated for a certain sample viewed from outside (b) A section view showing the mortar generated for a certain sample and its complex geometry

Since the coarse aggregates do not overlap the boundaries of the sample as mentioned in subsection 3.2.3, the mortar will cover all these boundaries except the two opposite sections where the steel bar intersects the outer surface of the sample, as can be seen in Figure 3.6(a). The boundaries of the mortar inside the sample are the exterior surfaces of the aggregates and of the steel bar, forming a very complex geometry as shown in Figure 3.6(b).

For the homogenous concrete samples that contain no aggregates, the generation procedure of aggregates is omitted. Thus, the program subtracts the volume of the steel bar from the total volume of the sample in order to calculate the volume of concrete.

3.2.5 Meshing of the pull-out test samples

Following the generation of the geometry of the pullout test samples, meshing is carried out. The mesh is generated via a script also developed in python language, which makes use of the SMESH meshing module plugged to Salome, and MG-CADSurf meshing tool within it. Due to the complex geometries and the different phases, an unstructured mesh is build, composed of linear tetrahedral elements.

The process is automatic and starts with the meshing of the surfaces of the different phases. To this aim, triangles are generated, meaning that the curved surfaces of the steel bar are discretized. The size of these triangles is controlled by a length parameter; in addition, the discretization of the curved surfaces is parameterized by a coefficient corresponding to the maximum admissible angle between two consecutive triangles. This leads in general to a large number of tetrahedral elements, especially for heterogeneous concrete. An example of the mesh of the aggregates can be seen in Figure 3.7 .

The size of a tetrahedral element varies widely throughout the sample. It is determined by calculating the average value of its three dimensions. The average size of the elements on the exterior surface of the mortar is larger than that of the elements inside the mortar block, and the elements with the smallest average size are at the steel-concrete interface. It has been indeed chosen to increase the number of elements at this interface which is of great importance for this study.

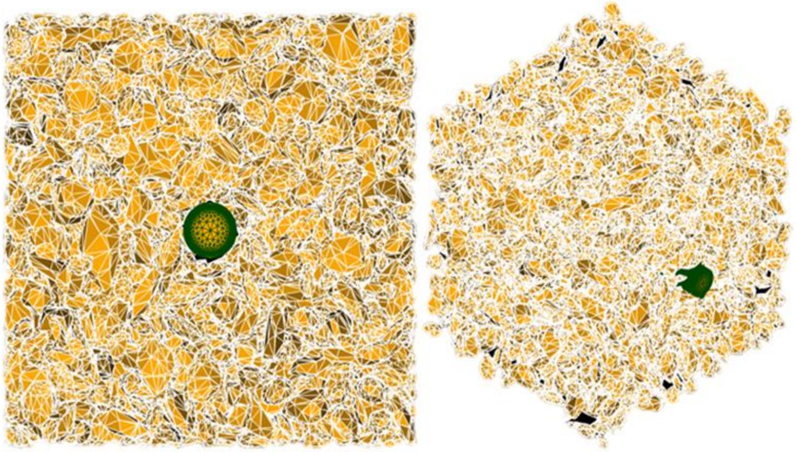

Figure 3.7 Sample meshing of aggregates in the generated samples

It is important to note that the meshes are voluntarily very fine, especially in the samples used in the non-linear simulations, in order to obtain accurate results. Although it is possible to reach close results with less finer mesh, the aim is also to visualize the distribution of damage and stresses in the mortar and concrete, which is better achieved when using fine meshes.

3.2.6 The steel-concrete interface

The steel-concrete interface is a surface made up of specific interface finite elements of zero thickness between the steel bar and the mortar or concrete. They are built up following the meshing of the sample in Salome after importing the generated mesh to the finite element code Cast3M, by duplicating the mesh nodes at the external surface of the steel bar in contact with mortar or concrete. Eventually, this produces a centrally hollow cylindrical shaped meshed surface surrounding the steel bar.

3.3 SIMULATIONS OF PULL-OUT TESTS USING LINEAR SPRING INTERFACE MODEL

3.3.1 Description of the test case

In order to verify the functionality of the model in simple cases, a simplified linear elastic case is initially considered to perform simulations, before moving to the more complicated nonlinear cases.

As mentioned previously in subsection 2.2.2.1, the pull-out test is carried out by direct pulling of a steel bar from the concrete block. A displacement is imposed on the external exposed face of the steel bar as shown in Figure 3.8, while the surrounding mortar face is restrained from moving in the same direction of the imposed displacement (x-direction). The other external exposed face of the steel bar on the opposite side of the block is free, at which the free end displacement FED is measured. In addition, two points P1 and P3 on the external concrete blocked face are restrained from moving in the y-direction as shown in Figure 3.8, while a third point P2 is restrained from moving in the z-direction, in order to prevent any solid movements of the whole microstructure.

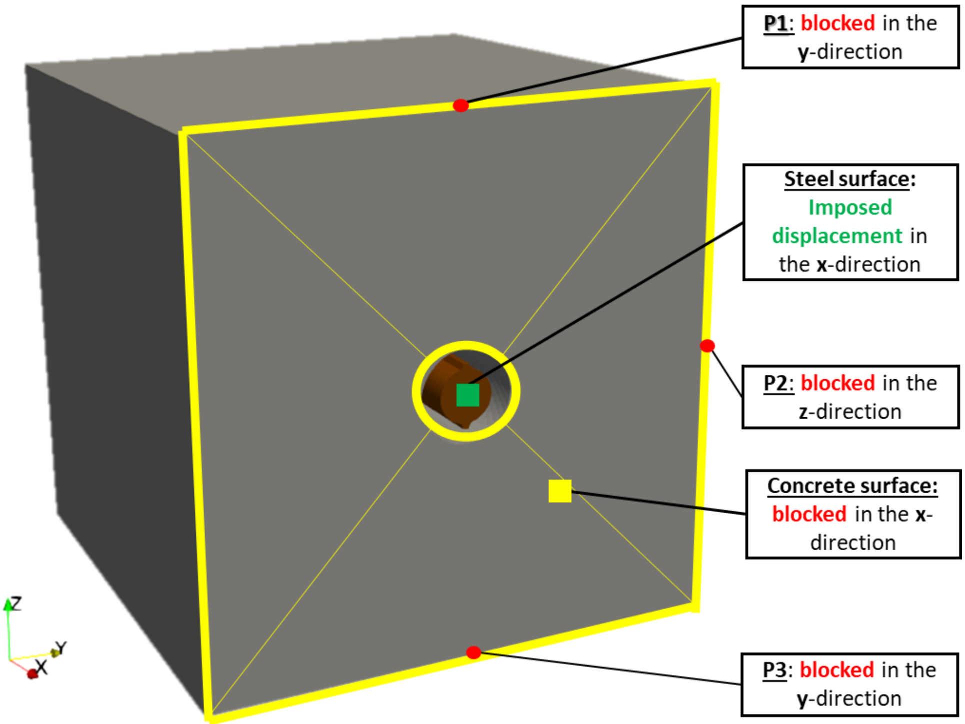

Figure 3.8 Boundary conditions applied on the generated pull-out samples

3.3.2 Generated samples

In order to perform linear pull-out tests simulations, two different samples are modelled, one with a herringbone bar and the other with a smooth bar.

For the herringbone ribbed bar used in this part, the adhesive length, or effective encasement length, is equal to one third the total length of the bar, as in the setup used in (Torre-Casanova et al., 2013). The adhesive part is modelled as a fully ribbed section, while the non-adhesive part does not include the transversal ribs, but only longitudinal ones. The detailed dimensions of the herringbone bar used are shown in Figure 3.9. The concrete cubic sample side length is 150 mm, and the total adhesive length is 50 mm. As explained in subsection 3.2.5, an unstructured mesh is generated using linear tetrahedral meshing elements. The number of mesh elements in the concrete and steel bar is about 1 116 000 and 450 000, respectively. The characteristic size of each mesh element at the outer surface of the concrete sample is equal to about 8 mm, while the triangular edge of each element at the steel concrete interface is almost 0.8 mm.

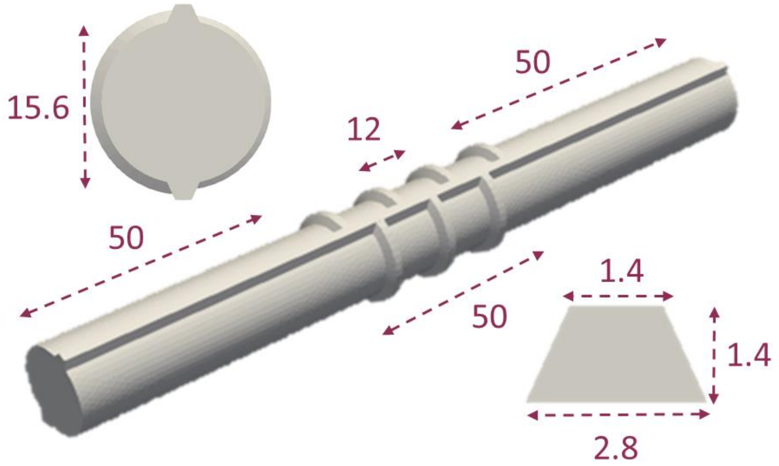

Figure 3.9 Dimensions of the modelled herringbone steel bar (in mm)

In addition, a sample with a smooth bar is generated for the sake of comparison, i.e. to study the effect of the ribs. The central region of the steel bar is adhesive, like the aforementioned herringbone bar, but it is fully smooth. The bar diameter is 16 mm. The concrete cubic sample side length is then 150 mm and the total adhesive length is 50 mm. The number of mesh elements in the concrete is 1 077 000 and in the steel bar 464 000. This is achieved by imposing the same characteristic size of mesh element at the outer surface and at the steel concrete interface as in the herringbone case.

3.3.3 Simulations and results

3.3.3.1 General description

The steel-concrete interface has a crucial role in the overall behavior as reported in all studies in literature. In this section, the elastic part of the interface is investigated. The two parameters studied are the normal stiffness K_n and the shear stiffnesse K_s, defined in section 2.4.2. Those parameters appear in a wide range of interface models. Usually, it is hard to determine them without using any experiment results, as they are numerical parameters.

The effects of these two parameters are studied in terms of free end displacements. To do so, linear simulations are performed using linear models for steel and concrete, where one stiffness parameter is fixed at a certain value while the other is varied from one simulation to another, then the corresponding free end displacement is recorded.

The normal stiffness quantifies the degree to which the material resist deformation in the normal direction between the two surfaces, which would be affected by both tension and compression forces. Considering the shape of the steel bar and the direction of the pulling force, which is parallel to the external cylindrical surface of the steel bar, the normal stiffness is expected to play an important role at the sides of ribs of the steel bar, with a less significant effect elsewhere.

Similarly, the shear stiffness quantifies the degree to which the material resist deformation in the direction parallel to the surfaces, which is obviously affected by shearing forces. It is expected to take the upper hand in all the surfaces whose direction is parallel to the axis of the steel bar, which are the cylindrical surface and the tips of the steel ribs. On the other hand, it is expected to play a less important role at the sides of the ribs.

Several simulations were carried out in order to check the validity of these two points summarized in Figure 3.10.

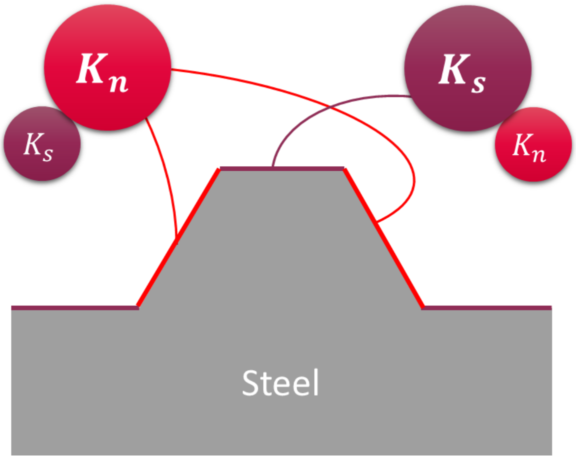

Figure 3.10 The dominating parameters at and near a rib of a steel bar

3.3.3.2 Variation of the shear stiffness

In order to study the effect of varying the shear stiffness, a group of simulations was carried out using the herringbone and the smooth samples defined in subsection 3.3.2 . Concrete and steel are both assigned elastic models, by taking steel's Young's modulus 200 GPa and concrete Young's modulus 25 GPa, while steel's Poisson's ratio is 0.3 and concrete's Poisson's ratio is set to 0.2 . The normal stiffness was fixed at certain values throughout all these simulations, while the shear stiffness was changed from one simulation to another, starting from $10^7\ N/m^3$ in the first couple of simulations up to $10^{18}\ N/m^3$ in the last two simulations. The values for the normal stiffness are 10^{10} , 10^{12} and $10^{15}\ N/m^3$. Those values are chosen in order to understand the general phenomenon, by covering the range of stiffnesses usually used, regardless of the specific assignment.

The imposed displacement on one of the exposed steel bar external sections was fixed at 0.05 mm throughout all simulations. The free end displacement was measured for each simulation at the center of the opposite exposed steel bar external section.

The plot of the free end displacements at the end of the simulations as a function of the shear stiffnesses for the two herringbone and smooth bars is shown in Figure 3.11. The free end displacement curves have the same lower bound in all cases, but they have a very different upper bound.

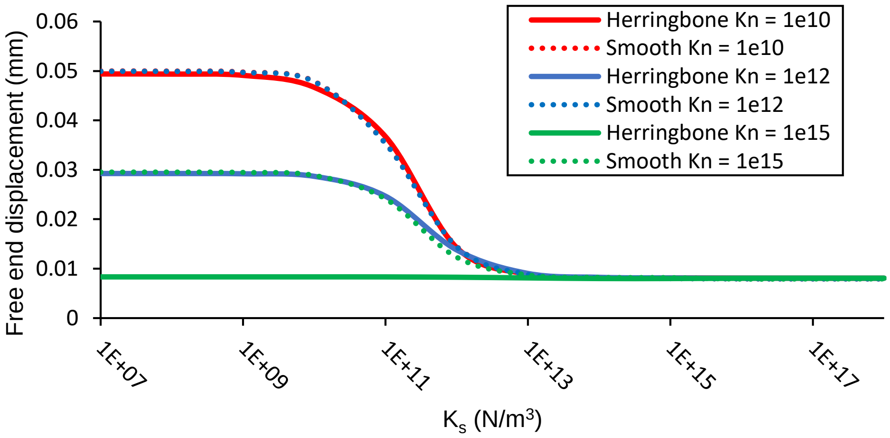

Figure 3.11 Variation of the free end displacement as a function of the shear stiffness for the herringbone sample and the smooth sample; normal stiffness K_n *is fixed at* 10^{10} , 10^{12} *and* $10^{15}\ N/m^3$ *in each group, and the final imposed displacement is 0.05 mm*

Based on Figure 3.11, each one of the curves can be divided into three different parts:

- For K_s in between $10^7\, N/m^3$ and $10^{10}\, N/m^3$, the free end displacement is almost constant at a unique maximum for each case:
  - For the herringbone sample: it varies based on the value of K_n, giving a lower displacement when K_n is high, and a displacement which is close to the imposed displacement when K_n is low.
  - For the smooth sample: it is almost equal to the imposed displacement, when K_n is low, but shows a certain resistance to pulling when K_n is $10^{15}\, N/m^3$.
- For K_s in between $10^{10}\, N/m^3$ and $10^{13}\, N/m^3$, the free end displacement decreases gradually, except for the herringbone case when K_n is $10^{15}\, N/m^3$ in which this drop is barely visible.
- For K_s greater than $10^{13}\, N/m^3$ the free end displacement is constant at an almost common minimum for all curves.

For the smooth bar sample, a low value for the shear stiffness has led to a total loss in the ability to resist the pulling force, when the normal stiffness, is low, but showed some resistance when the normal stiffness is high. This can somehow be justified by the ability of the shear stiffness to resist directly the slipping of the steel bar against the concrete (Figure 3.10). If the shear stiffness is so low as in the first parts of the curves, this ability to resist the pulling of bar will vanish and the bar will slip easily with no real resisting effort. Still, when the normal stiffness is high, it can play a role in preventing the total slipping of the bar.

On the other hand, the herringbone ribbed bar can still depend on its ribs to resist the pulling force up to a certain point, when its shear stiffness is low, except when the normal stiffness is low. Unlike the low normal stiffness case when herringbone almost fully slipped, a loss of slipping resistance did not lead to a full slipping of the bar when the normal stiffness is higher, but to an almost 60% and 30% slip, in where the total slip was certainly prevented by the ribs.

For the second part, the values of both the normal and shear stiffnesses are somehow close to each other for both samples. The ability to resist the slipping of the bar will increase for both cases as the shear stiffness increases. This is more marked for the smooth sample because the shear stiffness is fully dominant in this case, and the whole resistance of the bar depends mostly on the shear stiffness in the absence of the ribs. For ribbed sample, the ability to resist the pulling force increased too, mainly for the case with low normal stiffness, but obviously not in the same manner for other two cases that have a higher normal stiffness that already resists important part of the pulling.

For the last part, the two samples reached the same free end displacement as can be seen in Figure 3.11 . In this part, the shear stiffness is much higher than the normal stiffness, which leads to a total domination of the shearing resistance at this stage. The fully smooth bar case has the same free end displacement as the ribbed herringbone sample, meaning that the ribs did not play any role in preventing the slipping behavior, as the pulling resistance is already fully grabbed by the shear stiffness. As a conclusion, one can say that very high values of the shear stiffness clearly gives indistinguishable behavior in terms free end displacement for both the herringbone and smooth bar.

3.3.3.3 Variation of the normal stiffness

Another group of simulations was performed in order to study the effect of varying the normal stiffness. Unlike the previous case, the shear stiffness was fixe throughout all these simulations, while the normal stiffness was changed, starting from 10^7 N/m^3 in the first two simulations up to 10^{18} N/m^3 in the last two simulations, similar to the previous case. The values for the shear stiffness are 10^{10} , 10^{12} and 10^{15} N/m^3. Here again, those values are chosen in order to analyse the macroscopic response by covering the range of stiffnesses usually used.

The imposed displacement on one of the exposed steel bar external sections was fixed at 0.05 mm throughout all simulations likewise the previous case. The plot of the free end displacements at the end of the simulations as a function of the normal stiffnesses for the two samples is shown in Figure 3.12 .

As can be seen in Figure 3.12, each two curves have almost the same beginning and ending in this case unlike the previous case.

Concerning Figure 3.12, the curves for cases when K_s is 10^{10} N/m^3 and 10^{12} N/m^3 can be divided into three different parts:

- For K_n in between $10^7\ N/m^3$ and $10^{11}\ N/m^3$, the free end displacement is constant at a unique maximum for each case which are close to each other.
- For K_n in between $10^{11}\ N/m^3$ and $10^{16}\ N/m^3$, the free end displacement decreases gradually.
- For K_n from $10^{16}\ N/m^3$ to $10^{18}\ N/m^3$ and beyond, the free end displacement is barely decreasing with the increase of the normal stiffness, and all the cases have very close values.

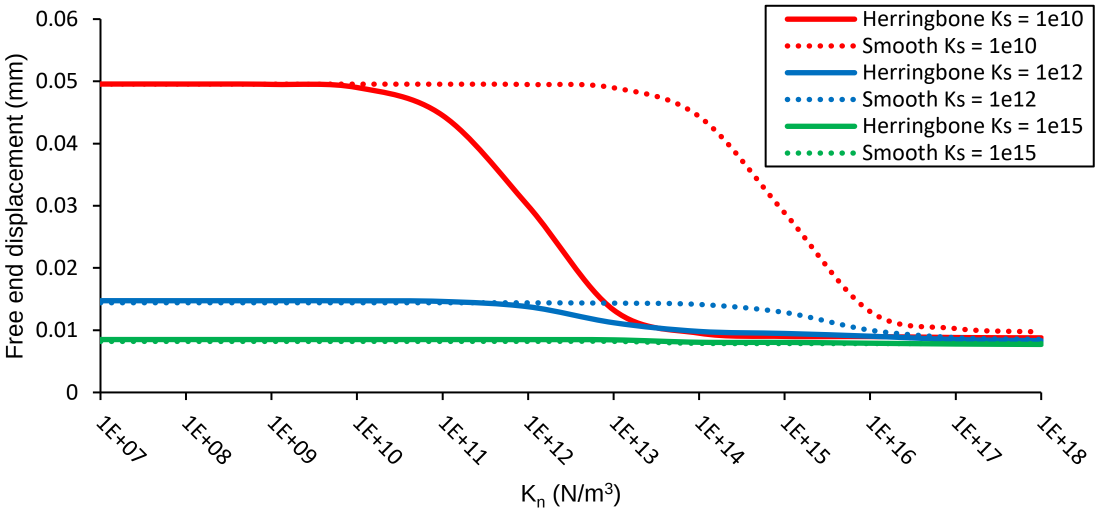

Figure 3.12 Variation of the free end displacement as a function of the normal stiffness for the herringbone sample and the smooth sample; shear stiffness K_s is fixed at 10^{10}, 10^{12} and $10^{15}\ N/m^3$ in each group, and the final imposed displacement is 0.05 mm

For the first part of the curves, a low value for the normal stiffness has led to a certain loss in the ability to resist the pulling force, when the value of the shear stiffness was fixed at $10^{12}\ N/m^3$. This can also be justified by the ability of the shear stiffness to resist directly the slipping of the steel bar against the concrete (Figure 3.10). When the value of the normal stiffness is low, both bars depend on their shear resistance to prevent sliding, and they both have very large surface where the shear stiffness dominates, as mentioned previously. The size of the surface of the smooth steel bar where the shear stiffness is expected to dominate is slightly larger compared to the size of the surface of the ribbed steel bar where the shear stiffness is expected to dominate. Thus, the steel bar in smooth sample is expected to have a higher resistance compared to the herringbone sample, which can probably explain the small difference between the free end displacements.

For the second part, the free end displacement of the ribbed steel bar had decreased with the increase of the normal stiffness. The ribs gained a certain strength to resist the slipping of the bar at this point, unlike the smooth steel bar that needed higher value of the normal stiffness in order to gain the resisting strength previously acquired by the ribbed bar. When the shear stiffness is high, this drop cannot be seen.

For the last part of the curves, the free end displacements kept decreasing very slowly and had a similar value throughout this interval. The shear stiffness still has an effect in this part too, as the normal stiffness is not fully controlling the slipping and preventing it, especially when the difference between the shear and normal stiffnesses is very high. It is important to keep in mind that the first part to encounter the pulling force in the pulling process is the cylindrical surfaces of the bars where the shear resistance certainly dominates. Although by definition the normal stiffness is not supposed to have a big influence on the smooth bar behavior, the effect is obvious in this case. Such very high normal stiffness can still effect the cylindrical surface of bar, preventing it from slipping easily, probably due to the compressive stresses in concrete.

It is important to note that although the free end displacement may be the same between the two samples, the displacement in within the steel bar may vary, especially near the ribs of herringbone steel bar, which can therefore show a different distribution of stresses. Thus, the free end displacement provides a partial view of the effectivity of the ribbed steel bar compared to the smooth bar, as it only shows the global resistance to slipping.

These results strengths, to a certain point, the validity of the two points stated in subsection 3.3.3.1 and shown in Figure 3.10 . Nonetheless, more studies should be performed using non-linear models, by coupling the elastic behavior of the interface model with the behavior of the surrounding concrete, which is the weakest material in this process.

3.4 SIMULATIONS ON PULL-OUT TESTS USING CLASSICAL NONLINEAR INTERFACE ELEMENTS

3.4.1 General description

In order to study the capability of classical nonlinear interface models to simulate the steel-concrete interface, more realistic simulations are performed using a damage model for concrete and two different SCI models.

The test case and the corresponding boundary conditions are the same as the ones described in subsection 3.3.1 and shown in Figure 3.8 .

3.4.2 Generated sample

In order to perform nonlinear pull-out tests simulations in this section, a smooth bar sample is modelled using the procedure described in section 3.2 . The adhesive length is half the total length of the bar, as defined in (RILEM, 1970). The diameter d of the cylindrical bar is 8 mm, and the concrete cubic sample side length is equal to $10d$ as recommended by (RILEM, 1970), that is 80 mm; the total adhesive length is then equal to $5d$, that is 40 mm. The number of mesh elements in the concrete and steel bar are 303 000 and 310 000, respectively. The characteristic size of each mesh element at the outer surface of the concrete sample is equal to about 5 mm, while the triangular edge of each element at the steel concrete interface is almost 0.4 mm, as shown in Figure 3.13 .

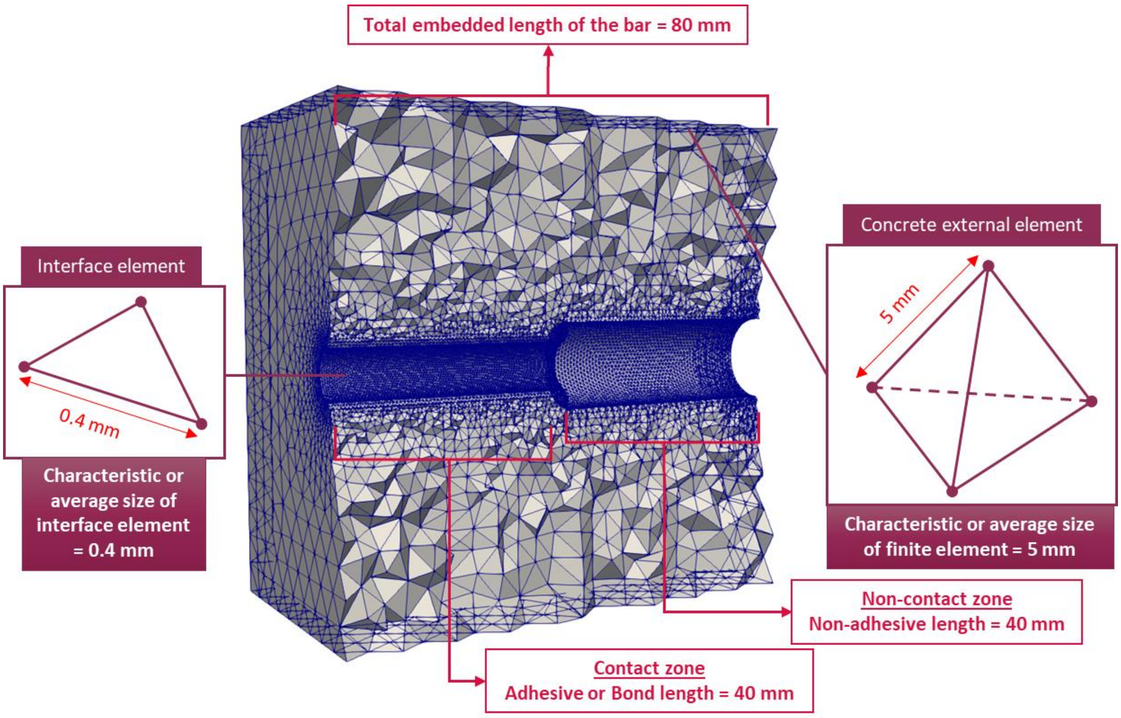

Figure 3.13 Concrete meshed section, showing the total embedded length of the bar that is divided into contact and non-contact zones, and the characteristic or average size of the sides of the interface surface element and the concrete external tetrahedral elements.

3.4.3 Nonlinear model for concrete: Mazars’ model and regularization

Concrete is to be assigned the Mazars damage model (Mazars, 1986, 1984), in order to be able to describe cracking phenomena through a damage parameter. It is one of the widely used damage models for geomaterials such as concrete. This model is able to reproduce the direct cracking under both tensile and compressive stresses (or strain). It is formulated as follows:

Constitutive law:

$$\sigma_{ij} = (1 - D)\mathbb{C}_{ijkl}\varepsilon_{kl} \tag{3.4}$$

where σ is the stress tensor, ε is the strain tensor, D is the total damage and $\mathbb{C}$ is the stiffness tensor. The criterion for damage evolution reads:

$$f\left(\varepsilon_{eq}, D\right) = \varepsilon_{eq} - \kappa(D) \tag{3.5}$$

where the threshold of damage growth $\kappa(D)$ and the equivalent strain ε_{eq} are written as:

$$\kappa(D) = \max_{history} \varepsilon_{eq} \quad \text{and} \quad \varepsilon_{eq} = \sqrt{\textstyle\sum_{i=1}^{3} \langle \varepsilon_i \rangle_+^2} \tag{3.6}$$

and the initial value of $\kappa(0) = \varepsilon_{D_0}$, where ε_{D_0} is the initial damage threshold, which can be related to the ultimate tensile stress of concrete in uniaxial tension $f_{t\,con}$ and Young’s modulus of the undamaged concrete E_{con} (Pijaudier-Cabot and Mazars, 2001):

$$\varepsilon_{D_0} = \frac{f_{t\,con}}{\mathrm{E}_{con}} \tag{3.7}$$

Also, $\langle\cdot\rangle_+$ represents the positive part of the principle strains ε_i. In order to emphasize the unsymmetrical behavior between tensile and compressive states of stresses, the total damage D is a linear combination of damage in tension D_t and in compression D_c following:

$$D = \alpha_t^{\beta} D_t + \alpha_c^{\beta} D_c \tag{3.8}$$

where D_t and D_c have their own evolution law:

$$D_{t,c} = 1 - \frac{\varepsilon_{D_0}\left(1 - A_{t,c}\right)}{\varepsilon_{eq}} - \frac{A_{t,c}}{\exp(B_{t,c}\left(\varepsilon_{eq} - \varepsilon_{D_0}\right))} \tag{3.9}$$

where $\alpha_c = 1 - \alpha_t$. α_t is computed from the strain and stress tensors such as:

$$\alpha_t = \sum_{i=1}^{3} \frac{\langle \varepsilon_{ti} \rangle \, \langle \varepsilon \rangle_+}{\varepsilon_{eq}^2} \tag{3.10}$$

where ε_{ti} are the principal values of the strain tensor due to traction (positive) stress, defined as follows:

$$\varepsilon_t = \frac{1 + \upsilon_{con}}{\mathrm{E}_{con}} \sigma^+ - \frac{\upsilon_{con}}{\mathrm{E}_{con}} tr(\sigma^+) \tag{3.11}$$

with the following partition for the stress tensor:

$$\sigma = \sigma^+ + \sigma^- \tag{3.12}$$

where σ^+ is the tensor containing the positive principal stresses and zero elsewhere, while σ^- is the tensor containing the negative principal stresses and zero elsewhere. υ_{con} is the Poisson's ratio of concrete, A_t is responsible for the residual stress and B_t for the descending slope after the peak in a uniaxial tension test, while A_c is responsible for the residual stress and B_c for the descending slope after the peak in a uniaxial compression test. In addition, β is a variable for correction of the shear in order not to neglect the effect of shearing, which will be underestimated if it is taken equal to 1 (Pijaudier-Cabot et al., 1991). In other words, the purpose of this varaible β is to reduce the effect of damage on the response of the material under shear compared to tension where $\alpha_t = 1$ (Pijaudier-Cabot et al., 1991).

According to (Hillerborg et al., 1976), softening models, such as Mazars damage model, leads to a strong mesh size dependency, in which a strain localization occurs in a certain group of elements redirecting the behavior in the structure. This can be seen in Figure 3.14(a), which shows the stress - displacement response of uniaxial tensile test performed on two concrete finite elements of different sizes. Thus, less energy is dissipated in the structure in such models when the mesh size is small. To prevent such effect, a regularization method is used based on Hillerborg concept of fracture energy (Hillerborg et al., 1976).

The evolution proposed in here is an exponential evolution, in which the damage due to tension D_t, initially proposed in equation (3.8) is replaced by the following equation :

$$D_t = 1 - \frac{\varepsilon_{D_0}}{\varepsilon_{eq}} \exp\left(B_t\left(\varepsilon_{D_0} - \varepsilon_{eq}\right)\right) \tag{3.13}$$

while B_t is calculated as follows:

$$B_t = \frac{l \cdot E_{con} \cdot \varepsilon_{D_0}}{G_{f\ con} - \frac{l \cdot {\varepsilon_{D_0}}^2}{2E_{con}}} \tag{3.14}$$

where l is the characteristic size of the finite element, $G_{f\ con}$ is the fracture energy and E_{con} is concrete's Young modulus. Thus, the value of B_t assigned in the pull-out simulations is unique to each finite element. The same response can be seen in Figure 3.14(b) for the two finite elements, which shows the stress-displacement behavior of uniaxial tensile simulations. By considering a regular tetrahedron formula, the characteristic size l is calculated as follows:

$$l = \sqrt[3]{\frac{12V}{\sqrt{2}}} \tag{3.15}$$

where V is the volume of the finite tetrahedral element.

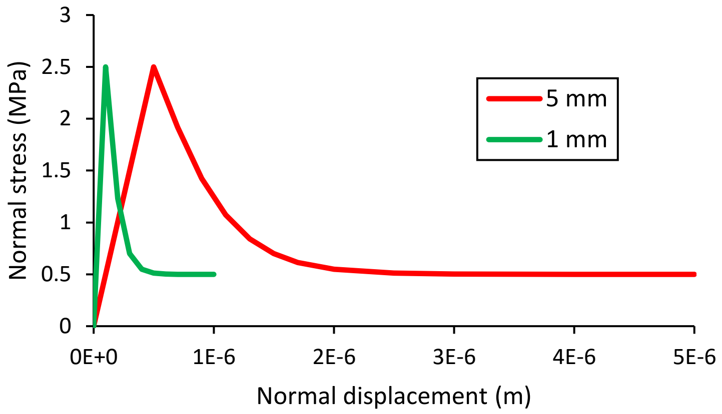

(a)

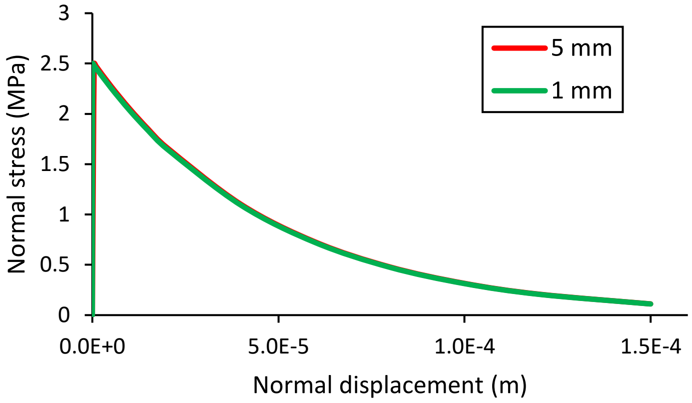

(b)

Figure 3.14 Stress - displacement response under tension on two concrete finite elements whose sizes are 1 mm and 5 mm of (a) the classical Mazars model using $A_t = 0.8$, $B_t = 17000$, $E_{con} = 25\ GPa$ *and* $f_{t\ con} = 2.5\ MPa$ *(b) the regularized Mazars model using* $G_{f\ con} = 120\ N/m$, $E_{con} = 25\ GPa$ *and* $f_{t\ con} = 2.5\ MPa$

As a consequence of the regularization, one can see that the stress-strain response becomes different for each element (to ensure the same stress – displacement curve).

Additionally, (Mier, 1984) showed that the stress-strain curve in compression is influenced by the slenderness of the specimen, unlike the stress-displacement curve, which was also found in different experimental results like (Comi and Perego, 2001; Jansen and Shah, 1997; Lee and Willam, 1997; Markeset, 1993; Rokugo and Koyanagi, 2018). Thus, just like in tension, numerical behavior in compression should be also independent of the size of the mesh elements. This justifies the need to develop a methodology for regularizing the compressive behavior of concrete. Hence, a similar problem occurs under compression when assigning A_c and B_c the values recommended by (Pijaudier-Cabot and Mazars, 2001), because the sizes of the finite elements may be very small. This effect can be seen in Figure 3.15 (a), in which a uniaxial compressive test is performed on a concrete cube whose Young's modulus is E_{con} = 25 GPa and maximum compressive strength is slightly larger than 30 MPa. The values of the parameters A_c and B_c are varied for each case until reaching a very similar general behavior, following the methodology from (Calixte et al., 2022). These chosen values of A_c and B_c that best fit are shown in Table 3.1, and the corresponding behavior can be seen in Figure 3.15 (b).

Table 3.1. Mazars parameters A_c and B_c assigned for different element sizes

$l(in\ mm)$	A_c	B_c
0.2	0.0033	4.9
1	0.0169	25
2	0.0343	50
3	0.0517	75
5	0.09	129

Finally, a fitted evolution law for each of these two parameters as a function of l is eventually used, by using a second-degree polynomial, as follows:

$$A_c = -335.9133\, l^2 + 16.2746\, l - 0.0002 \tag{3.16}$$

$$B_c = 338073.9767\, l^2 + 24023.4962\, l - 0.3277 \tag{3.17}$$

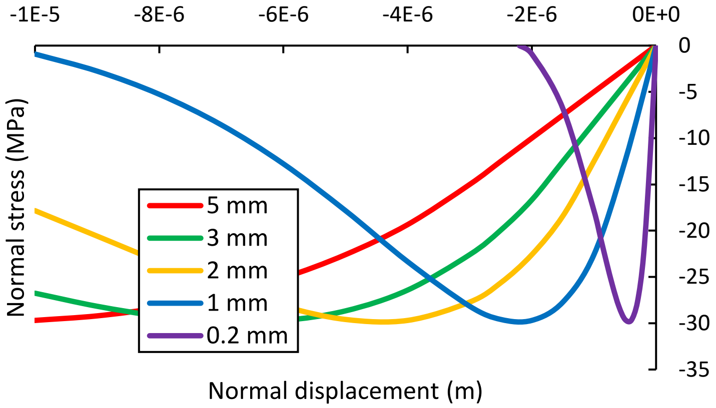

(a)

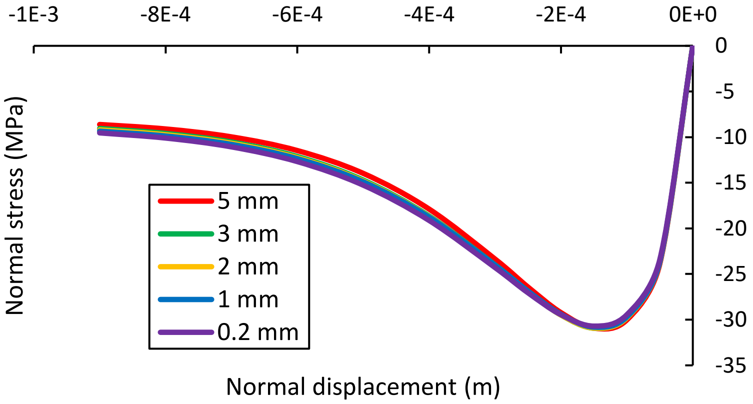

(b)

Figure 3.15 Stress - displacement response of Mazars model under compression on five concrete finite elements with prescribed sizes using (a) common values $A_c = 1.4,\ B_c = 1600$*; (b) modified values of* A_c *and* B_c *(see Table 3.1) unique for each case*

Regarding the other parameters of the concrete model, the shear correction coefficient is $\beta = 1.06$, which is within the acceptable range $1 \leq \beta \leq 1.06$. For instance, the more the value is close to lower limit, the more the effect of shearing is underestimated (Pijaudier-Cabot and Mazars, 2001). It also makes it more and more difficult to converge. Concrete's Young's modulus, Poisson's ratio and fracture energy in tension are too assigned for each case.

3.4.4 Nonlinear model for steel

The steel bar is assigned a classical perfect yielding elastic model, where its Young's modulus is 200 GPa and its Poisson's ratio is 0.3. The yield stress limit is 365 MPa followed by a perfect yield behavior for which the Von Mises stress will always be equal to the yield stress as the steel is strained.

3.4.5 Nonlinear steel-concrete interface models

3.4.5.1 Coulomb's frictional interface model

Coulomb's 3D interface frictional model is based on Mohr-Coulomb's failure criterion, and is intended to describe the debonding between concrete and steel bar. It was previously used in several applications to represent a sliding friction between two objects, such as recently in (Bui et al., 2021) where it was used to represent the mortar joint element between each two blocks in masonry walls.

In the elastic part of the model, the stress tensor σ of the interface element is governed by normal and shear stiffness of the interfaces K_n and K_s according to the linear elastic spring model formulation:

$$\begin{pmatrix}\sigma_n\\ \sigma_t\\ \sigma_h\end{pmatrix} = \begin{pmatrix}K_n & 0 & 0\\ 0 & K_s & 0\\ 0 & 0 & K_s\end{pmatrix}\begin{pmatrix}u_n\\ u_t\\ u_h\end{pmatrix} \qquad (3.18)$$

The interface failure occurs due to either shear or tension according to the Mohr-Coulomb's failure criterion simplified in Figure 3.16.

The maximum shear stresses $\sigma_{t\,max}$ and $\sigma_{h\,max}$ in the two tangential directions are given by:

$$\sigma_{s\,max} = C + |\min(\sigma_n, 0)| \cdot \tan\emptyset \qquad (3.19)$$

where C is the interface's cohesion, $\emptyset$ is the interface's friction angle, and $\min$ is the minimum between the two terms, meaning that only compressive stress is taken into account. The maximum normal stress $\sigma_{n\,max}$ is equal to the maximum tensile strength f_t, which should be predefined initially as one of the model parameters, taking into account the following constraint:

$$\sigma_{n\,max} = f_t \qquad and \qquad 0 \leq f_t \leq \frac{C}{\tan \emptyset} \qquad (3.20)$$

When f_t is null, the interface has no strength in tension, which means the two surfaces will instantly separate under any applied tension, resembling a contact formulation.

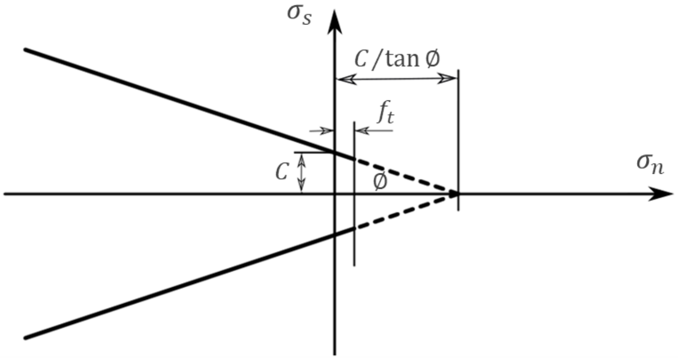

Figure 3.16 Mohr-Coulomb's failure criterion for the Coulomb's interface model

In order to observe the interface element behavior under different conditions, several simulations are performed on one interface element connecting two blocks to each other (Figure *3.17*), whose side length is 1 mm. A certain shearing or normal displacement is applied either in compression or in tension and the corresponding applied force is calculated.

The behavior in the normal direction for Coulomb's interface model is shown Figure 3.18(a). The maximum tensile strength f_t is taken equal to 3 MPa, the cohesion C is 3 MPa, the friction angle Ø is 45°, while the normal stiffness K_n and the shear stiffness K_s are both taken equal to 10^{11} N/m^3. These parameters are only chosen to illustrate graphically the behavior of the model in a simple case.

One can see that the compressive behavior is equivalent to a linear elastic spring model with no peak, which is due to the non-existence of failure in compression in this model and due to elastic behavior clearly stated in Eq. (3.18). Thus, the compressive behavior depends uniquely on the value of the normal stiffness K_n. On the other hand, the behavior in tension does not only depend on the normal stiffness K_n, but also on the maximum tensile strength f_t. One can see that the elastic behavior is similar to that in compression, and separation failure is captured when the normal stress reaches the maximum normal strength f_t, after which the normal stress decreases to zero instantly.

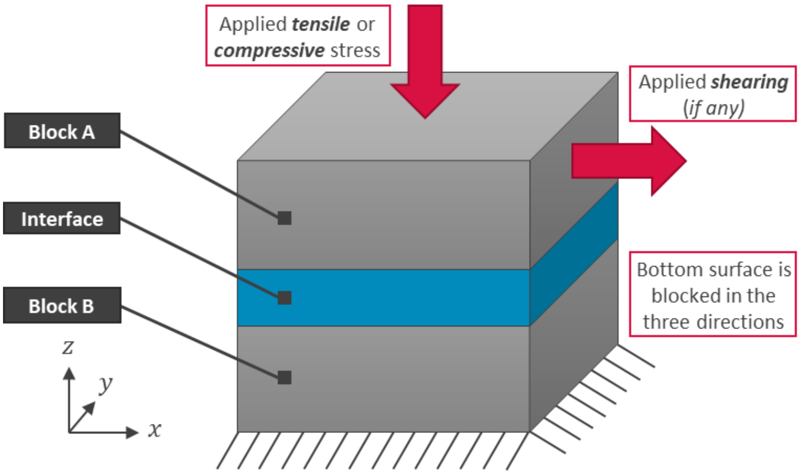

Figure 3.17 Geometric model for the one-interface element simulations

In addition, the tangential behaviors of the interface model are shown in Figure 3.18(b), after performing several simulations on the same interface element, by imposing a certain compressive displacement then applying a tangential displacement. The parameters are assigned the same values as the previous case, except for the friction angle $\emptyset$, which is assigned a different value in each simulation; 15°, 30° and 45° .

Concerning the tangential behavior with initial tensile displacement, one can deduce from Eq. (3.19) that imposing an initial tensile displacement will reproduce the same response as the pure shearing or tangential case without initial imposed normal displacement. By observing Figure 3.18(b), one can see that the tangential behavior is different from the exhibited behavior in the normal direction. This behavior consists of two parts: a linear increase in stress followed by a constant stress. The first part is the elastic part, which depends uniquely on the shear stiffness K_s. This behavior ceases when the maximum shear stress $\sigma_{s\,max}$ expressed in Eq. (3.19) is reached, maintaining a constant stress. This second part depends on the compressive stress applied σ_n according to Eq.(3.20), on the cohesion C and the friction angle $\emptyset$. The residual stress will always be equal to the peak stress, without any change in the stress during the post peak behavior, except if σ_n evolves.

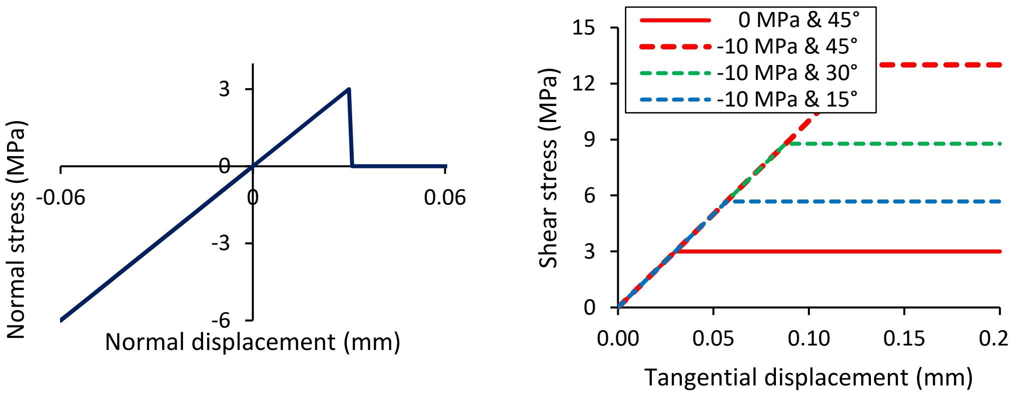

(a) *(b)*

Figure 3.18 For the Coulomb's interface model: (a) The normal stress versus the normal displacement (b) The shear stress versus tangential displacement under an imposed compressive displacement and for different values of the friction angle ∅ (in degrees)

3.4.5.2 Tvergaard's modified cohesive zone model

A modified version of Tvergaard's cohesive zone model, which was initially presented in (Tvergaard, 2003, 1990), and used in other works such as (Wu and Wriggers, 2015), is presented.

The displacement jump across the interface element $[\![u_i]\!]$ is obtained from the displacements u_i^+ and u_i^- of the points located on the top and bottom sides of the interface respectively, which are calculated with respect to a fixed coordinate system, as follows:

$$[\![u_i]\!] = u_i^+ - u_i^- \qquad (3.21)$$

where $[\![u_n]\!]$ is the normal displacement jump, $[\![u_t]\!]$ and $[\![u_h]\!]$ are the two tangential displacements jumps.

A parameter λ representing the equivalent opening of the interface is defined as follows:

$$\lambda = \sqrt{\langle [\![u_n]\!] \rangle_+^2 + \frac{[\![u_t]\!]^2 + [\![u_h]\!]^2}{\delta_s}} \tag{3.22}$$

$\langle\cdot\rangle_+$ indicates that the positive displacement jump is only considered. In addition, δ_s is the stiffness ratio defined as follows:

$$\delta_s = K_n/K_s \tag{3.23}$$

The damage indicator $\widetilde{\lambda}$ is calculated as a function of λ and of the initially assigned damage threshold λ_0 parameter:

$$\begin{cases} \widetilde{\lambda} = \lambda - \lambda_0 & if\ \lambda > \lambda_0\ and\ \ \dot{\widetilde{\lambda}} > 0 \\ \widetilde{\lambda} = max\left(\widetilde{\lambda_p}, 0\right) & if\ else \end{cases} \tag{3.24}$$

where $\widetilde{\lambda_p}$ represents the previous damage indicator attained, which is initially zero, and $\dot{\widetilde{\lambda}}$ is the evolution of the damage indicator, which has the same sign as $\widetilde{\lambda} - \widetilde{\lambda_p}$, and max represents the maximum between the two terms.

In the elastic part of the model, that is when $\lambda_0 > \lambda$, the behavior is governed by normal and shear stiffness of the interfaces K_n and K_s according to Eq. (3.18).

When there is no propagation of damage, or when the damage is still null, the evolution of the damage indicator $\dot{\widetilde{\lambda}} = 0$ and in this case, the normal stress σ_n is calculated as follows:

$$\begin{cases} \sigma_n = \dfrac{f_t}{\widetilde{\lambda} + \lambda_0} \exp\left(\dfrac{-f_t\,\widetilde{\lambda}}{G_f}\right) [\![u_n]\!] & if\ [\![u_n]\!] \geq 0 \\ \sigma_n = K_n [\![u_n]\!] & if\ [\![u_n]\!] < 0 \end{cases} \tag{3.25}$$

where f_t is the maximum tensile strength of the interface, and G_f is the fracture energy of the interface. Note that in order to maintain continuity of the normal stress when damage is null in Eq. (3.25), the normal stiffness K_n should be initially defined as follows:

$$K_n = f_t/\lambda_0 \tag{3.26}$$

while the tangential stress σ_s in each of the two tangential directions t and h is calculated as follows:

$$\sigma_s = \frac{f_t}{\widetilde{\lambda} + \lambda_0} \exp\left(\frac{-f_t\,\widetilde{\lambda}}{G_f}\right) \frac{[\![u_s]\!]}{\delta_s} \tag{3.27}$$

Notice that Eqs. (3.25) and (3.27) verify Eq. (3.18) when the damage is null, i.e. $\widetilde{\lambda} = 0$, which represents the elastic part of the model.

On the other hand, when $\dot{\widetilde{\lambda}} > 0$, damage D_{int} propagates in the interface and it is defined as:

$$D_{int} = 1 - \exp\left(\frac{-f_t\,\widetilde{\lambda}}{G_f}\right) \tag{3.28}$$

In this case, the normal stress is calculated as follows:

$$\begin{cases} \sigma_n = (1 - D_{int})\dfrac{f_t}{\lambda}[\![u_n]\!] = \dfrac{f_t}{\lambda} \exp\left(\dfrac{-f_t\,\widetilde{\lambda}}{G_f}\right)[\![u_n]\!] & if\ [\![u_n]\!] \geq 0 \\ \sigma_n = K_n [\![u_n]\!] & if\ [\![u_n]\!] < 0 \end{cases} \tag{3.29}$$

while the tangential stress in each direction is calculated as follows:

$$\sigma_s = \frac{f_t}{\lambda} \exp\left(\frac{-f_t\,\widetilde{\lambda}}{G_f}\right) \frac{[\![u_s]\!]}{\delta_s} \tag{3.30}$$

In order to understand graphically the behavior of Tvergaard's cohesive zone model, a simulation is done on one-interface element connecting two blocks to each other (Figure 3.17). First, a certain normal displacement is applied either in compression or in tension with no tangential displacement then the corresponding applied force is calculated, and the results are shown in Figure 3.19(a). The maximum tensile strength f_t is taken equal to

3 MPa, the fracture energy G_f is 200 N/m, the damage threshold λ_0 is 0.01 mm, while the normal stiffness K_n is calculated according to Eq. (3.26) and the shear stiffness K_s is taken equal to it, i.e. 3×10^{11} N/m^3. These parameters are only chosen to illustrate graphically the behavior of the model in a simple case.

One can see that the behavior is equivalent to an elastic spring model in compression, depending uniquely on the value of K_n. However, the behavior is different in tension. Before reaching the damage threshold λ_0, there is an elastic increase of the stress until reaching the peak, which is equivalent to the maximum tensile strength f_t. After reaching the peak stress, damage initiates and the normal stress decreases exponentially until reaching zero stress, and the area under the curve should be equal to the fracture energy G_f.

Second, the tangential responses are shown in Figure 3.19(b), after performing several simulations on the same interface element, by imposing a certain initial tensile displacement then applying a tangential displacement. The same values are maintained for the parameters of the interface model.

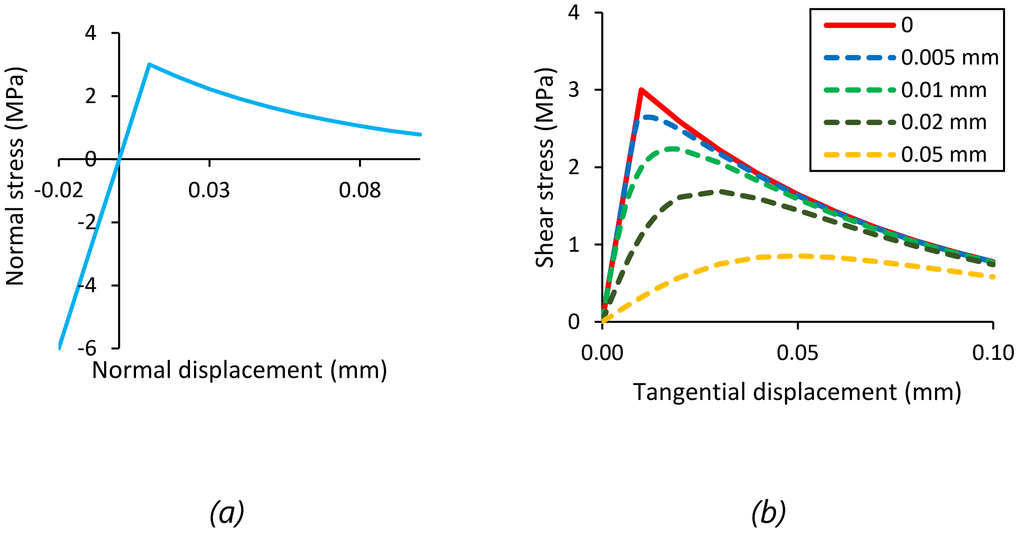

Figure 3.19 For the modified Tvergaard's interface model: (a) The normal stress versus the normal displacement (b) The shear stress versus the tangential displacement under an imposed normal positive displacement

Concerning the tangential behavior with initial imposed compressive displacement, one can see from Eq. (3.22) that the equivalent opening λ

itself depends on the positive normal displacement only. Thus, any compressive displacement applied would not change λ. Additionally, the tangential stress σ_s, which is either calculated by Eq. (3.27) or Eq. (3.30), depending on the case, is in both equations only affected by λ. As a result, σ_s is independent of the compressive displacement. Hence, the corresponding shear behavior will be the same as the pure shear behavior regardless of the value of the compressive displacement initially imposed.

In case of pure shear, the behavior is similar to the tensile behavior, while when a certain tensile displacement is initially imposed on the interface, one can see a drop in the peak shear stress. The higher the imposed displacement, the lower the peak shear stress. This is due to the propagation of damage in the interface before the application of tangential displacement for high tensile stresses, because the equivalent opening λ depends on the positive normal displacement according to Eq. (3.22).

3.5 SMOOTH BAR PULL-OUT TEST SIMULATIONS WITH CLASSICAL INTERFACE MODELS

In order to show the importance of the steel-concrete interface on the general behavior of the smooth bar in the pullout test, two simulations are performed on the smooth bar sample described in subsection 3.4.2, using the two different interface models described in subsection 3.4.5.2 and 3.4.5.1.

The aforementioned behaviors are introduced using the open source MFront code generator (Helfer et al., 2015; *MFront*, tfel.sourceforge.net), then they have been imported to the finite element code Cast3M along with the previously generated reinforced concrete model to perform the pull-out test simulations.

The experimental pull-out test results on a smooth bar from (Anwar Hossain, 2008) are extracted in order to compare it with the numerical results and check the validity of the interface models; it uses Portland concrete of 28 days, whose ultimate compressive strength is almost 31 MPa.

The damage in the interface may be interpreted as a direct damage of the concrete surrounding immediately the bar, since the interface actually resembles a concrete layer that is slightly weaker than the concrete block and experiencing complex phenomena. Thus, it plays the role of the first initial surface of contact of concrete with steel, at which a full damage reflects the start of the cracking phenomena in concrete. This shows a direct relation of the interface damage with the concrete volume.

Table 3.2 Assigned values to the parameters of the Mazars model for concrete in the smooth bar pull-out simulations

E_{con} (GPa)	v_{con}	$f_{t\,con}$ (MPa)	$G_{f\,con}$ (N/m)
25	0.2	2.5	120
ε_{D_0}	A_c	B_c	β
Eq. (3.7**)** $\Rrightarrow \mathbf{10^{-4}}$	Eq. (3.16)	Eq. (3.17)	1.06

In the two simulations performed using the aforementioned interface models, steel is assigned the perfect yield model as described in subsection 3.4.4, and concrete is assigned Mazars model with all the modifications described before in section 3.4.3. The values of the parameters for concrete are summarized in Table 3.2, and the values of the parameters assigned for each of the two interface models are shown in Table 3.3. These values are chosen in a way that they do not exceed the material properties of the surrounding concrete, since the interface resembles a less stiff concrete layer. The friction coefficient of the steel-concrete interface is considered 0.3, according to (Wang and Liu, 2004; Xu et al., 1994), while K_n is calculated from Eq. (3.26). Parameters, like K_s, are adjusted to produce parts of the experimental curve, since the aim here is to check the ability of any of the models to reproduce the general behavior. The mean bond stresses versus the free end displacement, which is the displacement measured at the free end of the steel bar, are plotted Figure 3.20 for the two simulations along with the experimental results.

One can see that the cohesive zone model is able to reproduce the peak stress along with the general post peak behavior, but not a non-null residual stress. On the contrary, Coulomb's interface model shows a different behavior, by maintaining an equivalent peak and residual stresses. This is related also to the shear stress formulas that ensure such behavior. One can see that both results are very similar to the behavior of the interface model under pure shearing or shearing with compression shown in Figure 3.19(b) and Figure 3.18(c). This is due to the smooth shape of the rebar where shearing dominates, and the low value of normal stresses. Additionally, no visible damage can be seen in concrete in both cases. This can be explained by the slipping failure that occurs in both cases, which is reflected in the full damage of the interface for the CZM that had obviously failed due to shearing.

Table 3.3. Assigned values to the parameters of the Tvergaard's CZM and Coulomb's interface model in the smooth bar pull-out simulations

Tvergaard's modified CZM	$K_n\ (\mathrm{N}/m^3)$	$K_s\ (\mathrm{N}/m^3)$	$f_t\ (MPa)$	$G_f\ (N/m)$	$\lambda_0(m)$
	$3.6\ \times 10^{10}$	4.5×10^{10}	1.8	80	5×10^{-5}
Coulomb's interface model	$K_n\ (\mathrm{N}/m^3)$	$K_s\ (\mathrm{N}/m^3)$	$f_t\ (MPa)$	$C\ (MPa)$	$\emptyset(°)$
	$3.6\ \times 10^{10}$	$4.5\ \times 10^{10}$	1.8	1.8	17

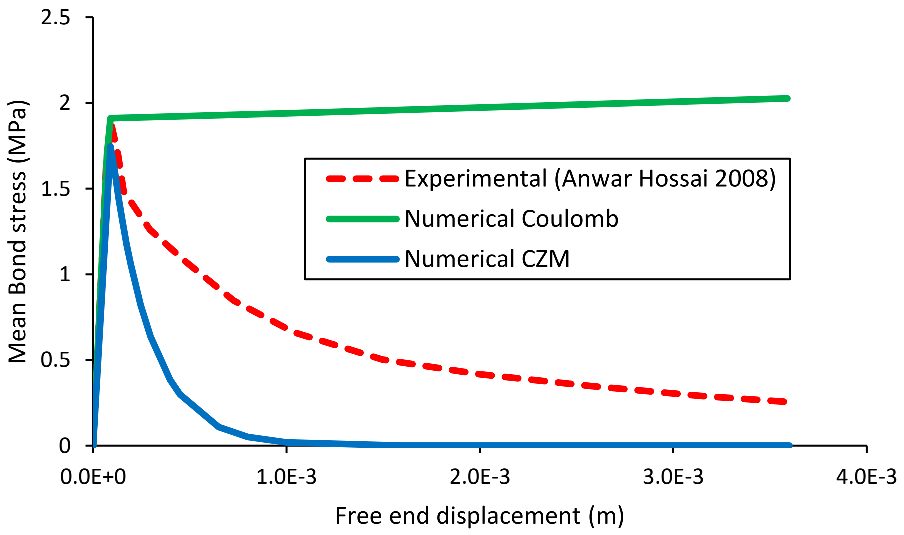

Figure 3.20 Numerical results of the two simulations using Tvergaard's CZM and Coulomb's interface model, compared to the experimental results extracted from (Anwar Hossain, 2008)

Based on the general experimental behavior, and due to the existence of a very small compressive stress, one can conclude that the smooth bar behavior is a direct reflection of the shearing behavior with (low) compression of the interface model. For the CZM, the disadvantage of this model in this case is the non-existence of any effect of compression on the shearing phenomenon, which leads always to zero residual shear stress. Still, an important advantage is the non-linear decrease of stress and the use of damage to represent the cracking in the interface, which is as stated before, a continuation of the surrounding concrete. On the other hand, an advantage of Coulomb's interface model is the constant none zero residual stress observed. However, this model does not contain damage and the residual stress is always close to the peak stress. Thus, a combination of both models is to be proposed, in order to take into account these advantages of both interface models.

3.6 CONCLUSIONS

In this chapter, the generation process of the pullout numerical samples was detailed, including the generation of the steel bar, the aggregates and the surrounding mortar or concrete, followed by the final applied mesh.

This generation procedure, which was previously used in other studies to represent coarse aggregates, can give a very good 3D representation of the reinforced concrete sample at the mesoscopic scale. It can capture the detailed geometry of the steel bar, especially the detailed shape of the ribs. A fine mesh can be used, which is essential for the purpose to study the distribution of cracks and stresses near the steel further on in this study. The mesh is certainly much more complicated when coarse aggregates are used, since they will control the meshing procedure. This certainly makes the simulations times consuming, but is still essential at such mesoscopic scale.

Linear simulations were performed on a smooth and a herringbone ribbed bar in order to study the stiffness parameters involved in the linear spring model in subsection 2.4.1.2. The study has proved the domination of the normal stiffness at the sides of the ribs, mobilizing the resistance in the normal direction, while the shear stiffness controls at the cylindrical part and the tips of the steel ribs, resembling the resistance in the direction parallel to the surfaces that is affected by shearing forces.

The last part of the chapter dealt with nonlinear simulations using non-linear model for concrete, steel and the steel-concrete interface. For concrete model, Mazars classical model and its regularization in tension was presented, along with the proposed modification in compression. It is essential to prevent the mesh dependency of the concrete model.

The inability of the corresponding behaviors of Tvergaards cohesive zone model and Coulomb’s frictional model, which were introduced in this chapter, to reproduce the experimental results of pull-out test extracted from literature was shown on a smooth bar sample. As expected and seen in Figure 3.20, the smooth bar pull-out test is directly affected by the interface model, as it reproduces the shearing behavior of the interface. This can be justified by the smooth shape of the bar experiencing very low normal stress, and where shearing behavior dominates. This justifies the need to propose a new model that combines the advantages of both cohesive zone and frictional models, in order to be able to reproduce the experimental behavior correctly.

The next chapter deals with the implementation of a frictional cohesive zone model, and includes simulations using a smooth bar compared to experimental results. In addition, the calibration of the proposed interface model is detailed.

4 DEVELOPMENT OF A NEW FRICTIONAL COHESIVE ZONE MODEL

4.1 INTRODUCTION

This chapter deals with the development and implementation of a new frictional cohesive zone model, named FCZM in the following chapters, and the calibration process of the model parameters using both smooth and ribbed bars.

It has been demonstrated in section 3.5 that classical approaches for the steel-concrete interface cannot correctly reproduce the general behavior of pull-out test. Thus, a new interface model should be implemented, which combines the advantages of the classical interface models introduced in susbections 3.4.5.1 and 3.4.5.2. Hence, the new frictional cohesive zone model proposed is a combination of an elastoplastic model, which is the Coulomb's frictional model (subsection 3.4.5.1), and a damage-based cohesive approach, which is the Tvergaard's cohesive zone model (subsection 3.4.5.2). It is based mainly on what was initially proposed by (Alfano and Sacco, 2006) as a 2D model, as part of frictional cohesive zone approaches discussed in subsection 2.4.2.4. According to (Alfano and Sacco, 2006), the cohesive crack propagation phenomena, which are governed by nonlinear fracture mechanics, can be modelled at a meso-mechanical level by assuming that a representative elementary area A of the interface can be decomposed into an undamaged part $(1 - D_{int})A$ and a completely damaged part $D_{int}A$, with the damage parameter D_{int} being the relative measure of the damaged part (Figure 4.1).

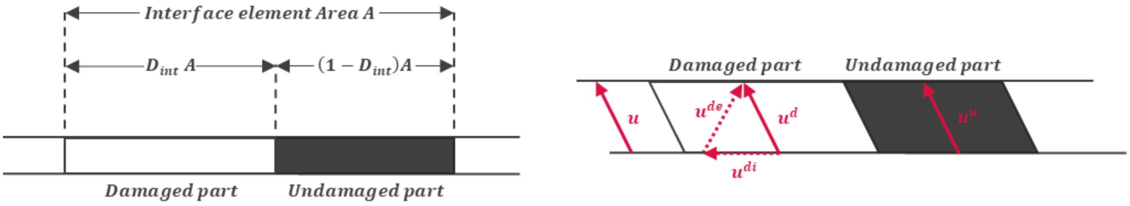

Figure 4.1 Meso-mechanical interpretation of the cohesive frictional interface model showing the decomposition of the representative interface element and the kinematic assumptions, based on (Alfano and Sacco, 2006)

In this model, which was generalized to a 3D approach in (Albarella et al., 2015; Roberto Serpieri et al., 2017; R. Serpieri et al., 2017), damage evolves based on Crisfield's bilinear damage model presented in (Alfano and

Crisfield, 2001), while the frictional behavior is governed by a Coulomb's law. Recently, (Jaaranen and Fink, 2021) used this 2D model to represent the contact between timber and concrete by varying the friction coefficient.

Here, the approach initially proposed in (Albarella et al., 2015; Alfano and Sacco, 2006) is extended by using the Tvergaard's cohesive zone model, along with certain modifications in compression to maintain continuity of stress when there is a sudden change in the type of stress, for describing the undamaged stress at the interface. The choice is made following the introduction of this interface model in subsection 3.4.5.2 and its application in section 3.5. Tvergaard's model has shown that it can give a better general behavior for the smooth case, when compared to Crisfield's model in (Serpieri and Alfano, 2011), except for the residual stress which is almost zero.

In the next part of the chapter, the calibration process is discussed with both the smooth and ribbed bar cases using the newly implemented FCZM, by comparing the corresponding results to experimental data for each case, followed by a verification of the method on another ribbed bar sample. In the last part, the results are finally analyzed in terms of damage and distributions of principle stresses.

4.2 THE FRICTIONAL COHESIVE ZONE MODEL

4.2.1 Description and formulation

In this section, a 3D interface model is proposed and detailed, based on the existence of a predefined interface of zero thickness between two volumetric elements, and on the possibility of a displacement jump across the interface element, as shown in Eq. (3.21). The frictional cohesive zone model proposed is a combination of a damage-based cohesive approach, which plays a role whenever the interface is not fully damaged, and an elastoplastic model that occurs whenever damage is initiated, and eventually fully controls the interface stress when the interface is fully damaged.

The initial frictional cohesive zone model proposed in 2D by (Albarella et al., 2015; Alfano and Sacco, 2006) used Crisfield's bilinear model (Alfano and Crisfield, 2001). Here by, as mentioned above it is modified using the Tvergaard's cohesive zone model for describing the undamaged stress at the interface. A modification is proposed in compression to prevent any discontinuity of the stress when the nature of normal stress is reversed from tension to compression and vice versa. In contrary to Crisfield's model, Tvergaard's CZM is adopted due to its more realistic post-peak behavior, and to prevent reaching a null stress, which may lead to some numerical problems.

The model is implemented using the open source MFront code generator (Helfer et al., 2015), then it has been imported to the finite element code Cast3M to perform the pull-out test simulations.

Similarly to (Alfano et al., 2006; Alfano and Sacco, 2006), the element is divided into an undamaged part A_u, where the interface is fully bonded, and a damaged part A_d, where frictional contact takes place. This can be written as shown in Figure 4.1, where A is the area and D_{int} is the damage parameter of the interface element. In addition, the relative displacement u is assumed completely constant over the whole interface element, and the relative displacement in the damaged part u^d is divided into an elastic displacement u^{de} and an inelastic displacement u^{di} in the tangential direction only, since there is no contact in this part under tension. Moreover, the relative displacement of the undamaged part u^u is assumed to be fully elastic and equal to the elastic displacement of the undamaged part u^{ue}.

The interface total stress σ is supposed to be constant on each part. The stress on the undamaged part of the interface is denoted by σ^u, while the stress on the damaged part of the interface is denoted by σ^d.

Total stress σ:

The total stress σ is calculated according to the following additive formula:

$$\sigma = D_{int}\sigma^d + (1 - D_{int})\sigma^u \qquad (4.1)$$

Damaged part stress σ^d:

For the damaged part, the law deployed is considered as a perfect plastic behavior as there is no hardening. The normal part complies a unilateral elastic law, while a non-associative Coulomb's frictional law with tangential sliding (Simo and Hughes, 1998) is assigned to the tangential part. Hence, the displacement is decomposed, as previously mentioned, into an elastic displacement u^{de} and an inelastic displacement u^{di}, in which the inelastic part is fully tangential.

Taking into account that there is no contact in this part under tension, the stress of the damaged part of the interface σ^d is related to the elastic displacement u^{de} as follows:

$$\sigma^d = Hu^{de} = H\left(u\text{-}u^{di}\right) \qquad (4.2)$$

where H is defined as:

$$\begin{aligned} H &= diag\left[\left(1 - v\left(u_n - u_n^{di}\right)\right) K_n, K_s, K_s\right] \\ &= \begin{pmatrix} (1 - v(u_n))K_n & 0 & 0 \\ 0 & K_s & 0 \\ 0 & 0 & K_s \end{pmatrix} \end{aligned} \qquad (4.3)$$

where $diag[M]$ represents the terms on the diagonal of the matrix M.

Since the normal inelastic displacement $\mathrm{u}_\mathrm{n}^\mathrm{di}$ is always null, and v is the Heaviside function defined as:

$$v(x) = \begin{cases} 0 \; if \; x \geq 0 \\ 1 \; if \; x < 0 \end{cases} \qquad (4.4)$$

Thus, the term $(1 - \mathrm{v}(\mathrm{u_n}))$ is null when $\mathrm{u_n} \geq 0$, because it is a no tension relation by definition, and it is equal to 1 when $\mathrm{u_n} < 0$, representing the compressive behavior.

The inelastic displacement u^{di} represents the inelastic sliding that has occurred on the damaged part of the interface element. It is described in the framework of non-associated elastoplasticity as in (Alfano and Sacco, 2006) and (Simo and Hughes, 1998) by introducing a Coulomb yield friction function $\zeta(\sigma^d)$:

$$\zeta(\sigma^d) = \mu \cdot \langle\sigma_{dn}\rangle_- + \sqrt{(\sigma_{dt})^2 + (\sigma_{dh})^2} = \mu \cdot \sigma_{dn} + \sqrt{(\sigma_{dt})^2 + (\sigma_{dh})^2} \qquad (4.5)$$

where σ_{dn} is the normal stress in the damaged part and σ_{dt} and σ_{dh} are the two shear stresses in the damaged part in the two tangential directions t and h. μ is the friction coefficient and $\langle\cdot\rangle_-$ represents the negative part of the stress. The second equation is always true since σ_{dn} is always negative in accordance with Eqs. (4.2), (4.3) and (4.4).

The evolution of $\dot{u}^{di}$ is controlled by a non-associative relationship, which is expressed using a nonnegative plastic multiplier ω, which is a common choice in computational inelasticity (Simo and Hughes, 1998), according to the formula:

$$\dot{u}^{di} = \dot{\omega}\begin{pmatrix} 0 \\ \dfrac{\sigma_{dt}}{\sqrt{(\sigma_{dt})^2 + (\sigma_{dh})^2}} \\ \dfrac{\sigma_{dh}}{\sqrt{(\sigma_{dt})^2 + (\sigma_{dh})^2}} \end{pmatrix} \tag{4.6}$$

by considering Kuhn–Tucker conditions (Kuhn and Tucker, 1951) and in order to take into account the irreversible nature of frictional sliding:

$$\begin{cases} \dot{\omega} \geq 0 & (\mathbf{1}) \\ \zeta(\sigma^d) \leq 0 & (\mathbf{2}) \\ \dot{\omega}\,\zeta(\sigma^d) = 0 & (\mathbf{3}) \end{cases} \tag{4.7}$$

By using Eqs.(4.6) and (4.7), the inelastic displacement u^{di} can be calculated via the following procedure. The time interval is decomposed into a sequence of time increments by using a Newton-Raphson solution scheme. Let $(\cdot)^{\tau}$ and $(\cdot)^{\tau+\Delta\tau}$ denote the values of the variable $(\cdot)$ at the beginning and at the end of timestep. The aim is to calculate $u_{dit}^{\tau+\Delta\tau}$ and $u_{dih}^{\tau+\Delta\tau}$, which are the tangential inelastic displacements of the damaged part of the interface in the two directions t and h. At the time step $\tau + \Delta\tau$, u^{τ} and $u^{\tau+\Delta\tau}$ are known variables, and so are the previously calculated variables u_{dit}^{τ} and u_{dih}^{τ}, which is u_{di}^{τ}. Eventually, the equations to be solved are the following:

$$u_{di}^{\tau+\Delta\tau} = u_{di}^{\tau} + \Delta\omega^{\tau} \begin{pmatrix} 0 \\ \dfrac{\sigma_{dt}^{\tau+\Delta\tau}}{\sqrt{(\sigma_{dt}^{\tau+\Delta\tau})^2 + (\sigma_{dh}^{\tau+\Delta\tau})^2}} \\ \dfrac{\sigma_{dh}^{\tau+\Delta\tau}}{\sqrt{(\sigma_{dt}^{\tau+\Delta\tau})^2 + (\sigma_{dh}^{\tau+\Delta\tau})^2}} \end{pmatrix} \tag{4.8}$$

$$\Delta\omega^{\tau} \geq 0 \tag{4.9}$$

$$\mu \cdot \sigma_{dn}^{\tau+\Delta\tau} + \sqrt{(\sigma_{dt}^{\tau+\Delta\tau})^2 + (\sigma_{dh}^{\tau+\Delta\tau})^2} \leq 0 \tag{4.10}$$

$$\Delta\omega^{\tau}\left(\mu \cdot \sigma_{dn}^{\tau+\Delta\tau} + \sqrt{(\sigma_{dt}^{\tau+\Delta\tau})^2 + (\sigma_{dh}^{\tau+\Delta\tau})^2}\right) = 0 \tag{4.11}$$

First, an elastic prediction is calculated, by using the previous inelastic displacement according to the equation:

$$\sigma_{de}^{\tau} = \mathrm{H}^{\tau+\Delta\tau}(\mathrm{u}^{\tau+\Delta\tau} - u_{\mathrm{di}}^{\tau}) \tag{4.12}$$

Then, a trial value of the yield function $\zeta\left(\sigma_{de}^{\tau+\Delta\tau}\right)$ is calculated, leading to two cases :

- If $\zeta\left(\sigma_{de}^{\tau+\Delta\tau}\right)$ is negative in accordance with Eq. (4.10), then there is no evolution of the inelastic variables. Thus, $\dot{\omega} = 0$, and so the new values of the variables are calculated according to Eqs. (4.2) and (4.8) as follows:

$$\begin{gathered} u_{di}^{\tau+\Delta\tau} = u_{di}^{\tau} \\ \sigma_{d}^{\tau+\Delta\tau} = \mathrm{H}^{\tau+\Delta\tau}\left(\mathrm{u}^{\tau+\Delta\tau} - u_{di}^{\tau+\Delta\tau}\right) \end{gathered} \tag{4.13}$$

- if $\zeta\left(\sigma_{de}^{\tau+\Delta\tau}\right)$ is positive, then $\Delta\omega^{\tau}$ should be strictly positive, or else $u_{di}^{\tau+\Delta\tau} = u_{di}^{\tau}$ according to Eq. (4.8), resulting in a positive yield function, contrary to Eq. (4.10). Thus, Eq. (4.11) will be fulfilled when $\zeta\left(\sigma_{d}^{\tau+\Delta\tau}\right) = 0$. After some development, the following solution is reached:

$$\Delta\omega = \frac{1}{K_s}\left(\zeta\left(\sigma_{de}^{\tau+\Delta\tau}\right)\right) = \frac{1}{K_s}\left(\mu \cdot \sigma_{den}^{\tau+\Delta\tau} + \sqrt{(\sigma_{det}^{\tau+\Delta\tau})^2 + (\sigma_{deh}^{\tau+\Delta\tau})^2}\right) \tag{4.14}$$

$$\sigma_{dn}^{\tau+\Delta\tau} = \sigma_{den}^{\tau+\Delta\tau} \tag{4.15}$$

$$\sigma_{dt}^{\tau+\Delta\tau} = -\mu \cdot \sigma_{den}^{\tau+\Delta\tau} \frac{\sigma_{det}^{\tau+\Delta\tau}}{\sqrt{(\sigma_{det}^{\tau+\Delta\tau})^2 + (\sigma_{deh}^{\tau+\Delta\tau})^2}} \tag{4.16}$$

$$\sigma_{dh}^{\tau+\Delta\tau} = -\mu \cdot \sigma_{den}^{\tau+\Delta\tau} \frac{\sigma_{deh}^{\tau+\Delta\tau}}{\sqrt{(\sigma_{det}^{\tau+\Delta\tau})^2 + (\sigma_{deh}^{\tau+\Delta\tau})^2}} \tag{4.17}$$

These equations are used to calculate the inelastic displacement u_{di} according to Eq. (4.8), then σ_d according to Eq. (4.2).

Undamaged part stress σ^u:

Tvergaard’s cohesive zone model is used here to represent the stress in the undamaged part of the interface, with some additional modifications applied in order to take into account the non-linear behavior, especially under compression. On contrary to Crisfield’s model where the damage evolution is linear in tension, Tvergaard’s model has an exponential evolution that is believed to be more realistic in particular in the smooth bar case which reflects the evolution of the interface model, as previously seen. In addition, as mentioned no zero stress is reached finally, which prevents the occurrence of convergence problems in the numerical solving process.

The parameter λ representing the equivalent opening of the interface is defined according to Eq. (3.22) and the stiffness ratio δ_s is defined according to Eq. (3.23). The damage indicator $\widetilde{\lambda}$ is also calculated based on Eq. (3.24), while the damage variableD_{int} is determined as follows:

$$D_{int} = 1 - \exp\left(\frac{-f_t\,\widetilde{\lambda}}{\varsigma\, G_f}\right) \tag{4.18}$$

where ς is a non-zero correcting coefficient to be assigned, f_t is the maximum tensile strength of the interface and G_f is the fracture energy.

In addition, the normal stiffness K_n is defined according to Eq. (3.26).

The undamaged part stress σ^u is calculated based on the following equation:

$$\sigma^u = \Gamma K u \tag{4.19}$$

$$\sigma^u = \begin{pmatrix} \sigma_{un} \\ \sigma_{ut} \\ \sigma_{uh} \end{pmatrix} \;\; ; \;\; \Gamma = (\beta \quad \alpha \quad \alpha) \;\; ; \;\; K = \begin{pmatrix} K_n & 0 & 0 \\ 0 & K_s & 0 \\ 0 & 0 & K_s \end{pmatrix}$$

$$; \;\; u = \begin{pmatrix} u_n \\ u_t \\ u_h \end{pmatrix}$$

This can be simplified as:

$$\begin{cases} \sigma_{un} = \beta K_n u_n \\ \sigma_{us} = \alpha K_s u_s \end{cases} \tag{4.20}$$

where s represents the two tangential directions t and h.

The two coefficients α and β are introduced in order to reflect the damaged and non-damaged cases, and to try to represent a more logical behavior of the shear stress under compression. In Tvergaard's modified cohesive zone model, shearing with initial compression is the same as the pure shearing case. Here instead, it is modified to produce a stiffer response when compression is applied, which seems realistic since a higher effort is in general needed to shear when this certain surface is under compression.

The coefficient β is defined as follows:

$$\begin{cases} \beta = 1 & For \;\; D_{int} = 0 \;\; and \quad \forall \;\; \sigma_{dn} \\ \beta = \dfrac{\lambda_0}{\lambda} & For \;\; D_{int} \neq 0 \;\; and \quad \sigma_{dn} \geq 0 \\ \beta = \exp\left(\dfrac{f_t\,\widetilde{\lambda}}{\varsigma\,G_f}\right) & For \;\; D_{int} \neq 0 \;\; and \quad 0 \geq \sigma_{dn} \end{cases} \tag{4.21}$$

while the coefficient α is defined as follows:

$$
\begin{cases}
\alpha = 1 & For\ D_{int} = 0 \quad and \quad \forall\ \sigma_{dn} \\
\alpha = \dfrac{\lambda_0}{\lambda} & For\ D_{int} \neq 0 \quad and \quad \sigma_{dn} \geq 0 \\
\alpha = \dfrac{\frac{\lambda_0}{\lambda} + D - 1}{\gamma}\sigma_{dn} + \dfrac{\lambda_0}{\lambda} & For\ D_{int} \neq 0 \quad and \quad 0 \geq \sigma_{dn} \geq \gamma \\
\alpha = 1 - D = \exp\left(\dfrac{-f_t\,\widetilde{\lambda}}{\varsigma\, G_f}\right) & For\ D_{int} \neq 0 \quad and \quad \gamma \geq \sigma_{dn}
\end{cases}
\tag{4.22}
$$

where σ_{dn} is the normal stress in the damaged part of the interface that is calculated using Eqs. (4.2) and (4.3). γ is a stress value, taken -1 MPa in here, but it can be changed. It is a small value chosen in order to maintain continuity of stress when the displacement changes from positive to negative or the opposite, preventing any kind of sudden drop in stress and preserving the smooth continuity of stress, which will be shown clearly below.

Note that the three values of β in Eq. (4.21) are introduced so that the term $(1 - D_{int})\sigma_{un}$ is equal to Tvergaard's normal stresses σ_n defined in Eqs. (3.25) and (3.29) when $\varsigma = 1$. The first two values of α in Eq. (4.22) are also chosen so that the term $(1 - D_{int})\sigma_{us}$ is equal to the Tvergaard's shear stresses σ_s defined in Eqs. (3.27) and (3.30), except when the element is under normal compressive stress. Here, the proposed modification to Tvergaard's σ_s is in the fourth value, which gives a stiffer response when there exists a compressive stress. In addition, the third value is assigned in order to maintain continuity between the second and the fourth case, when there is a change in the direction of the displacements, to prevent a sudden drop in stress.

Eventually, the new 3D zero thickness frictional cohesive zone interface model introduced has combined the Tvergaard's damage-based cohesive zone approach that plays a role whenever the interface is not fully damaged, and an elastoplastic model that is Coulomb's frictional model, which occurs whenever damage is initiated, and finally controls utterly the interface stress when the interface element is entirely damaged. The input parameters and coefficient that are used in this model, and have to be calibrated, are listed in Table 4.1.

Table 4.1 List of input parameters and coefficients of the newly implemented FCZM

Symbol	Unit	Description
δ_s	$-$	Stiffness ratio of the interface element
f_t	MPa	Ultimate tensile stress of the interface element
G_f	N/m	Fracture energy of the interface element
λ_0	m	Initial damage threshold of the interface element
μ	$-$	Friction coefficient
ς	$-$	Correcting coefficient for the softening behavior

4.2.2 Validation of the implemented model

In order to verify the implementation of the FCZM, several simulations are performed on one interface element connecting two blocks to each other (Figure 3.17), whose side length is 1 mm, in order to observe the interface element behavior under different conditions. The values assigned to the parameters of FCZM described above in these one-element simulations are shown in Table 4.2. Additionally, the coefficient ς defined in Eq. (4.18) is taken equal to 1. The choice is only to show the different aspects of the model, but it will be calibrated and related to the material parameters in the next section.

Table 4.2 Assigned values to the parameters of the FCZM in the one-joint element simulations

δ_s	$f_t\ (MPa)$	$G_f\ (N/m)$	$\lambda_0 (m)$	μ
$\mathbf{1}$	3	300	2×10^{-5}	0.4

Comparing the frictional cohesive zone model and Tvergaard's cohesive zone model described in subsection 3.4.5.2 in Figure 4.2(a), one can see that the behavior in tension reflects purely the behavior of the Tvergaard's model, and so does the behavior in compression. Obviously, friction in pure tension or compression plays no role. Thus, the Tvergaard's cohesive zone model is totally reflected in the overall results. The tangential behavior is also investigated by performing several simulations on the same interface element. A certain normal stress, either tension or compression, is initially imposed then a tangential displacement is applied. The corresponding tangential displacements and applied shear stresses are recorded, and plotted as shown in Figure 4.2(b) and Figure 4.2(c).

Similarly to the tensile case, the pure shear case shown in Figure 4.2(b) reflects Tvergaard's model pure shear case. This is also the case when a certain tensile stress is initially imposed.

To sum up, one can see that in case of pure tension, pure compression, and pure shear and shearing with initial tension, friction has no role, and Tvergaard's modified model is entirely reflected by the FCZM model. This can be inferred from the values β and α defined in Eqs. (4.21) and (4.22), respectively.

On the other hand, the behavior when shearing with initial compression is different and more complex. The peak stress goes beyond f_t when there is an initial compression σ_N , and keeps increasing whenever the initial compressive stress is increased. This can be observed in Figure 4.2(b), and in Figure 4.2(c) where higher compressive stresses are imposed. In addition, the residual stress is equal to $|\mu\, \sigma_N|$. One can see that for high compressive stresses like -20 MPa, the peak stresses is similar to the residual stress, which is similar to the behavior captured when using Coulomb's interface model described in subsection 3.4.5.1. This shows the transition from the Tvergaard's modified cohesive zone model to a more frictional model like Coulomb's interface model as the imposed compressive stress increases. This behavior is in accordance with what is numerically observed using Crisfield's damage model in (Albarella et al., 2015).

Figure 4.3 shows the two terms that form the total shear stress. As discussed before, one can see that the shear stress of the undamaged part of the interface behaves like a cohesive zone model, while the shear stress of the damaged part of the interface behaves like a frictional model, with a nonlinear initial increase, unlike Coulomb's interface model behavior.

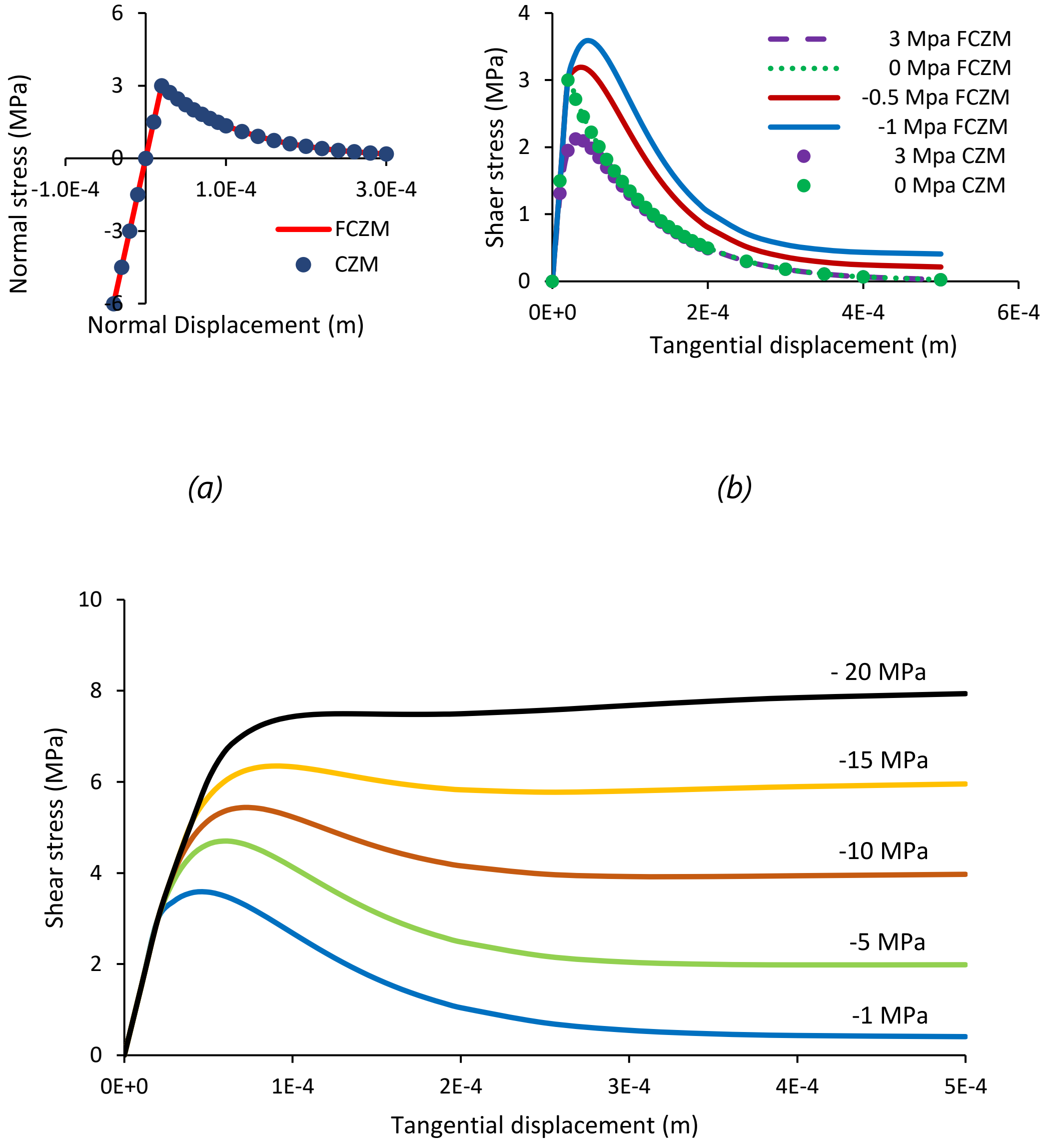

(a)

(b)

(c)

Figure 4.2 (a) Normal stress versus normal displacement for FCZM and CZM (b) Shear stress versus tangential displacement for the FCZM and CZM under different imposed normal stresses (c) Shear stress versus tangential displacement for the FCZM under different imposed compressive stresses

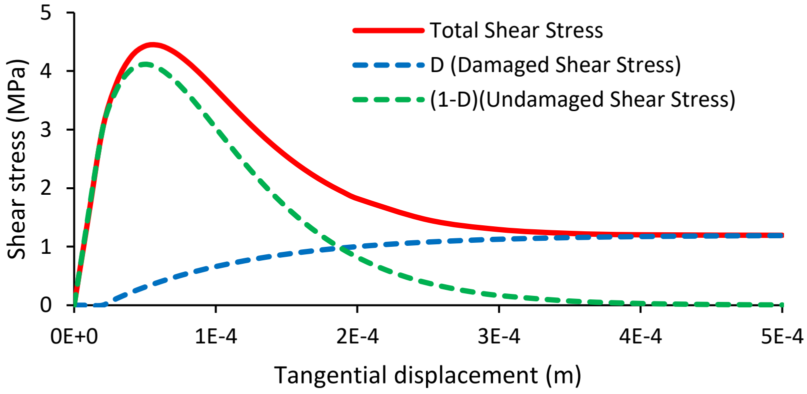

Figure 4.3 Total shear stress, damaged part's shear stress and undamaged part's shear stress versus tangential displacement for the frictional cohesive zone model under -3 MPa compressive stress

The damage evolutions of the interface element under different initial tensile imposed displacements are shown in Figure 4.4, including the pure case without initial imposed displacement. Recall that damage does not evolve under pure compression, so the damage evolution under initial compression is the same as the evolution in the case without any initial imposed displacement. One can see that the evolution is non-linear, which is because of the exponential evolution used in Tvergaard's model. The initial value of damage is related to the state of the interface element before the application of the shear loading.

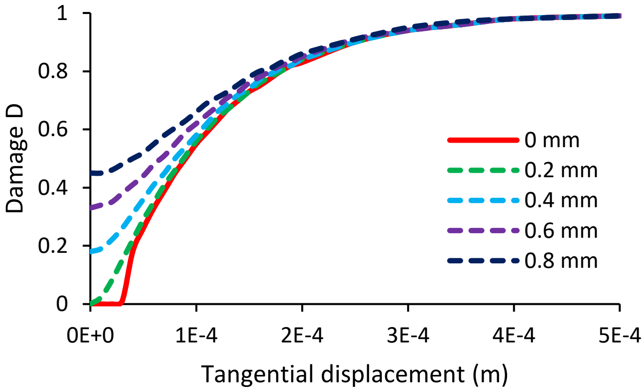

Figure 4.4 Damage evolution for the frictional cohesive zone model in pure shearing mode and in shearing preceded by different initial tensile imposed displacements

Moreover, a couple of simulations are performed to verify the continuity of the shear stress under a varied normal stress, using the same data from Table 4.2.

The first simulation is performed by imposing a certain initial compressive displacement, then applying a shear displacement as previously done, until reaching a certain tangential displacement, at which no additional shearing is applied. At this point, the tangential displacement is fixed, and the imposed compressive displacement is reversed gradually until reaching a certain positive tensile displacement. The detailed results are shown in Figure 4.5.

The imposed normal and tangential displacements are plotted in Figure 4.5(a) as function of the different stages, named in the time order: O, A, B, C, D, E and F. The shear stresses versus the tangential and normal displacements are plotted in Figure 4.5(b) and Figure 4.5(d) respectively, and the normal stress versus the normal displacement in Figure 4.5(c).

The behavior captured in Figure 4.5(b) is expected, based on the description of the simulation. The first part of the curve (from the origin point O to C) is identical to those of the simulations previously performed, without reversing the normal stress (Figure 4.2(b) and Figure 4.2(c)). In the second part (C to F), the tangential displacement is fixed; the shear stress will decrease when reversing the normal displacement from compression to tension. This explains the vertical line observed, which represents a continuous and linear decrease of the shear stress.

In Figure 4.5(c), the compressive displacement is linearly applied until reaching -0.02 mm (curve OA), and then a shearing is applied. This cannot be viewed as a curve on the Figure, as the normal stress is fixed and the normal displacement is not being changed (point AB and BC). Thus, the entire shearing process is represented by the point (-0.02 mm; -3 MPa). After that, the shear displacement is fixed, and the normal displacement is reversed gradually by taking the same path used initially when the compressive displacement was applied (curves CD and DE). When normal displacement becomes positive (curve EF), the behavior will be similar to the non-linear behavior previously obtained, but without an initial elastic behavior like the one obtained in Figure 4.2(a). This is because the interface is already damaged, since the tangential displacement reached is equal to 0.1 mm, while the damage threshold λ_0 is equal to 0.02 mm. This also explains the lower peak stress obtained.

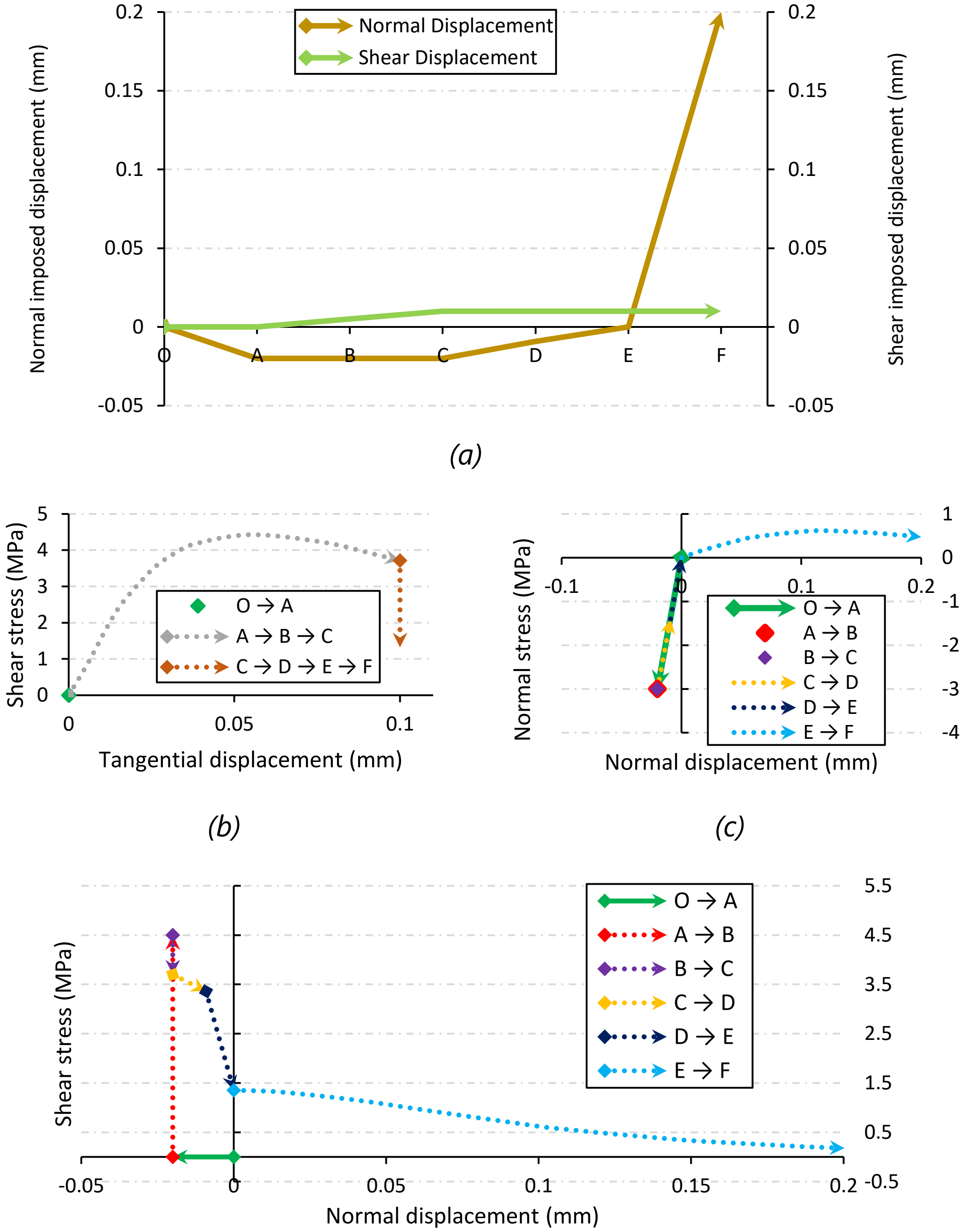

(a)

(b) *(c)*

(d)

Figure 4.5 Results for FCZM under an initial imposed compressive displacement -0.02 mm with shearing followed by the application of tensile displacement: (a) normal and tangential imposed displacement at the different stages from O to F; (b) shear stress versus tangential displacement; (c) normal stress versus normal displacement; (d) shear stress versus normal displacement

In Figure 4.5(d), one can see the effect of the different values of the coefficient α. In the first simulation, -0.02 mm compressive displacement is initially imposed (curve OA), then shearing is applied, which is represented by the vertical line AB, reaching a shear peak stress equal to around 4.5 MPa, then decreasing until 3.7 MPa (curve BC) as in Figure 4.5 (b). At this point, the shear displacement is fixed, and the normal displacement is gradually reversed. The shear stress starts decreasing linearly with a constant slope (curve CD), until reaching a specific compressive displacement which is equivalent to 1MPa compressive stress, at which the slope changes (curve DE). This is because α changes from the fourth case to the third case according to the different conditions in Eq. (4.22). The linear behavior changes to a nonlinear behavior taking the second value for α when the normal displacement becomes positive (curve EF). From here on, the behavior is expected, as the interface is already damaged, and the shear stress will decrease to zero.

The choice of the third case for α in Eq. (4.22) can be justified in here, as if this case does not exist, the shear stress will keep decreasing linearly (curve CD) with the same slope until reaching zero normal displacement, hence omitting curve (DE). Thus, the curve will be discontinuous at this point, since the shear stress will drop instantly in accordance with the second value that α takes under tension.

In the same manner, a second simulation is performed in a way that an initial tensile stress is imposed, and then a shearing displacement is applied, until reaching a certain tangential displacement, at which no additional shearing is applied. Then, the tangential displacement is fixed, and the imposed tensile stress is reversed gradually until reaching a certain compressive stress. The detailed results are shown in Figure 4.6. The imposed normal and tangential displacements are plotted in Figure 4.6 (a) as function of the different stages, named in the time order from o to f, and the shear stresses versus the tangential and normal displacements in Figure 4.6 (b) and Figure 4.6 (d) accordingly. Likewise the first simulation, this simulation acts in the same way, and the different values of α are reflected directly on the behavior. The whole behavior is verified to be continuous.

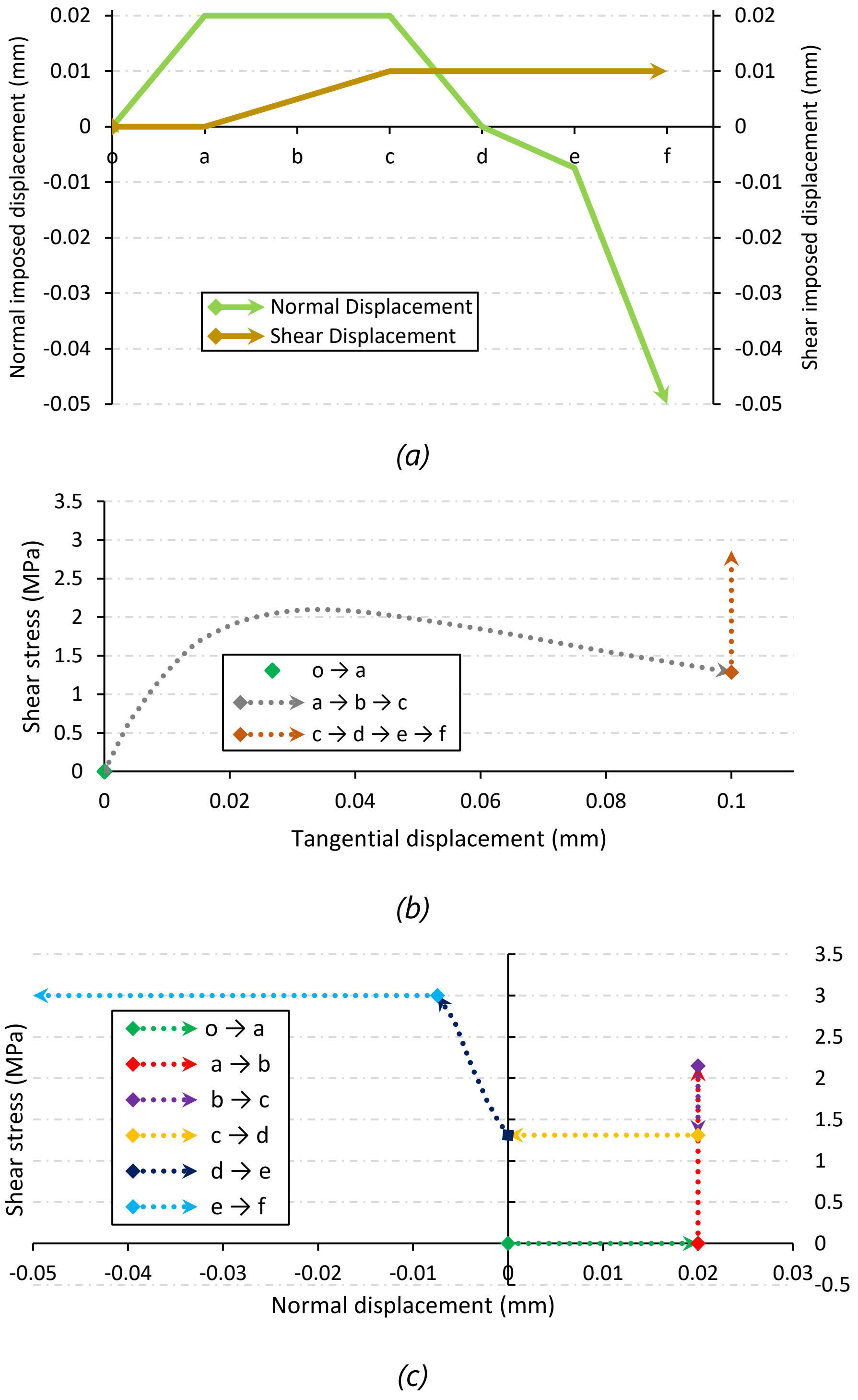

Figure 4.6 Results for FCZM under an initial imposed tensile displacement of 0.02 mm with shearing followed by the application of compressive displacement: (a) normal and tangential imposed displacement at the different stages from o to f ; (b) shear stress versus tangential displacement; (c) shear stress versus normal displacement

4.3 CALIBRATION OF THE IMPLEMENTED FCZM

We describe in this section the main aspects related to the identification procedure of parameters of the FCZM, listed in Table 4.1, based on pull out test simulation results with smooth and ribbed bars.

4.3.1 Verification and calibration using the smooth bar sample

4.3.1.1 General description and generated sample

In order to verify the functionality of the newly implemented frictional cohesive zone model developed in section 4.2 when assigned to the steel-concrete interface, a group of simulations is performed on a smooth bar sample. The test case and the corresponding boundary conditions are the same as the ones described in subsection 3.3.1 and shown in Figure 3.8 .

As in section 3.5, the experimental pull-out test results on a smooth bar are extracted from (Anwar Hossain, 2008). The smooth sample introduced in subsection 3.4.2 and shown in Figure 3.13 is used here.

4.3.1.2 Calibration process

In this simulation, steel is assigned the perfect yield model as described in subsection 3.4.4. Additonally, concrete is assigned Mazars model with the extensions described before in section 3.4.3. The values of parameters summarized in Table 3.2 are used, since the same experimental case is simulated. Thus, concrete's Young's modulus is 25 GPa, ultimate tensile stress $f_{t\ con}$= 2.5 MPa, while fracture energy is 120 N/m.

As mentioned, in this procedure parameters are varied separately or in parallel at the same time, in order to study their effect on the general behavior. Four parameters are considered: f_t , λ_0 , δ_s and G_f and the coefficient ς. After varying the parameters in parallel and analyzing different combinations, it has been observed that the parameters can be divided into two main categories, those that control principally the peak of the mean bond stress and it's maximum value: f_t, λ_0 and δ_s, while G_f, along with ς, control the post peak behavior. In addition, a unique combination of the parameters f_t, λ_0 and δ_s gives a unique peak of mean bond stress and the associated displacement, which can be seen clearly in Figure 4.7. Plenty of different combinations were applied, and one can conclude that it is not possible to reach the same exact peak stress and the exact displacement at the peak, using two different combinations. Thus, although it is possible to get a similar peak stress for two different values of f_t by changing both λ_0 and δ_s, the corresponding displacement at the peak is clearly not the same. Eventually, adjusting those parameters will finally give a good fit. Those final values assigned to the parameters are shown in Table 4.3. The separate variation for each parameter is discussed below to show the effect of each parameter, after which a general calibration for each parameter is to be eventually concluded. In these separate variations, the other unvaried parameters are fixed to the values shown in Table 4.3. As this calibration process is manual, and difficult due to the presence of several parameters, a potential future work may be done on a numerical campaign using design of experiments (DOE) methods, to facilitate the calibration process and make it more systematic.

Table 4.3 Assigned values to the parameters of the FCZM in the smooth bar pullout simulation

$\boldsymbol{\delta_s}$	$\boldsymbol{f_t\ (MPa)}$	$\boldsymbol{G_f\ (N/m)}$	$\boldsymbol{\lambda_0 (m)}$	$\boldsymbol{\mu}$	$\boldsymbol{\varsigma}$
0.3	1.8	85	5×10^{-5}	0.3	8

Figure 4.8 shows the results of the simulations for different values of f_t, all of which are considered to be less than or equal to $f_{t\ con}$ since the interface layer is supposed to be a weaker layer with many irregularities. One can see that f_t obviously affects the peak stress. The value f_t= 1.8 MPa gives the best fit. Therefore, the ratio ξ between concrete tensile ultimate stress and the interface ultimate stress is ξ = 0.72. We assume that this identified ratio may be applied on the other simulations without any need to recalibration, according to the following formula:

$$f_t = \xi\ f_{t\ con} \tag{4.23}$$

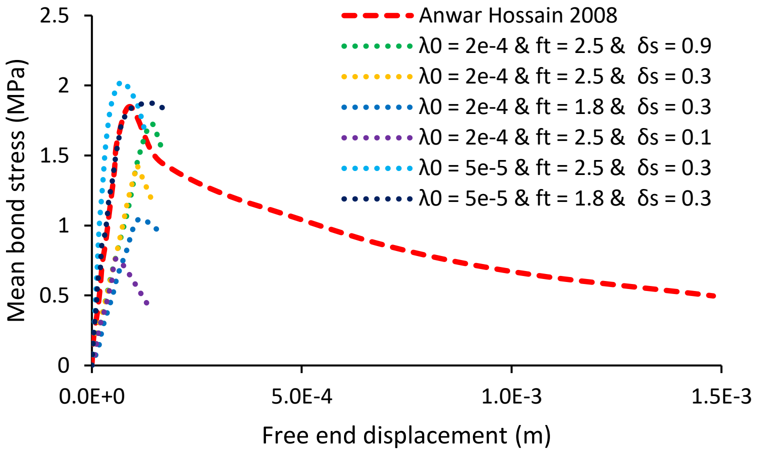

Figure 4.7 Mean bond stress versus free end displacement for the numerical simulations performed on the sample having a smooth bar and for the experimental results extracted from (Anwar Hossain, 2008) by varying $\boldsymbol{f_t}$ *(in MPa),* $\boldsymbol{\lambda_0}$ *(in m) and* $\boldsymbol{\delta_s}$

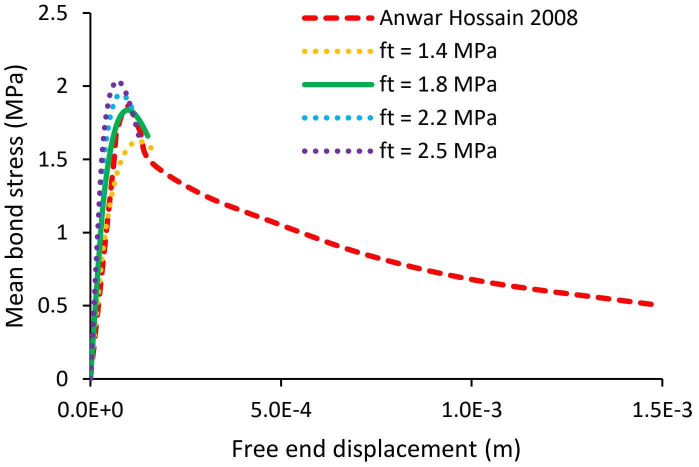

Figure 4.8 Mean bond stress versus free end displacement for the numerical simulations performed on the sample having a smooth bar and for the experimental results extracted from (Anwar Hossain, 2008) by varying $\boldsymbol{f_t}$

For the initial damage threshold λ_0, one can expect this value to be constant from one simulation to another, as long as concrete's initial damage strain parameter ε_{D_0} assigned in Mazars model in section 3.4 has the same value calculated according to Eq. (3.7). This interface damage threshold λ_0 controls the displacement position of the peak stress and is identified as shown in Figure 4.9. One can see that the best fit is obtained when $\lambda_0 = 5 \times$

$10^{-5}\ m$, which will be used for the further simulations. Note that although this value affects both damage initiation in tension and in shearing, the shearing obviously dominates in such cases. In terms of shearing and frictional behavior, one do expect the interface to behave differently compared to concrete as it is the surface of contact with steel, where unlike the other parts of concrete, frictional and shearing behavior parallel to the axis of the bar dominates.

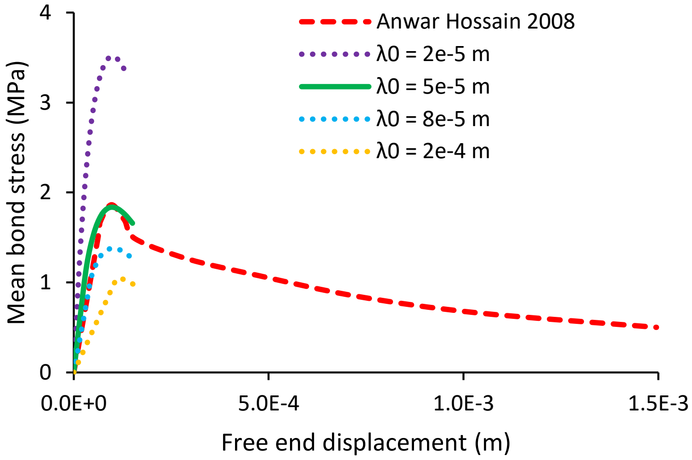

Figure 4.9 Mean bond stress versus free end displacement for the numerical simulations performed on the sample having a smooth bar and for the experimental results extracted from (Anwar Hossain, 2008) by varying $\boldsymbol{\lambda_0}$

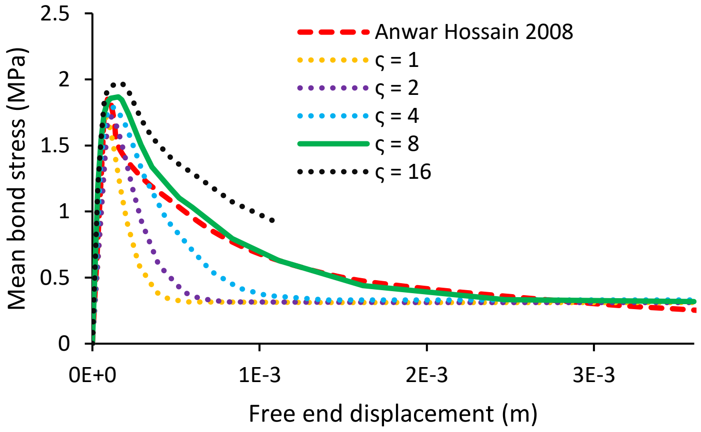

Figure 4.10 Mean bond stress versus free end displacement for the numerical simulations performed on the sample having a smooth bar and the experimental results extracted from (Anwar Hossain, 2008) by varying $\boldsymbol{\varsigma}$

In a similar way, the stiffness ratio δ_s is varied in order to get the best fit, which is reached when $\delta_s = 0.3$. This sensitive ratio will be discussed in more details in the ribbed bar section. A formulation will be reached based on the smooth and the ribbed bar simulations, allowing us to identify the ratio without the need of prediction from then on.

The fracture energy G_f, which is a function of the tensile strength and the softening behavior of the interface, is considered less than that of concrete. The proposition is that the tensile behavior of concrete and interface is not the same (Eq. (3.23)), while the softening behavior is supposed to be same, but should be corrected by the coefficient ς. Thus, the fracture energy G_f is calculated using the same coefficient ξ previously identified, as follows:

$$G_f = \xi G_{f\,con} \tag{4.24}$$

In addition, the effect of the coefficient ς used to correct the softening behavior introduced in Eq. (4.18) can be observed in Figure 4.10. One can see that the best fit is when $\varsigma = 8$, which is considered the reference simulation. For other values of this coefficient ς, the post peak behavior is not very well reproduced. In particular, a more brittle post peak behavior is obtained for smaller values of ς. This coefficient will be kept constant in all simulations, while the parameter G_f will be changed and determined using Eq. (4.24) depending on the fracture energy of concrete, as these two values have the same purpose and effect on the fracture energy, as seen in Eq. (4.18), and their variation affects the post peak behavior in the same manner.

Finally, the friction coefficient of the steel-concrete interface is considered 0.3, based on (Wang and Liu, 2004; Xu et al., 1994) among others.

Thus, almost all the parameters are now related to the surrounding material, except for δ_s, which needs an additional calibration. The identified ratios and coefficients will be applied directly to the parameters in the ribbed bar simulations in order to check and verify the functionality of both of the calibration procedure and the FCZM.

Following the verification of the ability of the FCZM to capture the behavior of the pull-out test on a sample with a smooth bar (Figure 4.11), we now assess its performance on a more complex and common case with a spiral-ribbed bar.

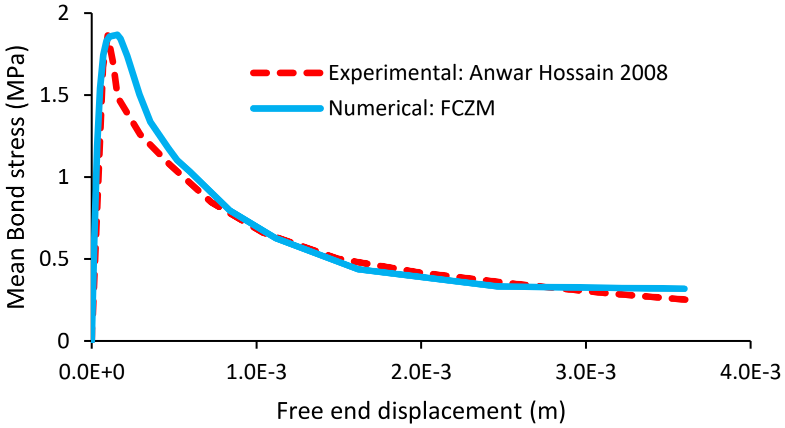

Figure 4.11 The reference simulation of pull-out test with smooth bar performed using the FCZM with the final values assigned to the FCZM parameters as shown in Table 4.3, compared to the experimental results extracted from (Anwar Hossain, 2008)

4.3.2 Application on a ribbed bar case and complementary calibration process

4.3.2.1 Generated sample

In order to perform additional calibration on the stiffness ratio δ_s , simulations are performed using a sample with a spiral ribbed bar. The pull-out test experimental results used for comparison in this simulation are those derived from (La Borderie and Pijaudier-Cabot, 1992). A numerical sample with a spiral ribbed bar is generated using the procedure described in section 3.2 . A cubic sample is generated that takes into account the experimental concrete cover and nominal diameter of the bar. Hence, the concrete cubic sample side length is 80 mm, and bar's nominal diameter is 8mm. The total adhesive length is 40 mm, which is half the total length of the bar, as in (RILEM, 1970). The detailed dimensions of the spiral bar used are shown in Figure 4.12 . Finally, an unstructured mesh is applied using linear tetrahedral meshing elements as detailed in subsection 3.2.5. The characteristic size of each mesh element at the outer surface of the concrete sample is equal to about 5 mm, while the triangular edge of each element at the steel concrete interface is almost 0.4 mm. As a result, the number of mesh elements in the steel bar is 298 000, while the number of mesh elements in the concrete is 308 000.

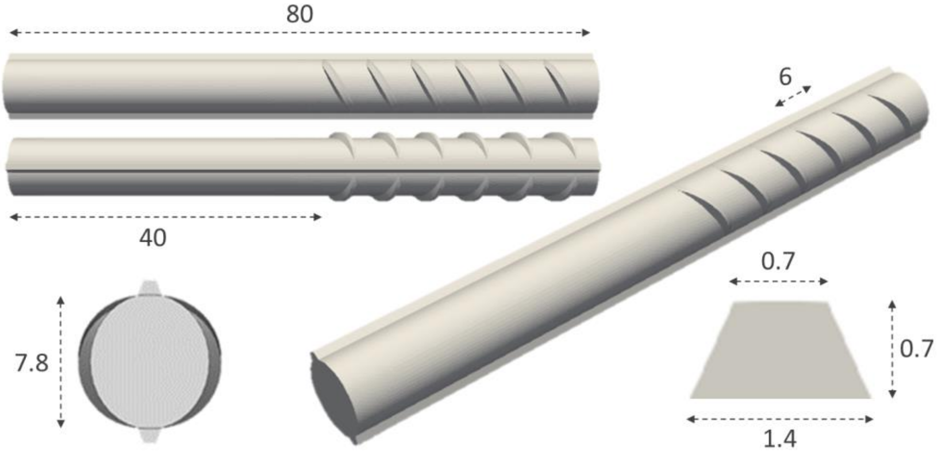

Figure 4.12 Dimensions of the modelled spiral steel bar (in mm)

Similarly to the was previously explained, the test case and the corresponding boundary conditions are the same as the ones described in subsection 3.3.1 and shown in Figure 3.8 .

4.3.2.2 Additional calibration process

In this simulation, steel is assigned the perfect yield model as described in subsection 3.4.4. Moreover, concrete is assigned Mazars model with all the modifications described before in section 3.4.3. In addition, based on the experimental data, concrete's Young's modulus is considered 30 GPa, and Poisson's ratio is 0.25. Concrete's ultimate tensile stress $f_{t\,con}$ is 3 MPa and the corresponding fracture energy is 130 N/m. For the compressive damage parameters A_c and B_c, the same methodology described in subsection 3.4.3 is applied. As a result, A_c is calculated using Eq. (3.16), while B_c is assigned based on the following equation :

$$B_c = 340589.7285\, l^2 + 20577.3197\, l - 0.5075 \tag{4.25}$$

where l is the characteristic size of the finite element, calculated according to Eq. (3.15). The values of the parameters of the concrete are summarized in Table 4.4.

Also for the FCZM, the final values assigned to the parameters, which are based on the calibration process mentioned in subsection 4.3.1.2, except for δ_s, are shown in Table 4.4 .

Table 4.4. Assigned values to the parameters of the Mazars model for concrete and final values assigned to the parameters of the FCZM in the spiral bar pull-out simulation

Concrete parameters			
E_{con} (GPa)	v_{con}	$f_{t\,con}$ (MPa)	$G_{f\,con}$ (N/m)
$\mathbf{30}$	0.25	3	130
ε_{D_0}	A_c	B_c	β
Eq. (3.7**)** $\Rrightarrow$ $\mathbf{10^{-4}}$	Eq. (3.16)	Eq. (4.25)	1.06

FCZM parameters		
δ_s	f_t (MPa)	G_f (N/m)
0.16	Eq. (4.23) $\Rrightarrow$ 2.16	Eq. (4.24) $\Rrightarrow$ 97
$\lambda_0(m)$	μ	ς
$\mathbf{5 \times 10^{-5}}$	0.3	8

The initial value extracted from the smooth bar simulation for δ_s cannot actually produce the experimental behavior. Thus, the stiffness ratio δ_s is assigned a different value in each simulation in order to understand its effect on the overall behavior, and in order to complete the calibration process before final validation. The mean bond stresses versus the bar displacement along with the experimental results extracted from (La Borderie and Pijaudier-Cabot, 1992) are shown in Figure 4.13.

By considering the case produced when $\delta_s = 0.16$, one can see that the macroscopic curve agrees well with experimental results. While when the value of δ_s is lower, the behavior seems to be much stiffer at later stages, and it is much weaker when this value is greater than unity. Still, at the beginning of the loading phase, one can see an initial change of slope for all four cases. This transition of slope is smooth when δ_s is smaller, while it tends to form an initial peak when this value is higher. Obviously, one needs to assign a value for δ_s smaller than 1 in order to capture a more realistic behavior.

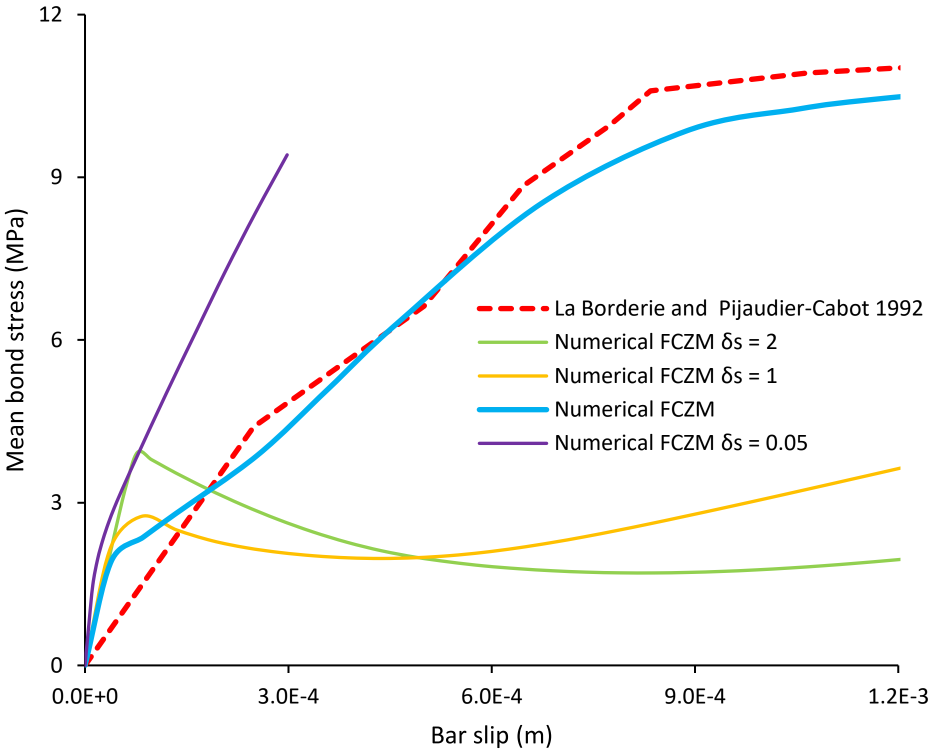

Figure 4.13 Mean bond stress versus bar slip for the numerical simulations performed on the 8 mm spiral sample using different stiffness ratios and the corresponding experimental results extracted from (La Borderie and Pijaudier-Cabot, 1992)

One can see that the two stiffness ratios used for the smooth bar simulation and the ribbed bar simulation are different. A certain relation should be proposed in order to prevent the prediction of this parameter in each simulation. Since K_n depends uniquely on f_t and λ_0 according to Eq. (3.26), and since δ_s is a direct ratio between K_n and K_s according to Eq. (3.23), one can relate δ_s to both parameters. However, by taking into consideration that λ_0 was kept constant in both cases, and by taking into account the variation of the ultimate tensile stress f_t of the interface in each case, one can propose a direct linear interpolation between δ_s and f_t. For instance, by considering the smooth bar simulation values, which are f_t = 1.8 MPa and δ_s = 0.3, and the ribbed bar simulation values, which are f_t = 2.16 MPa and δ_s = 0.16, the following linear formulation is proposed:

$$\delta_s = -0.3889 \times 10^{-6}\, f_t + 1$$
$$\delta_s = -0.3889 \times 10^{-6}\; \xi\, f_{t\,con} + 1 \qquad (4.26)$$

4.3.3 Verification of the calibration process using a spiral ribbed bar sample

4.3.3.1 Generated sample

In order to verify the calibration process, another simulation is performed using a sample with a spiral ribbed bar. The pull-out test experimental results for comparison are those derived from (Xu et al., 2017). The test results considered are those of specimen M-C50-F0, which includes high strength concrete C50 with a ribbed steel bar. The nominal diameter of the bar is 16 mm, while its adhesive length is 80 mm. Based on these properties, a numerical sample is generated and meshed using the procedure described in section 3.2. The characteristic size of each mesh element at the outer surface of the concrete sample is equal to about 8 mm, while the triangular edge of each element at the steel concrete interface is almost 0.8 mm. As a result, the number of mesh elements in the steel bar and the concrete are 487 000 and 1 279 000, respectively.

The boundary conditions applied are the same as the ones described in subsection 3.3.1 and shown in Figure 3.8.

4.3.3.2 Verification of the calibration process

Once again, steel is assigned the perfect yield model as described in subsection 3.4.4, and concrete the Mazars model with all the modifications described in section 3.4.3. For the compressive damage parameters A_c and B_c, the same methodology described in subsection 3.4.3 is again applied, giving two relations as a function of the characteristic size l of the interface element, where A_c is calculated using Eq. (3.16), while B_c is calculated using the following equation:

$$B_c = 251095.4475\, l^2 + 19284.2475\, l - 0.2227 \qquad (4.27)$$

The values of the parameters of the concrete are summarized in Table 4.5.

The calibration process, recalled and summarized in Table 4.6, is applied in this simulation to determine the values of the parameters of the FCZM. The coefficient ξ is taken 0.72, calculated in subsection 4.3.1.2. The stiffness ratio δ_s, interface ultimate tensile stress f_t and interface fracture energy G_f are calculated according to Eqs. (4.26), (4.23) and (4.24), respectively, which gives 0.02, 2.52 MPa and 108 N/m, accordingly. As mentioned in subsection 4.3.1.2, λ_0 is taken 5×10^{-5} m. The friction coefficient μ of the steel-concrete interface is still considered 0.3, based on (Wang and Liu, 2004; Xu et al., 1994). Finally, the correcting coefficient ς is fixed to 8, as mentioned in subsection 4.3.1.2.Those values are summarized in Table 4.5 .

Table 4.5 Assigned values to the parameters of the Mazars model for concrete and the final values assigned to the parameters of the FCZM in the 16 mm spiral bar sample pull-out simulation

Concrete parameters			
E_{con} (GPa)	v_{con}	$f_{t\,con}\ (MPa)$	$G_{f\,con}\ (N/m)$
35	0.2	3.5	150
ε_{D_0}	A_c	B_c	β
Eq. (3.7) ⇛ 10^{-4}	Eq. (3.16)	Eq. (4.27)	1.06

FCZM parameters		
δ_s	$f_t\ (MPa)$	$G_f\ (N/m)$
Eq. (4.26) ⇛ 0.02	Eq. (4.23) ⇛ 2.52	Eq. (4.24) ⇛ 108
$\lambda_0(m)$	μ	ς
5×10^{-5}	0.3	8

The corresponding results are shown in Figure 4.14 in terms of mean bond stress versus free end displacement and are compared to the experimental data. One can see that the general behavior is correctly reproduced using the assigned values for the FCZM parameters. Thus, we consider that the FCZM is able to reproduce the ribbed bar pullout test behaviors by applying simple formulations for the parameters. Hence, the final values for the calibration of the parameters and coefficients of FCZM are as listed in Table

4.6.

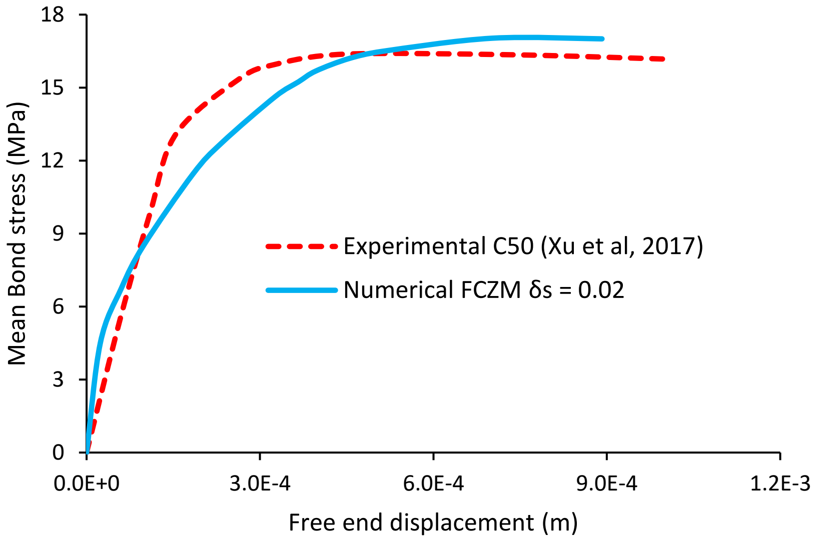

Figure 4.14 Mean bond stress versus free end displacement for the numerical simulation performed on 16 mm spiral ribbed bar sample and the corresponding experimental results extracted from (Xu et al., 2017)

Table 4.6 Values assigned to the parameters and the coefficients of the FCZM based on the calibration process

δ_s	$f_t\ (MPa)$	$G_f\ (N/m)$	$\lambda_0(m)$	μ
$-0.3889\ \xi\ \mathrm{f_{t\,con}} + 1$	$\xi f_{t\ con}$	$\xi G_{f\ con}$	5×10^{-5}	0.3 based on (Wang and Liu, 2004; Xu et al., 1994)
ξ		ς		
0.72		8		
$f_{t\ con}$ **in MPa ;** $G_{f\ con}$ **in N/m**				

4.4 DISCUSSION OF THE RESULTS

Following the calibration of the FCZM, the damage and stresses distributions in two of the simulations are considered and discussed, in particular the results of the reference simulation for the smooth sample in subsection 4.3.1.2, and those of the 8 mm ribbed sample in subsection 4.3.2.2.

4.4.1 Smooth sample

In this part, the results obtained for the simulation performed on the smooth bar sample in subsection 4.3.1.2, whose macroscopic behavior is plotted in Figure 4.11, are analyzed.

Figure 4.15 shows the distribution of damage in the concrete and the interface at the end of the simulation, when the free end displacement is 3.6 mm. One can see that there is almost no visible damage in the concrete, but only in the interface which is fully damaged. This can explain the similarity between the interface model in shearing under compression and the result of the simulation, since the whole damage phenomena are mainly occurring at the interface itself. This eventually leads to the total loss of adhesion and the slipping of the steel bar without affecting significantly the concrete volume, but almost exclusively the steel-concrete interface.

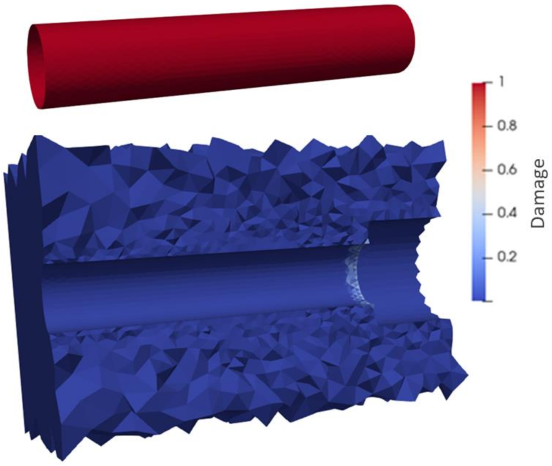

Figure 4.15 Distribution of damage in the concrete and the interface at the end of the simulation (FED = 3.6 mm) for the reference simulation performed on the smooth sample using FCZM

Figure 4.16 shows the values of the stresses in the steel-concrete interface elements along a certain line at the interface at three different free end displacements FED.

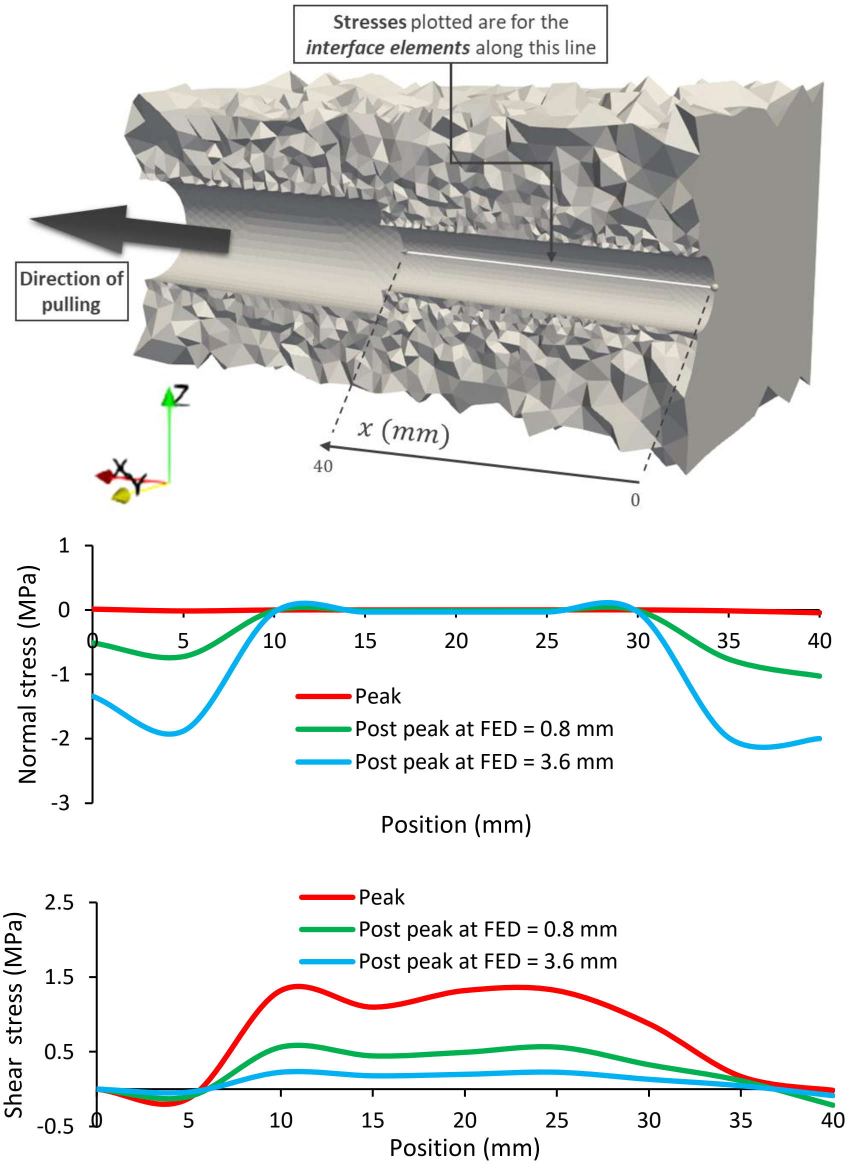

Figure 4.16 Normal stress, and the shear stress in the direction parallel to the axis of the steel bar, in the steel-concrete interface elements at three different FED for the reference simulation

One can observe the variation of normal and shear stresses in the direction parallel to the axis of the bar of the interface elements as a function of the FED. Apparently, the normal compressive stress keeps increasing in magnitude after the post peak near the two ends of the interface, and those normal stresses are almost null along the length of the interface in the central part at different moments during the simulation. Additionally, at the peak, the values near the ends of the interface are already very small and the normal stresses appears to be homogenous. On the other hand, the shear stresses are almost null near the ends of the interface while they are more homogenous in the central part of the interface. The shear stresses decreases as the free end displacement keeps increasing. Such behavior is expected since the steel bar starts losing part of its adhesion.

4.4.2 Spiral ribbed sample

In here, the results obtained for the simulation performed on the 8 mm spiral ribbed sample in subsection 4.3.2.2 are analyzed.

Figure 4.17(a) shows the distribution of the damage D in the concrete at different stages. Clearly, damage deepens inside the concrete block with the increase of the external loading. Figure 4.17(b) shows the full cracks at the end of the loading. One can see that the fully damaged cracks are similar to what was observed in other studies like (Jin et al., 2020a). It can be described by a crack at each rib and an inclined crack at the last rib near the unconstrained concrete surface. One can see that concrete is fully damaged at the ribs, and less damaged in between two ribs. Such damaged concrete is what is expected at the surface of contact, and corresponds to what is observed experimentally, like shown in (Goto, 1971). It is because the ribs prevent the bar from slipping, thus applying an additional pressure on the surrounding concrete, which leads to the initiation of the inclined cracks at the top of each rib.

Figure 4.18 shows the distribution of damage in the interface elements. Damage starts increasing with the imposed displacement until reaching 1, i.e. full damage of the interface, before the end of the simulation. One observation is that the inclined surfaces of the transversal ribs which are directed toward the positive x-direction of bar pulling, are less damaged at each stage compared to the interface elements that are on the cylindrical surface. This can be explained by the very definition of λ in Eq. (3.22), in which compression does not increase the damage in the interface. These surfaces are under compression, since the concrete in front of the ribs is being crushed by the transversal ribs. Thus, only tangential displacements can increase λ. Nonetheless, these tangential displacements are smaller in the inclined ribs compared to the tangential displacements of the interface elements present at the cylindrical surface of the bar.

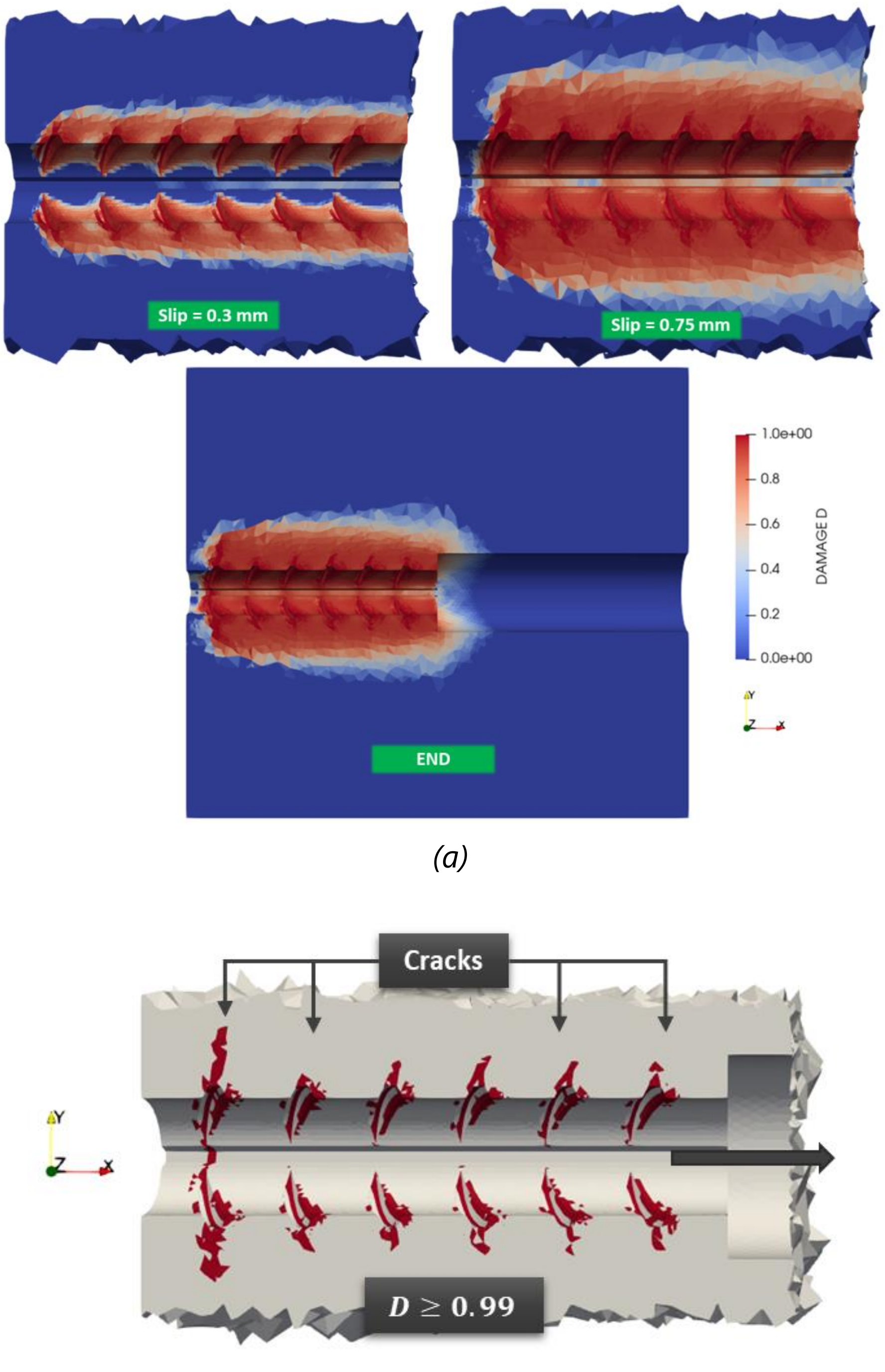

(a)

(b)

Figure 4.17 Spiral ribbed sample; (a) distribution of damage D in the concrete at different displacements (b) full cracks in the concrete ($D \geq 0.99$) at the end of the simulation

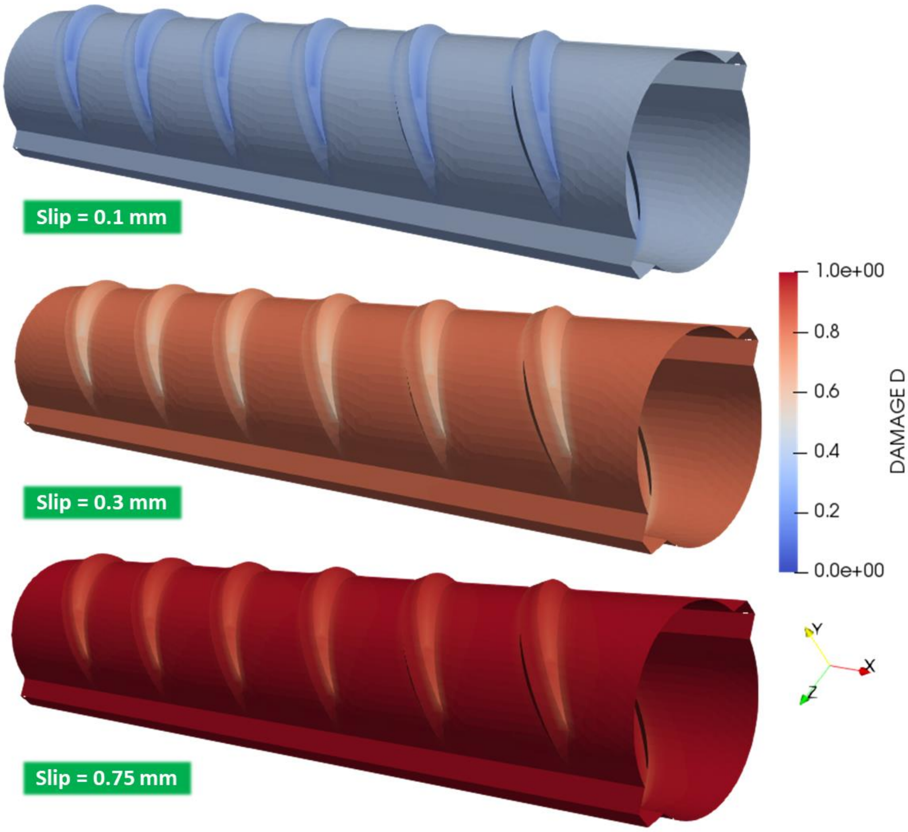

Figure 4.18 Distribution of damage in the interface at different displacements in the simulation performed on the spiral ribbed bar sample ; direction of pullings is in the x-direction.

The principle stresses in the concrete are visualized in Figure 4.19 and Figure 4.20 at the end of the loading (slip= 1.2 mm). In Figure 4.19(a), one can see that the elements having tensile principle stresses in all three directions are slightly extending from the ribs, in an inclined direction, with a main extension behind the last rib. This mostly coincides with the fully damage pattern observed in Figure 4.17(b). On the other hand, Figure 4.19(b) shows that the concrete elements in front of the ribs have compressive stresses in the three principle directions. This can be related to the phenomenon of crushing that occurs at this area because of the movement of the ribs when applying the pulling effort.

In Figure 4.20, we can observe the existence of very large compressive stresses in some of the elements. These elements are in front of the ribs and are subjected to compressive stresses in the three principal directions. The behavior is very complex near steel-concrete interface and it is difficult to extract any experimental results from pull-out tests at this scale. Due to the lack of such experimental data that could quantify or visualize this phenomenon, one cannot evaluate and compare the principle stresses obtained. The existence of such very high compressive stresses can be related to the concrete's model, as Mazars model could be not particularly well adapted to describe such uncommon states of stresses. Hence, in the future, it could be instructive to investigate more deeply the behavior in this region with different approaches to model the concrete behavior subjected to high compressive states of stresses.

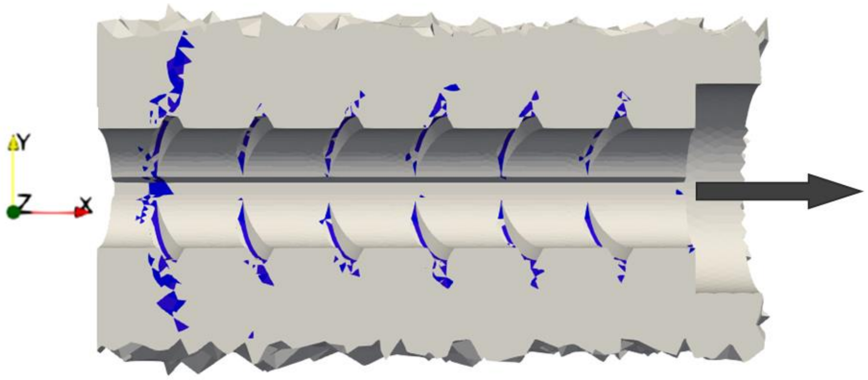

(a)

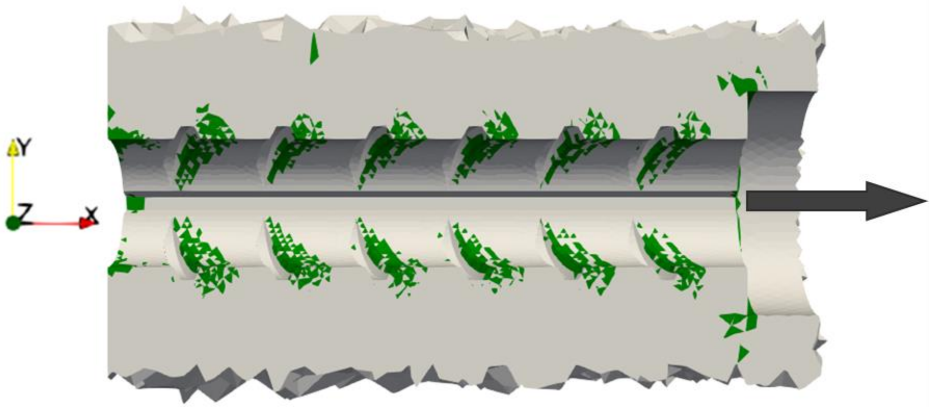

(b)

Figure 4.19 At the end of the simulation on the spiral ribbed bar sample: (a) concrete regions in blue having tensile principle stresses in the three directions (b) concrete regions in green having compressive principle stresses in the three directions

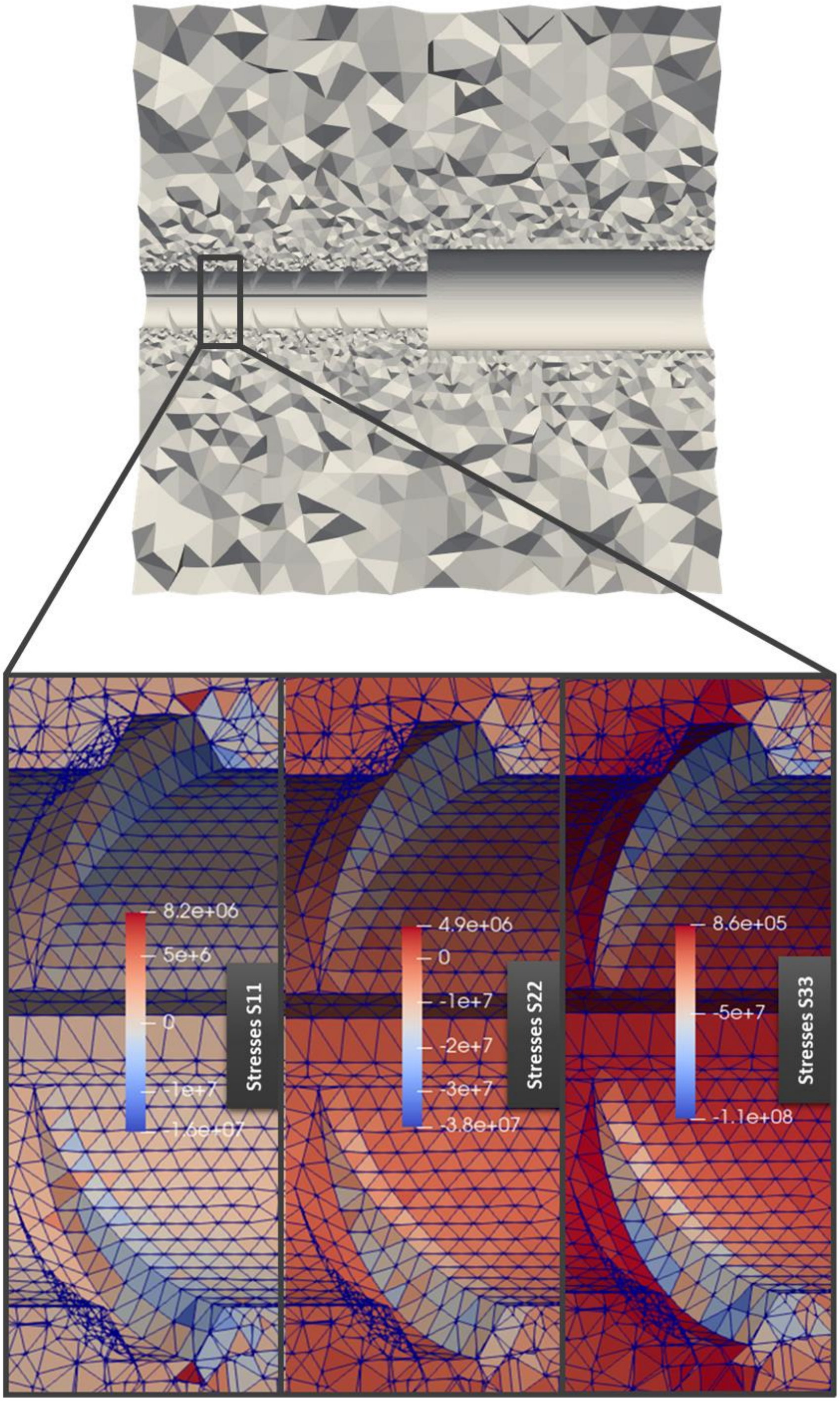

Figure 4.20 Distribution of the three principle stresses in a specific region at the steel-concrete surface for the spiral ribbed bar sample at the end of the simulation

4.5 CONCLUSIONS

In this chapter, a frictional cohesive zone model was presented in details, and a calibration procedure was applied to identify its parameters.

The FCZM was able to reproduce the experimental behavior after an appropriate adjustment of the parameters. This model has overcome the main limitations of the CZM and Coulomb's frictional interface model in reproducing the experimental behavior of the smooth bar pullout simulation. This strengthen the conclusion of Chapter 3 about the smooth bar, which is apparently directly affected by the interface model, and only negligibly by the volumetric models representing both concrete and steel.

In addition, the model was able to reproduce the behaviors of pull out tests using ribbed bars. A calibration was applied to the interface model parameters, and it proved that it is possible to get good results by applying such procedure. The parameters of the FCZM were related to the surrounding concrete and steel throughout this process.

Furthermore, the fully damaged patterns representing cracks in the concrete visualized for the ribbed bar sample were close to the patterns observed previously in other numerical simulations in literature (Jin et al., 2020a). One crack is initiated from the tip of each transversal rib, and all those cracks have a similar inclination pattern with respect to the axial position of the steel bar.

Moreover, the existence of tensile principle stresses in all three directions have been observed in the fully damaged regions. However, concrete elements in front of the ribs have compressive stresses in the three principle directions, which can be related to the phenomenon of crushing that occurs because of the movement of the ribs when applying the pulling effort. Additionally, there exist some very large compressive stresses in some of the elements. Unfortunately, one cannot evaluate and compare the principle stresses obtained because of the lack of any experimental data that quantify or visualize this phenomenon. Still, the concrete's model could be responsible for the existence of such very high compressive stresses, as it is not well adapted for such uncommon states of stresses.

Although some existing steel-concrete interface models are able to reproduce the overall behavior of the pull-out tests, they mainly succeed when using a sample with ribbed bar. However, such models cannot in general easily capture the overall behavior when using a smooth bar. For example, contact friction formulation used recently in (Jin et al., 2022, 2021a, 2020a; Liu et al., 2022b, 2022a) has proved to be well-adapted to 3D approach, and has been further used in different related studies (Jin et al., 2020b; Zhang et al., 2022). Nonetheless, it seems not able to reproduce efficiently the response of concrete-steel bond with smooth bar. Additionally, such formulations have a big cost in terms of computational time (Lebon, 2003) when used with even more finer meshes compared to (Jin et al., 2022, 2021a, 2020a; Liu et al., 2022b, 2022a). In order to analyze results locally at a very small scale near each rib as done in subsection 4.4.2, there is a clear interest to use a different approach. Likewise, the 3D frictional approach used recently in (Chiriatti et al., 2019) possesses a similar difficulty when applied on large meshes. The FCZM introduced is able to reproduce both the behavior of smooth and ribbed bars, and, although it has a non negligible computational cost, this cost is likely to be less than that of contact frictional approaches when used with this big number of elements as modeled here. Those very fine meshes are required to study the effects of the steel-concrete interface through the mean bond stress-displacement behavior and distributions of the damage and stresses locally.

FCZM can be used to investigate the effects of many phenomena and aspects that are hardly observed when using macroscopic models. For instance, the FCZM will be used in a mesoscopic study to elaborate the effect of including coarse aggregates in the concrete mix, instead of homogenous concrete as considered in here. In addition, it can also help in understanding the effect of the geometry of the ribs on the bond behavior. These geometries are usually ignored on a macroscopic scale used to model bigger structures. Thus, it may aid in giving additional information about the parameters that should be included in the macroscopic models, and/or in calibrating these parameters. Those two applications are one of the concerns of this study.

The next chapter deals with the numerical applications of the FCZM, including the simulations using heterogeneous concrete with coarse aggregates, the effect of different shapes of the steel bar representing different mechanical interlocks and the effect of external confinement.

5 NUMERICAL APPLICATIONS OF THE FRICTIONAL COHESIVE ZONE MODEL

5.1 INTRODUCTION

Following the implementation of the FCZM described in section 4.2, and the calibration of the model on different pull-out test samples, numerical applications are performed in this chapter using this interface model to study different aspects related to the steel-concrete bond.

In the first section, simulations are applied on samples with heterogeneous concrete, which is divided into mortar and coarse aggregates. The aim is to analyze the effects of aggregates on the bond behavior at the mesoscale.

The second section deals with the geometrical properties of the steel-concrete interface, by studying the effect of varying the dimensions of the steel ribs, and comparing the results using two different steel bars, in order to verify the importance of the shapes of the ribs, as discussed in subsection 2.2.2.3.

The third section aims to verify the importance of confinement on the bond behavior. Its effect is studied by applying active confinement on the external surfaces of the concrete section, and then comparing the results accordingly to experimental results.

5.2 HETEROGENEOUS CONCRETE WITH COARSE AGGREGATES

In this section, heterogeneous concrete is used instead of homogeneous concrete, by dividing the concrete into coarse aggregates and the surrounding mortar, together forming and taking the properties of the concrete volume. The usage of heterogeneous concrete aims at identifying if the aggregates have global or local impacts on the behavior.

5.2.1 General description

In order to perform the simulations using the newly implemented frictional cohesive zone model described in section 4.2 on samples having heterogeneous concrete, a certain procedure is followed. Since the heterogeneous concrete is made up of mortar and embedded aggregates, both mortar and coarse aggregates together should give the same behavior as the homogenous concrete on representative samples. Likewise homogenous concrete, mortar is assigned Mazars model, introduced in subsection 3.4.3. Thus, one should expect mortar to have different material and damage parameters from concrete. Aggregates are going to be assigned an elastic behavior, since cracks propagate in the weaker material, which is mortar. Hence, the aim first is to determine the material and damage parameters of mortar, based on the macroscopic properties of homogenous concrete. To do so, uniaxial tensile and compressive tests are performed on heterogeneous concrete samples, and then the results are compared to the results of uniaxial tensile and compressive tests performed on homogenous concrete samples, in order to validate the mortar parameters.

After the calibration process on uniaxial tests, pull-out tests simulations are performed on generated samples having heterogeneous concrete, whose properties are the same as those of the aforementioned heterogeneous concrete samples. The corresponding pull-out test boundary conditions are the same as the ones described in subsection 3.3.1 and shown in Figure 3.8. The numerical pull-out results are compared to the pull-out test experimental results derived from (La Borderie and Pijaudier-Cabot, 1992), which were used in subsection 4.3.2.

5.2.2 Generated samples

5.2.2.1 Pull-out test generated samples

In order to perform pull-out tests simulations, three pull-out heterogeneous concrete samples are generated in order to have more than one result, named shortly SAgg1, SAgg2 and SAgg3. The concrete in these samples is a two phase material made up of coarse aggregates and surrounding mortar, while the steel bar is a spiral ribbed bar. The geometrical properties of the sample generated in subsection 4.3.2.1 are preserved.

For all the three samples, the percentage by volume of aggregates is taken equal to 35%. Usually, fine and coarse aggregates make 60-80% of concrete by volume, of which 55% are fine aggregates and 45% are coarse aggregates, making the choice of 35% realistic. In addition, the minimum range dimension of the particles is 4.5 mm, while the largest dimension of aggregates should not exceed 32 mm. All three samples have exactly the same grading of coarse aggregates. The difference between the three samples results from the generation and placement procedure, as described in subsection 3.2.3, which gives different number, positioning and sizes of aggregates in the samples. This produces a more statistical based study, by trying to check the effects of these factors on the overall results. The grading and distribution of aggregates are chosen in a way that they fall within the acceptable standard limits provided by (ASTM Standard C33, 2003), which can be seen in Figure 5.1.

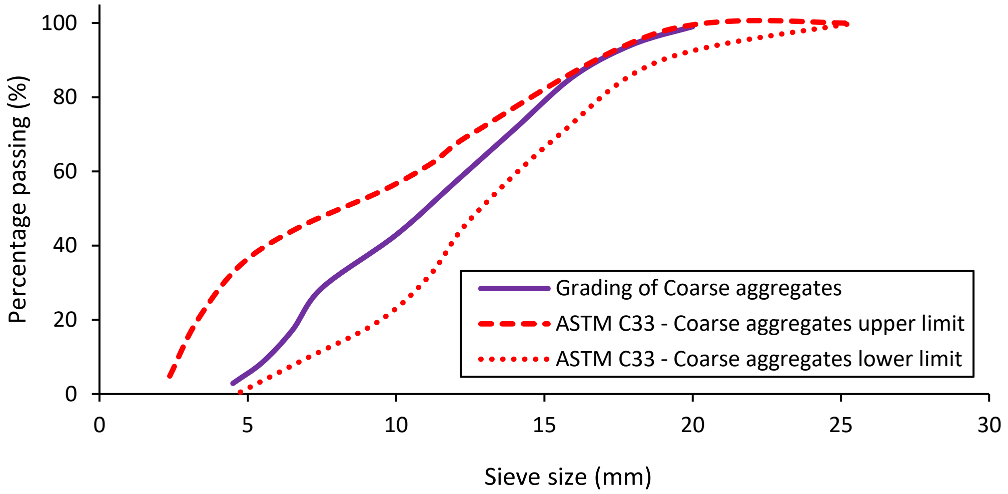

Figure 5.1 Grading of the coarse aggregates in the heterogeneous concrete, compared to the standard limits provided by (ASTM Standard C33, 2003)

Table 5.1 Meshing elements in the pull-out generated samples

Name	**Number of coarse aggregates**	**Number of meshing elements of**		
		Steel bar	**Coarse aggregates**	**Mortar**
SAgg1	1291	291 000	256 000	685 000
SAgg2	1245	292 000	247 000	659 000
SAgg3	1276	291 000	253 000	684 000

One can see that the chosen grading is fully contained within ASTM C33 standard limits. As a result of the random generation process, the number of coarse aggregates in samples SAgg1, SAgg2 and SAgg3 is 1291, 1245 and 1276, respectively.

As detailed in subsection 3.2.5, an unstructured mesh is finally built on the three generated samples using linear tetrahedral elements. The triangular edge of each element at the steel-concrete interface is almost 0.4 mm in each of the three samples. The meshing results for the three samples SAgg1, SAgg2 and SAgg3 are listed in Table 5.1, and sample SAgg3 is visualized in Figure 5.2.

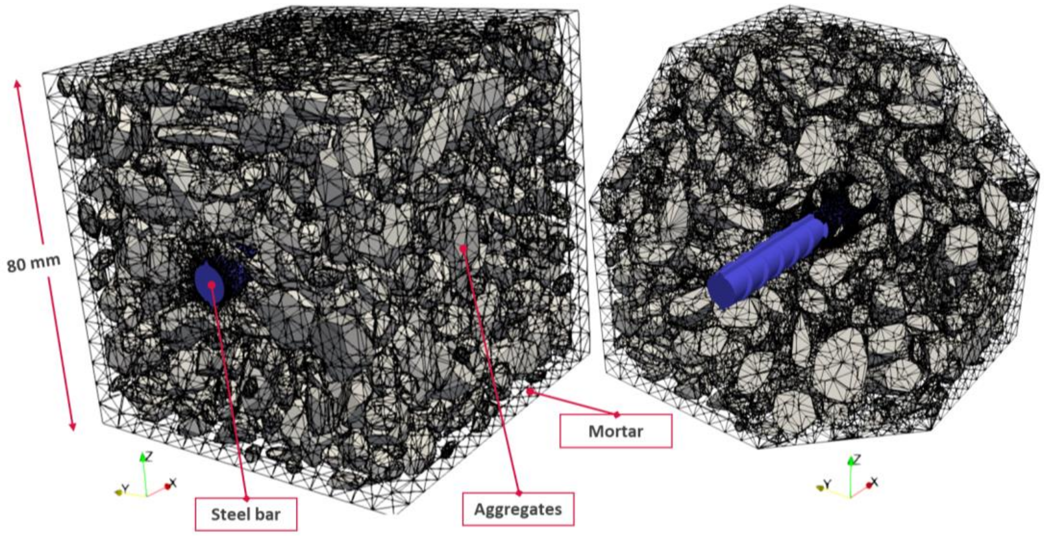

Figure 5.2 Visualization of sample SAgg3, showing the aggregates phase (in white), ribbed steel bar (in blue) and mortar (transparent)

5.2.2.2 Concrete cubic generated samples

In order to perform uniaxial tensile and compressive numerical tests to determine the values of the parameters of mortar, three heterogeneous cubic concrete samples are generated, named shortly CubeA, CubeB and CubeC, in order to have an idea of the representativity. The side length of each sample is 80 mm, which is chosen to limit the mesh size. The dimension is also based on the pullout test samples previously generated in subsection 5.2.2.1, which preserves the dimensions and the properties of the pull-out samples. Similarly, the percentage of volume of coarse aggregates is 35% for all the concrete samples, and the same grading of coarse aggregates shown in Figure 5.1 is also used in the 3 cubic samples. Those samples are finally meshed, as shown for sample CubeB in Figure 5.3, and the corresponding mesh results are shown in Table 5.2.

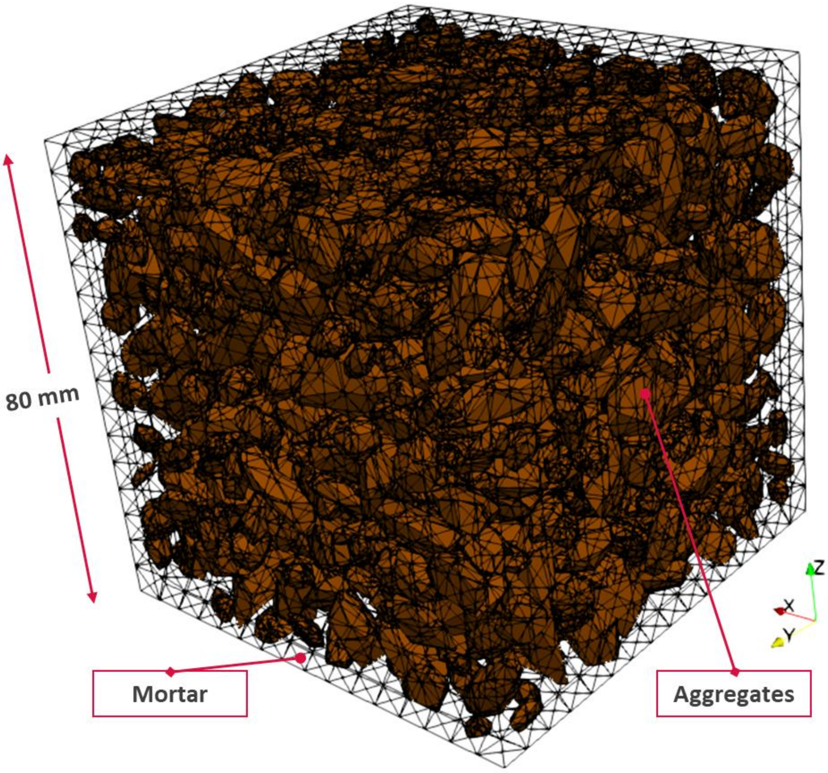

Figure 5.3 Visualization of sample CubeB, showing the aggregates phase (colored) and mortar (transparent)

Table 5.2 Meshing elements in the cubic heterogeneous concrete generated samples

Name	**Number of coarse aggregates**	**Number of meshing elements of**	
		Coarse aggregates	**Mortar**
CubeA	1269	252 000	600 000
CubeB	1252	247 000	590 000
CubeC	1295	257 000	615 000

In addition, a homogenous concrete cubic sample is generated in order to compare the uniaxial tests results from both homogeneous and heterogeneous concretes. Likewise the heterogeneous samples, the side length of the homogenous sample is 80 mm. The number of mesh elements of the concrete is 130 000, which is expected to be less than the three aforementioned heterogeneous samples considering it is a one-phase material with no steel bar.

5.2.3 Identification of the mechanical properties of mortar

In order to determine the material and damage parameters of mortar, the three heterogeneous concrete samples CubeA, CubeB and CubeC and the homogenous sample generated in subsection 5.2.2.2 are considered.

In the homogenous concrete model, concrete is assigned the same values to the parameters that were previously used in the pull-out test performed in subsection 4.3.2.2. Those values are listed in Table 4.4.

In the heterogeneous concrete model, mortar is assigned Mazars damage model, described in 3.4.3, while a simple elastic model is assigned to the coarse aggregates, in which the Young's modulus E_{agg} is 70 GPa and the Poisson's ratio v_{agg} is 0.3, as in (Bary et al., 2017). In addition, the contact between the aggregates and the mortar is considered to be perfect. This is limits the number of parameters to be determined, which would have increased if an interface model was assigned to aggregates-mortar interfaces. This perfect contact will certainly affect the values of the parameters of mortar.

In order to predict a first estimation of the mechanical properties of mortar, homogenization approaches are used. In such schemes, mortar represents the matrix part and aggregates represents the inclusive phase. Hansen model, introduced in (Hansen, A. et al., 1989), proposed a micromechanical equation to calculate the Young's modulus of concrete:

$$E_{con} = \left(\frac{p_{mor}E_{mor} + (1 + p_{agg})E_{agg}}{(1 + p_{agg})E_{mor} + p_{mor}E_{agg}}\right)E_{mor} \qquad (5.1)$$

where p_{agg} is the percentage of aggregates by volume, which is 0.35, while p_{mor} is the percentage of mortar by volume, which is 0.65.

Similarly, Young's modulus can be calculated by Cavento model, proposed by (Counto, 1964) as follows:

$$\frac{1}{E_{con}} = \frac{1-\sqrt{p_{agg}}}{E_{mor}} + \frac{1}{\left(\frac{1-\sqrt{p_{agg}}}{\sqrt{p_{agg}}}\right)E_{mor} + E_{agg}} \qquad (5.2)$$

Likewise, batch model introduced in (Baalbaki et al., 1992) proposed the following simple equation to calculate Young's modulus:

$$E_{con} = {E_{mor}}^{p_{mor}} \cdot {E_{agg}}^{p_{agg}} \qquad (5.3)$$

By using these equations, E_{mor} is calculated using concrete and aggregates mechanical parameters. Hansen, Cavento and batch models give 20.6 GPa, 19.63 GPa and 19.57 GPa, respectively. Still, these approaches cannot calculate the Poisson's ratio.

Mori-Tanaka homogenization scheme, which was first introduced by (Mori and Tanaka, 1973), is a well-known scheme that can be used to determine both mortar's Young's modulus and Poisson's ratio from those of concrete and aggregates. For elastic isotropic behaviors and randomly oriented aggregates (if not spherical), the scheme can be described as follows:

$$\mathbb{T}_{con} = (p_{mor}\mathbb{T}_{mor} + p_{agg}\mathbb{T}_{agg}\mathbb{C}_p)(p_{mor}\mathbb{I} + p_{agg}\mathbb{C}_p)^{-1} \qquad (5.4)$$

where $\mathbb{T}_{con}$, $\mathbb{T}_{mor}$ and $\mathbb{T}_{agg}$ are the 4rth order elasticity tensors of concrete, mortar and aggregates, respectively, which depend on Young's modus and Poisson's ratio of each material. $\mathbb{I}$ is the 4rth order identity tensor. $\mathbb{C}_p$ is the tensor of strain localization of aggregates calculated as follows:

$$\mathbb{C}_p = \left(\mathbb{I} + \mathbb{S}_p : (\mathbb{T}_{mor})^{-1} : [\mathbb{T}_{mor} - \mathbb{T}_{agg}]\right)^{-1} \qquad (5.5)$$

where $\mathbb{S}_p$ is the Eshelby tensor, which depends on the geometrical form for the aggregates. By considering spherical shapes for the aggregates, elements of Eshelby tensor are calculated as follows:

$$\mathbb{S}_{p_{1111}} = \mathbb{S}_{p_{2222}} = \mathbb{S}_{p_{3333}} = \frac{7 - 5v_{mor}}{15(1 - v_{mor})}$$

$$\mathbb{S}_{p_{1122}} = \mathbb{S}_{p_{2233}} = \mathbb{S}_{p_{3311}} = \mathbb{S}_{p_{1133}} = \mathbb{S}_{p_{2211}} = \mathbb{S}_{p_{3322}} = \frac{5v_{mor} - 1}{15(1 - v_{mor})} \tag{5.6}$$

$$\mathbb{S}_{p_{1212}} = \mathbb{S}_{p_{2323}} = \mathbb{S}_{p_{3131}} = \frac{4 - 5v_{mor}}{15(1 - v_{mor})}$$

By applying Mori-Tanaka scheme, supposing spherical particles, it yields E_{mor} = 21.2 GPa. One can see the highest value for Young's modulus between Hansen model, Cavento model, batch model and Mori-Tanaka scheme is when applying the latter. Using Mori-Tanaka by supposing ellipsoidal particles with an aspect ratio of 3, E_{mor} will almost be 23 GPa. Since the considered polyhedron particles are closer in shape to ellipsoidal particles having an aspect ratio of 3 than to spherical particles, E_{mor} and v_{mor} are taken equal to those calculated by applying Mori-Tanaka on ellipsoidal particles, which are 23 GPa and 0.22, respectively.

Concerning the damage parameters, regularization is used in tension by applying the procedure described in subsection 3.4.3. Mortar's fracture energy is considered to be 70 N/m as a first estimate, which is close to values observed experimentally in (Restuccia et al., 2020), while mortar's ultimate tensile stress $f_{t\,mor}$ is chosen so that the peak stress of the homogenous and heterogeneous case is the same. In addition, β is taken 1.06 as done in subsection 3.4.3.

The normal stress versus the normal displacement of the uniaxial tensile tests of the homogenous concrete sample and CubeA sample are shown in Figure 5.4, for different values of $f_{t\,mor}$ and $G_{f\,mor}$.

From Figure 5.4, one can see that the best fit is reached when $f_{t\,mor}$= 2.8 MPa and $G_{f\,mor}$ = 110 N/m. Thus, according to Eq. (3.7), ε_{D_0} is 1.2×10^{-4}. One can see that the value of the fracture energy is now larger than what is expected for mortar. Still, we expect to get a lower value if an imperfect aggregate-mortar interface is used, which has certainly an effect on the overall behavior. Still, a separate study and calibration is needed in this case, as it has an effect on both the pattern and the slope of the stress-displacement curve too. For instance, by assigning linear elastic model, used in subsection 3.3.3, to the aggregate-mortar interface, and by simple variation of the stiffness, one can see a change in the whole slope as shown in Figure 5.5. Thus, the current choice is acceptable for the current study.

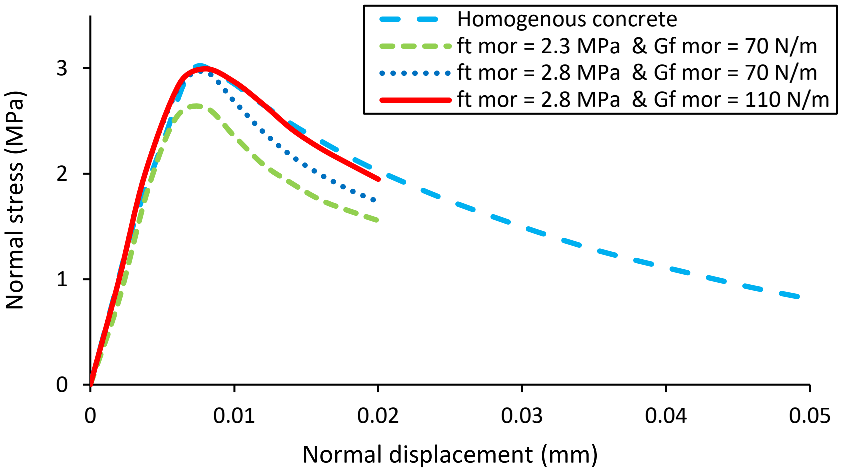

Figure 5.4 Normal stress versus normal displacement for uniaxial tensile tests performed on the homogenous concrete sample using the values listed in Table 4.4 for Mazars model parameters, and on CubeA by taking $E_{mor} = 23\ GPa$*, and choosing different values for* $G_{f\ mor}$ *and* $f_{t\ mor}$

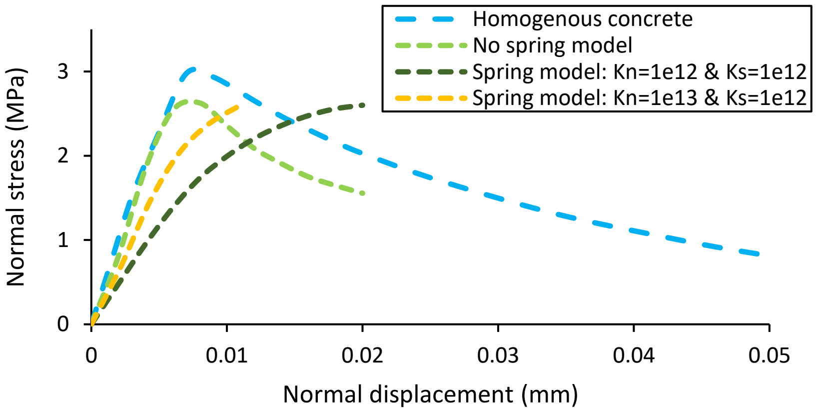

Figure 5.5 Normal stress versus normal displacement for uniaxial tensile tests performed on the homogenous concrete sample using the values listed in Table 4.4 for Mazars model parameters, and on CubeA by taking $E_{mor} = 23\ GPa$*, with linear spring model for the mortar-aggregates interface; Stiffnesses are in* N/m^3

In order to verify these results, simulations are performed on the other two samples CubeB and CubeC, using the same values used in CubeA simulation.

The corresponding results are shown in Figure *5.6*. One can see that those values gave a good fit for the three different samples. As a result, tensile damage parameters and material parameters of mortar will be fixed to the aforementioned values, while the compressive parameters are kept intact to this point.

Regarding the compressive behavior, uniaxial compressive tests are performed on the homogenous and heterogeneous samples. For the homogenous concrete, as previously stated, concrete is assigned the same values as the parameters that were used in the pull-out test performed in subsection 4.3.2.2, which are listed in Table *4.4*. For the heterogeneous sample, the mechanical and damage parameters of mortar are fixed as mentioned before, and $A_{c\,mor}$ varied starting from the initial value of A_c defined by Eq. (3.16*)* and $B_{c\,mor}$ is varied from the initial value of B_c defined in Eq. (4.25*)*, until reaching the best fit. By varying the parameters, and performing several tests, one can get a good fit when $A_{c\,mor} = 0.3A_c$ and $B_{c\,mor} = B_c$, which are written in details as follows:

$$A_{c\,mor} = 0.3A_c \; = -100.774\, l^2 + 4.8824\, l - 0.00006 \qquad (5.7)$$

$$B_{c\,mor} = B_c = 340589.7285\, l^2 + 20577.3197\, l - 0.5075 \qquad (5.8)$$

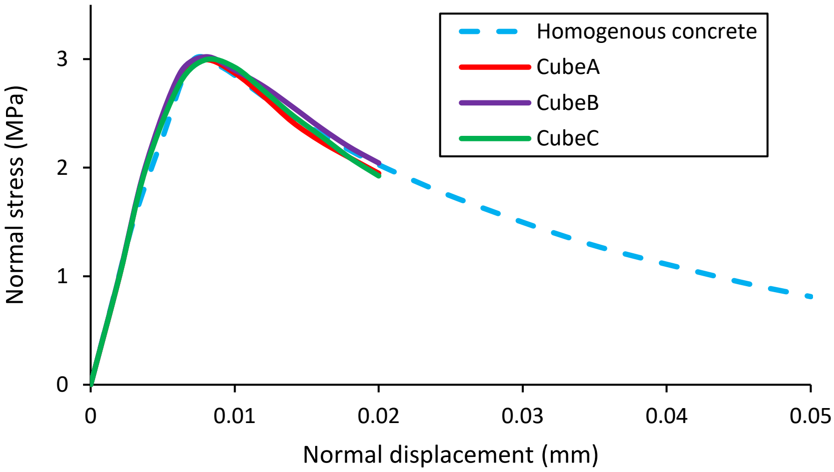

Figure 5.6 Normal stress versus normal displacement for uniaxial tensile tests performed on the homogenous concrete sample using the values listed in Table 4.4 for Mazars model parameters, and on CubeA, CubeB and CubeC by taking $E_{mor} = 23\ GPa$, $f_{t\,mor} = 2.8\,MPa$ *and* $G_{f\,mor} = 110\,N/m$

The normal stress versus normal displacement for the uniaxial compressive tests performed on the homogenous concrete sample and samples CubeA, CubeB and CubeC using the aforementioned values for the parameters are shown in Figure *5.7*. One can see that those values gave a good fit for the three different samples. As a result, compressive damage parameters $A_{c\,mor}$ and $B_{c\,mor}$ are assigned according to Eqs. (5.7*)* and (5.8*)*, respectively. Similarly to the fracture energy, the adjustment of $A_{c\,mor}$ could be affected by the type of contact between aggregates and mortar. Introducing an interface will affect the tensile parameters and as a consequence the compressive parameters, and requires a different calibration.

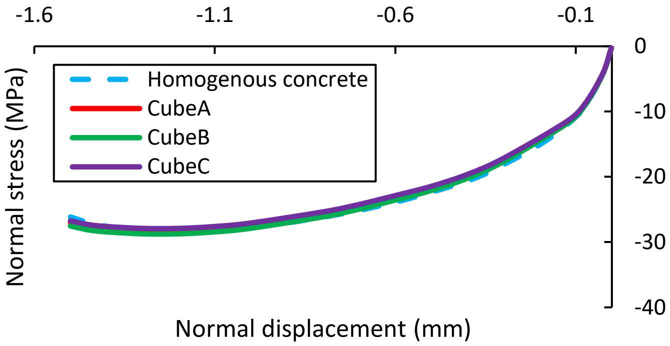

Figure 5.7 Normal stress versus normal displacement for uniaxial compressive tests performed on the homogenous concrete sample using the values listed in Table 4.4 for Mazars model parameters, and on CubeA, CubeB and CubeC by taking $A_{c\,mor}$ and $B_{c\,mor}$ according to Eqs. (5.7) and (5.8), respectively

Finally, the values assigned to the different parameters of mortar are summarized in Table *5.3*.

Table 5.3 Assigned values to the parameters of Mazars model for mortar

$\boldsymbol{E_{mor}}$ **(GPa)**	$\boldsymbol{v_{mor}}$	$\boldsymbol{f_{t\,mor}\,(MPa)}$	$\boldsymbol{G_{f\,mor}\,(N/m)}$
23	0.22	2.8	110
$\boldsymbol{B_t}$	$\boldsymbol{A_{c\,mor}}$	$\boldsymbol{B_{c\,mor}}$	$\boldsymbol{\beta}$
Eq. (3.14**)**	Eq. (5.7)	Eq. (5.8)	1.06

5.2.4 Discussions on the results of pull-out test simulations

In order to perform simulations on heterogeneous concrete pull-out samples, the three heterogeneous concrete pull-out samples SAgg1, SAgg2 and SAgg3, generated in subsection 5.2.2.1, are considered. Additionally, the results of the pull-out test performed on homogeneous concrete samples detailed in subsections 4.3.2.2 and 4.4.2 are also considered.

In the heterogeneous simulations, steel is assigned the perfect yield model as described in subsection 3.4.4, mortar is assigned Mazars model using the parameters described in Table 5.3. The steel-mortar interface is assigned FCZM described in section 4.2, using the values for the parameters shown in Table 5.3, since the steel-concrete bond in the heterogeneous case do not differ from the homogenous case. In other words, the steel-concrete interface is still the surface of contact between steel and concrete, regardless of the phases within concrete. Mortar is one of the phases of concrete, which forms, together with aggregates, the homogeneous concrete that is in contact with steel. Thus, if aggregates were in contact with the steel bar, and they were part of this mix, the FCZM parameters would not be changed, as the calibration and assignment of the parameters is based on the properties of the homogeneous concrete containing them, and not on the phase that is in contact with steel.

As done in subsection 5.2.3, the aggregates are assumed linear elastic with $E_{agg} = 70$ GPa and $v_{agg} = 0.3$. Additionally, the contact between the aggregates and the mortar is considered to be perfect. The mean bond stress versus the bar's displacement for the three simulations are plotted in Figure 5.8.

One can observe that the overall behavior for the three samples is almost the same. In addition, the initial part of the curves is the same for the homogenous case and the heterogeneous cases, but the final part shows that the peak bond stress for the homogenous case is slightly higher than that of the heterogeneous cases. One explanation is that the presence of aggregates affects the orientation and propagation of cracks. To analyze more closely the results, damage in the mortar should be visualized.

In order to compare the damage behavior, the distribution of damage in concrete for the homogenous case, and in mortar for the heterogeneous cases, are shown. To do so, a certain volume of the sample is extracted, as shown in Figure *5.9*. This volume includes entirely the steel-concrete interface, and the surrounding zones in the three directions. The dimension of the extracted volume in the x (bar) direction is 50mm, including the 40 mm adhesive part of the bond, and 40 mm in both the y direction and the z directions.

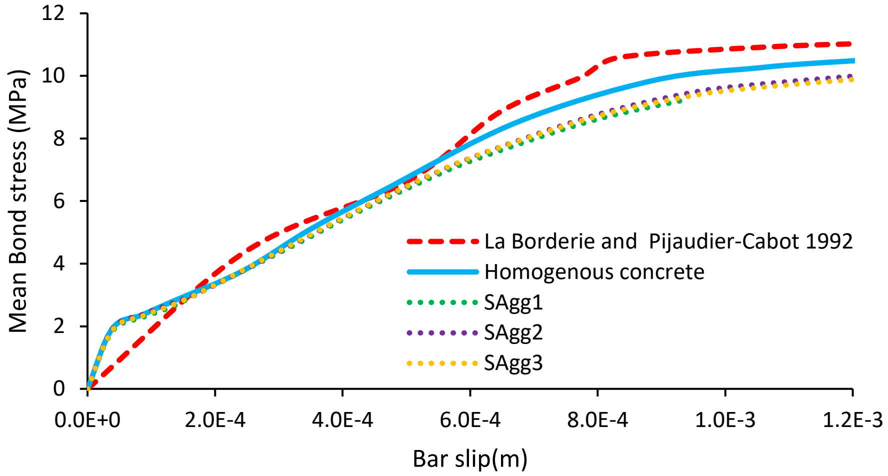

Figure 5.8 Mean bond stress versus slip for the homogenous pull-out test discussed in subsection 4.3.3.2, and for the heterogeneous pull-out test simulations performed on samples SAgg1, SAgg2 and SAgg3

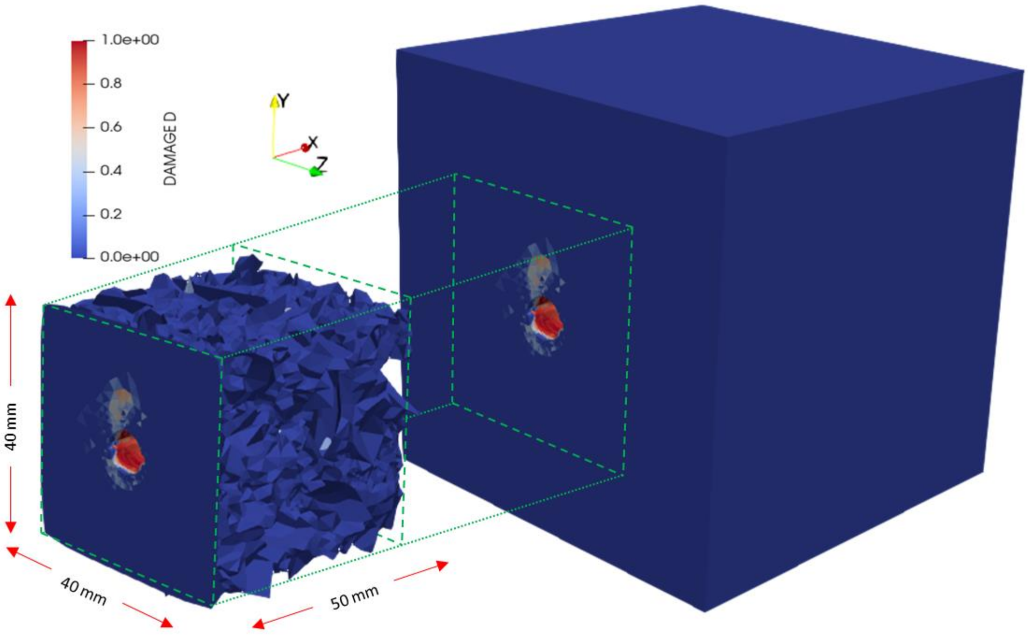

Figure 5.9 The extracted volume, whose dimensions are 50 mm in the x direction, 40 mm in y direction and 40 mm in z direction

The distributions of damage for the four cases at the central part of the extracted volume when bar's displacement is 1 mm are shown in Figure *5.10*.

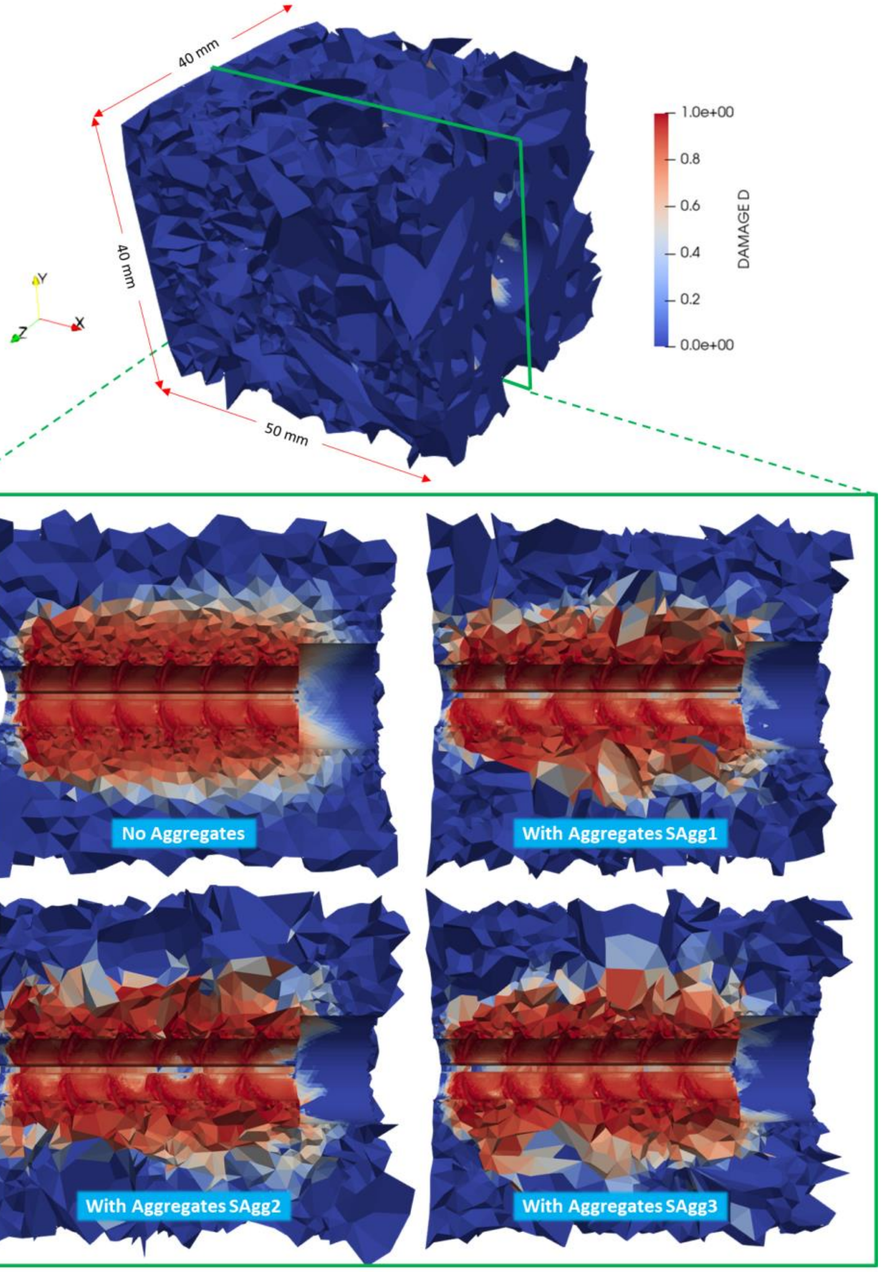

Figure 5.10 Distribution of damage in concrete for the homogenous case, and in mortar for the three heterogeneous cases, at the central plane normal to the z-axis of the extracted volume, when bar's displacement is 1 mm

One can see that the region where damage is not null is almost the same for the four different cases. Still, it is not easy to make a comparison between these cases visually. Hence, a certain parameter or index should be used for comparison. For this sake, we propose a global unitless damage parameter Δ, which calculates the average damage in the considered volume, using the following formula:

$$\Delta = \frac{\sum D_k V_k}{\sum V_k} \tag{5.9}$$

where D_k and V_k are the damage and the volume of the k^{th} finite element of the considered volume, respectively. Damage for an element is calculated as the average damage associated to the four nodes forming the tetrahedral element. The summation Σ covers all the finite elements in the volume.

By considering the extracted volumes shown in Figure *5.9* for the homogenous and heterogeneous samples, the corresponding values of the global damage parameter of the extracted volume Δ_{se} are calculated using Eq. (5.9*)* when bar's displacement is 1mm, along with volume V_{se} of the extracted volume. Similarly, the global damage parameter for all the whole sample Δ_t is calculated using Eq. (5.9*)* for the four samples, when bar's displacement is 1mm, along with whole considered volume V_t. The detailed results are summarized in Table *5.4*.

From Table *5.4*, one can see that the global damage Δ_t in the total volume is higher in the homogenous case, when compared to the heterogeneous case. For the extracted section, global damage Δ_{se} is lower in the homogenous case, compared to the heterogeneous case. Indeed, it is not appropriate to compare the ratios of global damage Δ for the total volume to that of the extracted volume since the percentage of aggregates differs, by checking the ratio of volumes $V_t/V_{t\ homogenous}$ and $V_{se}/V_{se\ homogenous}$ for the heterogeneous cases.

Although the values of the global damage parameter for the heterogeneous samples are close to each other, a certain difference in values exits. This is due to the different distribution of aggregates in the sample, which affects the directions of the cracks in the mortar and may reorient others. The exact distributions and shapes of the aggregates can only be determined by 3D tomography images, which should lead to a different final damage value, but that should still be close to the ones already calculated. Δ_t is higher in the homogenous case because damage can propagate anywhere in such concrete, without being affected by the presence of aggregates. This is not the case in heterogeneous samples, where these aggregates block the propagation of damage, and force it to go around the particles.

Table 5.4 Values of the global damage Δ of the extracted volume and the total volume for the homogenous sample and the three heterogeneous samples SAgg1, SAgg2 and SAgg3, along with the volume of each extracted volume in each case, all when bar's displacement is 1 mm

Parameter	Homogenous	SAgg1	SAgg2	SAgg3
V_t (in mm^3)	499 231	324 500.2	324 500.2	324 500.2
$V_t/V_{t\ homogenous}$	100%	65%	65%	65%
Δ_t	0.023325	0.020724	0.022031	0.021038
$\Delta_t/\Delta_{t\ homogenous}$	100%	88.85%	94.45%	90.2%
V_{se} (in mm^3)	93 185.4	53 533.6	54 557.6	53 093.6
$V_{se}/V_{se\ homogenous}$	100%	57.45%	58.55%	56.98%
Δ_{se}	0.124962	0.125752	0.13127	0.129602
$\Delta_{se}/\Delta_{se\ homogenous}$	100%	100.63%	105.05%	103.71%
V_{se}/V_t	0.1866	0.165	0.1681	0.1636
Δ_t/Δ_{se}	0.1866	0.165	0.1678	0.1636

Figure *5.11* shows the distribution of the fully damaged cracks, i.e. D≥0.99, for the homogenous sample and the three heterogeneous samples, when bar's displacement is 1 mm. One can see that in all cases, cracks are mainly surrounding the ribs. The general pattern is similar in all cases, although some cracks are blocked at certain positions by aggregates in the heterogeneous samples.

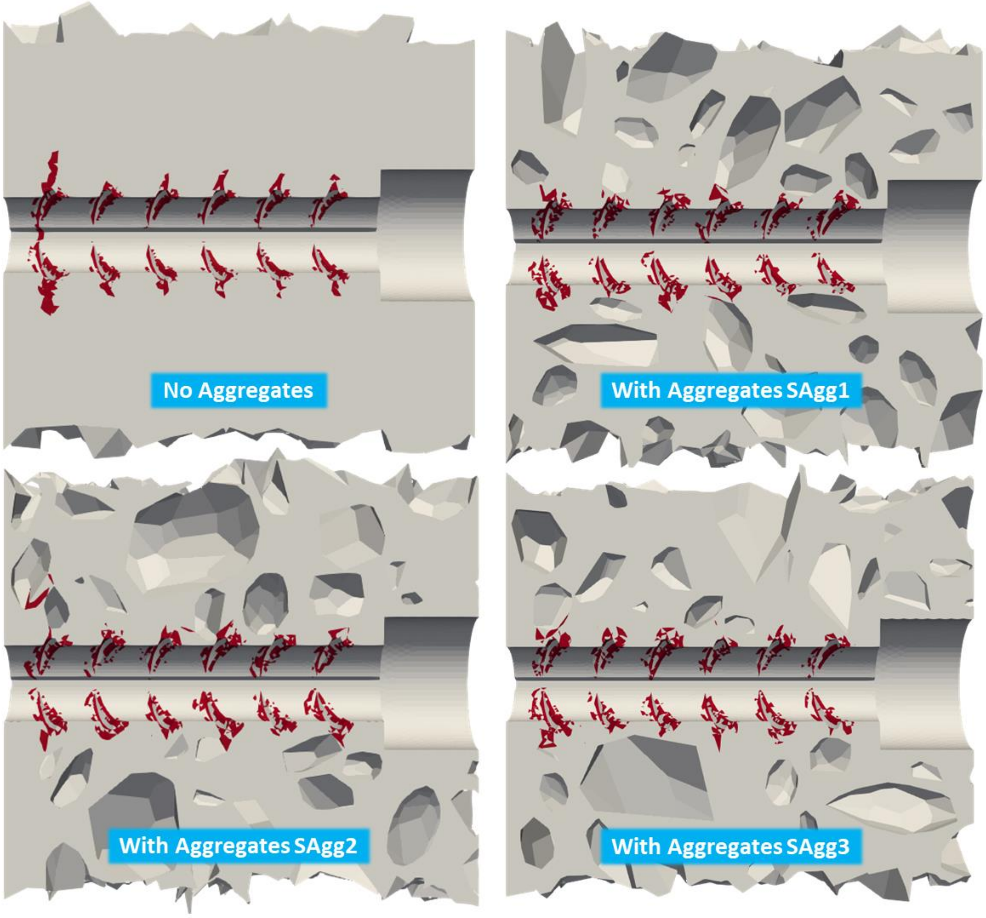

Figure 5.11 Full damage ($D \geq 0.99$) in concrete for the homogenous case, and in mortar for the three heterogeneous cases, at the central plane normal to the z-axis of the extracted volume, when bar's displacement is 1 mm

Figure *5.12* shows the regions in concrete in the homogenous sample and in mortar in the three heterogeneous samples where compressive stresses exist in the three principle directions.

In all the cases, the regions where there exist compressive stresses in all three principle directions are mainly in front of the ribs. Additionally, one can see that there are several regions near the aggregates in the heterogeneous samples, which are also under three compressive principle stresses. These are mainly at the mortar aggregates interface, where mortar and aggregates interact as the stresses resulting from the pulling force affect the concrete block.

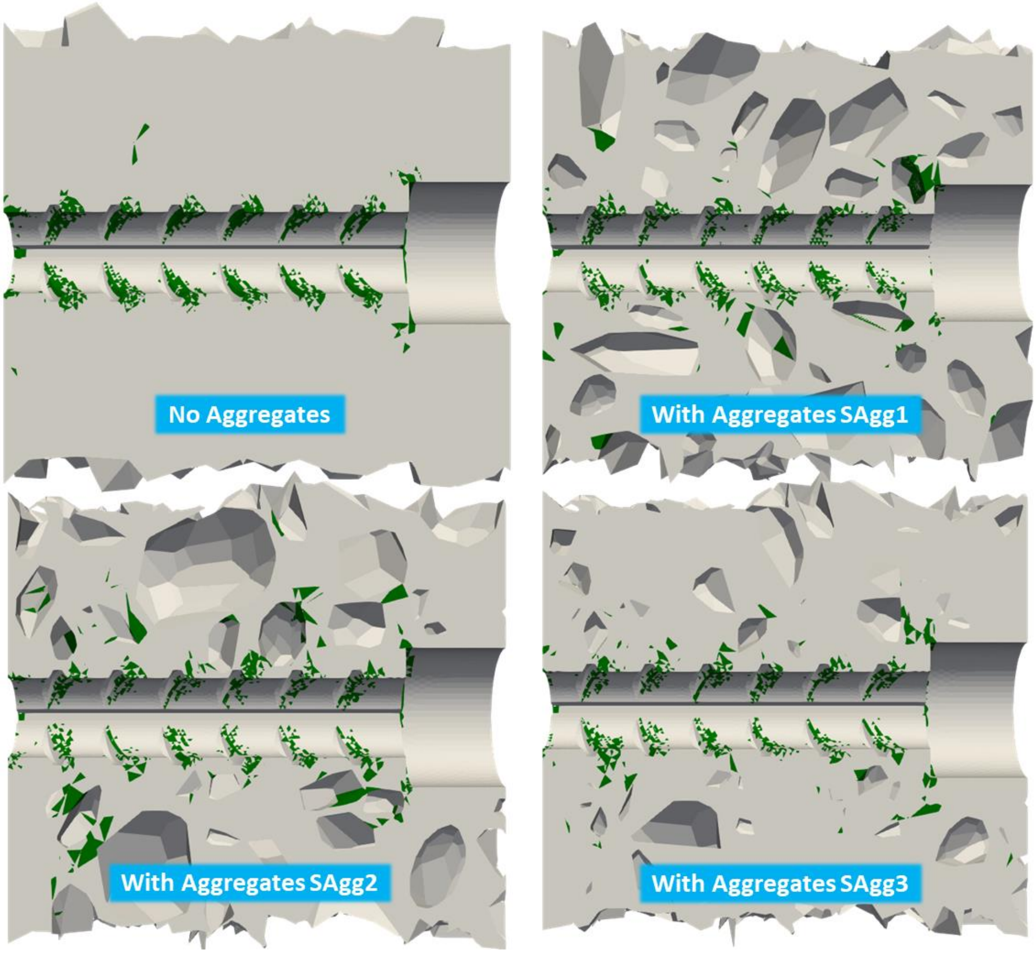

Figure 5.12 Concrete and mortar regions having three compressive principle stresses for the homogenous case and the three heterogeneous cases, at the central plane normal to the z-axis of the extracted volume, when bar's displacement is 1 mm

As a conclusion, one can say that even using heterogeneous concrete, it is possible to reproduce the macroscopic behavior using FCZM for the steel-concrete interface. The propagation of damage in the heterogeneous sample appears similar to that in the homogenous sample. However, for each heterogeneous case, the global damage is not the same, which shows the effect of the placement and distribution of aggregates in the mortar block. Adding of aggregates had increased the computational cost importantly, and also led to additional convergence difficulties. Still, the outcome difference is not that huge compared to this cost, especially in terms of mean bond stresses. One expects to get similar bond stress as long as the properties of concrete are preserved in homogenous concrete, as those properties have an effect on the bond behavior as stated in subsection

2.2.2.3. Still, the interface is mainly affected by the concrete region very close to the steel bar, and not deep inside the concrete block. For example, the phenomena that exist near the interface, described in subsection 2.2.1, can lead to the entrapping of some finer aggregates near the interface, which may affect the interface behavior. Coarse aggregates may not be very close to the concrete surface, contrary to finer aggregates (sand) that are present in this region near the interface. Fine aggregates can also affect the directions and initiation of cracks, especially with their very huge number. However, adding such aggregates near the interface is complex in practice since they lead to much finer meshes, exceeding several millions elements in the sample. This is extremely difficult to perform such simulations, especially with already existing convergence problems with the presence of coarse aggregates alone. One can say that as long as the properties of concrete are correctly assigned, homogenous concrete is sufficient to produce satisfactory results in terms of bond strength. Finally, since the interface region is more important than the concrete block, it may be affected by more crucial phenomena, like the shape of the ribs changing the shape of interface itself. This is the concern of the next section.

5.3 EFFECT OF THE SHAPE OF THE STEEL BAR RIBS

In this section, the effect of varying the shapes of the steels’ ribs on the macroscopic behavior is studied numerically, in order to understand the importance of modelling the exact geometry of the steel-concrete interface, and its general influence on the bond behavior.

5.3.1 General description

To analyze the effect of the geometrical shape of the ribs, pull-out test simulations are performed using the newly implemented frictional cohesive zone model described in section 4.2 on homogenous concrete samples. The corresponding pull-out test boundary conditions are the same as the ones described in subsection 3.3.1 and shown in Figure 3.8.

First, simulations are performed on samples having a steel bar with only one rib, to understand the effect of changing the dimensions of the rib in a certain pattern on the bond behavior. Next, a pull-out simulation is performed using a herringbone steel bar, and the results are compared to those of a spiral bar.

5.3.2 Pull-out test simulations using samples with a one-rib bar

In this section, simulations are performed on samples with one-rib bar, in which the geometry of the rib in each sample differs in terms of thickness, height or inclination angle. The aim is to study the effect of the varying rib's surface area on the bond strength, and to verify that the bond stress increases with the increase of the rib's surface area in accordance with the state-of-the-art in subsection 2.2.2.3.

5.3.2.1 Generated samples

Nine cubic homogenous concrete samples with one-rib bar are generated using the procedure described in section 3.2. In all the samples, the total length of the steel bar is 80 mm, the adhesive length is 40 mm and the side length of the cubic samples is 80 mm. The steel bar is formed of a cylindrical part whose diameter is 8 mm, and of one transversal rib at the middle of the adhesive part of the bar, with no longitudinal ribs. The shape bar, along with its total surface area, non-adhesive surface area, adhesive surface area and the rib's surface area are all shown in Figure 5.13. Notice that the rib's surface area is fully included in the adhesive surface area.

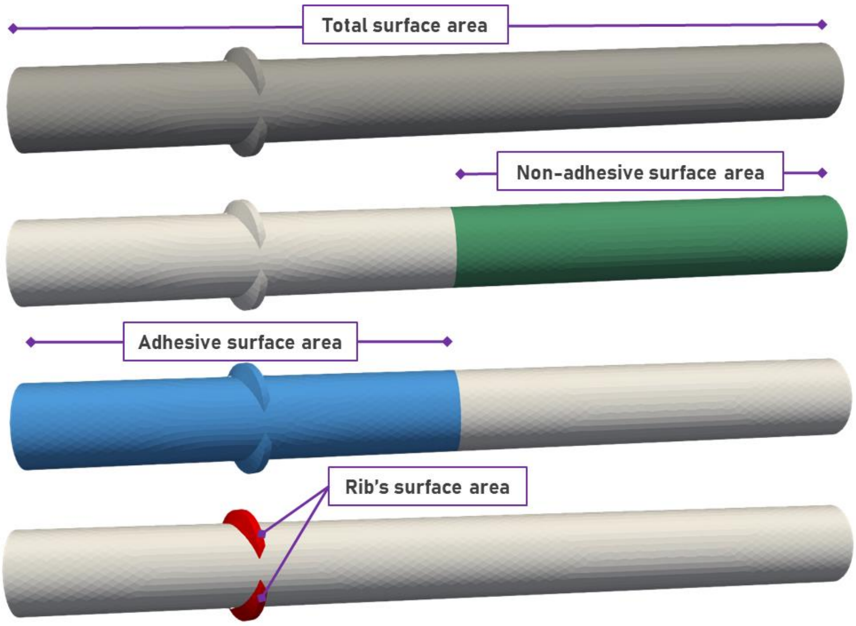

Figure 5.13 Total surface area (in grey), non-adhesive surface area (in green), adhesive surface area (in blue) and rib's surface area (in red) for a one-rib steel bar

All the ribs are spiral ribs having an isosceles trapezoidal section as shown in Figure 5.14. The larger width is the bottom part of the rib embedded in the cylindrical part, while the smaller width is the farthest point from the cylindrical surface, and the height of the rib defines the perpendicular distance between the larger and the smaller widths. The angle of the rib is the one in between the larger width and the sides of the trapezoid.

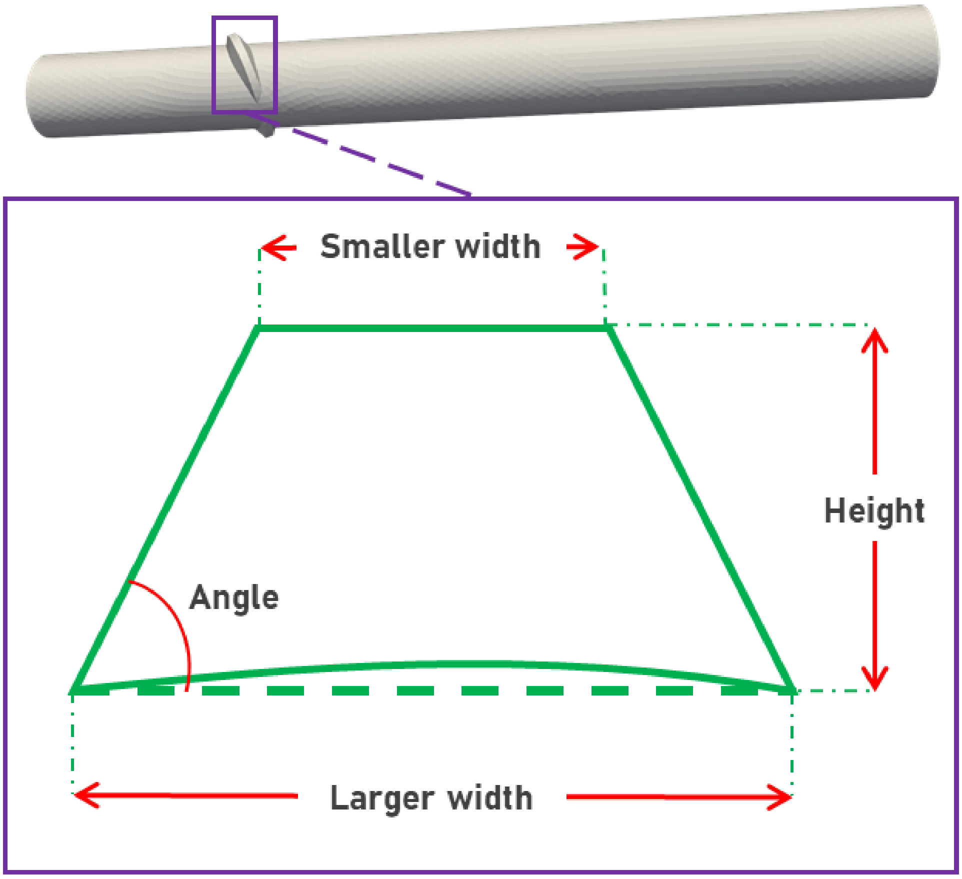

Figure 5.14 Geometrical parameters of the isosceles trapezoidal ribs of the steel bar

These nine samples are divided into three groups. In the reference sample, the smaller width, the larger width, the height and the angle of the rib are 0.8 mm, 1.6 mm, 0.8 mm and 63.4°, respectively. The detailed dimensions of the different ribs of the samples within the three groups are shown in Figure 5.15.

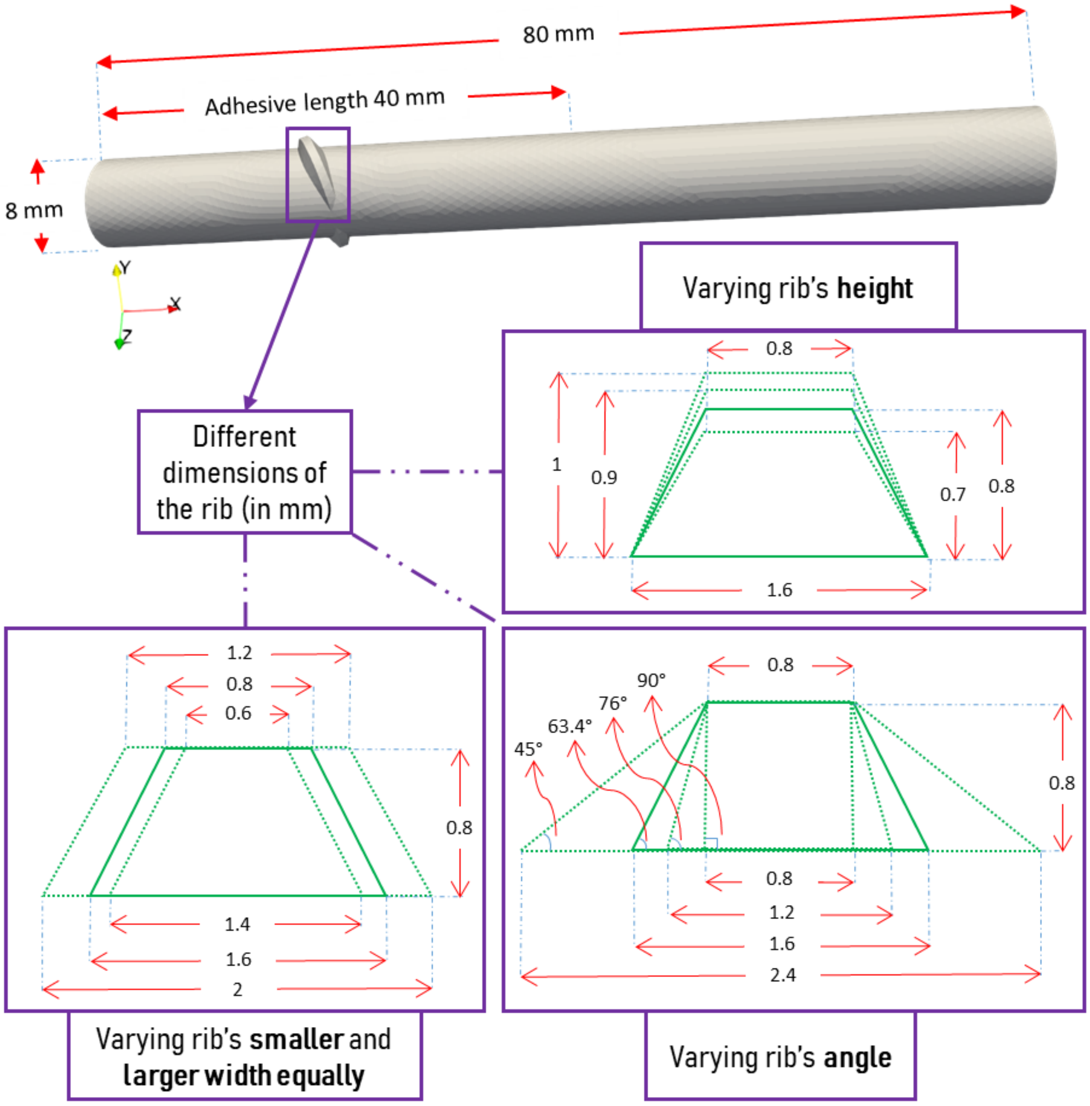

Figure 5.15 Detailed dimensions of the different one-rib steel bars modelled

Each of the three divided groups, shown in Figure *5.15*, has a certain intended variation pattern of at least one of the four aforementioned dimensions of the rib. The patterns can be described as follows:

a) Varying rib's height: It is made up of four samples, including the reference sample. In these four samples, the smaller and the larger width of the rib are fixed to 0.8 mm and 1.6 mm, respectively, while the rib's height differs in each sample: 0.7 mm, 0.8 mm, 0.9 mm and 1mm. As a result, the rib's angle changes slightly from one case to another.

b) Varying rib's smaller and larger width equally: It is made up of three samples, including the reference sample. In these three samples, the height and angle of the rib are fixed to 0.8 mm and 63.4°, respectively, while the rib's smaller and larger width are varied equally from one sample to another, in a way that the difference between these two is fixed to 0.8 mm. The smaller widths are 0.6 mm, 0.8 mm and 1.2 mm, while in the same order for the three samples, the larger widths are 1.4 mm, 1.6 mm and 2 mm.

c) Varying rib's angle: It is made up of four samples, including the reference sample. In these four samples, the smaller and the height of the rib are both fixed to 0.8 mm, while the rib's angle differs in each sample: 45°, 63.4°, 76° and 90°. As a result, the larger width changes too: 2.4 mm, 1.6 mm, 1.2 mm and 0.8 mm.

Finally, an unstructured mesh is generated using linear tetrahedral meshing elements as detailed in subsection 3.2.5. The characteristic size of each mesh element at the outer surface of the concrete sample is equal to about 7 mm, while the triangular edge of each element at the steel concrete interface is almost 0.6 mm.

5.3.2.2 Discussion on the results

Several pull-out simulations are performed on the generated homogenous concrete one-rib samples. Steel is assigned the perfect yield model as described in subsection 3.4.4 and concrete the Mazars model using the parameters described in Table 4.4. The interface is assigned the FCZM described in section 4.2, using the values for the parameters shown in Table 4.4.

The mean bond stress versus the free end displacement for the nine simulations are plotted in Figure 5.16, by showing each group on one graph. In here, the mean bond stress is calculated by dividing the pulling force by the exact adhesive surface area, which is calculated using the CAD code Salome.

One can see in Figure *5.16*(a) that the mean bond stress at FED = 2 mm is higher when the rib's height increases. For instance, Figure *5.17*(a) shows that the mean bond stress increases, almost linearly in this case, with the increase of the height of the rib. Similarly, increasing the smaller and larger width equally has increased the mean bond stress according to Figure *5.16*(b). However, Figure *5.16*(c) shows that higher angles have given lower mean bond stresses, which can be seen in Figure *5.17*(b), when plotting the mean bond stress at FED = 2 mm, with respect to the rib's angle. Apparently, the decrease is not linear, as the mean bond stress from the two cases 76° and 90° is almost the same.

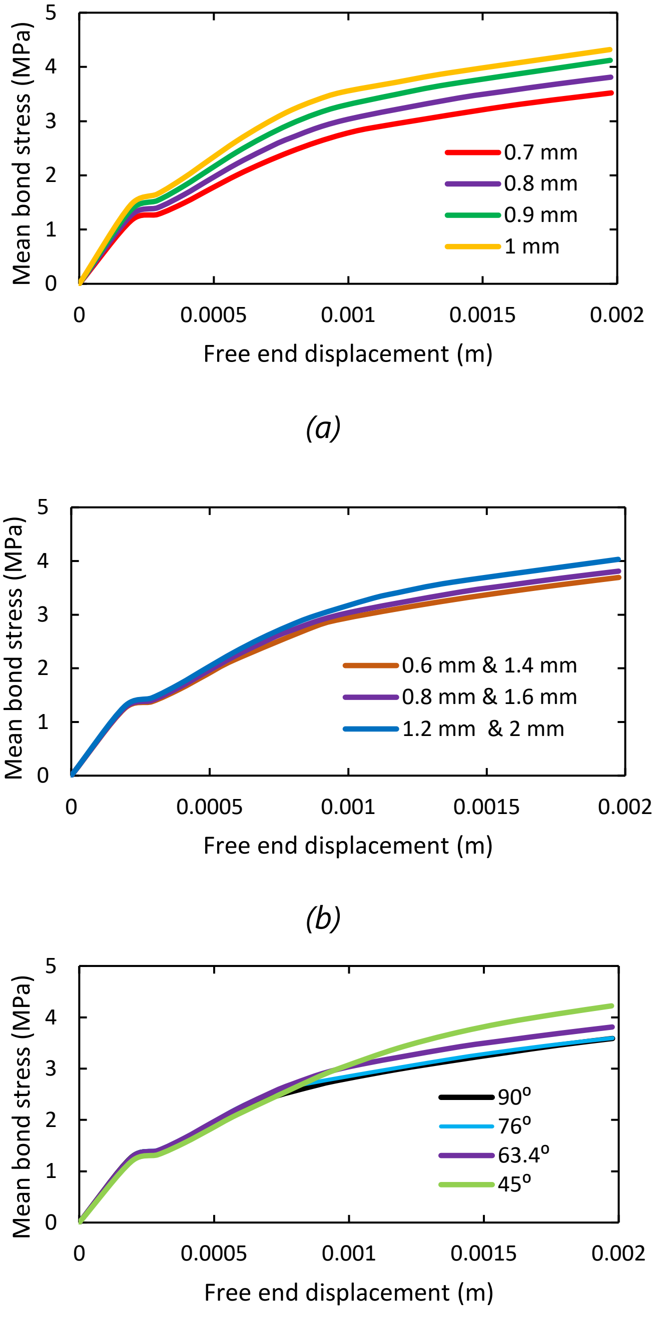

Figure 5.16 Mean bond stress versus free end displacement for the pull-out tests performed on the samples with one-rib steel bar having: (a) different rib's height; (b) different smaller and larger width; (c) different rib's angle

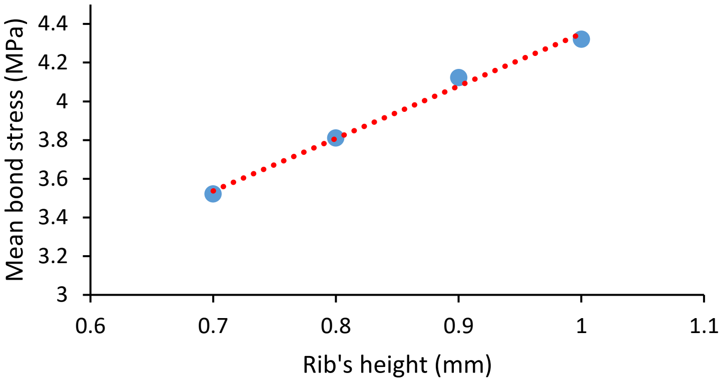

(a)

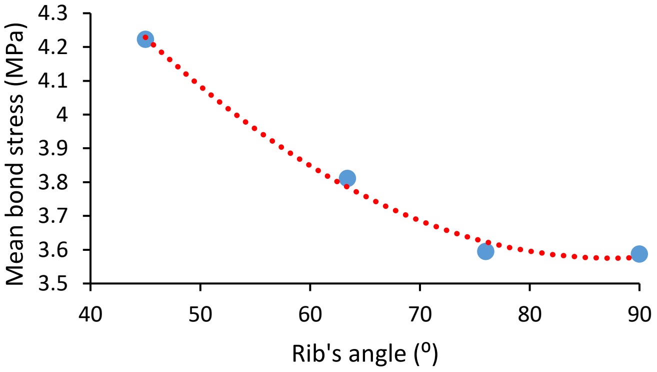

(b)

Figure 5.17 Mean bond stress, at FED = 2 mm, versus: (a) rib's height for the first group, whose pattern is varying rib's height; (b) rib's angle for the third group, whose pattern is varying rib's angle

In order to explain the reasons behind these results, it is essential to compare the behavior with respect to the rib's surface area, and the adhesive surface area of the steel bar for each case. The rib's surface area represents the area of non-cylindrical surfaces of the adhesive part of the steel bar. The adhesive surface area and the rib's surface for all the samples are listed in Table 5.5.

Using the data from Figure 5.16 and Table 5.5, the mean bond stresses when the free end displacement is 2 mm, versus the rib's surface area for the three groups of simulations are plotted in Figure 5.18.

Table 5.5 Adhesive surface area and ribs surface area for the one-rib steel bars

Sample		Adhesive SA (in mm²)	Rib's SA (in mm²)	Adhesive SA -Rib's SA (in mm²)
Reference		1033.161	61.544	971.617
Reference but rib's height is:	0.7 mm	1028.901	56.735	972.166
	0.9 mm	1037.763	66.648	971.115
	1 mm	1042.674	71.959	970.715
Reference but rib's smaller and larger width are, respectively:	0.6 mm & 1.4 mm	1032.291	56.478	975.813
	1.2 mm & 2 mm	1035.084	71.687	963.397
Reference but rib's angle is:	45°	1028.719	78.249	950.47
	76°	1037.851	57.056	980.795
	90°	1044.678	55.226	989.452

One can see that in all the three cases, the mean bond stress increases with the increase of the rib's surface area. This coincides with the property stated in the state-of-the-art in subsection 2.2.2.3, concerning the increase of the mechanical effect of the ribs on the bond stress, when the relative rib area of steel bar increases.

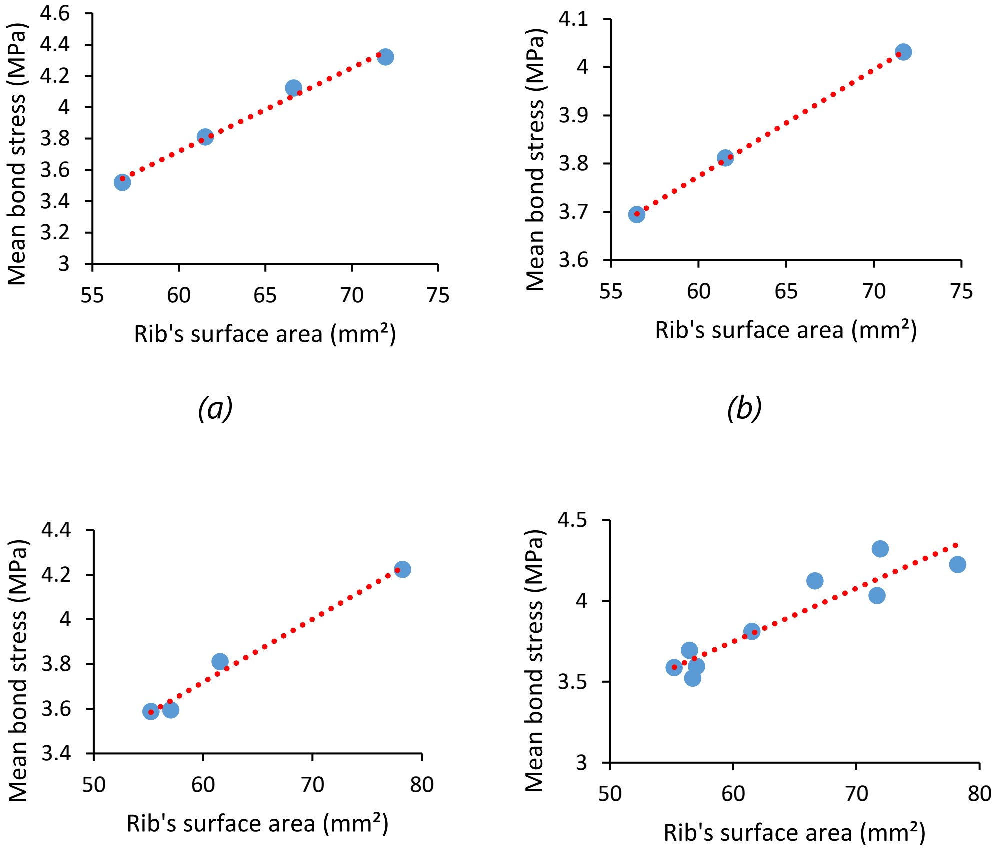

(a) *(b)*

(c) *(d)*

Figure 5.18 Mean bond stress, at FED = 2 mm, versus rib's surface area for the groups of samples having the following pattern: (a) varying rib's height; (b) varying rib's smaller and larger width equally; (c) varying rib's angle (d) all three groups together

For each group, the following discussions and conclusion can be made:

a) Varying rib's height: When increasing the height of the rib, the rib's surface area increases and so does the adhesive surface area. Still, the increase in the adhesive surface area is mainly related to the increase in rib surface area. The increase in the bond stress is directly related to the increase of embedment of the rib in the concrete. This certainly augments the interaction of the concrete with the rib, thus resisting more the pulling force at the inclined sides of the rib.

b) Varying rib's smaller and larger width equally: In this case, the rib's surface area increases importantly, mainly at the tips of the rib, while the adhesive surface area slightly increases. The mean bond stresses increase, but not as much as they did when increasing the height of the rib. This is because by increasing the height of the ribs, the surface areas of the inclined sides of the ribs increases, while increasing the widths equally increases the tips of the ribs, and keeps the sides almost the same. The tips of the ribs are parallel to the direction of pulling, which mean shearing mainly dominates and gives less effect to the normal stresses, while those normal stresses are much more effective at the inclined surfaces, along with the shear forces. These points were discussed using linear simulations in section 3.3.

c) Varying rib's angle: in this case, one can see that adhesive surface area increases with the increase of the angle. On the contrary, the rib's surface area decreases. This explains the decrease in the mean bond stress with the increase of the angle. Although a rib with 90° angle is expected to block more forces normally, the surface area of the rib itself decreases. This case shows that it is more important to increase the surface area of the rib, than to increase that of the cylindrical part through the adhesive surface area.

For instance, the increase of the surface area of the rib and the increase of the adhesive surface area are not directly related. This can be seen in Figure *5.19*, where the adhesive surface area for all the bars are plotted as a function of the rib surface area. The Pearson correlation coefficient, which is a measure of linear correlation between these two sets, calculated as the ratio between their covariance and the product of their standard deviations, is almost -0.15, close to 0, which means there is no direct relation between the surface area of the rib and the adhesive surface area of the bar. This is expected, as one can make different adhesive surface areas by using different dimensions of the ribs, thus choosing to increase or decrease the rib's surface area within the adhesive surface area.

As a conclusion, one can say that the model has shown that the increase of the rib surface area is the main parameter that affects the bond stress, and not the total adhesive surface area. Thus, an increase in the rib surface area increases the bond stress, which is in accordance with the conclusion previously reached in (Cairns and Jones, 1995; Darwin and Graham, 1993; Metelli and Plizzari, 2014; Tastani and Pantazopoulou, 2010; Zuo and Darwin, 2000), as discussed in subsection 2.2.2.3. This shows the importance of modelling the ribs at the mesoscopic scale, as a slight change in the dimensions leads to a change in the bond behavior. Note that those conclusions are likely to be valid for similar shapes and configurations of ribs.

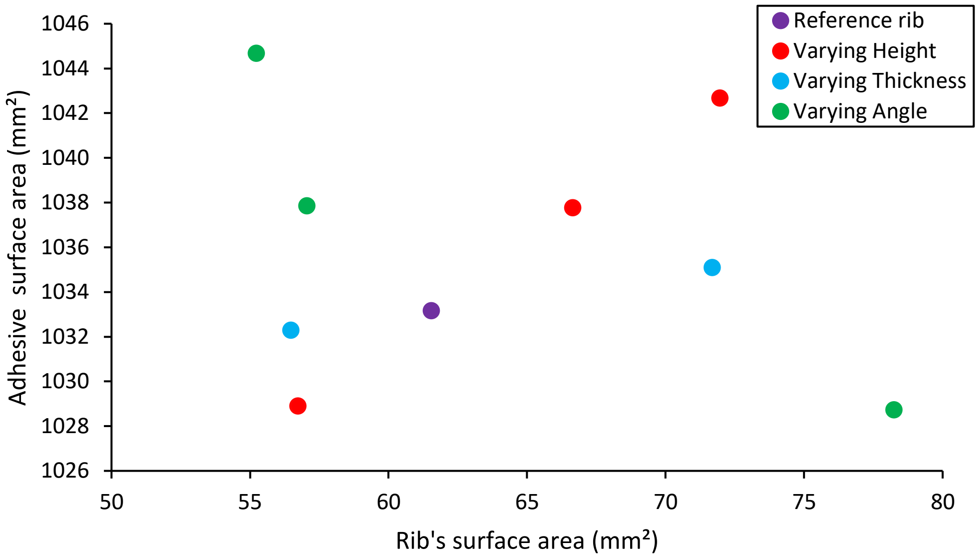

Figure 5.19 Distribution of the adhesive surface area of the bar with respect to the rib's surface area

5.3.3 Pull-out test simulation using rectangular ribbed bar

5.3.3.1 Generated sample

In order to check the effect of increasing the rib's height of a steel bar with multiple ribs in a practical situation, two simulations are performed using two samples each with a rectangular-ribbed bar, and the corresponding results are compared to experimental results extracted from (Tastani and Pantazopoulou, 2010).

Two rectangular ribbed bars, h1.1 and h0.5, are generated using the procedure described in section 3.2. The dimensions of these modelled steel bars and concrete samples are similar to the ones tested in (Tastani and Pantazopoulou, 2010). The difference between two bars is in their rib's height: it is 1.1 mm for h1.1 and 0.5 mm for h0.5. The side length of both concrete cubic samples is 60 mm, and the adhesive length of the ribbed bars is also 60 mm. The detailed dimensions of the two rectangular ribbed bars used are shown in Figure 5.20.

Eventually, an unstructured mesh is applied using linear tetrahedral meshing elements as detailed in subsection 3.2.5. The characteristic size of each mesh element at the outer surface of the concrete sample is equal to 5 mm, while the triangular edge of each element at the steel concrete surface of contact is almost 0.6 mm. As a result, the number of mesh elements for h1.1 bar in the steel bar is 39 000 and in concrete is 145 000, while for h0.5 bar it is 39 000 in the steel bar and 149 000 in concrete.

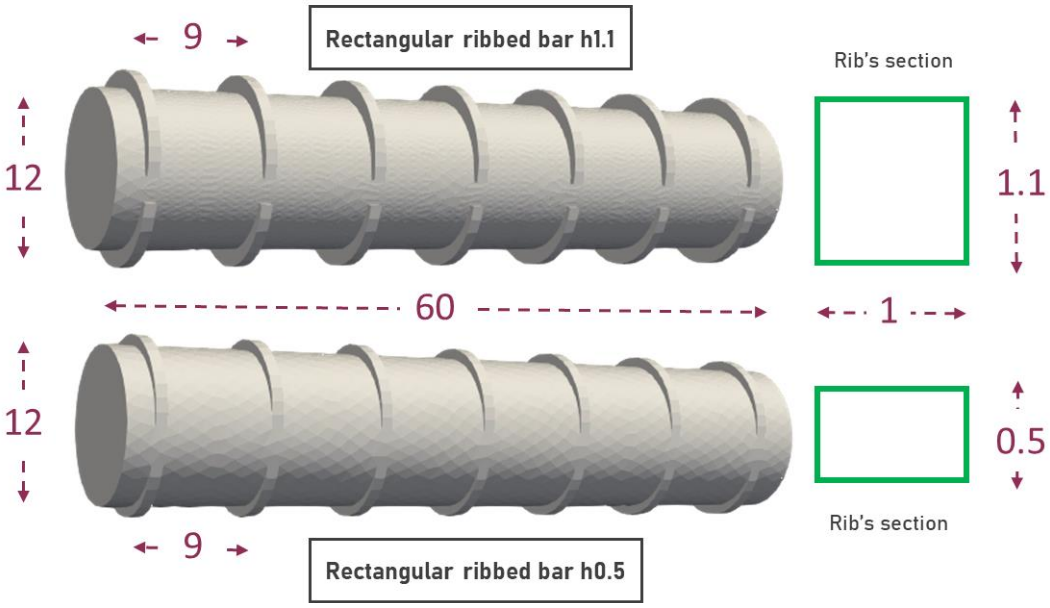

Figure 5.20 Dimensions of the two modelled rectangular ribbed steel bars h0.5 and h1.1 (in mm)

5.3.3.2 Simulations and results

In this simulation, steel is as before assigned the perfect yield model as described in subsection 3.4.4, while concrete is assigned Mazars model with all the modifications described in section 3.4.3. In addition, based on the experimental data, concrete's ultimate tensile stress $f_{t\,con}$ is 2 MPa, and concrete's compressive stress is 27 MPa. The corresponding fracture energy is taken 120 N/m. For the compressive damage parameters A_c and B_c, the same methodology described in subsection 3.4.3 is applied. For the FCZM, the values assigned are based on the calibration process mentioned in subsection 4.3.1.2, and summerized in Table 4.6. As result, $K_s = 4.91 \times 10^{11}$ N/m^3, f_t = 1.4 MPa, G_f = 86 N/m, $\lambda_0 = 5 \times 10^{-5}$m and μ=0.3. The mean bond stress versus bar's slip for the rectangular ribbed samples and the corresponding experimental results are plotted in Figure 5.21.

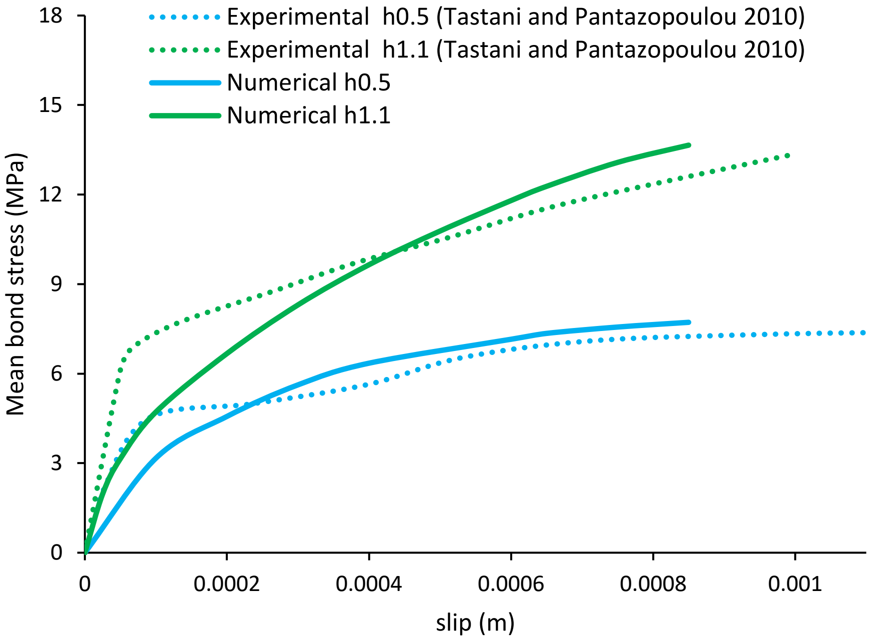

Figure 5.21 Mean bond stress versus bar's slip for the rectangular ribbed pull-out simulations compared to the experimental results extracted from (Tastani and Pantazopoulou, 2010)

One can see that h1.1 bar produced much stiffer response compared to h0.5. This is in accordance with experimental results shown, although the initial part of the curve in the numerical case is slightly different form the experimental case, but still acceptable. Experimentally, the initial peak is reached instantly, after which the curve shows many slight decrease and increase, so that only the general pattern is reproduced here. Note that the concrete cover is two times less than what is recommended in subsection 2.2.2.1, which may lead to splitting failure.

The results indicate that the increase of the bond stress is directly related to the increase in the height of the ribs. For instance, when the rib height has increased by 120%, the bond stress experimentally increased by almost 90%. This proves the great importance of the geometry of the ribs, and their effect on the bond behavior.

Finally, we conclude that the FCZM was able to reproduce the macroscopic bond behavior by changing the dimensions of the ribs in a practical situation. More complicated shapes may lead to much more complicated behavior, like when using a herringbone and spiral bar, which is dealt with numerically in the next section.

5.3.4 Pull-out test simulation using herringbone ribbed bar

5.3.4.1 Generated sample

In order to understand the effect of changing the shapes of the ribs on a steel bar with multiple ribs in a practical situation, a simulation is performed using a sample with a herringbone ribbed bar, which is described in subsection 3.2.2. In order to compare the results to a spiral pull-out simulation, the results of the pull-out test performed and detailed in subsections 4.3.3.2 and 4.4.2 are considered as well.

For a scientific comparison, the geometrical properties of the spiral sample are maintained, and a herringbone sample is generated using the procedure described in section 3.2. Thus, the side length of this concrete cubic sample is 80 mm. Like the spiral bar, the adhesive length of the herringbone bar is 40 mm, and its total length is 80 mm. The detailed dimensions of the herringbone bar used are shown in Figure 5.22. The adhesive surface area of the herringbone bar is 1265.184 mm² and is then almost equal to that of the spiral bar 1262.334 mm², using the dimensions chosen. Still, the ribs' surface areas are different, which are 634.933 mm² and 645.987 mm² for the spiral and herringbone bars, respectively.

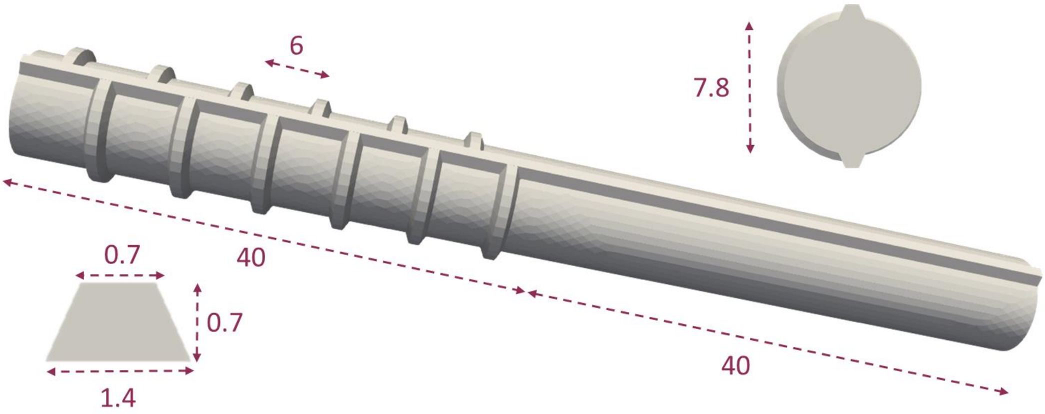

Figure 5.22 Dimensions of the modelled herringbone steel bar (in mm)

Eventually, an unstructured mesh is applied using linear tetrahedral meshing elements as detailed in subsection 3.2.5. The characteristic size of each mesh element at the outer surface of the concrete sample is equal to 5 mm, while the triangular edge of each element at the steel concrete surface of contact is almost 0.4 mm. As a result, the number of mesh elements for the herringbone sample in the steel bar is 307 000, while the number of mesh elements in the concrete is 277 000.

5.3.4.2 Discussion on the results

Since the comparison is done with spiral simulation performed in subsection 4.3.2.2, steel, concrete and the steel-concrete interface of the generated herringbone sample are assigned the same models used for the aforementioned spiral simulation.

The mean bond stress versus the free end displacement for the spiral and the herringbone simulations are plotted in Figure 5.23.

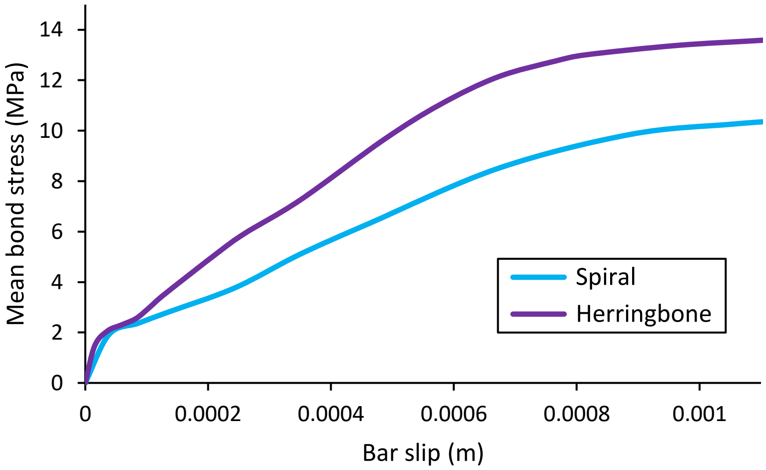

Figure 5.23 Mean bond stress versus bar’s displacement for the herringbone and spiral pull-out simulations

One can see that the herringbone sample shows a stiffer response compared to the spiral sample. Although both samples have the same models for the different materials, the same values for the parameters, and even almost the same adhesive surface area between steel and concrete, the bond behavior is different. This can be explained by comparing the total ribs’ surface area, containing both transversal and longitudinal ribs, listed in Table 5.6, and the shapes of the ribs of the two steel bars.

Based on the conclusions made in subsection 5.3.2.2, one expects the bar with higher ribs’ surface area to produce a higher mean bond stress, which is the case in here, see Table 5.6. Still, the difference between the two surface areas is very small, about 1.7%, compared to the difference in mean bond stress, which is about 33.8%.

Table 5.6 Adhesive surface area, ribs' surface area and mean bond stress when bar's slip is 1 mm, for the spiral and herringbone bars

Bar type	Spiral	Herringbone
Adhesive surface area (mm^2)	1262.334	1265.184
Ribs' surface area (mm^2)	634.933	645.987
Ribs' SA/Spiral bar rib's SA	100%	101.7%
Mean bond stress (MPa) at 1 mm	10.12	13.54
Bond stress/Spiral bar bond stress, both at 1 mm	100%	133.8%

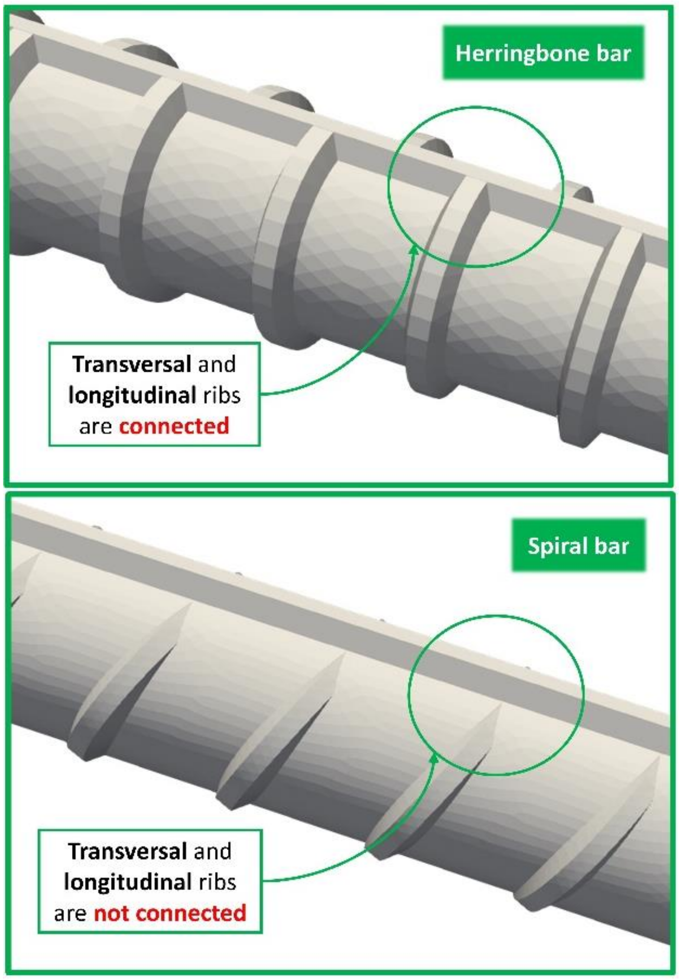

Figure 5.24 A closer view of the herringbone and the spiral steel bars

This can be justified by the geometry of the herringbone bar when compared to the spiral bar: by getting a closer look to Figure 5.24, one can see that the herringbone bar does not only differ from the spiral bar in the shapes and the orientation of the transversal ribs, but also in the connection between the longitudinal and transversal ribs. Indeed, the longitudinal ribs and transversal ribs are connected in the herringbone bar. This is not the case in the spiral bar, where the two ends of the transversal ribs lay on the cylindrical surface itself, before reaching the longitudinal rib. Thus, the surface area of the longitudinal ribs in the spiral bar is higher when compared to that of the herringbone. Hence, although the two ribs' surface areas are close, their nature is different. More inclined surfaces of the transversal ribs are included in the herringbone rib's surface area, while less areas from the longitudinal ribs are included. The longitudinal ribs are parallel to the direction of pulling and to the axis of the bar, thus are much less effective in blocking the movement compared to the transversal ribs, as mainly shear behavior dominates at their surfaces. As expected, one can conclude that not only the ribs' surface area of the bar is important, but its nature has a crucial role on the steel-concrete bond behavior. It also shows that the model is capable to account for this aspect and to predict accordingly the difference of behavior.

By trying to quantify these differences for the spiral and the herringbone ribs, two parameters are considered: the surface area of one side of the rib and the normal projected surface area, which are shown in 2D in Figure *5.25*.

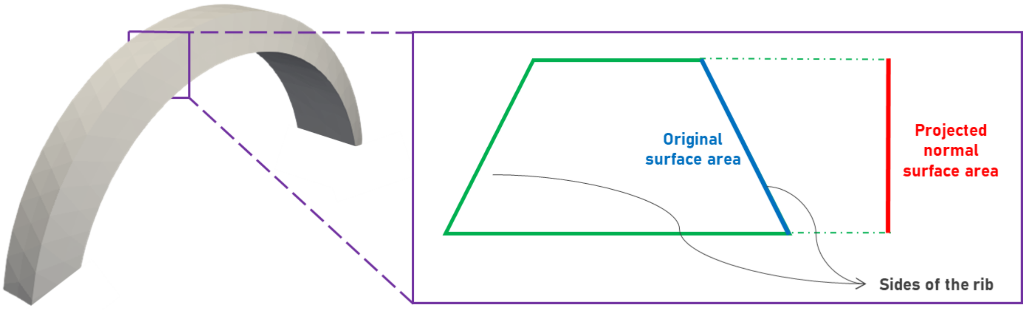

Figure 5.25 Original surface area (in blue) and normal projected surface area (in red) of one side of a steel bar rib in 2D

The surface area of one side of the rib for the part shown in Figure *5.25* is 10.869 mm² for the spiral rib and 11.284 mm² for the herringbone rib. Thus, the original surface area for the herringbone rib's side is only 4 % larger than that of the spiral rib. However, when projecting the side of the rib on the plane perpendicular to the axis of the bar, the normal projected area for the spiral rib is 8.0448 mm^2 while it is 10.0924 mm^2 for the herringbone rib. Hence, the normal projected area for the herringbone rib is 25.45% more than that of the spiral rib. This value is significanlty different, and it can explain the important increase in the bond stress.

Still, one cannot say that the projected area is sufficient to predict the increase in the bond strength. For instance, very recently (Higuchi et al., 2022) performed experimental tests on steel plates having uncommon ribs, i.e. triangular and semicircular ribs. The height of the triangular isosceles ribs considered was the same as the radius of the semicircular ribs and the thickness of the triangular ribs is equivalent to the diameter of the circle as shown in Figure *5.26*. Thus, the nodes of triangular rib are fully included on the circumference of the semicircular rib, and the triangular rib itself can fit within the semicircular rib. Hence, the normal projected area of these two ribs is exactly the same. Still, the average bond stress for the circular rib was slightly higher. The difference here is related to the original surface area of the sides of each rib. The circular rib has a bigger surface area before projection, compared to the triangular rib. Hence, it is essential to compare both the original surface area and the normal projected surface area of the side of the rib. Nonetheless, the normal projected surface area appears more important, as the case when both sides have the same original surface area is rare.

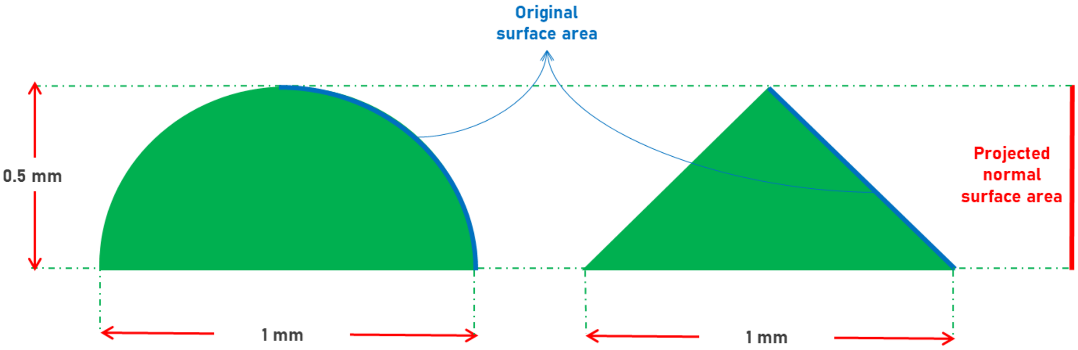

Figure 5.26 Original surface area (in blue) and projected surface area (in red) in 2D for a semicircular rib and a triangular rib used in (Higuchi et al., 2022)

In addition, one could say that the orientation of the spiral rib in between the two longitudinal ribs may have an effect also on the behavior. Indeed, although the rib surface area is a good parameter to predict the bond increase, it considers the effect of all the rib surfaces the same. Still, surface where normal effect dominates are much more important, as seen here. They can give a better prediction of the bond increase, and they neglect the effect of the parts of the ribs that are parallel to the cylindrical part of the bar, like the tips of the ribs.

Thus, one important parameter to check is the projected normal surface area of the side of the rib. This parameter when compared to a reference rib can give a correct prediction of the bond strength variation, especially when the two ribs have very similar geometry. To elucidate more deeply its influence, experimental pull-out tests should be performed using common shapes of the ribs of the steel bar, like the spiral shape, by varying the dimensions of the ribs like in subsection 5.3.2, on more than one sample. These detailed experimental results can be used to calibrate more accurately the projected normal area parameter by taking into account the effect of the orientation of the rib itself, and the different original surface areas of the side of the rib, as it is important in some cases as observed in (Higuchi et al., 2022). Still, with the lack of such experimental results, the projected normal surface area of the side of the rib can be used directly and can give a good prediction.

In order to compare the distributions of damage in the samples, the same volume previously extracted in Figure *5.9* is considered, and the distribution of full damage are shown in Figure *5.27*. One can see that the full damage is similar to a certain point, except that the damage in last rib is slightly more extended, and more inclined.

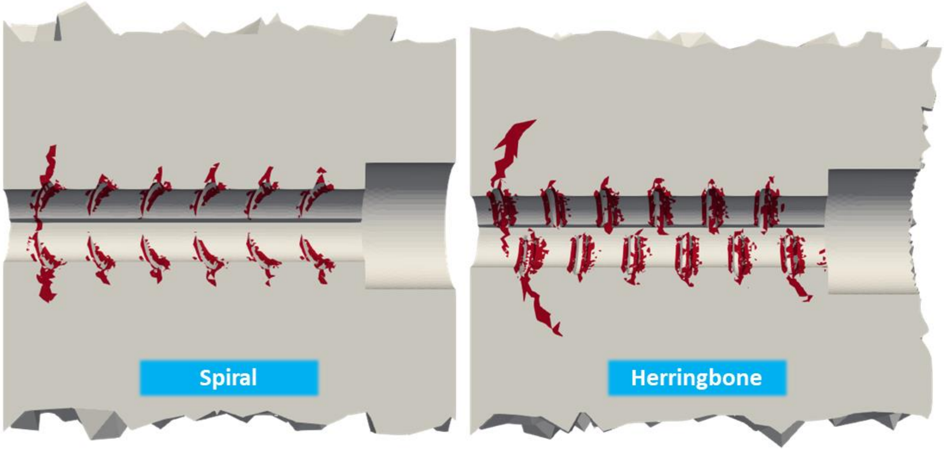

Figure 5.27 Pull-out test simulations on the spiral and herringbone samples, at ID=1 mm, showing the full damage ($D \geq 0.99$) in concrete at the central

plane normal to the z-axis of the extracted section

As a conclusion, the herringbone bar gives a stiffer bond response compared to the spiral bar. The shape of the ribs has an important effect on the bond behavior in pull-out test, in which the bond stress increases with the increase of ribs' surface area. Nonetheless, the nature of the rib surface area has also a very important effect on the bond stress. Thus, the increase of the ribs' surface area is not enough to predict the increase in the bond strength, and it is essential to check and characterize the nature of the ribs' surface area. The projected normal surface of the side of the transversal rib is an important parameter that can be used to predict the bond strength variation. A function can be introduced in macroscopic models to take into account this variation, where a simulation is performed on a certain rib case and this value will be one for this reference case, then by choosing another bar having different dimensions of its rib, the coefficient will be equivalent to the normal projected surface area of the new bar divided by that of the reference case. Finally, this study highlights the importance of the mechanical interlock on the bond behavior, as stated previously by (Lin et al., 2019). It has also shown the ability of FCZM to reproduce this behavior using different shapes of ribs.

5.4 EFFECT OF EXTERNAL CONFINEMENT

In this section, the effect of applying an active confinement on pullout samples is investigated, in order to check the ability of the FCZM to reproduce the macroscopic bond behavior in this case.

5.4.1 General description and considered sample

In order to understand the effect of applying an external confinement on the macroscopic bond behavior, simulations are performed using a sample with a spiral ribbed bar. The simulation is performed on the same spiral sample described in subsection 4.3.2, and the results of the corresponding pull-out test performed and detailed in subsections 4.3.2.2 and 4.4.2 are considered, along with pull-out test experimental results extracted from (La Borderie and Pijaudier-Cabot, 1992).

In order to apply an external confinement on the sample, the initial boundary conditions are modified as shown in Figure 5.28. In this set up, 5 MPa normal compressing stress is imposed on the four concrete surfaces parallel to the x direction.

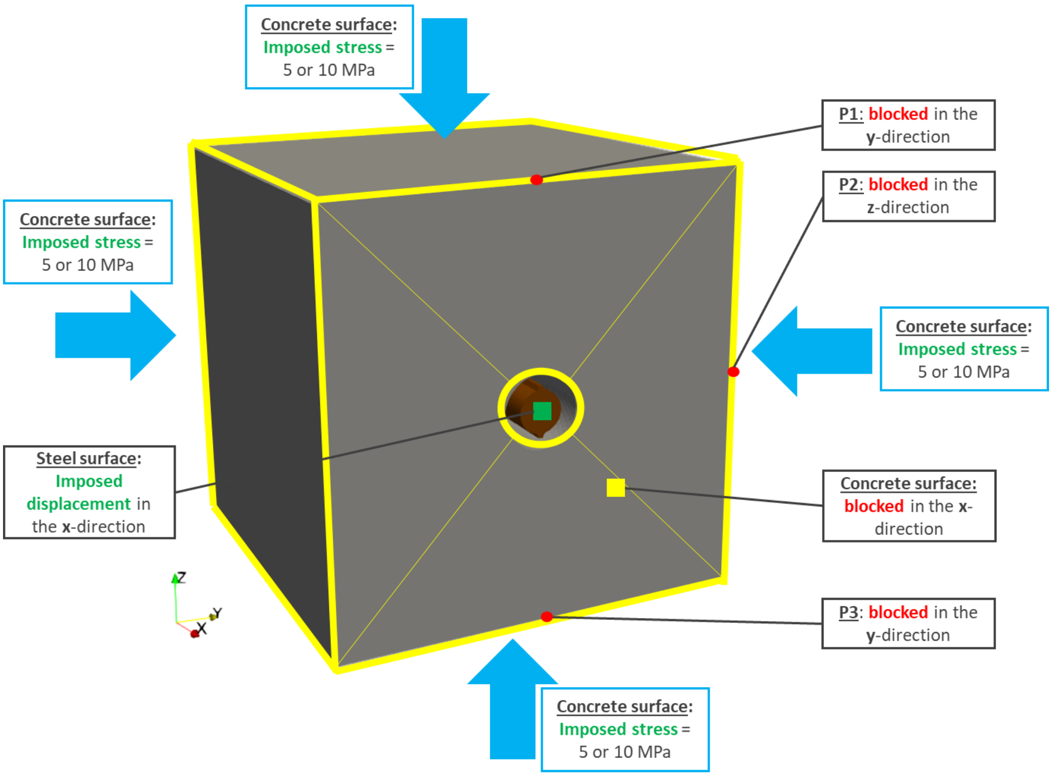

Figure 5.28 Boundary condition of the pull-out test simulation under external confinement

5.4.2 Discussion on the pull-out results

Steel, concrete and the steel-concrete interface of the spiral sample are assigned the same models used in the simulation performed and discussed in subsections 4.3.2.2 and 4.4.2.

The mean bond stress versus the free end displacement for the spiral simulations with and without external confinement, along with the experimental results, are shown in Figure 5.29.

One can see that the sample under confinement experiences a stiffer response. This is in accordance with what is observed experimentally. Such behavior is expected as the external confinement of concrete plays an additional role in making it more difficult for the cracks to propagate, and adds an additional compressive stress at the steel-concrete interface. Nevertheless, the response is weaker when compared to experimental results. It is important to note that even experimentally it is difficult to observe the confinement effect when the concrete cover is large. This is the reason why (Malvar, 1992) used thin concrete layer, since the effect will be more important and possible to capture. Still, this may lead to splitting failure. Under confinement, concrete gains additional resistance, and cracks are affected by supplementary compressive stresses that limit their formation and propagation. Thus, the concrete behavior at the mesoscale is important in this case. For instance, (Tastani and Pantazopoulou, 2010) proposed to calibrate the model when under confinement by changing the properties of concrete and the properties of the interface, in order to introduce the confinement effects and reproduce correctly the behavior. This can be done by modifying concrete compressive stress and interface friction.

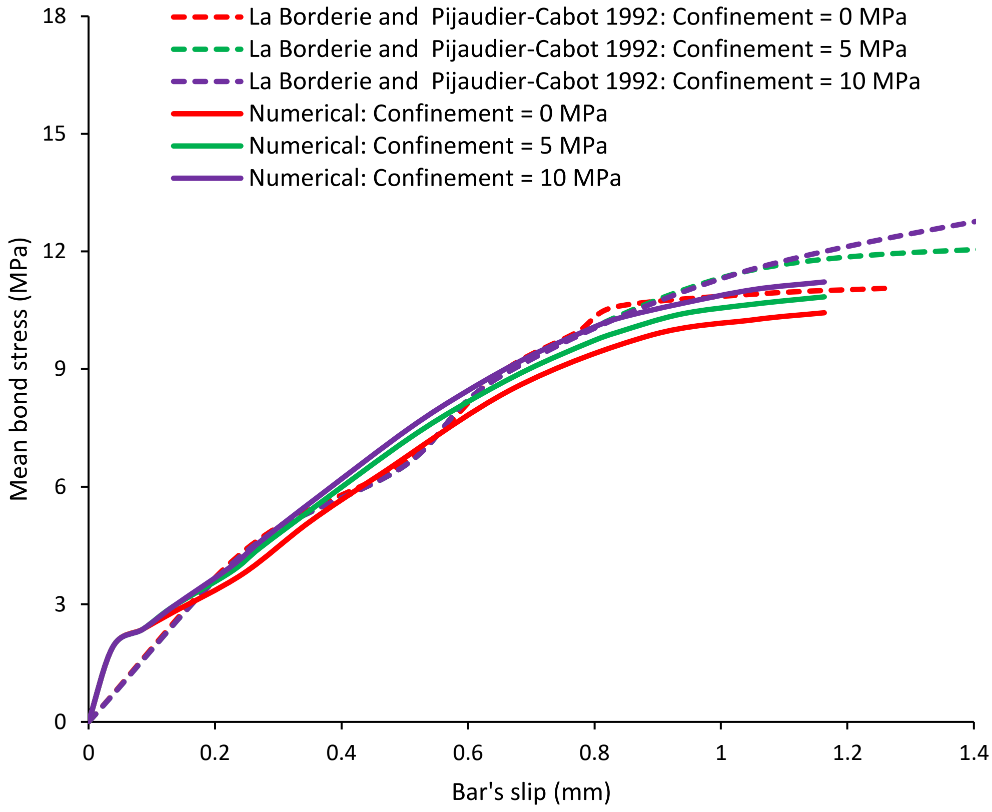

Figure 5.29 Mean bond stress versus free end displacement of the pull-out test performed on the spiral sample under 0 MPa, 5 MPa or 10 MPa external confinement, compared to the experimental results extracted from (La Borderie and Pijaudier-Cabot, 1992)

As a conclusion, the sample under confinement gives a stiffer response compared to the unconfined sample in pull-out simulations; this is in accordance with what was mentioned in subsection 2.2.2.3 concerning the influence of active confinement, as observed in (La Borderie and Pijaudier-

Cabot, 1992; Malvar, 1992). Thus, the model is able to reproduce to some extent confinement effects, although less obviously when using thick concrete covers, since confinements effects depends directly on the concrete cover as stated in subsection 2.2.2.3.

5.5 CONCLUSIONS

In this chapter, several numerical applications were discussed, using the FCZM for the steel-concrete interface, presented in chapter 4.

In the first part, concrete was divided into two-phase material, made up of coarse aggregates and surrounding mortar. The material and damage parameters of mortar were determined using a procedure that aims to get the same uniaxial tensile and compressive behaviors for the homogenous and heterogeneous concrete. Pull-out test simulations were performed on three heterogeneous samples, who differ in the placement and generation procedure of aggregates. It was eventually proved that it is possible to reproduce the macroscopic behavior using heterogeneous concrete. In addition, for each heterogeneous case, the global damage is not the same, which shows the importance of the placement and distribution of aggregates in the mortar block, and its effect on the global damage in the whole sample. Still, the computational cost is much higher than the simulations with homogenous concrete, but the bond stress difference is not that big. Thus, taking a homogenous concrete proves to be more efficient.

In the second part, the mechanical interlock between steel and concrete was studied numerically. One rib-bar was used first to study the effect of changing the dimensions of one rib. It was shown that for given rib shape and configuration (i.e. spiral), the increase of the rib surface area is the main parameter that affects the bond stress, and not the total adhesive surface area, which is in accordance with the conclusion previously reached in (Cairns and Jones, 1995; Darwin and Graham, 1993; Metelli and Plizzari, 2014; Tastani and Pantazopoulou, 2010; Zuo and Darwin, 2000), as discussed in subsection 2.2.2.3. After then, two simulations were performed on ribbed samples having rectangular ribs with two heights, and were compared to experimental results. The result had shown the ability of the FCZM to simulate the behavior due to the effect of different ribs. It has also strengthen the aforementioned conclusions about the one-rib bar. Following, a sample with herringbone bar was used, to replace the spiral bar previously used in the samples in subsections 4.3.2, 4.3.3.2 and 0. It has shown a stiffer bond response compared to the spiral bar. Since both bars have very similar ribs' surface area, this shows that the nature of the rib surface area has a very important effect on the bond stress, not only its value. This proves the importance of the mechanical interlock on the bond behavior, as stated previously by (Lin et al., 2019), especially at the mesoscopic scale. Thus, it is important to model the ribs at the mesoscopic scale, since a small change in the dimensions may influence significantly the bond behavior, depending on the shape nature of the each rib. In addition, the normal projected area of the side of the transversal rib is the most important parameter that can be used to predict the variation of the bond strength. This simple parameter can be introduced to macroscopic models, as this aspect is not captured in macroscopic models, which to a certain point neglect the detailed geometry of the bar.

In the last part, an external confinement was applied on the spiral sample. Numerical results were compared to experimental ones, and they have shown a stiffer response when compared to the unconfined sample in pull-out simulations. This is in accordance with what was mentioned in subsection 2.2.2.3, concerning the influence of active confinement on the bond stress, as observed in (La Borderie and Pijaudier-Cabot, 1992; Malvar, 1992). Still, the behavior was less stiff when compared to experimental results. This can be related to the concrete model, which plays the main role in transporting the confining stresses inside the sample before reaching the interface. In addition, smaller concrete covers are expected to give a stiffer response, as the active confinement is directly related to the concrete cover as stated in subsection 2.2.2.3.

The FCZM was able to give satisfactory results when applied to different numerical cases. It has shown the high importance of modelling the exact geometry of the ribs of the steel bar, which is a crucial aspect that is not much dealt with in details in literature. This aspect has a great impact on the bond strength of the steel-concrete bond in reinforced concrete structures. One can say it is very essential to take into account the geometry of the rib by certain parameters in macroscopic models, like projected normal surface area, which gives importantly different bond stresses. This would aid these models, used at the structural scale, in reaching more accurate bond strengths for the simulated reinforced concrete structures.

Furthermore, the addition of coarse aggregates at the mesoscopic scale, which has a much higher computational cost, shows that taking a homogenous concrete is sufficient to evaluate the bond stress. Moreover, it shows different damage patterns depending on the distribution of the aggregates in the concrete mix, which shows the importance of introducing aggregates at these zones to predict the exact cracking. Still, coarse aggregates are not solely in control for the crack propagation, but more importantly fine aggregates just near the vicinity of the interface. However, introducing finer aggregates would increase the already large-size mesh greatly, making it extremely difficult to perform such studies. In addition, due to the lack of experimental data on the exact distribution of the meso-cracks just near the interface, it possesses an additional difficulty on proofing that for a given distribution of aggregates, the cracking phenomena performed numerically is very close to that produced experimentally. This can be only limited by the general description of the phenomena described in subsection 2.2.2.2, concerning the formation of one major crack at the tip of each rib with 45° inclination. The distribution of the aggregates numerically would change the evolution and patterns of these cracks at the mesoscale. It is also important to assign to mortar the correct model behavior that can reproduce the cracking phenomena once these data are available.

The next chapter shows the overall conclusions of the work, and some perspectives.

6 CONCLUSIONS AND PERSPECTIVES

6.1 CONCLUSIONS

The global objective of this thesis was to develop modeling tools at the mesoscopic scale to better understand the underlying phenomena of the steel-concrete bond, because this region is of great importance for cracking description. Simulations on pullout tests were performed at the mesoscopic scale using a certain proposed methodology mainly based on implementing a 3D frictional cohesive zone interface model. Effect of adding coarse aggregates, using different shapes of the ribs and applying external confinement were then studied.

In Chapter 1, a general introduction was done, and the objectives of the thesis were presented, followed by the adopted methodology.

In Chapter 2, a bibliographic study was done. It focused especially on the complex physical phenomena occurring at the steel-concrete interface. The pull-out test commonly used for characterizing the bond was introduced along with the different properties that affect the corresponding bond stress-bond slip law. The macroscopic and mesoscopic scales of the modeling of the bond were discussed, and the main procedures for describing both numerical concrete and steel-concrete bond in literature were presented. In particular, zero-thickness interface models were discussed; mainly the elastic spring model, frictional model, cohesive zone model and the frictional cohesive zone model. Based on this bibliographic study, and to reach the objective of the thesis, the decision was made to model 3D samples that take into account the detailed geometry of the steel ribs, which was rarely done previously in literature, and paved the way for studying the effect of the interlock mechanisms. In addition, the finite element method was chosen in order to deploy developed tools in Cast3M, Salome and MFront, which can be effectively used for different finite element applications.

In Chapter 3, the detailed procedure of generation of the numerical three dimensional pull-out test specimens was presented. It used *Combs* script, mainly for generating the aggregates in the considered matrix. In this thesis, the generation of the steel bar and the detailed geometry of its ribs were introduced to the script, giving the option to generate different shapes of steel bars. Those samples were meshed using a sufficiently fine mesh to study accurately the distribution of cracks and stresses near the steel. Linear simulations, including linear spring interface element model for the bond, were then performed on a smooth and a herringbone ribbed bar in order to study the stiffness parameters. As expected, the shear stiffness dominates at the cylindrical part and at the tips of the steel ribs, while the normal stiffness dominates at the sides of the ribs. Those basic studies cleared the way for performing non-linear simulations using non-linear models for concrete and steel-concrete interfaces.

Mazars damage model (Mazars, 1986, 1984) was used in the concrete to represent the fracture phenomena, i.e. initiation and propagation of cracks. It was supplemented by an exponential Hillerborg regularization in tension, and modifications in compression were also introduced in order to prevent a mesh dependency of the damaged response in compression. Those modifications proved to be essential to prevent the mesh dependency of the concrete model.

Classical models were considered at this stage to evaluate their validity when assigned to the steel-concrete interface. The formulations of the modified Tvergaard’s cohesive zone model, initially presented in (Tvergaard, 2003, 1990; Wu and Wriggers, 2015), and Coulomb’s frictional interface models, were introduced and their response analyzed on one-interface element. The inability of these two models to reproduce accurately the experimental results extracted from literature on pull-out test carried out on a smooth bar sample was demonstrated. This highlighted the drawbacks of these two models and encouraged the proposition of a new model that includes the advantages of both cohesive zone and frictional models, in order to reproduce the experimental behavior correctly.

In Chapter 4, a new frictional cohesive zone model (FCZM) was proposed, and its detailed formulation and implementation on one-interface element were presented. The proposed FCZM is a combination of the two aforementioned CZM and frictional model. The FCZM was able to reproduce the experimental behavior of the smooth bar after an appropriate adjustment of the parameters, overcoming the limitations of the CZM and Coulomb’s frictional interface model. Furthermore, the model was capable to reproduce the behavior of pull out test with ribbed bar samples. A certain calibration was applied to the interface model parameters, by relating most of these parameters to the surrounding concrete and steel properties, and it proved to give good results. In addition, the full damage pattern was very similar to what was observed in previous numerical simulations in literature, showing one crack at the top of each rib and an extended crack at the last rib. Moreover, the regions with fully damaged concrete are mostly under either tensile stresses in the three principal directions. On the other hand, the regions in front of the ribs were all under compressive stresses in three directions, at which very high compressive stresses were observed.

In Chapter 5, the FCZM was used in different numerical applications. It was first deployed to examine the effect of including coarse aggregates in the concrete mix, instead of homogenous concrete. Parameters of mortar were calibrated based on those of homogenous concrete previously used. Simulations were performed on three different samples, and the ability of the model to reproduce the macroscopic behavior using heterogeneous concrete was proved. Still, the global damage in the sample, used to compare the amount of damage in the mortar volume, had given different values for each heterogeneous case. This was explained by the different placements and distributions of aggregates in the mortar block. However, it showed that considering a heterogeneous sample, which has a very high computational cost, leads to small differences in mean bond stress when compared to results with homogenous samples. Hence, the conclusion reached is that taking a homogenous concrete seems sufficient to evaluate this macroscopic quantity. However, it may be insufficient if e.g. an accurate estimation of damage is needed, in order for instance to predict cover cracking.

Another important aspect studied was the effect of the geometry of the ribs on the bond behavior, since macroscopic models usually ignore this characteristic. Simulations on bars with one rib-bar were performed, by varying the dimensions of the rib. It was found that the bond strength was affected mainly by the rib surface area, and not the total adhesive surface area, which was in accordance with some conclusions previously reached in literature. Simulations performed on two ribbed bars with different rectangular sections had shown good results when compared to experiment. This proved even more the importance of the mechanical interlock on the bond behavior, as stated previously by (Lin et al., 2019). Following, herringbone bar was used and compared to the spiral bar previously used. It had shown a stiffer bond response compared to the spiral bar. Since both bars had similar surface area, the difference in the bond stress was related to the nature of the rib surface area. This is because the rib surface area usually calculated contains surface areas that are parallel to the cylindrical surface and surface areas that intersect the cylindrical surface. It is thus important to model the ribs at the mesoscopic scale, due to the sensitivity of the bond stress to the dimensions and the shape of the ribs. This additional information can be used and included as a parameter in the macroscopic models for their calibration. The normal projected area of the side of the transversal rib is here considered as the most important parameter that can be adopted by macroscopic models to predict the variation of the bond strength.

Another applications studied is the effect of the external confinement on a ribbed sample. A stiffer response was shown when compared to the unconfined sample in pull-out simulations, which coincides with the observations in literature. However, the behavior was less stiff when compared to experimental results. Thus, it would be interesting to validate this aspect of the model by comparing with samples having smaller cover thickness.

It is important to note that the numerical model has a high computational cost, and even higher when including aggregates. The difficulty of convergence is another problem related to the nonlinear behaviors considered. They may limit the application domain of the methodology, and prevent investigating more deeply some aspects.

6.2 PERSPECTIVES

Following the conclusions of this thesis, several perspectives can be proposed:

- At the mesoscale, a more accurate analysis of the distribution of damage and stresses in the concrete near the interfaces could be carried out with a different model for concrete behavior; in particular, the effects of tri-compressive states of stresses could be investigated by means of consistent and appropriate criteria. One possibility is to propose a phase field approach by taking different criterions in tension and compression. In addition, effect of creep and shrinkage of concrete on the overall behavior is to be analyzed with the influence of the loading, environmental, hydric and thermal conditions, as well as the impact of material properties changes due to the use of different types of cement. Still, this would always face the convergence difficulty and computational cost obstacles.

- In nuclear applications, where transfer properties are important, it is possible to extend this model in order to analysis the transport capacities at the steel/concrete interface. Moreover, it can be applied to study the corrosion of the steel bar, by taking into account the detailed geometry of the ribbed bar and expansions due to the formation of corrosion products.

- The proposed FCZM is not only specific to the steel-concrete interface. It can be applied for other engineering applications like assigning it to the mortar joint of the masonry walls (D'Altri et al., 2018), UHPC-NC composite member (Tong et al., 2022), timber-concrete interface (Jaaranen and Fink, 2021) and many other composite-like materials in which CZM is applied, but where the frictional effect could be important like fiber-matrix interfaces (Heshmati et al., 2018; zhang and Huang, 2022) and aggregates-mortar interface (Wu and Wriggers, 2015).

- Due to the lack of experimental data on pullout test with steel bar having various dimensions and shapes of ribs, it would be of interest to add such data to the pool of bond studies. Recently, (Higuchi et al., 2022) tried different shapes of ribs built using 3D printing. Still, the steel plates used were rectangular, not circular, and smooth in two sides. It would be valuable to perform several pull-out tests using an approach similar to the one adopted in subsection 5.3.2, that is, to vary one of the dimensions (including the height, angle, thickness and orientation) at a time and to observe the effect. Using different shapes of the bars having equivalent surface areas is important and such data is missing in literature. More than one experiment should be done on each case to be representative, as sometimes the experiments performed on the same bar do not give very close results, like in (Higuchi et al., 2022). The results of such long-term study would be very valuable and unique, and could give an alternative and complementary view on the mechanical interlock, and help understand the importance of the shape of the ribs, which are usually neglected at large scales.

- At the macroscopic scale, the models should evolve more by including more precisely the effect of the mechanical interlock. This can be done by introducing the projected normal surface area of the rib, which can be quantified using CAD. Macroscopic models that neglect the geometry of the rib may give similar results when varying the geometry of the ribs, which is not realistic. A challenge would be able to predict this coefficient using the projected normal surface area of the one side of the rib, which can give a good prediction of the variation in the bond strength. Moreover, it is expected to reach a very accurate prediction after obtaining the aforementioned experimental data.

LIST OF REFERENCES

Abrams, D.A., 1913. Tests of bond between concrete and steel (No. 71). University of Illinois at Urbana Champaign, College of Engineering.

Albarella, M., Serpieri, R., Alfano, G., Sacco, E., 2015. A 3D multiscale cohesive zone model for quasi-brittle materials accounting for friction, damage and interlocking. European Journal of Computational Mechanics 24, 144–170. https://doi.org/10.1080/17797179.2015.1096674

Alfano, G., Crisfield, M.A., 2001. Finite element interface models for the delamination analysis of laminated composites: mechanical and computational issues. Int. J. Numer. Meth. Engng. 50, 1701–1736. https://doi.org/10.1002/nme.93

Alfano, G., Marfia, S., Sacco, E., 2006. A cohesive damage–friction interface model accounting for water pressure on crack propagation. Computer Methods in Applied Mechanics and Engineering 196, 192–209. https://doi.org/10.1016/j.cma.2006.03.001

Alfano, G., Sacco, E., 2006. Combining interface damage and friction in a cohesive-zone model. Int. J. Numer. Meth. Engng. 68, 542–582. https://doi.org/10.1002/nme.1728

Alzyoud, S., Wong, H.S., Buenfeld, N.R., 2016. Influence of reinforcement spacers on mass transport properties and durability of concrete structures. Cement and Concrete Research 87, 31–44. https://doi.org/10.1016/j.cemconres.2016.05.006

Ambati, M., Gerasimov, T., De Lorenzis, L., 2015. A review on phase-field models of brittle fracture and a new fast hybrid formulation. Comput Mech 55, 383–405. https://doi.org/10.1007/s00466-014-1109-y

Andrade, C., Alonso, C., Molina, F., 1993. Cover cracking as a function of rebar corrosion: Part II–Numerical model. Materials and Structures 26, 532–548. https://doi.org/doi.org/10.1007/BF02472864

Angst, U.M., Geiker, M.R., Michel, A., Gehlen, C., Wong, H., Isgor, O.B., Elsener, B., Hansson, C.M., François, R., Hornbostel, K., Polder, R., Alonso, M.C., Sanchez, M., Correia, M.J., Criado, M., Sagüés, A., Buenfeld, N., 2017. The steel–concrete interface. Mater Struct 50, 143. https://doi.org/10.1617/s11527-

017-1010-1

Anwar Hossain, K.M., 2008. Bond characteristics of plain and deformed bars in lightweight pumice concrete. Construction and Building Materials 22, 1491–1499. https://doi.org/10.1016/j.conbuildmat.2007.03.025

Arriaga, M., Waisman, H., 2018. Multidimensional stability analysis of the phase-field method for fracture with a general degradation function and energy split. Comput Mech 61, 181–205. https://doi.org/10.1007/s00466-017-1432-1

Asai, M., Terada, K., Ikeda, K., Suyama, H., Fujii, K., 2003. Meso-scopic numerical analysis of concrete structures by a modified lattice model. Doboku Gakkai Ronbunshu 2003, 19–30. https://doi.org/10.2208/jscej.2003.731_19

ASTM Standard C33, 2003. Specification for Concrete Aggregates. ASTM International, West Conshohocken, PA, 2003. https://doi.org/10.1520/C0033-03

Baalbaki, W., Aicin, P.-C., Ballivy, G., 1992. On Predicting Modulus of Elasticity inHigh-Strength Concrete. ACI Materials Journal 89. https://doi.org/10.14359/1843

Barbosa, M.T.G., 2002. Evolution of the Behavior of the Bond in High Strength Concrete, in: Materials Research. Presented at the Third International Conference on high-Performance Concrete, Performance and Quality Concrete Structure, American Concrete Institute, Recife, Pernambuco.

Barbosa, M.T.G., Sánchez Filho, E. de S., Oliveira, T.M. de, Santos, W.J. dos, 2008. Analysis of the relative rib area of reinforcing bars pull out tests. Mat. Res. 11, 453–457. https://doi.org/10.1590/S1516-14392008000400013

Barenblatt, G.I., 1962. The Mathematical Theory of Equilibrium Cracks in Brittle Fracture, in: Advances in Applied Mechanics. Elsevier, pp. 55–129. https://doi.org/10.1016/S0065-2156(08)70121-2

Bary, B., Bourcier, C., Helfer, T., 2017. Analytical and 3D numerical analysis of the thermoviscoelastic behavior of concrete-like materials including interfaces. Advances in Engineering Software 112, 16–30. https://doi.org/10.1016/j.advengsoft.2017.06.006

Bazant, Z.P., Tabbara, M.R., Kazemi, M.T., Pijaudier-Cabot, G., 1990. Random Particle Model for Fracture of Aggregate or Fiber Composites. J. Eng. Mech. 116, 1686–1705. https://doi.org/10.1061/(ASCE)0733-9399(1990)116:8(1686)

Bensabra, H., Azzouz, N., 2013. Study of Rust Effect on the Corrosion Behavior of Reinforcement Steel Using Impedance Spectroscopy. Metall and Mat Trans A 44, 5703–5710. https://doi.org/10.1007/s11661-013-1915-4

Bernachy-Barbe, F., Bary, B., 2019. Effect of aggregate shapes on local fields in 3D mesoscale simulations of the concrete creep behavior. Finite Elements in Analysis and Design 156, 13–23. https://doi.org/10.1016/j.finel.2019.01.001

Bernard, F., Kamali-Bernard, S., Prince, W., 2008. 3D multi-scale modelling of mechanical behaviour of sound and leached mortar. Cement and Concrete Research 38, 449–458. https://doi.org/10.1016/j.cemconres.2007.11.015

Berto, L., Simioni, P., Saetta, A., 2008. Numerical modelling of bond behaviour in RC structures affected by reinforcement corrosion. Engineering Structures 30, 1375–1385. https://doi.org/10.1016/j.engstruct.2007.08.003

Bhargava, K., Ghosh, A.K., Mori, Y., Ramanujam, S., 2006. Model for cover cracking due to rebar corrosion in RC structures. Engineering Structures 17. https://doi.org/10.1016/j.engstruct.2005.11.014

Bolander, J.E., Choi, S., Duddukuri, S.R., 2008. Fracture of fiber-reinforced cement composites: effects of fiber dispersion. Int J Fract 154, 73–86. https://doi.org/10.1007/s10704-008-9269-4

Borden, M.J., Hughes, T.J.R., Landis, C.M., Verhoosel, C.V., 2014. A higher-order phase-field model for brittle fracture: Formulation and analysis within the isogeometric analysis framework. Computer Methods in Applied Mechanics and Engineering 273, 100–118. https://doi.org/10.1016/j.cma.2014.01.016

Bouazaoui, L., Li, A., 2008. Analysis of steel/concrete interfacial shear stress by means of pull out test. International Journal of Adhesion and Adhesives 28, 101–108. https://doi.org/10.1016/j.ijadhadh.2007.02.006

Bourcier, C., Dridi, W., Chomat, L., Laucoin, E., Bary, B., Adam, E., 2014. Combs: open source python library for RVE generation. Application to microscale diffusion simulations in cementitious materials. SNA + MC 2013 - Joint International Conference on Supercomputing in Nuclear Applications +

Monte Carlo. https://doi.org/10.1051/snamc/201402107

Bourdin, B., Francfort, G.A., Marigo, J.-J., 2008. The Variational Approach to Fracture. J Elasticity 91, 5–148. https://doi.org/10.1007/s10659-007-9107-3

Bourdin, B., Francfort, G.A., Marigo, J.-J., 2000. Numerical experiments in revisited brittle fracture. Journal of the Mechanics and Physics of Solids 48, 797–826. https://doi.org/10.1016/S0022-5096(99)00028-9

Brancherie, D., Ibrahimbegovic, A., 2009. Novel anisotropic continuum-discrete damage model capable of representing localized failure of massive structures: Part I: theoretical formulation and numerical implementation. Engineering Computations 26, 100–127. https://doi.org/10.1108/02644400910924825

Bui, T.-T., Limam, A., Sarhosis, V., 2021. Failure analysis of masonry wall panels subjected to in-plane and out-of-plane loading using the discrete element method. European Journal of Environmental and Civil Engineering 25, 876–892. https://doi.org/10.1080/19648189.2018.1552897

Caballero, A., López, C.M., Carol, I., 2006. 3D meso-structural analysis of concrete specimens under uniaxial tension. Computer Methods in Applied Mechanics and Engineering 195, 7182–7195. https://doi.org/10.1016/j.cma.2005.05.052

Cairns, J., Jones, K., 1995. Influence of rib geometry on strength of lapped joints: an experimental and analytical study. Magazine of Concrete Research 47, 253–262. https://doi.org/10.1680/macr.1995.47.172.253

Calixte, R., Jason, L., Davenne, L., 2022. Partial to Full Composite Action in Steel–Concrete Sandwich Beams: Development of a Modeling Strategy and Comparison to Standards. International Journal of Civil Engineering. https://doi.org/10.1007/s40999-022-00747-8

Camacho, G.T., Ortiz, M., 1996. Computational modelling of impact damage in brittle materials. International Journal of Solids and Structures 33, 2899–2938. https://doi.org/10.1016/0020-7683(95)00255-3

Casanova, A., Jason, L., Davenne, L., 2012. Bond slip model for the simulation of reinforced concrete structures. Engineering Structures 39, 66–78. https://doi.org/10.1016/j.engstruct.2012.02.007

Chandra, N., Li, H., Shet, C., Ghonem, H., 2002. Some issues in the application of cohesive zone models for metal–ceramic interfaces. International Journal of Solids and Structures 39, 2827–2855. https://doi.org/10.1016/S0020-7683(02)00149-X

Chapman, R.A., Shah, S.P., 1987. Early-age Bond Strength in Reinforced Concrete. ACI Materials Journal 84. https://doi.org/10.14359/2438

Cheng, P., Zhu, H., Zhang, Y., Jiao, Y., Fish, J., 2022. Coupled thermo-hydro-mechanical-phase field modeling for fire-induced spalling in concrete. Computer Methods in Applied Mechanics and Engineering 389, 114327. https://doi.org/10.1016/j.cma.2021.114327

Chi, Y., Yu, M., Huang, L., Xu, L., 2017. Finite element modeling of steel-polypropylene hybrid fiber reinforced concrete using modified concrete damaged plasticity. Engineering Structures 148, 23–35. https://doi.org/10.1016/j.engstruct.2017.06.039

Chiriatti, L., Mercado-Mendoza, H., Apedo, K.L., Fond, C., Feugeas, F., 2019. A study of bond between steel rebar and concrete under a friction-based approach. Cement and Concrete Research 120, 132–141. https://doi.org/10.1016/j.cemconres.2019.03.019

Comi, C., Perego, U., 2001. Numerical aspects of nonlocal damage analyses. Revue européenne des éléments finis 10, 227–242. https://doi.org/10.1080/12506559.2001.11869249

Counto, U.J., 1964. The effect of the elastic modulus of the aggregate on the elastic modulus, creep and creep recovery of concrete. Magazine of Concrete Research 16, 129–138. https://doi.org/10.1680/macr.1964.16.48.129

D’Altri, A.M., Miranda, S. de, Castellazzi, G., Sarhosis, V., 2018. A 3D detailed micro-model for the in-plane and out-of-plane numerical analysis of masonry panels. Computers & Structures 206, 18–30. https://doi.org/10.1016/j.compstruc.2018.06.007

Daoud, A., Lorrain, M., 2003. Influence de la position des armatures sur l’adhérence des bétons autoplaçants: interprétation par analyse d’image. Materials and Structures 36, 231–237. https://doi.org/10.1007/BF02479616

Daoud, A., Lorrain, M., Elgonnouni, M., 2002. Résistance à l’arrachement d'armatures ancrées dans du béton autoplaçant. Materials and Structures 35, 395–401. https://doi.org/10.1007/BF02483142

Daoud, A., Maurel, O., Laborderie, C., 2013. 2D mesoscopic modelling of bar–concrete bond. Engineering Structures 49, 696–706. https://doi.org/10.1016/j.engstruct.2012.11.018

Darwin, D., Graham, E.K., 1993. Effect of Deformation Height and Spacing on Bond Strength of Reinforcing Bars. ACI Structural Journal 90, 646–657.

Dehestani, M., Mousavi, S.S., 2015. Modified steel bar model incorporating bond-slip effects for embedded element method. Construction and Building Materials 81, 284–290. https://doi.org/10.1016/j.conbuildmat.2015.02.027

Desnerck, P., Schutter, G.D., Taerwe, L., 2010. A local bond stress-slip model for reinforcing bars in self-compacting concrete, in: Proceedings of Fracture Mechanics of Concrete and Concrete Strucures–Assesment, Durability, Monitoring and Retrofitting of Concrete Strucures. Presented at the FraMCoS-7, Seoul, South Korea, pp. 771–778.

Doi, K., Hiromoto, S., Shinohara, T., Tsuchiya, K., Katayama, H., Akiyama, E., 2020. Role of mill scale on corrosion behavior of steel rebars in mortar. Corrosion Science 177, 108995. https://doi.org/10.1016/j.corsci.2020.108995

Dominguez, N., 2005. Etude de la liaison-acier enter l'acier et le béton: de la modélisation du phénomène à la formulation d'un élément enrichi 'Béton Armé', PhD thesis, Ecole Normale Supérieure de Cachan.

Dominguez, N., Brancherie, D., Davenne, L., Ibrahimbegović, A., 2005. Prediction of crack pattern distribution in reinforced concrete by coupling a strong discontinuity model of concrete cracking and a bond-slip of reinforcement model. Engineering Computations 22, 558–582. https://doi.org/10.1108/02644400510603014

Drucker, D.C., Prager, W., 1952. Soil mechanics and plastic analysis or limit design. Quarterly of Applied Mathematics 10, 157–165.

Duan, H.L., Yi, X., Huang, Z.P., Wang, J., 2007. A unified scheme for prediction of effective moduli of multiphase composites with interface effects. Part I: Theoretical framework. Mechanics of Materials 39, 81–93. https://doi.org/10.1016/j.mechmat.2006.02.009

Dugdale, D.S., 1960. Yielding of steel sheets containing slits. Journal of the Mechanics and Physics of Solids 8, 100–104. https://doi.org/10.1016/0022-5096(60)90013-2

Eddy, L., Nagai, K., 2016. Numerical simulation of beam-column knee joints with mechanical anchorages by 3D rigid body spring model. Engineering Structures 126, 547–558. https://doi.org/10.1016/j.engstruct.2016.07.054

Elices, M., Rocco, C., Roselló, C., 2009. Cohesive crack modelling of a simple concrete: Experimental and numerical results. Engineering Fracture Mechanics 76, 1398–1410. https://doi.org/10.1016/j.engfracmech.2008.04.010

Eligehausen, R., Popov, E., Bertero, V., 1983. Local Bond stress slip relationship of deformed bars under generalized excitations (No. 83/23). EERC, University of California, Berkeley.

Feng, D.-C., Wu, J.-Y., 2018. Phase-field regularized cohesive zone model (CZM) and size effect of concrete. Engineering Fracture Mechanics 197, 66–79. https://doi.org/10.1016/j.engfracmech.2018.04.038

Feng, X., Zuo, Y., Tang, Y., Zhao, X., Lu, X., 2011. The degradation of passive film on carbon steel in concrete pore solution under compressive and tensile stresses. Electrochimica Acta 58, 258–263. https://doi.org/10.1016/j.electacta.2011.09.035

Fichant, S., La Borderie, C., Pijaudier-Cabot, G., 1999. Isotropic and anisotropic descriptions of damage in concrete structures. Mechanics of Cohesive-frictional Materials 4, 339–359. https://doi.org/10.1002/(SICI)1099-1484(199907)4:4<339::AID-CFM65>3.0.CO;2-J

Foulk, J.W., Allen, D.H., Helms, K.L.E., 2000. Formulation of a three-dimensional cohesive zone model for application to a finite element algorithm. Computer Methods in Applied Mechanics and Engineering 183, 51–66. https://doi.org/10.1016/S0045-7825(99)00211-X

Francfort, G.A., Marigo, J.-J., 1998. Revisiting brittle fracture as an energy minimization problem. Journal of the Mechanics and Physics of Solids 46, 1319–1342. https://doi.org/10.1016/S0022-5096(98)00034-9

Fraternali, F., Angelillo, M., Fortunato, A., 2002. A lumped stress method for plane elastic problems and the discrete-continuum approximation. International Journal of Solids and Structures 39, 6211–6240. https://doi.org/10.1016/S0020-7683(02)00472-9

Gedik, Y.H., Nakamura, H., Yamamoto, Y., Kunieda, M., 2011. Evaluation of three-dimensional effects in short deep beams using a rigid-body-spring-model. Cement and Concrete Composites 33, 978–991. https://doi.org/10.1016/j.cemconcomp.2011.06.004

Geubelle, P.H., Baylor, J.S., 1998. Impact-induced delamination of composites: a 2D simulation. Composites Part B: Engineering 29, 589–602. https://doi.org/10.1016/S1359-8368(98)00013-4

Goto, Y., 1971. Cracks Formed in Concrete Around Deformed Tension Bars. ACI Journal Proceedings 68. https://doi.org/10.14359/11325

Grassl, P., 2009. A lattice approach to model flow in cracked concrete. Cement and Concrete Composites 31, 454–460. https://doi.org/10.1016/j.cemconcomp.2009.05.001

Griffith, A.A., 1921. The phenomena of rupture and flow in solids. Philosophical Transactions of the Royal Society of London. Series A Containing Papers of a Mathematical or Physical Character 221, 163–198. https://doi.org/10.1098/rsta.1921.0006

Häfner, S., Eckardt, S., Luther, T., Könke, C., 2006. Mesoscale modeling of concrete: Geometry and numerics. Computers & Structures 84, 450–461. https://doi.org/10.1016/j.compstruc.2005.10.003

Hallett, S.R., Harper, P.W., 2015. 2 - Modelling delamination with cohesive interface elements, in: Camanho, P.P., Hallett, Stephen R. (Eds.), Numerical Modelling of Failure in Advanced Composite Materials, Woodhead Publishing Series in Composites Science and Engineering. Woodhead Publishing, pp. 55–72. https://doi.org/10.1016/B978-0-08-100332-9.00002-5

Hamouine, A., Lorrain, M., 1995. Etude de la résistance à l'arrachement de barres enrobées dans du béton de hautes performances. Materials and Structures 28, 569–574. https://doi.org/10.1007/BF02473188

Hansen, A., Roux, S., Herrmann, H.J., 1989. Rupture of central-force lattices. J. Phys. France 50, 733–744. https://doi.org/10.1051/jphys:01989005007073300

Hashin, Z., 1991. Thermoelastic properties of particulate composites with imperfect interface. Journal of the Mechanics and Physics of Solids 39, 745–762. https://doi.org/10.1016/0022-5096(91)90023-H

Hayashi, D., Nagai, K., Eddy, L., 2017. Mesoscale Analysis of RC Anchorage Performance in Multidirectional Reinforcement Using a Three-Dimensional Discrete Model. J. Struct. Eng. 143, 04017059. https://doi.org/10.1061/(ASCE)ST.1943-541X.0001780

Helfer, T., Michel, B., Proix, J.-M., Salvo, M., Sercombe, J., Casella, M., 2015. Introducing the open-source mfront code generator: Application to mechanical behaviours and material knowledge management within the PLEIADES fuel element modelling platform. Computers & Mathematics with Applications 70, 994–1023. https://doi.org/10.1016/j.camwa.2015.06.027

Herrmann, H.J., Hansen, A., Roux, S., 1989. Fracture of disordered, elastic lattices in two dimensions. Phys. Rev. B 39, 637–648. https://doi.org/10.1103/PhysRevB.39.637

Heshmati, M., Haghani, R., Al-Emrani, M., André, A., 2018. On the strength prediction of adhesively bonded FRP-steel joints using cohesive zone modelling. Theoretical and Applied Fracture Mechanics 93, 64–78. https://doi.org/10.1016/j.tafmec.2017.06.022

Higuchi, R., Jewett, J.L., Carstensen, J.V., 2022. Experimental investigation of ribbing pattern effect on the bonding qualities of water jet cut steel reinforcement. Architecture, Structures and Construction. https://doi.org/10.1007/s44150-022-00068-3

Hillerborg, A., Modéer, M., Petersson, P.-E., 1976. Analysis of crack formation and crack growth in concrete by means of fracture mechanics and finite elements. Cement and Concrete Research 6, 773–781. https://doi.org/10.1016/0008-8846(76)90007-7

Hofacker, M., Miehe, C., 2013. A phase field model of dynamic fracture: Robust field updates for the analysis of complex crack patterns. Int. J. Numer. Meth. Engng 93, 276–301. https://doi.org/10.1002/nme.4387

Hrennikoff, A., 1941. Solution of Problems of Elasticity by the Framework Method. Journal of Applied Mechanics 8, A169–A175. https://doi.org/10.1115/1.4009129

Hutchinson, J.W., Evans, A.G., 2000. Mechanics of materials: top-down approaches to fracture. Acta Materialia 48, 125–135. https://doi.org/10.1016/S1359-6454(99)00291-8

Ibrahimbegovic, A., Boulkertous, A., Davenne, L., Brancherie, D., 2010. Modelling of reinforced-concrete structures providing crack-spacing based on X-FEM, ED-FEM and novel operator split solution procedure: MODELLING OF RC STRUCTURES. Int. J. Numer. Meth. Engng. 83, 452–481. https://doi.org/10.1002/nme.2838

Ilgadi, O.B., 2013. Advanced three-dimensional analysis of concrete structures using nonlinear truss models. Phd Thesis. Colorado University, Colorado, USA.

Irwin, G.R., 1958. Fracture, in: Flügge, S. (Ed.), Elasticity and Plasticity / Elastizität Und Plastizität. Springer Berlin Heidelberg, Berlin, Heidelberg, pp. 551–590. https://doi.org/10.1007/978-3-642-45887-3_5

Jaaranen, J., Fink, G., 2021. Cohesive-frictional interface model for timber-concrete contacts. International Journal of Solids and Structures 230–231, 111174. https://doi.org/10.1016/j.ijsolstr.2021.111174

Jansen, D.C., Shah, S.P., 1997. Effect of length on compressive strain softening of concrete. Journal of engineering mechanics 123, 25. https://doi.org/10.1061/(ASCE)0733-9399(1997)123:1(25)

Jin, L., Li, X., Zhang, R., Du, X., 2022. Modelling of bond behavior of deformed bar embedded in concrete after heating to high temperatures: A mesoscale study. Construction and Building Materials 334, 127456. https://doi.org/10.1016/j.conbuildmat.2022.127456

Jin, L., Li, X., Zhang, R., Du, X., 2021a. Bond-slip behavior between concrete and deformed rebar at elevated temperature: Mesoscale simulation and formulation. International Journal of Mechanical Sciences 205, 106622. https://doi.org/10.1016/j.ijmecsci.2021.106622

Jin, L., Liu, M., Zhang, R., Du, X., 2020a. 3D meso-scale modelling of the interface behavior between ribbed steel bar and concrete. Engineering Fracture Mechanics 239, 107291. https://doi.org/10.1016/j.engfracmech.2020.107291

Jin, L., Wang, T., Jiang, X., Du, X., 2019a. Size effect in shear failure of RC beams with stirrups: Simulation and formulation. Engineering Structures 199, 109573. https://doi.org/10.1016/j.engstruct.2019.109573

Jin, L., Yu, W., Du, X., Yang, W., 2020b. Meso-scale simulations of size effect on concrete dynamic splitting tensile strength: Influence of aggregate content and maximum aggregate size. Engineering Fracture Mechanics 230, 106979. https://doi.org/10.1016/j.engfracmech.2020.106979

Jin, L., Yu, W., Du, X., Yang, W., 2019b. Dynamic size effect of concrete under tension: A numerical study. International Journal of Impact Engineering 132, 103318. https://doi.org/10.1016/j.ijimpeng.2019.103318

Jin, L., Yu, W., Li, D., Du, X., 2021b. Numerical and theoretical investigation on the size effect of concrete compressive strength considering the maximum aggregate size. International Journal of Mechanical Sciences 192, 106130. https://doi.org/10.1016/j.ijmecsci.2020.106130

Kiousis, P.D., Papadopoulos, P.G., Xenidis, H., 2010. Truss Modeling of Concrete Columns in Compression. J. Eng. Mech. 136, 1006–1014. https://doi.org/10.1061/(ASCE)EM.1943-7889.0000142

Kuhn, H.W., Tucker, A.W., 1951. Nonlinear Programming, in: Proceedings of the Second Berkeley Symposium on Mathematical Statistics and Probability. Presented at the 2nd Berkeley Symposium, Berkeley, California, U.S.A, pp. 481–492.

La Borderie, C., Pijaudier-Cabot, G., 1992. Influence of the state of the stress in concrete on the behaviour of steel concrete interface. Concrete fracture mechanics of structures, Colorado, USA.

Lancaster, R., 1989. SPACERS for reinforced concrete. Concrete (London) 23, 27–28.

Larrard, T. de, Bary, B., Adam, E., Kloss, F., 2013. Influence of aggregate shapes on drying and carbonation phenomena in 3D concrete numerical samples. Computational Materials Science 72, 1–14. https://doi.org/10.1016/j.commatsci.2013.01.039

Lebon, F., 2003. Contact problems with friction: models and simulations. Simulation Modelling Practice and Theory 11, 449–463. https://doi.org/10.1016/S1569-190X(03)00060-1

Lee, J., Fenves, G.L., 1998. Plastic-Damage Model for Cyclic Loading of Concrete Structures. Journal of Engineering Mechanics 124, 892–900. https://doi.org/10.1061/(ASCE)0733-9399(1998)124:8(892)

Lee, Y.-H., Willam, K.J., 1997. Anisotropic vertex plasticity formulation for concrete in-plane stress. Journal of engineering mechanics 123, 714–726. https://doi.org/10.1061/(ASCE)0733-9399(1997)123:7(714)

Leite, J.P.B., Slowik, V., Mihashi, H., 2004. Computer simulation of fracture processes of concrete using mesolevel models of lattice structures. Cement and Concrete Research 34, 1025–1033. https://doi.org/10.1016/j.cemconres.2003.11.011

Li, B., Tran, C.T.N., 2008. Reinforced concrete beam analysis supplementing concrete contribution in truss models. Engineering Structures 30, 3285–3294. https://doi.org/10.1016/j.engstruct.2008.05.002

Li, L., Sagüés, A.A., 2001. Chloride Corrosion Threshold of Reinforcing Steel in Alkaline Solutions—Open-Circuit Immersion Tests. Corrosion 57, 19–28. https://doi.org/10.5006/1.3290325

Li, S., Thouless, M., Waas, A., Schroeder, J., Zavattieri, P., 2005. Use of a cohesive-zone model to analyze the fracture of a fiber-reinforced polymer-matrix composite. Composites Science and Technology 65, 537–549. https://doi.org/10.1016/j.compscitech.2004.08.004

Lilliu, G., Mier, J.G.M. van, 2003. 3D lattice type fracture model for concrete. Engineering Fracture Mechanics 70, 927–941. https://doi.org/10.1016/S0013-7944(02)00158-3

Lin, H., Zhao, Y., Feng, P., Ye, H., Ozbolt, J., Jiang, C., Yang, J.-Q., 2019. State-of-the-art review on the bond properties of corroded reinforcing steel bar. Construction and Building Materials 213, 216–233. https://doi.org/10.1016/j.conbuildmat.2019.04.077

Liu, M., Jin, L., Chen, F., Zhang, R., Du, X., 2022a. 3D meso-scale modelling of the bonding failure between corroded ribbed steel bar and concrete. Engineering Structures 256, 113939. https://doi.org/10.1016/j.engstruct.2022.113939

Liu, M., Jin, L., Zhang, R., Chen, F., Du, X., 2022b. Combined effect of corrosion and strain rate on the bond behavior: A two-stage simulation. International Journal of Mechanical Sciences 227, 107438. https://doi.org/10.1016/j.ijmecsci.2022.107438

Lowes, L.N., Moehle, J.P., Govindjee, S., 2004. Concrete-Steel Bond Model for Use in Finite Element Modeling of Reinforced Concrete Structures. ACI Structural Journal 101, 12. https://doi.org/10.14359/13336

Lubliner, J., Oliver, J., Oller, S., Oñate, E., 1989. A plastic-damage model for concrete. International Journal of Solids and Structures 25, 299–326. https://doi.org/10.1016/0020-7683(89)90050-4

Lundgren, K., 2005. Bond between ribbed bars and concrete. Part 2: The effect of corrosion. Magazine of Concrete Research 57, 383–395. https://doi.org/10.1680/macr.2005.57.7.383

Lutz, L.A., Gergely, P., 1967. Mechanics of Bond and Slip of Deformed Bars in Concrete. ACI Journal Proceedings 64, 711–721. https://doi.org/10.14359/7600

Malvar, L.J., 1992. Bond of Reinforcemen Under Controlled Confinement. ACI Materials Journal 89, 593–601.

Mammoliti, L.T., Brown, L.C., Hansson, C.M., Hope, B.B., 1996. The influence of surface finish of reinforcing steel and ph of the test solution on the chloride threshold concentration for corrosion initiation in synthetic pore solutions. Cement and Concrete Research 26, 545–550. https://doi.org/10.1016/0008-8846(96)00018-X

Mang, C., Jason, L., Davenne, L., 2016. Crack opening estimate in reinforced concrete walls using a steel–concrete bond model. Archives of Civil and Mechanical Engineering 16, 422–436. https://doi.org/10.1016/j.acme.2016.02.001

Mang, C., Jason, L., Davenne, L., 2015. A new bond slip model for reinforced concrete structures: Validation by modelling a reinforced concrete tie. Engineering Computations 32, 1934–1958. https://doi.org/10.1108/EC-11-2014-0234

Markeset, G., 1993. Failure of concrete under compressive strain gradients. Dr. ing. PhD diss., Thesis 1993: 110. The Norwegian Institute of Technology, Trondheim, Norway.

Mazars, J., 1986. A description of micro- and macroscale damage of concrete structures. Engineering Fracture Mechanics 25, 729–737. https://doi.org/10.1016/0013-7944(86)90036-6

Mazars, J., 1984. Application de la mécanique de l'endommagement au comportement non linéaire et à la rupture du béton de structure. These de Docteur-Es-Sciences presentee a l'Universite Pierre et Marie Curie-Paris.

Mazzucco, G., Xotta, G., Pomaro, B., Salomoni, V.A., Faleschini, F., 2018. Elastoplastic-damaged meso-scale modelling of concrete with recycled aggregates. Composites Part B: Engineering 140, 145–156. https://doi.org/10.1016/j.compositesb.2017.12.018

Metelli, G., Plizzari, G.A., 2014. Influence of the relative rib area on bond behaviour. Magazine of Concrete Research 66, 277–294. https://doi.org/10.1680/macr.13.00198

MFront, tfel.sourceforge.net.

Miehe, C., Hofacker, M., Welschinger, F., 2010. A phase field model for rate-independent crack propagation: Robust algorithmic implementation based on operator splits. Computer Methods in Applied Mechanics and Engineering 199, 2765–2778. https://doi.org/10.1016/j.cma.2010.04.011

Mielenz, R.C., Wolkodoff, V.E., Backstrom, J.E., Burrows, R.W., 1958. Origin, Evolution, and Effects of the Air Void System in Concrete. Part 1 - Entrained Air in Unhardened Concrete. ACI Journal Proceedings 55, 95–121. https://doi.org/10.14359/11371

Mier, J.G.M.V., 1984. Strain-softening of concrete under multiaxial loading conditions, PhD. Citeseer.

Mohammed, I., Liechti, K.M., 2000. Cohesive zone modeling of crack nucleation at bimaterial corners. Journal of the Mechanics and Physics of Solids 48, 735–764. https://doi.org/10.1016/S0022-5096(99)00052-6

Mohammed, T.U., Hamada, H., 2006. Corrosion of steel bars in concrete with various steel surface conditions. ACI Materials Journal 103, 233–242. https://doi.org/10.14359/16606

Monti, G., Filippou, F.C., Spacone, E., 1997. Analysis of hysteretic behavior of anchored reinforcing bars. Structural Journal 94, 248–261.

Mori, T., Tanaka, K., 1973. Average stress in matrix and average elastic energy of materials with misfitting inclusions. Acta Metallurgica 21, 571–574. https://doi.org/10.1016/0001-6160(73)90064-3

Nagai, K., Sato, Y., Ueda, T., 2005. Mesoscopic Simulation of Failure of Mortar and Concrete by 3D RBSM. Journal of Advanced Concrete Technology 3, 385–402. https://doi.org/10.3151/jact.3.385

Needleman, A., 1997. Numerical modeling of crack growth under dynamic loading conditions. Computational Mechanics 19, 463–469. https://doi.org/10.1007/s004660050194

Needleman, A., 1987. A continuum model for void nucleation by inclusion debonding. Journal of Applied Mechanics 54, 525–531. https://doi.org/10.1115/1.3173064

Ngo, D., Scordelis, A.C., 1967. Finite Element Analysis of Reinforced Concrete Beams. ACI Journal Proceedings 64, 152–163. https://doi.org/10.14359/7551

Nguyen, D., Lawrence, C., La Borderie, C., Matallah, M., Nahas, G., 2010. A mesoscopic model for a better understanding of the transition from diffuse damage to localized damage. European Journal of Environmental and Civil Engineering 14, 751–776. https://doi.org/10.1080/19648189.2010.9693261

Nguyen, Q.T., Caré, S., Berthaud, Y., Millard, A., Ragueneau, F., 2011. Experimental and numerical behaviour of reinforced mortar plates subjected to accelerated corrosion. International Journal for Numerical and Analytical Methods in Geomechanics 35, 1141–1159. https://doi.org/10.1002/nag.947

Nguyen, T.T.H., Bary, B., de Larrard, T., 2015. Coupled carbonation-rust formation-damage modeling and simulation of steel corrosion in 3D mesoscale reinforced concrete. Cement and Concrete Research 74, 95–107. https://doi.org/10.1016/j.cemconres.2015.04.008

Nguyen, V.P., Stroeven, M., Sluys, L.J., 2012. Multiscale failure modeling of concrete: Micromechanical modeling, discontinuous homogenization and parallel computations. Computer Methods in Applied Mechanics and Engineering 201–204, 139–156. https://doi.org/10.1016/j.cma.2011.09.014

Niwa, J., Choi, I.-C., Tanabe, T., 1995. Analytical Study For Shear Resisting Mechanism Using Lattice Model. Concrete library international 95–109.

Pantazopoulou, S.J., Papoulia, K., 2001. Modeling cover-cracking due to reinforcement corrosion in RC structures. Journal of engineering mechanics 127, 342–351.

Park, K., Paulino, G.H., 2013. Cohesive Zone Models: A Critical Review of Traction-Separation Relationships Across Fracture Surfaces. Applied Mechanics Reviews 64. https://doi.org/10.1115/1.4023110

Park, R., Paulay, T., 1991. Reinforced concrete structures. John Wiley & Sons.

Pijaudier-Cabot, G., Mazars, J., 2001. Damage models for concrete, in: Handbook of Materials Behavior, Chapter 6. Academic Press, pp. 500–512.

Pijaudier-Cabot, G., Mazars, J., Pulikowski, J., 1991. Steel-Concrete Bond Analysis with Nonlocal Continuous Damage. Journal of Structural Engineering 117, 862–882. https://doi.org/10.1061/(ASCE)0733-9445(1991)117:3(862)

Qu, J., 1993. The effect of slightly weakened interfaces on the overall elastic properties of composite materials. Mechanics of Materials 14, 269–281. https://doi.org/10.1016/0167-6636(93)90082-3

Rahulkumar, P., Jagota, A., Bennison, S.J., Saigal, S., 2000. Cohesive element modeling of viscoelastic fracture: application to peel testing of polymers. International Journal of Solids and Structures 37, 1873–1897. https://doi.org/10.1016/S0020-7683(98)00339-4

Raman, R.K.S., 2006. Characterisation of 'rolled-in', 'fragmented' and 'red' scale formation during secondary processing of steels. Engineering Failure Analysis 13, 1044–1050. https://doi.org/10.1016/j.engfailanal.2005.07.011

Raous, M., Karray, M.A., 2009. Model coupling friction and adhesion for steel-concrete interfaces. Int. J. Comput. Appl. Technol. 34, 42–51. https://doi.org/10.1504/IJCAT.2009.022701

Rehm, G., 1961. The fundamentals of bond between steel reinforcement and concrete. Deutsche association for steel reinforcement-concrete 138, 59.

Restuccia, L., Ferro, G.A., Suarez-Riera, D., Sirico, A., Bernardi, P., Belletti, B., Malcevschi, A., 2020. Mechanical characterization of different biochar-based cement composites. Procedia Structural Integrity 25, 226–233. https://doi.org/10.1016/j.prostr.2020.04.027

Rezazadeh, M., Carvelli, V., Veljkovic, A., 2017. Modelling bond of GFRP rebar and concrete. Construction and Building Materials 153, 102–116. https://doi.org/10.1016/j.conbuildmat.2017.07.092

Rice, J.R., Wang, J.-S., 1989. Embrittlement of interfaces by solute segregation. Materials Science and Engineering: A 107, 23–40. https://doi.org/10.1016/0921-5093(89)90372-9

Richard, B., Ragueneau, F., Cremona, C., Adelaide, L., Tailhan, J.L., 2010. A three-dimensional steel/concrete interface model including corrosion effects. Engineering Fracture Mechanics 77, 951–973. https://doi.org/10.1016/j.engfracmech.2010.01.017

RILEM, 1970. Essai portant sur l'adhérence des armatures de béton–essai par traction. Matériaux et Constructions 3, 175–178.

RILEM TC, 1994. RC 6 Bond test for reinforcement steel. 2. Pull-out test, 1983, in: RILEM Recommendations for the Testing and Use of Constructions Materials. E & FN SPON, pp. 218–220.

Rokugo, K., Koyanagi, W., 2018. Role of compressive fracture energy of concrete on the failure behavior of reinforced concrete beams, in: Applications of Fracture Mechanics to Reinforced Concrete. CRC Press, pp. 437–464.

Salem, H.M., Maekawa, K., 2004. Pre- and Postyield Finite Element Method Simulation of Bond of Ribbed Reinforcing Bars. J. Struct. Eng. 130, 671–680. https://doi.org/10.1061/(ASCE)0733-9445(2004)130:4(671)

Salome, www.salome-platform.org.

Samson, E., Marchand, J., Zuber, B., Skalny, J.P., 2002. Ettringite in air voids, in: Proceedings of International RILEM TC 186-ISA Workshop on Internal Sulfate Attack and Delayed Ettringite Formation. Presented at the International RILEM Workshop on Internal Sulfate Attack and Delayed Ettringite Formation, Villars, Switzerland.

Sanchez, M., Gregori, J., Alonso, C., García-Jareño, J.J., Takenouti, H., Vicente, F.,

2007. Electrochemical impedance spectroscopy for studying passive layers on steel rebars immersed in alkaline solutions simulating concrete pores. Electrochimica Acta 52, 7634–7641. https://doi.org/10.1016/j.electacta.2007.02.012

Schlangen, E., Garboczi, E.J., 1997. Fracture simulations of concrete using lattice models: Computational aspects. Engineering Fracture Mechanics 57, 319–332. https://doi.org/10.1016/S0013-7944(97)00010-6

Schlangen, E., Garboczi, E.J., 1996. New method for simulating fracture using an elastically uniform random geometry lattice. International Journal of Engineering Science 34, 1131–1144. https://doi.org/10.1016/0020-7225(96)00019-5

Schlangen, E., van Mier, J.G.M., 1992. Simple lattice model for numerical simulation of fracture of concrete materials and structures. Materials and Structures 25, 534–542. https://doi.org/10.1007/BF02472449

Serpieri, Roberto, Albarella, M., Alfano, G., Sacco, E., 2017. Analysis of failure in quasi-brittle materials by 3D multiplane cohesive zone models combining damage, friction and interlocking. Procedia Structural Integrity 3, 441–449. https://doi.org/10.1016/j.prostr.2017.04.066

Serpieri, R., Albarella, M., Sacco, E., 2017. A 3D two-scale multiplane cohesive-zone model for mixed-mode fracture with finite dilation. Computer Methods in Applied Mechanics and Engineering 313, 857–888. https://doi.org/10.1016/j.cma.2016.10.021

Serpieri, R., Alfano, G., 2011. Bond-slip analysis via a thermodynamically consistent interface model combining interlocking, damage and friction. Int. J. Numer. Meth. Engng. 85, 164–186. https://doi.org/10.1002/nme.2961

Serpieri, Roberto, Alfano, G., Sacco, E., 2015. A mixed-mode cohesive-zone model accounting for finite dilation and asperity degradation. International Journal of Solids and Structures 67–68, 102–115. https://doi.org/10.1016/j.ijsolstr.2015.04.005

Serpieri, R, Sacco, E., Alfano, G., 2015. A thermodinamically consistent derivation of a frictional-damage cohesive-zone model with different mode I and mode II fracture energies. European Journal of Mechanics - A/Solids 49, 13–25. https://doi.org/10.1016/j.euromechsol.2014.06.006

Simo, J.C., Hughes, T.J., 1998. Computational inelasticity, 1st ed. Springer New York, NY.

Söylev, T.A., François, R., 2006. Effects of Bar-Placement Conditions on Steel-Concrete Bond. Materials and Structures 39, 211–220. https://doi.org/10.1617/s11527-005-9030-7

Stefanoni, M., Angst, U.M., Elsener, B., 2018. Electrochemistry and capillary condensation theory reveal the mechanism of corrosion in dense porous media. Scientific Reports 8, 7407. https://doi.org/10.1038/s41598-018-25794-x

Suda, K., Misra, S., Motohashi, K., 1993. Corrosion products of reinforcing bars embedded in concrete. Corrosion science 35, 1543–1549. https://doi.org/10.1016/0010-938X(93)90382-Q

Taber, L.H., Belarbi, A., Richardson, D.N., 2002. Effect of Reinforcing Bar Contamination on Steel-Concrete Bond During Concrete Construction. ACI special publications 209, 839–862.

Tastani, S.P., Pantazopoulou, S.J., 2010. Direct Tension Pullout Bond Test: Experimental Results. Journal of Structural Engineering 136, 731–743. https://doi.org/10.1061/(ASCE)ST.1943-541X.0000159

Tepfers, R., 1979. Cracking of concrete cover along anchored deformed reinforcing bars. Magazine of Concrete Research 31, 3–12. https://doi.org/10.1680/macr.1979.31.106.3

The Finite element code Cast3M, www-cast3m.cea.fr.

Thilakarathna, P.S.M., Kristombu Baduge, K.S., Mendis, P., Vimonsatit, V., Lee, H., 2020. Mesoscale modelling of concrete – A review of geometry generation, placing algorithms, constitutive relations and applications. Engineering Fracture Mechanics 231, 106974. https://doi.org/10.1016/j.engfracmech.2020.106974

Tilanter, T., Rechardt, T., Solodovnik, A., Kunnos, G., Johanson, R., 1977. Bond of reinforcement in light-weight aggregate concrete. Helsinki University of Technology, Otaniemi, Finland.

Tong, T., Yuan, S., Wang, H., Liu, Z., Wang, J., 2022. Numerical insights on quasistatic behaviors of UHPC-NC composite members by a phase-field approach enhanced with a cohesive-frictional interface model. Composite Structures 297, 115948. https://doi.org/10.1016/j.compstruct.2022.115948

Torre-Casanova, A., Jason, L., Davenne, L., Pinelli, X., 2013. Confinement effects on the steel–concrete bond strength and pull-out failure. Engineering Fracture Mechanics 97, 92–104. https://doi.org/10.1016/j.engfracmech.2012.10.013

Torre-Casanova, A.T., 2012. Prise en compte de la liaison acier-beton pour le calcul de structures industrielles. Ecole normale superieure de Cachan - ENS Cachan.

Turgut, C., Jason, L., Davenne, L., 2020. Structural-scale modeling of the active confinement effect in the steel-concrete bond for reinforced concrete structures. Finite Elements in Analysis and Design 172, 103386. https://doi.org/10.1016/j.finel.2020.103386

Tvergaard, V., 2003. Cohesive zone representations of failure between elastic or rigid solids and ductile solids. Engineering Fracture Mechanics 70, 1859–1868. https://doi.org/doi.org/10.1016/S0013-7944(03)00128-0

Tvergaard, V., 1990. Effect of fibre debonding in a whisker-reinforced metal. Materials science and engineering: A 125, 203–213. https://doi.org/10.1016/0921-5093(90)90170-8

Tvergaard, V., Hutchinson, J.W., 1992. The relation between crack growth resistance and fracture process parameters in elastic-plastic solids. Journal of the Mechanics and Physics of Solids 40, 1377–1397. https://doi.org/10.1016/0022-5096(92)90020-3

Van Mier, J.G.M., Van Vliet, M.R.A., 2003. Influence of microstructure of concrete on size/scale effects in tensile fracture. Engineering Fracture Mechanics 70, 2281–2306. https://doi.org/10.1016/S0013-7944(02)00222-9

Venzal, V., Morel, S., Parent, T., Dubois, F., 2020. Frictional cohesive zone model for quasi-brittle fracture: Mixed-mode and coupling between cohesive and frictional behaviors. International Journal of Solids and Structures 198, 17–30. https://doi.org/10.1016/j.ijsolstr.2020.04.023

Volpi, E., Olietti, A., Stefanoni, M., Trasatti, S.P., 2015. Electrochemical characterization of mild steel in alkaline solutions simulating concrete environment. Journal of Electroanalytical Chemistry 736, 38–46. https://doi.org/10.1016/j.jelechem.2014.10.023

Walker, P.R., Batayneh, M.K., Regan, P.E., 1997. Bond strength tests on deformed reinforcement in normal weight concrete. Materials and Structures 30, 424–429. https://doi.org/10.1007/BF02498566

Wang, J., Duan, H.L., Zhang, Z., Huang, Z.P., 2005. An anti-interpenetration model and connections between interphase and interface models in particle-reinforced composites. International Journal of Mechanical Sciences 47, 701–718. https://doi.org/10.1016/j.ijmecsci.2004.12.014

Wang, X., Liu, X., 2004. Modeling bond strength of corroded reinforcement without stirrups. Cement and Concrete Research 34, 1331–1339. https://doi.org/10.1016/j.cemconres.2003.12.028

Wang, Y., Zheng, Y., Wang, X., 2019. Mesoscopic damage evolution on bonding interface and its influence on macroscopic performance deterioration of reinforced concrete member. International Journal of Computational Materials Science and Engineering 8, 1950005. https://doi.org/10.1142/S2047684119500052

Wells, G.N., de Borst, R., Sluys, L.J., 2002. A consistent geometrically non-linear approach for delamination. International Journal for Numerical Methods in Engineering 54, 1333–1355. https://doi.org/10.1002/nme.462

Wu, J.-Y., 2017. A unified phase-field theory for the mechanics of damage and quasi-brittle failure. Journal of the Mechanics and Physics of Solids 103, 72–99. https://doi.org/10.1016/j.jmps.2017.03.015

Wu, T., Wriggers, P., 2015. Multiscale diffusion–thermal–mechanical cohesive zone model for concrete. Comput Mech 55, 999–1016. https://doi.org/10.1007/s00466-015-1149-y

Xiong, X., Xiao, Q., 2021. Meso-scale simulation of bond behaviour between retarded-bonded tendons and concrete. Engineering Structures 228, 111410. https://doi.org/10.1016/j.engstruct.2020.111410

Xu, S., Li, A., Wang, H., 2017. Bond properties for deformed steel bar in frost-damaged concrete under monotonic and reversed cyclic loading. Construction and Building Materials 148, 344–358.

https://doi.org/10.1016/j.conbuildmat.2017.05.090

Xu, X.-P., Needleman, A., 1994. Numerical simulations of fast crack growth in brittle solids. Journal of the Mechanics and Physics of Solids 42, 1397–1434. https://doi.org/10.1016/0022-5096(94)90003-5

Xu, Y., Shen, W., Wang, H., 1994. An experimental study of bond-anchorage properties of bars in concrete. Journal of Building Structures 15, 26–37.

Xu, Z., Hao, H., Li, H.N., 2012a. Mesoscale modelling of dynamic tensile behaviour of fibre reinforced concrete with spiral fibres. Cement and Concrete Research 42, 1475–1493. https://doi.org/10.1016/j.cemconres.2012.07.006

Xu, Z., Hao, H., Li, H.N., 2012b. Mesoscale modelling of fibre reinforced concrete material under compressive impact loading. Construction and Building Materials 26, 274–288. https://doi.org/10.1016/j.conbuildmat.2011.06.022

Yamamoto, Y., Nakamura, H., Kuroda, I., Furuya, N., 2014. Crack propagation analysis of reinforced concrete wall under cyclic loading using RBSM. European Journal of Environmental and Civil Engineering 18, 780–792. https://doi.org/10.1080/19648189.2014.881755

Yang, Z.-J., Li, B.-B., Wu, J.-Y., 2019. X-ray computed tomography images based phase-field modeling of mesoscopic failure in concrete. Engineering Fracture Mechanics 208, 151–170. https://doi.org/10.1016/j.engfracmech.2019.01.005

Yi, J., Wang, L., Floyd, R.W., Zhang, J., 2020. Rotation-affected bond strength model between steel strand and concrete. Engineering Structures 204, 110060. https://doi.org/10.1016/j.engstruct.2019.110060

Zaitsev, Y., Wittmann, F., 1981. Simulation of crack propagation and failure of concrete. Mat. Constr. 14, 357–365. https://doi.org/doi.org/10.1007/BF02478729

Zhang, J., Wang, Zhiyong, Yang, H., Wang, Zhihua, Shu, X., 2018. 3D meso-scale modeling of reinforcement concrete with high volume fraction of randomly distributed aggregates. Construction and Building Materials 164, 350–361. https://doi.org/10.1016/j.conbuildmat.2017.12.229

Zhang, R., Jin, L., Liu, M., Du, X., Liu, J., 2022. Refined modeling of the interfacial behavior between FRP bars and concrete under different loading rates. Composite Structures 291, 115676. https://doi.org/10.1016/j.compstruct.2022.115676

zhang, W., Huang, Y., 2022. Three-dimensional numerical investigation of mixed-mode debonding of FRP-concrete interface using a cohesive zone model. Construction and Building Materials 350, 128818. https://doi.org/10.1016/j.conbuildmat.2022.128818

Zhao, Y., Wu, Y., Jin, W., 2013. Distribution of millscale on corroded steel bars and penetration of steel corrosion products in concrete. Corrosion Science 66, 160–168. https://doi.org/10.1016/j.corsci.2012.09.014

Zheng, Z., Zeng, C., Tian, C., Wei, X., 2022. Mesoscale numerical investigation on the size effect of concrete uniaxial compressive strength under different contact friction. Construction and Building Materials 346, 128416. https://doi.org/10.1016/j.conbuildmat.2022.128416

Zhou, Y., Jin, H., Wang, B., 2019. Modeling and mechanical influence of meso-scale concrete considering actual aggregate shapes. Construction and Building Materials 228, 116785. https://doi.org/10.1016/j.conbuildmat.2019.116785

Zuo, J., Darwin, D., 2000. Bond slip of high relative rib area bars under cyclic loading. ACI Structural Journal 97, 331–334. https://doi.org/10.14359/864

RÉSUMÉ ÉTENDU EN FRANÇAIS

L'objectif global de cette thèse était de développer des outils de modélisation à l'échelle mésoscopique pour mieux comprendre les phénomènes sous-jacents de la liaison acier-béton, car cette région est d'une grande importance pour la description de la fissuration des structures en béton armé. Des simulations sur des essais d'arrachement ont été réalisées en 3D à l'échelle mésoscopique en utilisant une méthodologie principalement basée sur la mise en œuvre d'un modèle d'interface de zone cohésive avec frottement. L'effet de l'ajout de granulats, l'utilisation de différentes formes de nervures sur les aciers et l'application d'un confinement externe ont ensuite été étudiés.

Dans un premier temps une étude bibliographique a été réalisée. Elle s'est concentrée en particulier sur les phénomènes physiques complexes qui se produisent à l'interface acier-béton. L'essai d'arrachement couramment utilisé pour caractériser l'adhérence a été présenté ainsi que les différentes propriétés qui affectent la loi correspondante de contrainte et de glissement de l'adhérence. Les échelles macroscopique et mésoscopique de la modélisation de la liaison ont été discutées et les principales procédures de description numérique de la liaison acier-béton dans la littérature ont été présentées. En particulier, les modèles d'interface d'épaisseur nulle ont été discutés : modèle de ressort élastique, modèle de friction, modèle de zone cohésive et modèle de zone cohésive frictionnelle. Sur la base de cette étude bibliographique, et pour atteindre l'objectif de la thèse, le choix a été fait de modéliser des échantillons 3D qui prennent en compte la géométrie détaillée des nervures en acier, ce qui était rarement fait auparavant dans la littérature, et qui ouvre la voie à l'étude de l'effet des mécanismes de verrouillage. En outre, la méthode des éléments finis a été choisie afin de déployer les outils développés dans Cast3M, Salome et MFront, qui peuvent être utilisés efficacement pour différentes applications.

Ensuite, la procédure détaillée de génération des spécimens d'essai d'arrachement tridimensionnels numériques a été présentée. Elle utilise le script Combs, principalement pour générer les agrégats dans la matrice considérée. Dans cette thèse, la génération de la barre d'acier et la géométrie détaillée de ses nervures ont été introduites dans le script, donnant la possibilité de générer différentes formes de barres d'acier. Ces échantillons ont été maillés avec un maillage suffisamment fin pour étudier avec précision la distribution des fissures et des contraintes à proximité de l'acier. Des simulations linéaires, incluant un modèle d'élément d'interface linéaire pour la liaison, ont ensuite été réalisées sur une barre lisse et une barre nervurée en chevron afin d'étudier les paramètres de rigidité. Comme prévu, la rigidité en cisaillement domine dans la partie cylindrique et aux extrémités des nervures en acier, tandis que la rigidité normale domine sur les côtés des nervures. Ces études de base ont ouvert la voie à la réalisation de simulations non linéaires à l'aide de modèles d'endommagement pour le béton et non linéaire pour les interfaces acier-béton.

Le modèle d'endommagement de Mazars (Mazars, 1986, 1984) a été utilisé dans le béton pour représenter les phénomènes de rupture, c'est-à-dire l'initiation et la propagation des fissures. Il a été complété par une régularisation exponentielle de Hillerborg en tension, et des modifications en compression ont également été introduites afin d'éviter une dépendance du maillage de la réponse endommagée en compression.

Les modèles classiques ont été considérés à ce stade pour évaluer leur validité lorsqu'ils sont affectés à l'interface acier-béton. Les formulations du modèle de zone cohésive de Tvergaard modifié, initialement présenté dans (Tvergaard, 2003, 1990 ; Wu et Wriggers, 2015), et les modèles d'interface frictionnelle de Coulomb, ont été introduits et leur réponse analysée sur un élément à une interface. L'incapacité de ces deux modèles à reproduire avec précision les résultats expérimentaux extraits de la littérature sur l'essai d'arrachement réalisé sur un échantillon de barre lisse a été démontrée. Ceci a mis en évidence les inconvénients de ces deux modèles et a encouragé la proposition d'un nouveau modèle qui intègre les avantages des deux modèles de zone cohésive et de friction, afin de reproduire correctement le comportement expérimental.

Sur la base de ce résultat, un nouveau modèle de zone cohésive avec frottement (FCZM) a été proposé, et sa formulation détaillée ainsi que sa mise en œuvre sur un élément à une interface ont été présentées. Le modèle FCZM proposé est une combinaison des deux modèles de zone cohésive et de frottement susmentionnés. Le FCZM a pu reproduire le comportement expérimental de la barre lisse après un ajustement approprié des paramètres, en surmontant les limites du modèle de zone cohésive et du modèle d'interface frictionnelle de Coulomb. En outre, le modèle a été capable de reproduire le comportement de l'essai d'arrachement avec des échantillons de barres nervurées. Une certaine calibration a été appliquée aux paramètres du modèle d'interface, en reliant la plupart de ces paramètres aux propriétés du béton et de l'acier environnants, ce qui a donné de bons résultats. En outre, le modèle d'endommagement a produit des résultats similaire à ce qui a été observé dans des simulations numériques issues de la littérature, montrant une fissure au sommet de chaque nervure et une fissure étendue à la dernière nervure. De plus, les régions où le béton est entièrement endommagé sont principalement soumises à des contraintes de traction dans les trois directions principales. D'autre part, les régions devant les nervures étaient toutes sous des contraintes de compression dans les trois directions principales, où des intensités de contraintes très élevées ont été observées.

Par la suite, le FCZM a été utilisé dans différentes applications numériques. Il a d'abord été déployé pour examiner l'effet de l'inclusion de granulats grossiers dans le mélange de béton, au lieu d'un béton homogène. Les paramètres du mortier ont été calibrés sur la base de ceux du béton homogène précédemment utilisé. Des simulations ont été effectuées sur trois échantillons différents, et la capacité du modèle à reproduire le comportement macroscopique en utilisant un béton hétérogène a été prouvée. Cependant, l'endommagement global de l'échantillon, utilisé pour comparer la quantité d'endommagement dans le volume de mortier, a donné des valeurs différentes pour chaque cas hétérogène. Ceci a été expliqué par les différents placements et distributions des granulats dans le volume de mortier. Ainsi, la prise en compte d'un échantillon hétérogène, qui a un coût de calcul très élevé, conduit à de petites différences dans la contrainte d'adhérence moyenne par rapport aux résultats avec des échantillons homogènes. La conclusion est donc que la prise en compte d'un béton homogène semble suffisante pour évaluer cette quantité macroscopique. Cependant, cela peut être insuffisant si, par exemple, une estimation précise de l'endommagement est nécessaire afin de prédire la fissuration dans la zone d’enrobage de l’armature .

Un autre aspect important étudié était l'effet de la géométrie des nervures sur le comportement de la liaison, car les modèles macroscopiques ignorent généralement cette caractéristique. Des simulations sur des barres avec une seule nervure ont été réalisées en faisant varier les dimensions de la nervure. Il a été constaté que la force d'adhérence était principalement affectée par la surface de la nervure, et non par la surface totale adhésive, ce qui est en accord avec certaines conclusions tirées précédemment dans la littérature. Les simulations effectuées sur deux barres nervurées de sections rectangulaires différentes ont donné de bons résultats par rapport à l'expérience. Cela prouve encore plus l'importance du verrouillage mécanique sur le comportement de l'adhésif, comme l'ont indiqué précédemment (Lin et al., 2019). Ensuite, une barre à chevrons a été utilisée et comparée à la barre en spirale utilisée précédemment. Elle a montré une réponse de liaison plus rigide par rapport à la barre en spirale. Les deux barres ayant une surface similaire, la différence dans la contrainte de liaison est liée à la nature de la surface de la nervure. En effet, la surface des nervures habituellement calculée contient des surfaces parallèles à la surface cylindrique et des surfaces qui coupent la surface cylindrique. Il est donc important de modéliser les nervures à l'échelle mésoscopique, en raison de la sensibilité de la contrainte de liaison aux dimensions et à la forme des nervures. Cette information supplémentaire peut être utilisée et incluse comme paramètre dans les modèles macroscopiques pour leur calibration. La surface normale projetée du côté de la nervure transversale est ici considérée comme le paramètre le plus important qui peut être adopté par les modèles macroscopiques pour prédire la variation de la force de liaison.

Dans la dernière partie, l'effet du confinement externe sur un échantillon nervuré a été étudié. Une réponse plus rigide a été montrée en comparaison avec l'échantillon non confiné dans les simulations d'arrachement, ce qui coïncide avec les observations de la littérature. Cependant, le comportement était moins rigide lorsque comparé aux résultats expérimentaux. Ainsi, il serait intéressant de valider cet aspect du modèle en le comparant avec des échantillons ayant une épaisseur d’enrobage plus faible.

Il est important de noter que le modèle numérique a un coût de calcul élevé, et encore plus élevé lorsqu'il inclut les agrégats. La difficulté de convergence est un autre problème lié aux comportements non linéaires considérés. Ils peuvent limiter le domaine d'application de la méthodologie, et empêcher d'approfondir certains aspects.

Suite aux conclusions de cette thèse, plusieurs perspectives ont été proposées. Numériquement, à la méso-échelle, des analyses supplémentaires pourraient être effectuées en utilisant un modèle de béton différent, et pour étudier l'influence des effets thermiques et hydriques. De même, à l'échelle macroscopique, les modèles pourraient évoluer en incluant davantage l'effet des formes des nervures des barres d'acier, en utilisant une certaine fonction de prédiction. D'autre part, il faut davantage de résultats expérimentaux d'essais d'arrachement qui étudient l'effet de la variation de la géométrie des barres d'acier, ce qui serait unique et précieux. En outre, la méthode FCZM proposée n'est pas seulement spécifique à l'interface acier-béton, car elle peut être appliquée à d'autres applications techniques.